# Delft University of Technology

# High Accuracy Terrestrial Positioning Based on Time Delay and Carrier Phase Using Wideband Radio Signals

Dun, H.

**Important note**
To cite this publication, please use the final published version (if applicable).
Please check the document version above.

# High Accuracy Terrestrial Positioning Based on Time Delay and Carrier Phase Using Wideband Radio Signals

# High Accuracy Terrestrial Positioning Based on Time Delay and Carrier Phase Using Wideband Radio Signals

## Proefschrift

ter verkrijging van de graad van doctor
aan de Technische Universiteit Delft,
op gezag van de Rector Magnificus prof. ir. T.H.J.J. van der Hagen,
voorzitter van het College voor Promoties,
in het openbaar te verdedigen op Maandag 4, oktober 2021 om 17:30 uur

door

## Han DUN

Master of Engineering in Communication and Information System,
Shanghai University, Shanghai, China,
geboren te Hubei, China.

Dit proefschrift is goedgekeurd door de promotoren.

Samenstelling promotiecommissie bestaat uit:

| | |
|---|---|
| Rector Magnificus, | voorzitter |
| Dr. ir. C. C. J. M. Tiberius, | Technische Universiteit Delft, promotor |
| Prof. dr. ir. R. F. Hanssen, | Technische Universiteit Delft, promotor |

*Onafhankelijke leden:*

| | |
|---|---|
| Prof. dr. Y. J. Morton, | University of Colorado, Boulder, Verenigde Staten |
| Prof. dr. H. Kuusniemi, | Finnish Geospatial Research Institute, Finland |
| Prof. dr. G. Seco-Granados, | Autonomous University of Barcelona, Spanje |
| Prof. dr. ir. G. J. T. Leus, | Technische Universiteit Delft |
| Prof. dr. ir. P. J. G. Teunissen, | Technische Universiteit Delft |

*In memory of my great-grandfather,*
*Yibang Shen* (沈義榜)

# Contents

# Summary

**High Accuracy Terrestrial Positioning Based on Time Delay and Carrier Phase Using Wideband Radio Signals**

Accurate position solutions are in high demand for many emerging applications. Global navigation satellite systems (GNSS), however, may not meet the required positioning performance, especially in urban environments, due to multipath and weak received power of the GNSS signal that can be easily blocked by surrounding objects. To achieve a high ranging precision and improve resolvability of unwanted reflections in urban areas, a large signal bandwidth is required. In this thesis, a terrestrial positioning system using a wideband radio signal is developed as a complement to the existing GNSS, which can provide a better ranging accuracy and higher received signal power, compared to GNSS.

In the terrestrial positioning system presented in this thesis, a wideband ranging signal is implemented by means of a multiband orthogonal frequency division multiplexing (OFDM) signal. All transmitters are synchronized by time and frequency reference signals, which are optically distributed through the white-rabbit precision time protocol (WR-PTP). Like in GNSS, the to-be-positioned receiver is not synchronized to the transmitters.

Positioning takes place through range measurements between a number of transmitters and the receiver. Time delay and carrier phase are to be estimated from the received radio signal, which propagated through a multipath channel. This estimation is done on the basis of the channel frequency response and using the maximum likelihood principle. To determine whether or not reflections need to be considered in the estimation model, a measure of dependence is introduced to evaluate the change of the precision (i.e., variance), and the measure of bias is introduced to assess the bias of the estimator when the reflection is not considered.

Also, a methodology is proposed for sparsity-promoting ranging signal design in this thesis. Based on a multiband OFDM signal, ranging signal design comes to sparsely select as few signal bands as possible. Using fewer signal bands for ranging leads to less computational complexity in time delay and carrier phase estimation, while the ranging performance can still benefit from a large virtual signal bandwidth, which is defined by the entire bandwidth between the two signal bands at the spectral edges. It is proposed to use the Cramér-Rao lower bound (CRLB) of time delay estimation, the measure of dependence, and the measure of bias as constraints in ranging performance, and formulate an optimization problem to design a sparse multiband signal.

Given the configuration of the terrestrial positioning system, mathematical models for positioning based on time delay and carrier phase measurements are

developed. Using a single epoch of time delay measurements, one can instantaneously obtain a receiver position solution. However, positioning only based on carrier phase requires a series of measurements with a change in geometry. Due to phase biases which are different among different transmitters, and which cannot be separated from the carrier phase cycle ambiguities, the ambiguities are treated as constant float-valued parameters. The receiver needs to move over a large distance, such that the precision of the ambiguity-float position solution can converge to centimeter-level. On the other hand, to account for the phase biases, it is proposed to use corrections produced by taking a so-called snapshot set of carrier phase measurements from all transmitters, at a known position. Then, by taking differences between the carrier phase measurements and the snapshot corrections, the integer nature of the carrier phase cycle ambiguity can be exploited. Consequently, one can obtain the so-called ambiguity-fixed position solution, with high precision as soon as the ambiguities are fixed to integer numbers.

Furthermore, the clock offset obtained along with the receiver position coordinates through the positioning model can be used for receiver frequency synchronization. Through the time-delay-based positioning model, the receiver frequency offset can be coarsely estimated, and consequently can be applied in carrier phase tracking, as a prior compensation. Since the carrier phase measurement is much more precise than the time delay measurement, a fine estimate for the receiver frequency offset can consequently be computed through the carrier-phase-based positioning model.

Finally, based on the developed prototype system, outdoor experiments were conducted to evaluate the feasibility of using the WR-PTP to optically distribute the time and frequency reference for positioning, and to assess the positioning performance of the proposed system and algorithms. The developed experimental prototype system consists of six transmitters, and the ranging signal is transmitted at a central frequency of 3960 MHz with a total bandwidth of 160 MHz. In addition, this ranging signal is periodically transmitted every 1 ms, as a burst packet for a duration of about 0.14 ms. Based on time delay measurements, the position root-mean-square-error (RMSE) is typically at the one decimeter-level, and the precision is at centimeter-level. The standard deviation of the coarse frequency offset estimator is found to be less than 0.05 ppm. Using carrier phase measurements, the RMSE of the ambiguity-float position solution is at decimeter to centimeter-level, and the standard deviation of the fine frequency offset estimator is found to be less than 0.02 ppm. After accounting for the phase biases among the transmitters, the ambiguity-fixed position solution can provide a centimeter-level accuracy and a millimeter-level precision once the ambiguities are fixed into integer numbers, which only requires little receiver displacement.

In conclusion, the proposed and developed terrestrial positioning system can serve as a robust local alternative for precise positioning, or a complement to the existing GNSS in urban environments.

# Samenvatting

**Hoog nauwkeurige terrestrische plaatsbepaling gebaseerd op tijdvertraging en draaggolffase van breedband radiosignalen**

Nauwkeurige plaatsbepaling is nodig voor vele nieuwe toepassingen. Satellietnavigatiesystemen (GNSS) kunnen niet aan alle plaatsbepalingseisen daarvoor voldoen, in het bijzonder in stedelijk gebied, ten gevolge van reflecties en een zwak ontvangen vermogen van het GNSS signaal, dat eenvoudig afgeschermd kan worden door omliggende objecten. Om afstandmeting met grote precisie te realiseren, en ook om ongewenste reflecties in het ontvangen signaal in stedelijk gebied te kunnen onderscheiden, is een grote signaal-bandbreedte nodig. In dit proefschrift wordt een terrestrisch plaatsbepalingssysteem ontwikkeld, als aanvulling op de bestaande satellietnavigatiesystemen, op basis van breedband radiosignalen, die een betere afstandmetingsnauwkeurigheid en een hoger ontvangen signaalvermogen kunnen leveren, vergeleken met satellietnavigatie.

In het terrestrisch plaatsbepalingssysteem, voorgesteld in dit proefschrift, is een breedband signaal voor afstandmeting geïmplementeerd door middel van multiband orthogonal frequency division multiplexing (OFDM). De zenders worden gesynchroniseerd door optische tijd- en frequentie-referentiesignalen, die gedistribueerd worden door het white-rabbit precision time protocol (WR-PTP). Zoals in satellietnavigatie is de in plaats te bepalen ontvanger niet gesynchroniseerd met de zenders.

Plaatsbepaling vindt plaats door afstandmeting tussen een aantal zenders en de ontvanger. Van het ontvangen signaal, dat mede via reflecties bij de ontvanger arriveert, dienen tijdvertraging, welke de tijd is die verstreken is sinds het moment van uitzenden, en draaggolffase geschat te worden. Deze schatting wordt uitgevoerd op basis van de kanaal-frequentie-respons, gebruikmakend van het maximum likelihood principe. Om te bepalen of reflecties al dan niet in het schattingsmodel meegenomen moeten worden, is een maat voor afhankelijkheid geïntroduceerd om de verandering in precisie (variantie) te kunnen evalueren, en een maat voor de systematische fout om de systematische fout te kunnen vaststellen wanneer een reflectie niet in het model meegenomen wordt.

Verder wordt een methodologie voorgesteld voor een schaarsheid-bevorderend signaalontwerp voor afstandmeting. Gebaseerd op een multiband OFDM signaal, komt signaalontwerp neer op het schaars selecteren van zo weinig mogelijk signaalbanden. Het gebruik van minder signaalbanden vraagt rekenkundig minder voor de schatting van de tijdvertraging en de draaggolffase, terwijl de nauwkeurigheid van afstandmeting profiteert van een grote virtuele signaalbandbreedte,

welke gedefinieerd wordt door de gehele bandbreedte gelegen tussen de twee uiterste signaalbanden. Vanuit de nauwkeurigheid van afstandmeting worden voorwaarden opgelegd aan de Cramér-Rao ondergrens van tijdvertragingsschatting, de maat voor afhankelijkheid, en de maat voor systematische fout, en daarmee wordt een optimalisatieprobleem geformuleerd voor het ontwerp van een schaars multiband signaal.

Gegeven de configuratie van het plaatsbepalingssysteem zijn wiskundige modellen ontwikkeld voor plaatsbepaling op basis van metingen van tijdvertraging en draaggolffase. Met tijdvertragingsmetingen op één enkel tijdstip kan men instantaan de ontvanger positie bepalen. Plaatsbepaling op basis van draaggolffasemetingen vereist een serie van metingen waarbij een verandering van de geometrie optreedt. Als gevolg van systematische fase-fouten, die per zender verschillend zijn, en die niet te onderscheiden zijn van de draaggolffasemeerduidigheden, worden de meerduidigheden als constante reëelwaardige parameters behandeld. De ontvanger moet zich over een behoorlijke afstand verplaatsen, alvorens een centimeter-precieze plaatsbepalingsoplossing verkregen kan worden. Anderzijds kunnen deze systematische fase-fouten in rekening gebracht worden door correcties te gebruiken, die verkregen worden uit een momentopname van draaggolffasemetingen van alle zenders, genomen op een bekende positie. Door vervolgens verschillen te nemen tussen de fasemetingen en deze correcties, kan het geheeltallig karakter van de draaggolffasemeerduidigheid benut worden. Daarmee kan men een plaatsbepalingsoplossing verkrijgen waarbij de meerduidigheden vastgezet worden op gehele getallen, en een hoge precisie direct bereikt wordt, zo snel de meerduidigheden vastgezet zijn.

De klokfout, die via het plaatsbepalingsmodel tegelijkertijd met de ontvanger positie-coördinaten verkregen wordt, kan gebruikt worden om de ontvanger-frequentie te synchroniseren. Middels het tijdvertraging gebaseerde plaatsbepalingsmodel kan de ontvanger-frequentieverschuiving globaal geschat worden, en vervolgens toegepast worden, als a-priori compensatie, in het draaggolffasemetingsproces. Daar de draaggolffasemeting veel preciezer is dan de tijdvertragingsmeting, kan een precieze schatting voor de ontvanger-frequentieverschuiving vervolgens bepaald worden met het plaatsbepalingsmodel op basis van draaggolffasemetingen.

Tot slot zijn buiten-experimenten uitgevoerd om de haalbaarheid van het gebruik van WR-PTP om een tijd- en frequentie-referentie optisch te distribueren voor plaatsbepaling te evalueren, en om de plaatsbepalingsprestaties van het voorstelde systeem en de voorgestelde algoritmes vast te stellen. Het ontwikkelde experimentele prototype systeem bestaat uit zes zenders en het signaal voor afstandmeting wordt uitgezonden op een frequentie van 3960 MHz, met een totale bandbreedte van 160 MHz. Dit signaal wordt periodiek elke 1 ms uitgezonden, voor een duur van 0.14 ms. Met tijdvertragingsmetingen is de plaatsbepalingsnauwkeurigheid, uitgedrukt in root-mean-square-error (RMSE), typisch op decimeter-niveau, met een precisie op centimeter-niveau. De standaardafwijking van de globale schatter voor de frequentieverschuiving is kleiner dan 0.05 ppm. Met draaggolffasemetingen loopt de RMSE van de positieoplossing met reëelwaardige fa-

semeerduidigheden van centimeter- tot decimeter-niveau, en is de standaardaf-
wijking van de precieze schatter voor de frequentieverschuiving kleiner dan 0.02
ppm. Wanneer de systematische fase fouten van de zenders in rekening gebracht
worden kan de positieoplossing, waarbij de fasemeerduidigheden op gehele ge-
tallen vastgezet zijn, welk slechts een kleine verplaatsing van de ontvanger vereist,
een nauwkeurigheid leveren op centimeter-niveau en een precisie op millimeter-
niveau.

Samenvattend kan het voorgestelde en ontwikkelde plaatsbepalingssysteem
fungeren als een robuust lokaal alternatief voor precieze plaatsbepaling, of als een
aanvulling op bestaande satellietnavigatiesystemen in stedelijk gebied.

# 总结

**利用宽带信号基于时延和载波相位的高精准路基定位系统**

新兴的应用及场景对定位的准确度（accuracy）提出了越来越高的要求。由于全球导航定位系统（Global Navigation Satellite Systems, GNSS）易受多径误差影响及接收功率较弱等缺陷，使其信号在某些复杂的环境中，如城市或室内，容易被周围的建筑物遮挡，从而无法满足用户对于高精度定位的需求。本文提出了一种基于宽带测距信号的路基定位理论，并搭建了系统原型，通过增加测距信号的带宽以提升 GNSS 接收机对于多径的分辨能力，从而达到了高精度定位的目的。与既有的全球导航卫星系统相比，该路基定位系统可提供更高的定位精度及更强的接收信号功率，因此可作为全球导航卫星系统的补充或替代产品。

本文所提出的路基定位系统中使用的宽带测距信号是通过多带频分复用（Orthogonal Frequency-Division Multiplexing, OFDM）技术实现，并基于"白兔"精确时间协议（White-Rabbit Precision Time Protocol, WR-PTP）利用光以太网数据传输链路将发射机的时间和频率上的同步。类似于全球导航定位系统，接收机钟一般不与发射机的钟同步。

该路基定位系统通过测量所有发射机和接收机之间的距离，实现接收机的位置确定。该距离利用最大似然准则和信道频率响应，从接收到的无线测距信号中估计传输时延和载波相位获得。本文提出并了独立程度（measure of dependence）这一指标来量化由于在模型中考虑反射分量对估计精确度（precision）的影响，同时本文利用偏差程度（measure of bias）来衡量由于在模型中忽略反射分量所引入的偏差。

此外，本文同时提出了一种设计稀疏测距信号的方法。该方法基于多带 OFDM 信号，使得测距信号设计可转化成尽可能稀疏地选择信号频带。该方法的优势在于使用较少的信号频带测距，降低了时延估计和载波相位估计的计算复杂度，同时定位的精准度也受益于较大的虚拟信号带宽。该虚拟信号带宽定义为两个左右边缘频带之间的频率差。本文利用时延估计的克拉美罗下界、独立程度和偏差程度作为测距性能的约束来描述最优化问题，并以此设计稀疏的测距信号。

本文同时建立了基于传输时延和载波相位观测值的路基定位数学模型。该模型通过信号的传输时延进行定位，可以实现单历元确定接收机位置。由于在不同的发射机的载波相位中含有不同的相位偏差，其相应的相位整周模糊度将作为浮点常数进行估计。值得注意的是利用载波相位进行定位则需要定位几何条件发生变化。接收机通常需要移动较大的距离才能使得接收机位置坐标浮点解（ambiguity-float solution）的准确度收敛到厘米级。此外，我们可以在已知位置上对所有发射机进行载波相位观测，并基于原始"快照"（snapshot）测量值产生校正数。通过计算载波相位观测值与校正数之间的差值消除不同接收机之间的不同载波偏差所带来的影响，恢复相位模糊度的整周特性，并作为整数值进行估计。在将载波相位整周模糊度固定为整数值后，我们便能获得具有高精度的模糊度固定解（ambiguity-fixed

solution)。

在本文提出的路基定位模型中，接收机与发射机的频率同步通过估计接收机钟差实现。接收机的频偏可以利用基于传输时延的定位模型所得到的钟差来粗略地估计，因此在载波相位跟踪时该频偏可得以补偿，进而避免产生周跳。相比于传输时延，载波相位可以提供更高的测距精度，因此本文利用基于载波相位的路基定位模型所计算得到的残留钟差实现了细频偏估计。

最后，本文搭建了该路基定位系统的原型，通过户外实验验证了利用商用光纤网络基于 WR-PTP 技术实现定位发射机时间和频率同步的可能性，并验证了所开发的路基定位原型系统的性能。该路基定位原型系统由六个发射机组成。测距信号的中心载波频率为 3960 MHz，可用带宽为 160 MHz。此外，测距信号以 0.14 毫秒的突发包的形式每 1 毫秒周期性地传输。利用传输时延观测值得到的定位解的均方根误差一般在分米级，其精度一般在厘米级。粗频偏估计的标准差小于 0.05 ppm。利用载波相位得到的模糊度浮点定位解的均方根误差在分米到厘米级之间，且细频偏估计的标准差小于 0.02 ppm。通过改正不同接收机之间的相位偏差，载波相位模糊度可以被固定为整数，以此得到接收机位置的模糊度固定解。固定解可以实现厘米级的准确度和毫米级的精度，且接收机只需要移动较短的距离。

作为结论，本文中提出并开发的路基定位系统可以作为既有的全球导航卫星系统的局部替代或补充，并用于城市环境下的精准定位。

# 1

# Introduction

Global Navigation Satellite Systems (GNSSs) are widely used to provide position, navigation and timing (PNT) services. In an open space and favorable operation circumstances, a meter-level positioning accuracy can be achieved using code delay measurements in stand-alone mode. A centimeter level accuracy can be achieved using carrier phase measurements either with an additional reference station or based on corrections provided by typically a global infrastructure. However, atmospheric perturbation, multipath and blockage can make GNSS fail to provide accurate position solutions in urban canyons and closed environments.

As the GNSS signals penetrate through the ionosphere which retard their propagation speed with respect to free space, an extra time delay that could be more than 300 ns in worst case scenario, will be introduced in the observation [1]. To improve the positioning accuracy, differential GNSS (DGPS) is generally applied to eliminate such errors with two GNSS-receivers (i.e., reference station and rover, up to about 10 km baseline)[2], which is also known as RTK (real time kinematic) based on the carrier phase measurements with integer ambiguity resolution, or PPP (precise point positioning)-RTK [3] if correction information provided by a reference network is available. Moreover, a geomagnetic storm, characterized by increased ionosphere range delays, and scintillation effects [4], will largely increase the occurrence of cycle-slips, and introduce a decimeter to meter level error in single-frequency GPS-PPP [5].

In addition, the GNSS signals only occupy a few MHz of bandwidth [6], which provides a limited time resolution. For example, given a 10 MHz signal bandwidth (i.e., chip-rate) [7], the corresponding chip time is 0.1 $\mu$s (i.e., 30 m in distance). Therefore, if the additional delay of the reflected path is less than 0.1 $\mu$s, such a reflection will be overlapped with the LoS path in the received signal. Consequently, time delay estimation and carrier phase estimation, which are commonly used to obtain the observables for positioning, will easily be affected by multipath [8] in urban scenarios, where precise positioning, however, is highly demanded.

As the GNSS satellites fly in medium Earth orbit (MEO) with more than 20000

**1**

km of propagation distance, the received signal power from the GNSS satellite is very low, typically about -130 dBm or less [9]. Hence, the GNSS signal can be easily blocked in urban scenarios and indoor environments, and could also be jammed by natural or man-made interference [6].

Therefore, considering the aforementioned limitations of the existing GNSS, also because accurate position solutions recently become much needed in various emerging applications, such as automated driving and intelligent transportation [10, 11, 12], internet-of-things [13, 14], emergency services [15], etc., various terrestrial positioning systems have recently been proposed as complements to the GNSS, and can be used in GNSS challenged outdoor and indoor environments.

## 1.1. Radio-based Terrestrial Positioning System

In this section, a brief review of existing radio-based terrestrial positioning system is provided. Unlike in GNSS, in a terrestrial positioning system, the radio transmitters (i.e., pseudolites, or anchor/base stations) are generally fixed and static. Firstly, different types of commonly used ranging signals are presented. Secondly, synchronization among the radio transmitters is discussed, as the ultimate positioning performance depends on the quality of synchronization. Lastly, the ranging observables that are often used for positioning are introduced.

### 1.1.1. Ranging Signals

In principle, any type of signal can be used to obtain range information. Generally, the most commonly used ranging signals for terrestrial applications can be divided into four categories: GNSS/GPS(-like) narrow band signals, ultra-wideband (UWB) signals, signals-of-opportunity (SOP), and other signals designed/optimized specifically for ranging.

#### GPS/GNSS-like Narrowband Signal

GPS/GNSS(-like) narrowband signals are typically generated using direct sequence spread spectrum (DSSS) with binary phase shift keying (BPSK) modulation. The spreading waveform is a series of rectangular pulses determined by a pseudo-random noise (PRN) code (e.g., Gold sequences [16]). In addition, binary offset carrier (BOC) [17] signals are also used in GNSS, which offers spectral separation.

Using GPS-like signals, ground-based systems, such as Locata [18, 19, 20], form one type of solutions for terrestrial positioning. Radio transmitters (i.e., pseudolites) transmit a PRN code ranging signal in the 2.4 GHz ISM (Industrial Scientific Medical) band. With a licence, the PRN code can also be directly transmitted at GNSS frequencies [21, 22, 23]. Signal processing techniques and positioning models that have been used in GPS can be applied in these GPS-like systems without too much modification.

Nevertheless, due to a narrow signal bandwidth, typically about 10-20 MHz, ranging performance of using GPS-like signals will still be deteriorated in multipath conditions.

## UWB Signal

Ultra-wideband (UWB) signals have also been extensively studied for short-range (indoor) positioning [24, 25, 26, 27, 28, 29], due to its large signal bandwidth ($\geq 500$ MHz) and the resulting high time resolution.

Impulse radio (IR)-UWB system is generally used for ranging, in which a picosecond duration pulse is transmitted and received. However, due to a large signal bandwidth, it is difficult and expensive to acquire the signal with a sampling rate beyond the Nyquist frequency which will typically be in the order of Giga-samples per second. Energy detection (ED) is a widely used low-complexity UWB receiver architecture. Hence, unlike in a GNSS receiver, a locally generated reference signal is not needed to determine time delay, for example, based on correlation. On the other hand, based on ED and a specified threshold, the ranging distance of an IR-UWB system will be limited, as a large propagation distance results in a large attenuation of the UWB ranging pulse [30, 31].

Additionally, using a UWB signal, due to a high time resolution and the resulting resolvability, one will receive multiple pulses in multipath conditions, and needs to determine which pulse is associated with the direct propagation path. The positioning performance will deteriorate in non-line-of-sight (NLoS) conditions, without applying NLoS identification and mitigation techniques [32, 27, 33].

## Signal-of-Opportunities

Signals from existing communication systems can also be exploited for ranging and positioning as Signals of Opportunity (SOP), such as 3G/cellular CDMA (code division multiple access) [34, 35, 36], 4G/LTE (Long Term Evolution) [37, 38, 39, 13, 40, 41], 5G [42, 43, 44, 45], DVB-T (Digital Video Broadcast-Terrestrial) [46, 47, 48, 49, 50, 51], Bluetooth [52, 53, 54] and Wi-Fi [55, 56, 57, 58]. Although these SOPs can be easily accessed both in indoor and outdoor GNSS-challenged environments, such signals and systems are not specifically designed for precise positioning.

For communication, in order to compensate the distortion on the received signal due to multipath, channel estimation is generally needed. Based on the resulting channel frequency response, one can further estimate the range information particularly for the LoS path. However, synchronization among radio transmitters and continuous transmission may not be guaranteed, also due to a relatively limited signal bandwidth, the positioning accuracy generally remains at the meter-level.

## Other Signal Designs for Ranging

Recently, signal design has been investigated particularly for ranging and positioning. Unlike signal design in telecommunication, which aims to ultimately improve the overall data transmission rate, signal optimization for ranging is to improve the performance of time delay estimation when spectral resources are limited.

Placing signal power more toward the frequency band edges, will improve the precision of time delay estimation [59, 60, 61], according to the Gabor bandwidth (GB) and the Cramer-Rao lower bound (CRLB) analysis [62]. Hence, BOC signals

[17, 63] used in GNSS can offer a better ranging accuracy than the standard BPSK signals, although they were originally designed to avoid interference. Similarly, a Dirac-rectangular power spectral density (PSD) is proposed in [64], so that the GB can be largely increased by two additional Dirac pulses at the edges of the rectangular spectrum. If signal design is only based on the GB analysis, the ranging signal may become very sensitive to multipath effects. Therefore, a multivariate CRLB, which not only considers the parameter of interest and noise, but also the effects of reflections and interference, is considered as the performance criterion for signal design [65, 66]. To fully exploit the benefit provided by the designed signal based on the multivariate CRLB, unbiased estimation is required. However, obtaining an unbiased estimate is difficult to achieve in practice, as the multipath channel condition is generally not accurately known a priori.

### 1.1.2. Synchronization
Synchronization among transmitters is crucial for positioning, as one-way range information is directly retrieved from the measurement of the signal travel time. Unlike in GNSS satellites which equip expensive and stable atomic clock, the radio transmitters in a terrestrial system are generally synchronized either directly based on the received wireless signal, or through commonly distributed time and frequency reference signals (i.e., 1 PPS (pulse-per-second) and 10 MHz).

#### GNSS Time and Frequency Transfer
As existing GNSS anyway offers time and frequency transfer functionality, synchronization among radio transmitters can be achieved by using the received GNSS signals, assuming that these radio transmitters are at favourable locations. GNSS-based time synchronization can typically provide an accuracy in the order of 10 ns [67, 68], up to hundreds of nanoseconds. A nanosecond level accuracy is acceptable for most telecommunication system [69, 70]. However, this accuracy is not sufficient for positioning, as a 1 ns timing error is corresponding to an about 30 cm offset in distance.

Using a more advanced setup and processing technology like PPP [71], a nanosecond accuracy can be achieved. However, the system needs to be carefully calibrated. Additionally, in a GNSS-challenged environment, where a terrestrial positioning system comes to be needed, GNSS-based synchronization is unlikely to be achieved within an acceptable performance.

#### Wireless Synchronization
To be fully independent from GNSS, the terrestrial radio transmitters can be synchronized based on round-trip time synchronization using the wireless signal. For example, in the Locata system [19, 18], a so-called TimeLOC technology is proposed using code and carrier phase measurements for synchronization, and a 30 ps level accuracy is claimed. In an IR-UWB system, due to its large signal bandwidth and the resulting fine time-resolution, one can simply use time delay estimation for accurate synchronization. As presented in [72], an IR-UWB-based synchronization error can be in the order of 1 ns.

Since the performance of the wireless synchronization depends on the wireless channel condition, the locations of the pseudolites (radio-transmitters) should be carefully selected to avoid severe multipath. In addition, the system (e.g., the RF front-end, cabling) needs to be carefully calibrated.

**Time and Frequency Distribution through Coaxial Cables**
To avoid the impact of multipath on clock synchronization, like in [23], one can distribute the common time and frequency reference signals (i.e., 1 PPS and 10 MHz) through coaxial cables to all transmitters for synchronization. However, the temperature stability of coaxial cables is poor, which results in phase drifts and reduces the stability of the distributed reference signals [73]. These effects scale with the coaxial cable length, hence, such a system can only be implemented within a limited area.

**Time and Frequency Distribution through Optical Fibers**
Alternatively, optical fibers can be used to distribute time and frequency reference signals, which offer higher temperature stability than the coaxial cables, and can be used in long-distance networks. Like in [74], a nanosecond accuracy of synchronization can be achieved by using the commonly distributed time and frequency reference through a radio-over-fiber (RoF) link. Instead of directly transmiting time and frequency reference signals through the optical fiber, White Rabbit Precision Time Protocol (WR-PTP), initiated by CERN (European Organization for Nuclear Research), has recently been proposed for sub-nanosecond accuracy of synchronization along with deterministic Ethernet-based data transfer [75, 76, 77, 78].

### 1.1.3. Measurements for Positioning
There are different types of measurements obtained from a terrestrial system for positioning. Like in GNSS, time delay and carrier phase are also commonly used in terrestrial positioning system. As the received power of the ranging signal in the terrestrial system is much stronger than the one from GNSS, and is generally well above the noise level, received signal strength (RSS) can also be applied for ranging without deconvolving the received signal. Additionally, with the benefit of spatial diversity using an antenna array or a multiple-input and multiple-output (MIMO) system, angle-of-arrival (AoA) can also be exploited for positioning.

**Time-of-Arrival**
Positioning mainly relies on range measurements, and these ranges are commonly derived from time delay estimation or time-of-arrival (ToA) measurements based on the received signal.

Since the accuracy of time delay estimation is inversely proportional to the signal bandwidth, instead of using a GPS-like signal or other narrow band signal, one could, for example, use an ultra-wideband (UWB) signal [79, 80, 81] or other type of signal (e.g., a sparse multiband signal [82]) with a large signal bandwidth for ranging and positioning, which can achieve a high accuracy in time delay estimation.

The generalized correlation method [83, 84] (i.e., matched filter (MF)) is commonly used to determine the ToA. However, the resulting estimates are often biased in a multipath channel, as reflections are not considered in the locally generated reference signal. Therefore, a multi-branch cross-correlation [85, 86, 87] is proposed to mitigate the error introduced by multipath. Similarly, to improve the performance of time delay estimation in a multipath channel, one can jointly estimate the time delay for both LoS path and reflection based on a Maximum Likelihood (ML) principle [88, 39, 89]. However, multivariate ML estimation requires enormous computational power to obtain an unbiased solution [90]. With a lot of reflections, the problem may get ill-conditioned and be troublesome to solve properly. Therefore, subspace (or eigen-decomposition) methods, such as MUSIC (MUltiple SIgnal Classification), ESPRIT (Estimation of Signal Parameters via Rotational Invariance Technique) [91, 92, 93], have also been applied for time delay estimation, which largely reduce the computational complexity compared to the multivariate ML method, and also provide higher resolution than the simple MF method. However, the subspace methods require a large amount of snapshot measurements, based on either time, frequency or spatial diversity, to compute an accurate sample covariance matrix. Nevertheless, unbiasedness of the estimator derived from the subspace method cannot be guaranteed.

### Phase-of-Arrival

Compared with time-delay-based range measurements, carrier phase or phase-of-arrival (PoA) measurements can provide more precise range information due to the wavelength of the central carrier, which is generally much smaller than the sample interval. However, one can only estimate the fractional part of the carrier phase. Therefore, integer phase cycle ambiguities should be properly resolved for all transmitter-receiver links, in order to derive a unique position solution with high precision.

In GNSS, the carrier phase is obtained from the Q (quadrature) and I (in-phase) outputs of the correlator between the received signal and the replica code at the prompt branches through the arc-tangent [9]. Recently, carrier phase estimation using SOPs has also been investigated. For example, in [51], the carrier phase is proposed to be computed from a continuous middle sub-carrier of a DVB-T signal. In addition, for positioning, the carrier phase can be also be determined by integrating the estimated Doppler frequency offset over the observation period [94, 37, 45]. In [95], the carrier phase is proposed to be computed by taking the argument of the sum of the channel frequency response. Generally, the estimate of the carrier phase or the Doppler shift is obtained by using a phase locked loop (PLL) [96, 97].

### Angle-of-Arrival

An angle-of-arrival (AoA) measurement shows the direction of the received signal based on the phase difference among different antennas in an antenna array [98]. Using AoA measurements for positioning, the receiver no longer needs to be synchronized to the transmitters, but should be equipped with multiple antennas. However, given a limited number of antennas within finite dimensions and

1

the resulting limited spatial resolution, AoA measurements can easily be affected by multipath [93]. Therefore, the AoA measurement is generally used with other measurements to increase the positioning accuracy [99, 100].

### Received Signal Strength
As the longer the propagation distance is, the more signal will be attenuated, received signal strength (RSS) can also be exploit for ranging. Compared with the other types of measurements, the RSS is the easiest and cheapest observable that one can obtain for ranging. Neither additional hardware nor a complicated algorithm is needed to be implemented in a to-be-positioned user device (e.g., smartphone). During the COVID-19 pandemic, most contact tracing applications are generally based on RSS measurements from Bluetooth [101, 102]. However, RSS is sensitive to the wireless channel, such as shadowing, multipath, and the orientation of the wireless device [7]. Therefore, the ranging accuracy using RSS is at meter-level or worse [103, 104].

### 1.1.4. Requirements
Generally, to develop a terrestrial positioning system, one needs to consider the following requirements

- The radio transmitters should be synchronized in time and frequency.

- In order to compute the position solution of a radio receiver, the position of the transmitters should be measured/estimated a priori;

- In order to support emerging applications, such as IoT, unmanned driving, at least a sub-meter level positioning accuracy is required;

- A relatively large (virtual) signal bandwidth is needed to improve the resolvability of different paths and overcome multipath effects, which often occur in an urban and indoor environment.

## 1.2. "SuperGPS" Project
The work presented in this thesis is carried out in the context of the "SuperGPS" project: *accurate timing and positioning through an optical-wireless distributed time and frequency reference*, funded by the Dutch Research Council (NWO) under Grant 13970. Fig. 1.1 presents a vision of a hybrid optical-wireless terrestrial positioning system proposed in the SuperGPS project, which is also referred to as the *SuperGPS system* in this thesis. The proposed SuperGPS system aims to meet the requirements presented in section 1.1.4 using the following solutions.

In the proposed SuperGPS system, all radio transmitters (i.e., pseudolites) are synchronized with common reference signals (i.e., 10 MHz and 1 PPS) generated by a central atomic clock. The reference signals are distributed to each radio transmitter through an optical communication infrastructure using the White-Rabbit precision time protocol (WR-PTP) [77, 105]. Using optically distributed time and
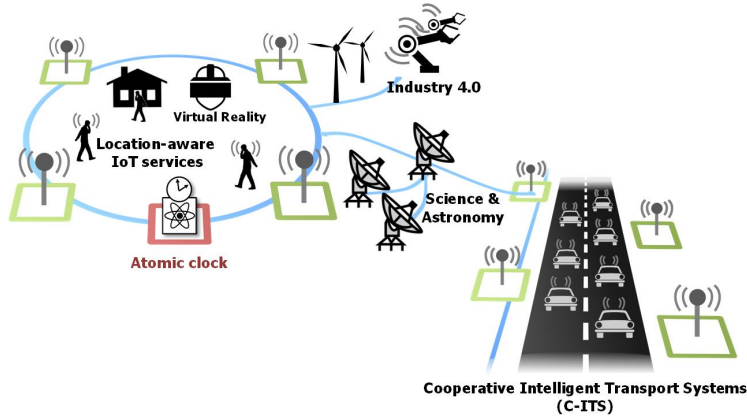
Figure 1.1: Schematic of hybrid optical-wireless terrestrial positioning system. Blue line: existing optical communication infrastructure, green square: radio transmitters, and red square: central atomic clock.

frequency reference signals through the existing optical communication infrastructure, provides the flexibility to expand the system over a large area. And synchronization, as is the case of wireless distribution of the reference signals among the transmitters, is not affected by multipath which is prominently present in an urban area.

In addition, the developed prototype system supports a large signal bandwidth (e.g., 160-320 MHz) for ranging, which improves the resolvability of reflections in a multipath channel. A decimeter level positioning accuracy is expected from the SuperGPS system.

## 1.3. Main Contributions and Thesis Outline

This section presents the structure of this thesis by contributions, which are published as the journal [J] and conference [C] articles presented in section 'List of Publications' (see the end of this thesis).

| Chapter | 2 | 3 | 4 | 5 | 6 | 7 |
|---------|---|---|---|---|---|---|
| **[J1]** | x | | x | | | |
| **[J2]** | | x | | x | | |
| **[J3]** | | | | | x | x |
| **[C1]** | x | | x | | | |
| **[C2]** | | x | | x | | |
| **[C3]** | | x | | x | | |
| **[C4]** | | | x | | | x |

**1**

### Chapter 2

In chapter 2, a multiband-OFDM (orthogonal frequency division multiplexing) signal model is introduced. OFDM has been widely used in existing telecommunication systems [37, 43, 46, 57], and multiband signals have also been adopted in UWB systems [106]. Therefore, to allow for an easy integration of the proposed system in other communication systems and to be time-efficient, a periodically transmitted burst-like multiband OFDM signal is selected as a ranging signal in this work. As the receiver is generally not synchronized to the transmitters, the impact of receiver frequency offset on the received multiband OFDM signal is presented in this chapter, and the received signal model also includes the effects of multipath.

> **Contribution**
>
> For purpose of ranging, develop measurement model particularly for multiband OFDM signal, and account for receiver frequency offset and multipath effects.

### Chapter 3

By exploiting the frequency relation among different signal bands, time delay estimation based on multiband OFDM signal is introduced in Chapter 3. The Cramer-Rao lower bound (CRLB) of time delay estimation is first analyzed. Then, based on the Maximum Likelihood (ML) principle, the time delay can be jointly estimated for a LoS path and reflections in a multipath channel. In a multipath channel, the *measure of dependence* and *measure of bias* are defined, and used to analyze the impact of a reflected path on time delay estimation. Other time delay estimation methods, such as matched filter (MF), subspace-based method (e.g., MUSIC, ESPRIT), inverse Fourier transform, and sparsity-promoting deconvolution method are also reviewed in this chapter.

> **Contribution**
>
> Using multiband OFDM signal, present ML-based time delay estimation, and means to analyze time-based ranging accuracy, and computational complexity, when considering and neglecting reflections in estimation model.

### Chapter 4

Carrier phase estimation based on a burst-like multiband OFDM signal is presented in Chapter 4. Similar to time delay estimation, based on the ML principle, the complex propagation gain of the LoS path can be jointly estimated with those from reflections. Then, the carrier phase is obtained by taking the argument of the LoS complex gain. The impact of a reflection on the accuracy and bias of complex gain estimation is analyzed. In addition, as the ranging signal is only periodically transmitted, cycle-slips could be introduced in (time series of) carrier phase measurements, as the receiver frequency offset will cause an additional phase rotation

**1**

during the transmission period, even when the receiver is stationary. Therefore, to avoid cycle-slips, it is proposed to estimate and compensate the receiver frequency offset before estimating the complex gain and the resulting carrier phase.

> ### Contribution
>
> Considering impact of receiver frequency offset, multipath, and non-continuous transmission scheme of multiband OFDM signal, introduce ML-based carrier phase estimation, and present solutions to avoid cycle slips in phase unwrapping particularly introduced by receiver frequency offset.

### Chapter 5

In Chapter 5, signal design particularly for ranging is proposed. Unlike for communication where the data rate is of interest, it is not necessary to occupy all available signal spectrum for ranging and position. The measure of dependence, which indicates how accuracy changes when a reflection is considered in the estimation model, the measure of bias that reflects how large the bias can be if a reflection is not considered in the estimation model, and the CRLB are used as criteria, to sparsely select only a few signal bands from a large spectrum range, as to create a large virtual signal bandwidth. Using a sparse multiband signal, the computational complexity of both time delay estimation and carrier phase estimation can be largely reduced, while the estimation performance is still comparable to using the entire frequency range.

> ### Contribution
>
> For positioning, develop method to sparsely select only few signal bands within large virtual signal bandwidth, which reduces computational complexity to obtain range information, and meets user specified ranging precision, while still offering strong resistance against multipath.

### Chapter 6

Positioning models using only time delay measurements, or only carrier phase measurements are presented in Chapter 6. Using *time-of-arrival (ToA)* measurements, the receiver position solution is computed along with the clock error caused by the receiver sampling frequency offset. As all transmitters are assumed to be synchronized through commonly distributed reference signals, position solutions can also be computed using the *Time-Difference-of-Arrival (TDoA)* measurement, in which the receiver-dependent clock error is eliminated.

On the other hand, carrier phase offers higher ranging precision than time delay. Hence, *phase-of-arrival (PoA)* or *phase-difference-of-arrival (PDoA)* measurements can be used for positioning, and the position solutions should be estimated along with the carrier phase cycle ambiguities. However, due to different initial carrier phase offsets and different hardware delays among the transmitters, the

carrier phase ambiguity of each transmitter-receiver link is no longer an integer number. Thus, only the so-called float solution can be obtained. Additionally, a large receiver displacement is required to create a sufficient change in geometry, so that the precision of the float solution can converge to a reasonable level. In order to exploit the integer nature of the carrier phase ambiguity, a snap-shot set of carrier phase measurements for all transmitters is proposed to be taken at a known position, and to be used as a correction file. By taking the difference between the corrections and the carrier phase measurements, the carrier phase ambiguities can be treated as integer numbers in the positioning models. Consequently, one can obtain the so-called fixed solution based on the integer ambiguity resolution, which can be done by using the LAMBDA (Least-squares AMBiguity Decorrelation Adjustment) method.

> **Contribution**
>
> Using carrier phase for precise positioning, propose to measure and use snapshot set of carrier phase measurements for all transmitters at known location as corrections, in order to be able to fix carrier phase cycle ambiguities to integer numbers and obtain so-called fixed position solutions. Present receiver frequency synchronization based on clock error estimated along with receiver coordinates in positioning model using time delay or carrier phase measurements.

### Chapter 7

Outdoor experimental positioning validation results obtained in realistic circumstances are presented in Chapter 7. The developed SuperGPS prototype system consists of six transmitters, and all transmitters are synchronized based on the optically distributed time and frequency reference signals through the WR-PTP. Using time delay measurements, a decimeter level positioning accuracy is achieved. Based on carrier phase measurements, a decimeter to centimeter level accuracy can be attained while using the float solution. By exploiting the integer nature of the carrier phase ambiguities, a quickly converging centimeter-level positioning accuracy is achieved for the fixed solution. Additionally, the clock error in time delay and carrier phase measurements, which is introduced by the receiver frequency offset and estimated along with the position coordinates, can be used for fine synchronization, and potentially be applied for terrestrial time and frequency transfer.

> **Contribution**
>
> Evaluate positioning performance, based on time delay and carrier phase using proposed sparse multiband OFDM burst-like signal in an on-purpose built prototype system, and demonstrate cm to dm level positioning accuracy in realistic outdoor scenario.

**1**

### Chapter 8
Conclusions of the work presented in this thesis, and recommendations of designing a terrestrial positioning system are summarized in Chapter 8.

# 2

# Multiband OFDM Signal Model

Orthogonal Frequency Division Multiplexing (OFDM) modulation has been widely used for various telecommunication systems, which largely improves the spectrum efficiency compared to a single-carrier modulation, and increases the resistance against inter-symbol interference (ISI) introduced by multipath. In this work, OFDM is also considered as the modulation of the ranging signal. In addition, to further improve the flexibility of spectrum management, a multiband OFDM signal is chosen. By considering the frequency relation among different signal bands placed at different locations in the spectrum, a large virtual signal bandwidth can be created, which ultimately improves the ranging accuracy.

In this chapter, we aim to develop the signal model of the multiband OFDM signal, which will be used to estimate the range information such as time delay and carrier phase. First, the concept of OFDM modulation is introduced. Then, as the receiver is generally not synchronized to the transmitters, the impact of the receiver frequency offset [107] on the received signal is presented, as well as the impact of multipath [108]. Finally, the implementation of a multiband signal and a measurement model of the sampled channel frequency response are introduced.

## 2.1. Concept of OFDM signal

Using the inverse fast Fourier transform (IFFT), an OFDM symbol is generated by modulating $N_s$ complex data points onto $N_s$ sub-carriers, as shown in Fig. 2.1. In order to combat inter-symbol interference (ISI) caused by a multipath channel, a guard interval (i.e., cyclic prefix, CP) with $N_g$ samples is added to every OFDM symbol [109]. Therefore, there are $N_g + N_s$ samples in each OFDM symbol, and

the $n$-th sample of the $q$-th OFDM symbol ($q \geq 0$) in baseband is given by

$$s_b[n] = \frac{1}{N_s} \sum_{i=-N_s/2}^{N_s/2-1} c_{i,q} \exp\left(j\frac{2\pi(q(N_g + N_s) + N_g + n)i}{N_s}\right), \quad n = \begin{cases} -N_g, \ldots, -1 & \text{(CP)} \\ 0, \ldots, N_s - 1 & \text{(data)} \end{cases},$$

(2.1)

where $i$ denotes the subcarrier index, and $c_{i,q}$ denotes the $q$-th complex symbol modulated on the $i$-th sub-carrier. The sampling interval is indicated by $T_s$ in the sequel, and $\Delta f$ is the subcarrier spacing, given by

$$T_s = \frac{1}{B}, \quad \Delta f = \frac{B}{N_s},$$

(2.2)

where $B$ denotes the bandwidth of the OFDM signal.
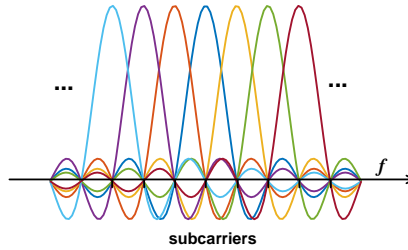


Figure 2.1: Spectrum of OFDM signal, $N_s$ subcarriers are separated by a spacing of $\Delta f$, and together span a bandwidth of $B$.

After digital-to-analog conversion (DAC), the baseband OFDM signal $s_b(t)$ is modulated on a carrier with frequency $f_c$. Hence, the passband OFDM signal $s_p(t)$ can be expressed as

$$s_p(t) = \Re\left\{s_b(t)e^{j2\pi f_c t}\right\},$$

(2.3)

where $\Re\{\cdot\}$ denotes the real part of a complex value.

At the receiver, the passband signal, perturbed by the channel and noise, is down-converted to baseband by the carrier frequency $f_c$

$$r_b(t) = 2\mathscr{F}_l\left\{(s_p(t) * h(t))\cos(2\pi f_c t + \vartheta)\right\} - j2\mathscr{F}_l\left\{(s_p(t) * h(t))\sin(2\pi f_c t + \vartheta)\right\}, \quad (2.4)$$

where $\mathscr{F}_l$ denotes low pass filter operator, $*$ denotes convolution, $h(t)$ denotes the channel impulse response, and $\vartheta$ denotes the constant carrier phase difference of the central carriers between the transmitter and the receiver, and is referred to as the *initial carrier phase offset*. If the receiver is not synchronized to the transmitters, the carrier frequency generated at the receiver will be different from the one

generated at the transmitter $f_c$, and its impact on the received signal will be introduced in the following section. In addition, to simplify the notation, the randomness introduced by the noise is omitted here, but it will be introduced in Section 2.5.

A burst-like signal packet, which consists of three OFDM pilot symbols (i.e., training symbols) as shown in Fig. 2.2, is currently implemented for ranging in the prototype SuperGPS system. The first two symbols are the normal pilot symbols, which are known to the receiver and will be used for (frame and symbol) synchronization and channel estimation. A PRN sequence, as an example, is modulated on the subcarriers, and it is identical for all transmitters in the developed prototype.

The last symbol is a shortened Moose's pilot symbol [110], in which only every other subcarrier is used, so that the first half of the symbol in time is equal to the second half, excluding the CP. In the last symbol, different transmitters use different Gold sequences on the activated subcarriers. The shortened Moose's symbol will be used for transmitter identification, and frequency offset estimation later on.
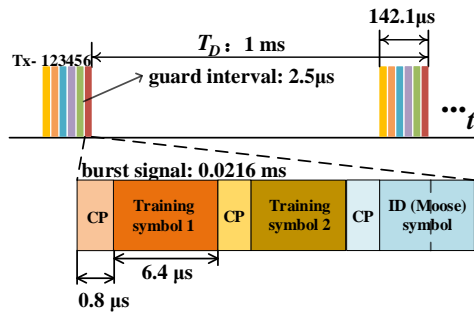


Figure 2.2: Each transmitter transmits a burst ranging signal in a TDM (time division multiplexing) scheme with a period of $T_D$. Each burst ranging packet consists of three OFDM symbols. Six transmitters are used in the prototype SuperGPS system.

To avoid interference among transmitters, a TDM scheme is applied. As shown in Fig. 2.2, each transmitter transmits its ranging signal in its own time slot, and the ranging signal is repeatedly transmitted with a period of $T_D$, so that spectrum resources not occupied by the positioning system, can be used for communication. Although a TDM scheme is applied, all transmitters should transmit their burst ranging signals within a relatively small interval, so that the changes in the sampling frequency offset and the central frequency offsets and the displacement of the receiver can be neglected within such an interval. As an example, shown in Fig. 2.2, for six transmitters, the burst ranging signals are transmitted within 142.1 $\mu$s and repeated every $T_D = 1$ ms.

## **2.2.** Frequency offset

In an asynchronous system, where all transmitters are synchronized, but the receiver runs on its own clock, there will be an offset in both the sampling frequency and the central carrier frequency, between the transmitters and the receiver. To quantify the frequency offset in an asynchronous system, we first define the normalized frequency offset (NFO) $\eta(t)$, which is given by

$$\eta(t) = \frac{\Delta f_c(t)}{f_c} = \frac{\Delta f_s(t)}{f_s}, \tag{2.5}$$

where $f_c$ and $f_s$ denote the central carrier frequency and the sampling frequency generated at the transmitter, respectively, $\Delta f_c(t)$ denotes the carrier frequency offset (CFO), and $\Delta f_s(t)$ denotes the sampling frequency offset (SFO) at the receiver.

Due to the CFO, the carrier frequency generated in the receiver is given by

$$f_c'(t) = f_c + \Delta f_c(t), \quad \Delta f_c(t) = \eta(t) f_c. \tag{2.6}$$

Hence, the passband signal after passing through the channel will be down-converted to baseband by the central frequency $f_c'(t)$.

In addition, in an asynchronous system, the mismatch of the sampling frequency between a receiver and a transmitter should be taken into consideration. Due to the SFO, the sampling frequency generated by the receiver is given by

$$f_s'(t) = f_s + \Delta f_s(t), \quad \Delta f_s(t) = \eta(t) f_s. \tag{2.7}$$

Consequently, the sample period in the receiver is written as follows

$$T_s'(t) = \frac{1}{f_s + \Delta f_s(t)} = \left(1 - \frac{\eta(t)}{1 + \eta(t)}\right) T_s. \tag{2.8}$$

If the normalized frequency offset $\eta(t)$ is generally at the level of a few ppm (parts-per-million) and much smaller than 1, (2.8) can be approximated by

$$T_s'(t) = \frac{1}{f_s'(t)} \approx T_s - \Delta T_s(t) = (1 - \eta(t)) T_s, \quad \Delta T_s(t) = \eta(t) T_s. \tag{2.9}$$

To simplify the notation, here we only consider a single-path channel, and analyse the impact of the CFO and the SFO on the time delay and carrier phase, as the quantities of interest for ranging. The single-path channel is assumed to be

$$h(t) = \alpha \delta(t - \tau(t)), \quad \tau(t) = \tau(t_0) - \int_{t_0}^{t} \frac{v(\zeta) \cos(\theta(\zeta))}{c} d\zeta, \tag{2.10}$$

where $\tau(t_0)$ denotes the initial propagation delay at the epoch $t_0$, and $v(t)$ the speed of the receiver, $\theta(t)$ denotes the angle-of-arrival of the signal at the epoch $t$ (with respect to the receiver velocity), $c$ denotes the speed of light, $[t_0, t]$ denotes the observation period. Without an accurate calibration of the system, $\tau(t_0)$ can also include the hardware delay, for example, from the RF front-ends.

Then, considering the CFO and the SFO, the received baseband signal defined in (2.4) is rewritten by

$$
\begin{aligned}
r_b(t) =& 2\mathscr{F}_l\left\{(s_p(t) * h(t))\cos(2\pi f_c'(t)t + \vartheta) - j(s_p(t) * h(t))\sin(2\pi f_c'(t)t + \vartheta)\right\} \\
=& \alpha s_b(t - \tau(t))\exp\left(-j\left(2\pi f_c\tau(t_0) + \phi_D(t) + \phi_\eta(t) + \vartheta\right)\right)
\end{aligned}
\tag{2.11}
$$

where $s_b(t)$ denotes the baseband OFDM ranging signal generated at the transmitter (cf.(2.1)),

$$
\begin{aligned}
\phi_D(t) &= -2\pi\int_{t_0}^{t}\Delta f_D(\zeta)\mathrm{d}\zeta, \quad \Delta f_D(t) = f_c\frac{v(t)\cos(\theta(t))}{c}, \\
\phi_\eta(t) &= 2\pi\int_{t_0}^{t}\Delta f_c(\zeta)\mathrm{d}\zeta, \quad \Delta f_c(t) = \eta(t)f_c,
\end{aligned}
\tag{2.12}
$$

$\phi_D$ denotes the accumulated Doppler phase offset, $\phi_\eta$ denotes the accumulated receiver phase offset due to the CFO, and $\Delta f_D$ and $\Delta f_c$ denotes the Doppler frequency offset and the carrier frequency offset, respectively. The derivation of (2.11) can be found in Appendix A.1.

Moreover, it is assumed that the propagation time delay and the frequency offset are constant within at least one OFDM symbol, hence the normalized frequency offset $\eta(t)$ can be replaced by $\eta[q]$ with the symbol index $q$. The $q$-th symbol of the received baseband OFDM signal after analog-to-digital conversion (ADC) is given by

$$
\begin{aligned}
r_b[q, n] =& r_b(t), \quad t = (q(N_s + N_g) + N_g + n)T_s', \\
=& \frac{\alpha}{N_s}\sum_{i=-N_s/2}^{N_s/2-1}c_{i,q}\exp\left(j2\pi f_i\left(n(1 - \eta[q])T_s - \Delta\tau[q]\right)\right) \\
& \times \exp\left(-j\left(2\pi\Delta\tilde{f}_c[q]n(1 - \eta[q])T_s + \tilde{\phi}[q]\right)\right),
\end{aligned}
\tag{2.13}
$$

where

$$
\Delta\tau[q] = \tau_\eta[q] + \tau[q] - \hat{\tau}_{\mathrm{sym}}[q], \quad \tau_\eta[q] = -\sum_{u=0}^{q-1}\left(\left(N_s + N_g\right) + N_g\right)\eta[u]T_s
$$

$$
f_i = \frac{i}{N_sT_s}, \quad \Delta\tilde{f}_c[q] = \Delta f_c[q] + \Delta f_D[q],
\tag{2.14}
$$

$$
\tilde{\phi}[q] = \begin{cases} 2\pi f_c\tau(t_0) + \phi_D[q - 1] + \phi_\eta[q - 1] + \vartheta, & q \geq 1 \\ 2\pi f_c\tau(t_0) + \vartheta, & q = 0, \end{cases}
$$

and $\hat{\tau}_{\mathrm{sym}}[q]$ denotes the time delay derived from symbol synchronization for the $q$-th symbol, which is an essential step to find the place to start the $N_s$-point FFT for OFDM demodulation [111]. Unlike for ranging, synchronization up to sample-level is sufficient for communication. Without oversampling, $\hat{\tau}_{\mathrm{sym}}[q]$ is with a resolution of the sample interval $T_s$.

As shown in (2.14), the received signal is delayed by the asynchronous receiver clock error $\tau_\eta[q]$ and the actual propagation time delay $\tau[q]$ in the $q$-th symbol. After the symbol synchronization, a part of delay will be remove by $\tau_{sym}[q]$, and thus $\Delta\tau[q]$ is referred to as the synchronization error.

After the FFT, the received data on the $k$-th sub-carrier of the $q$-th symbol is given as

$$
\begin{aligned}
R_k[q] =\; & \mathscr{F}\left\{r_b[q;n]\right\} = \sum_{n=0}^{N_s-1} r_b[q;n]\exp\left(-j2\pi\frac{kn}{N_s}\right) \\
=\; & \sum_{n=0}^{N_s-1}\sum_{i=-N_s/2}^{N_s/2-1} c_{i,q}\exp(j2\pi f_i(n(1-\eta[q])T_s - \Delta\tau[q])\exp\left(-j2\pi\frac{kn}{N_s}\right) \\
& \times \exp\left(-j\left(2\pi\Delta\tilde{f}_c[q]n(1-\eta[q])T_s + \tilde{\phi}[q]\right)\right) \\
=\; & \sum_{n=0}^{N_s-1} c_{k,q}\exp\left(-2\pi f_k(n\eta[q]T_s + \Delta\tau[q])\right)\exp\left(-j\left(\tilde{\phi}[q] + 2\pi\Delta\tilde{f}_c[q]n(1-\eta[q])T_s\right)\right) \\
& + \mathrm{ICI}_k[q],
\end{aligned}
$$

$$(2.15)$$

where the interchannel interference (ICI) on the subcarrier $k$, by the other subcarriers $i \neq k$, is given by

$$
\begin{aligned}
\mathrm{ICI}_k[q] =\; & \sum_{n=0}^{N_s-1}\sum_{i\neq k} c_{i,q}\exp\left(j2\pi\left(\frac{(i-k)n}{N_s} - f_i(n\eta[q]T_s + \Delta\tau[q]) - \Delta\tilde{f}_c[q]n(1-\eta[q])T_s\right)\right) \\
& \exp\left(-j\tilde{\phi}[q]\right) \\
=\; & \sum_{i\neq k} c_{i,q}\exp\left(j2\pi f_i\Delta\tau[q]\right)\sum_{n=0}^{N_s-1}\exp\left(j2\pi\frac{(i(1-\eta[q])-k)n - \beta[q]n(1-\eta[q])}{N_s}\right) \\
& \exp\left(-j\tilde{\phi}[q]\right),
\end{aligned}
$$

and

$$
\beta[q] = \frac{\Delta\tilde{f}_c[q]}{\Delta f},
$$

$\Delta f$ denotes the subcarrier spacing (cf.(2.2)).

As the normalized frequency offset $\eta$ is generally small (e.g., a few ppm), the

inter-channel interference can be approximated by

$$\text{ICI}_k[q] \approx \sum_{i \neq k} c_{i,q} \exp\left(j2\pi f_i \Delta\tau[q]\right) \sum_{n=0}^{N_s-1} \exp\left(j2\pi \frac{(i-k-\beta[q])n}{N_s}\right) \exp\left(-j\tilde{\phi}[q]\right)$$

$$= \sum_{i \neq k} c_{i,q} \left( \frac{\sin(\pi(i-k-\beta[q]))}{\sin\left(\pi\frac{i-k-\beta[q]}{N_s}\right)} \exp\left(j\pi\frac{(i-k-\beta[q])(N_s-1)}{N_s}\right) \exp\left(-j2\pi f_i \Delta\tau[q]\right) \right)$$

$$\exp\left(-j\tilde{\phi}[q]\right)$$

Due to the frequency offset $\Delta\tilde{f}_c[q]$ and the resulting $\beta[q] \neq 0$, caused by Doppler and the asynchronous reference signal, ICI will be introduced. In order to mitigate the ICI, one can coarsely estimate and compensate the frequency offset before estimating the channel frequency response. Though the residual frequency offset will still cause a minor remaining ICI. If the subcarrier spacing $\Delta f$ is chosen to be much larger than the frequency offset $\Delta\tilde{f}_c$, so that $\beta$ is small, then the ICI due to the frequency offset will be negligible [109].

If the ICI is negligible, (2.15) can be approximated by

$$R_k[q] \approx \frac{c_{k,q}}{N_s} \exp\left(-j2\pi f_k \Delta\tau[q]\right) \sum_{n=0}^{N_s-1} \exp\left(-j2\pi(\Delta\tilde{f}_c[q](1-\eta[q])T_s + f_k\eta[q])nT_s\right)$$

$$\exp\left(-j2\pi\tilde{\phi}[q]\right)$$

$$\approx c_{k,q} \underbrace{\exp\left(-j2\pi f_k \Delta\tau[q]\right)}_{(1)} \underbrace{\exp\left(-j\left(2\pi\Delta\tilde{f}_c[q]T_sN_s/2 + \tilde{\phi}[q]\right)\right)}_{(2)}.$$

$$(2.16)$$

Afterwards, the time delay measurement can be obtained by adding $\hat{\tau}_{\text{sym}}[q]$ and $\Delta\tau[q]$ derived from the phase of term (1) in (2.16). The carrier phase will be derived from the phase of term (2) in (2.16). More details on time delay and carrier phase estimation will be presented in Chapter 3 and Chapter 4, respectively.

## 2.3. Multipath

In this section, the impact of multipath on the received ranging signal is presented. A terrestrial positioning system is typically deployed in a GNSS-challenged environment, which will be associated with strong reflections of the signal on/by surrounding objects (e.g., buildings).

For notation simplicity, the symbol index $p$ will be removed in the following derivations. Given an $L$-path channel, the *sampled* complex baseband channel

impulse response is given by

$$h[n] = \sum_{l=1}^{L} x_l \delta(nT_s' - \Delta\tau_l),$$

$$x_l = \alpha_l \exp\left(-j\left(2\pi\Delta\tilde{f}_{c,l}T_sN_s/2 + \tilde{\phi}_l\right)\right)$$

$$= \alpha_l \exp\left(-j\left(\pi\Delta\tilde{f}_{c,l}/\Delta f + \tilde{\phi}_l\right)\right),$$

(2.17)

where

$$\Delta\tau_l = \tau_{\eta,l} + \tau_l - \hat{\tau}_{\text{sym}},$$

and $T_s'$ is the receiver sample interval, $\Delta\tau_l$ denotes the residual propagation delay of the $l$-th path after synchronization (cf. (2.14)), $x_l$ denotes the complex propagation gain, and $\alpha_l$ denotes the modulus of $x_l$ and is a real value. By default, $l = 1$ denotes the LoS path as we assume to have a LoS channel. In addition, $\tilde{\phi}_l$, which is determined by the CFO, the Doppler offset, and the propagation time delay, denotes the accumulated carrier phase on the central carrier $f_c$. In this work, carrier phase tracking explicitly refers to phase tracking of the central carrier frequency $f_c$.

Based on (2.16), the received frequency response in a multipath condition can be given by

$$\tilde{R}_k = \sum_{l=1}^{L} c_k \exp\left(-j2\pi f_k\Delta\tau_l\right) \alpha_l \exp\left(-j\left(\pi\Delta\tilde{f}_{c,l}/\Delta f + \tilde{\phi}_l\right)\right). \tag{2.18}$$

Using user pre-defined training symbols, $c_k$ is known a priori to the receiver. Then, the channel frequency response can be obtained by eliminating the data $c_k$ in (2.18). Afterwards, based on the phases of the subcarriers, one can estimate the time delay and carrier phase for positioning. However, if the reflections are not considered in the model for time delay and carrier phase estimation, the resulting estimators will become biased.

As an example, Fig. 2.3 illustrates how unconsidered reflections in a 3-path channel impact delay time and carrier phase estimation. In Fig. 2.3(a) (bottom), a cross-correlation between the received signal and the locally generated reference signal (i.e., matched filter (MF)) is used to determine the time delay/ToA. As the received signal contains not only the LoS path but also two reflected paths, and the reflections are not considered in the locally generated reference signal, the cost function implied by using the MF (see violet-solid line in the bottom of Fig. 2.3(a)) is offset from the one for the single LoS-path channel (see blue-dashed line).

Similarly, multipath can also introduce a bias in the carrier phase, if the reflections are not taken into consideration in estimating the carrier phase. Fig. 2.3(b) shows the diagram of the composite received carrier phasor. The blue-dashed arrow denotes the LoS phasor, and its phase has been normalized to zero. Considering a carrier with a frequency of 3960 MHz, the red-dashed arrow and the

yellow-dashed arrow stand for the reflection with a relative delay of 7.5 ns (i.e., 2.25 m) and 53.5 ns (i.e., 16.04 m), respectively. Without resolving these reflections in carrier phase estimation, the carrier phase derived from the composite phasor, as shown in the violet-solid arrow, will be offset from the actual LoS phasor (e.g., 0.1 of the wavelength in this example).
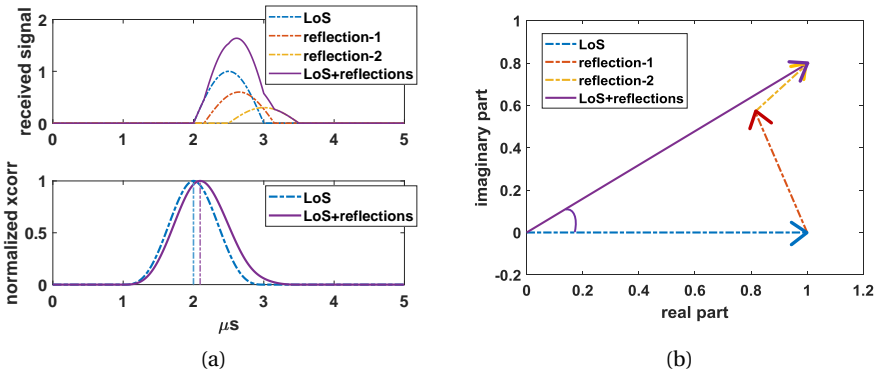


Figure 2.3: Considering a 3-path channel, (a) time delay estimation based on a cross-correlation approach, (b) diagram of received carrier phasor for carrier phase estimation. For illustration purpose, different relative delays are used in (a) and (b), while the relative gain of two reflections are fixed to 0.6 and 0.3.

Generally, multipath is unavoidable in a terrestrial positioning system. On the one hand, it is recommended to consider the reflections in the estimation model when computing the range observable for positioning. On the other hand, one could increase the bandwidth of the ranging signal, as to offer a higher time resolution, and consequently allow for a better resolution of reflections, and improve the accuracy of the range estimators.

## 2.4. Multiband Signal

In this section, the idea of a multiband signal is presented as one of the practical solutions to achieve a large signal bandwidth. Particularly, multiband OFDM has been adopted in UWB systems. The UWB frequency band is divided into multiple signal bands, which allows to process information over a much smaller bandwidth, and improves spectral flexibility. Each OFDM symbol is transmitted over one of the signal bands, based on a frequency hopping (FH) sequence (i.e., time-frequency codes) [106].

## Principle

Based on (2.3), the FH-based multiband RF signal can be written by

$$s_p(t) = \sum_m \Re \left\{ s_{b,m}(t - mT_G) \exp(j2\pi(f_c + f_m)t) \right\},$$

$$f_m = (m - M/2)\Delta f_G, \quad m = 1, 2, \ldots, M, \tag{2.19}$$

where $T_G$ denotes the time duration of a single transmission slot, $f_m$ denotes the central frequency of the $m$-th signal band over (relative to $f_c$), and $\Delta f_G$ denotes the hopping basis of central carrier for different signal bands. The frequency hopping sequences are assigned uniquely to avoid the interference. Then, at the receiver, different signal bands with different central carrier frequencies will be down-converted into baseband. For communication, each signal band is generally processed independently. Then, the time resolution is still limited by the bandwidth of each signal band.

For ranging, one is particularly interested in a large signal bandwidth, as the time resolution is the inverse of the signal bandwidth. By removing the timing offset in different signal bands (e.g., $mT_G$), so that the received signal from different bands can be coherently processed at the same time. To determine the time delay, one can exploit the frequency relation among different signal bands, and the resulting different phase rotations introduced by the frequency $f_m$ across different signal bands. Considering an $L$-path channel, the received signal from $M$ signal bands, in which the transmission timing offsets are removed, is given by

$$\boldsymbol{r}_b(t) = \begin{bmatrix} r_{b,1}(t) \\ r_{b,2}(t) \\ \vdots \\ r_{b,m}(t) \\ \vdots \\ r_{b,M}(t) \end{bmatrix} = \sum_{l=1}^{L} \underbrace{\begin{bmatrix} s_{b,1}(t - \tau_l) \exp\left(-j2\pi f_1 \tau_l\right) \\ s_{b,2}(t - \tau_l) \exp\left(-j2\pi f_2 \tau_l\right) \\ \vdots \\ s_{b,m}(t - \tau_l) \exp\left(-j2\pi f_m \tau_l\right) \\ \vdots \\ s_{b,M}(t - \tau_p) \exp\left(-j2\pi f_M \tau_l\right) \end{bmatrix}}_{(1)} \underbrace{\exp(-j2\pi f_c \tau_l)}_{(2)}. \tag{2.20}$$

By exploiting the phase of term (1) in (2.20), which depends not only on the subcarrier frequencies within each signal band but also the central frequency of each signal band $f_m$ (with respect to the central frequency $f_c$), one can estimate the propagation delay $\tau_l$ for $l = 1, \ldots, L$. Compared with the case of using a single band, the estimation performance is improved when using a multiband signal, due to the increase in the total signal bandwidth. If the term (1) in (2.20) is reconstructed, one can determine the carrier phase from the term (2) for positioning.

As shown in Fig. 2.4, there are $M$ available bands in the allocated signal spectrum that can be used for positioning or communication. We define the bandwidth between the two signal bands at the band edges as the *virtual signal bandwidth* (as shown in Fig. 2.4), no matter how many activated bands there are in

between. Hence, it is not needed to contiguously transmit all signal bands in order to create a large virtual signal bandwidth. If all activated signal bands can be exploited coherently for ranging, the ranging performance will consequently benefit from its large virtual signal bandwidth, instead of the sum of the bandwidth of each signal band. The selection of the signal bands for ranging will be introduced in Chapter 5.
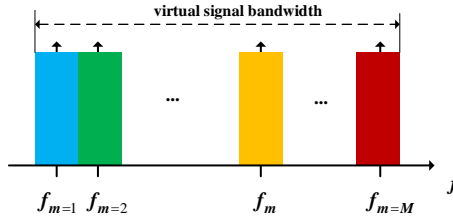


Figure 2.4: Spectrum of multiband OFDM signal for terrestrial precise positioning system, which consists of $M$ available signal bands and $N_s$ subcarriers in each signal band. Virtual signal bandwidth is defined by the bandwidth between two signal bands at the edges. Not all adjacent signal bands are needed to be used to create a large virtual signal bandwidth, so to be beneficial for ranging. In the sequel, we will use only $M_a$ out of $M$ bands.

## Implementation

In practice, each signal band needs to be up-converted to the corresponding radio frequency $f_c + f_m$ at the specific time-slot. However, the hopping carriers generated for different signal bands are generally not phase-synchronized, and the received multiband signal shown in (2.20) should be rewritten by

$$\tilde{\boldsymbol{r}}_b(t) = \boldsymbol{r}_b(t) + \begin{bmatrix} \exp\left(j\vartheta_1\right) \\ \exp\left(j\vartheta_2\right) \\ \vdots \\ \exp\left(j\vartheta_m\right) \\ \vdots \\ \exp\left(j\vartheta_M\right) \end{bmatrix}, \tag{2.21}$$

where $\vartheta_m$ denotes the phase offset in the $m$-th band, and $\vartheta_m$ can also be hop/time-dependent. Given the different phase offsets across different signal bands, one can no longer 'stitch' together all signal bands transmitted at different time slots to emulate a wide signal bandwidth.

To resolve the phase offsets introduced by the transmitters and the receiver hopping among different signal bands, like in [57], one needs to estimate the channel frequency response of the central subcarrier in each signal band, at both the receiver (with respect to the transmitter) and the transmitter (with respect to the receiver). Then by multiplying the measurements taken on both sides, the different phase offsets from different signal bands can be eliminated. However, applying such an approach requires strict time synchronization between the transmit-

**2**
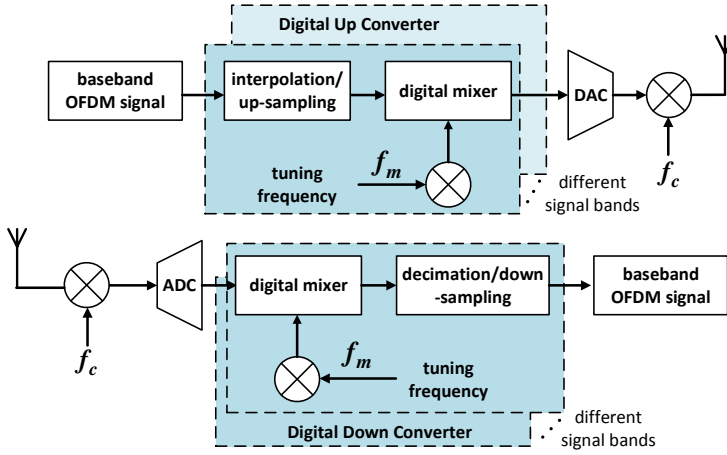


Figure 2.5: Schematic of multiband signal generation and reception using digital up-converter and digital down-converter.

ter and the receiver, so that both sides can measure the channel response at the same time instant.

In this work, to avoid possible phase offsets across different signal bands, all signal bands are transmitted and received simultaneously or sequentially through a single RF front-end with a fixed central carrier $f_c$. Hence, one no longer needs to calibrate the initial phase offset for each signal band. As shown in Fig. 2.5, the baseband signal of each band will be digitally up-converted to a specific intermediate frequency (IF) $f_m$ in the transmitter before the DAC. Then, the received signal after the ADC will be digitally down-converted by $f_m$ to the baseband signal. Using such a system may not reduce hardware cost, as a relatively high sampling DAC and ADC are still required to cover the entire virtual signal bandwidth. But the computational complexity of obtaining the range information can remain low, and the system can still offer a flexible spectrum management.

## **2.5.** Measurement Model

In this section, based on the multiband OFDM signal, the measurement model of the received signal is introduced, which will be used for time delay and carrier phase estimation in the following chapters. In practice, any modulation can be used in signal bands arbitrarily positioned in the frequency spectrum.

Considering the received samples from $m$-th signal band

$$\underline{r}_m[n] = r_m[n] + \underline{e}[n], \tag{2.22}$$

the complex additive white Gaussian noise (AWGN) is assumed to have the following distribution

$$\underline{e} \sim \mathcal{CN}\left(0, \, \sigma_n^2\right). \tag{2.23}$$

After frame synchronization and fast Fourier transformation (FFT), the channel frequency response of the subcarriers across the different signal bands can be obtained based on a training symbol. The response not only contains information on the time delay but also on the carrier phase. Details on modulation and demodulation of OFDM signals in each signal band are omitted here, and can be found in [109].

Based on received training symbol (2.20) from different signal bands, one can determine the channel frequency response. The *sampled channel frequency response* obtained from the $k$-th subcarrier in the $m$-th signal band is given by

$$\underline{H}_{k,m} = \frac{\tilde{R}_{k,m}}{c_{k,m}} + \underline{E}_{k,m}, \quad k = -\frac{N_s}{2}, \ldots, \frac{N_s}{2} - 1, \tag{2.24}$$

where $\underline{E}$ denotes the Fourier transform of the noise $\underline{e}$. As derived in [62], the PDF of the Fourier transform of AWGN is obtained by

$$\underline{E} \sim \mathscr{CN}\left(0, N_s\sigma_n^2\right). \tag{2.25}$$

Precise timing is generally not required in an OFDM-based communication system, as the guard interval (i.e., CP) can effectively mitigate multipath effects. In order to properly demodulate the signal, a simple frequency domain equalization is used to compensate for the distortion of the entire multipath channel, based on the sampled channel frequency response (cf. (2.24)) obtained from channel estimation. However, for the purpose of positioning, our aim is to estimate the time delay and the carrier phase specifically of the LoS path in a multipath channel, from the sampled channel frequency response.

In the present explanation, for convenience and ease of the description and derivation in this work, each OFDM signal band is assumed to have the same bandwidth and each contains $N_s$ subcarriers, but this can be different in practice. To extract the range information, one can consider the frequency relation among different signal bands, and stack up all frequency response measurements taken from the activated subcarriers in the different signal bands as a vector $\boldsymbol{H}$,

$$\boldsymbol{H} = \begin{bmatrix} \boldsymbol{H}_1^{\mathrm{T}} & \ldots & \boldsymbol{H}_m^{\mathrm{T}} & \ldots & \boldsymbol{H}_M^{\mathrm{T}} \end{bmatrix}^{\mathrm{T}}$$
$$\boldsymbol{H}_m = \begin{bmatrix} H_{-N_s/2,m} & \ldots & H_{k,m} & \ldots & H_{N_s/2-1,m} \end{bmatrix}^{\mathrm{T}}. \tag{2.26}$$

To improve spectral efficiency and to decrease computational complexity, not all signal bands are needed for this task. Hence, one can use $M_a$ out of $M$ signal bands shown in Fig. 2.4.

Based on (2.20) and (2.25), the measurement model for the sampled channel frequency response is given by

$$\underline{H} \sim \mathscr{CN}\left(\mathbb{E}\{\underline{H}\}, \boldsymbol{Q_H}\right),$$
$$\mathbb{E}\{\underline{H}\} = \mathscr{F}\{h[n]\} = \boldsymbol{A}(\Delta\tau)\boldsymbol{x}, \quad \boldsymbol{Q_H} = N_s\sigma_n^2\boldsymbol{I}_{N_sM_a} = \sigma^2\boldsymbol{I}_{N_sM_a}, \tag{2.27}$$

where

$$A(\Delta\boldsymbol{\tau}) = \begin{bmatrix} \boldsymbol{a}(\Delta\tau_1) & \boldsymbol{a}(\Delta\tau_2) & ... & \boldsymbol{a}(\Delta\tau_L) \end{bmatrix}$$

$$\boldsymbol{a}(\Delta\tau_l) = \begin{bmatrix} \boldsymbol{a}_1(\Delta\tau_l)^{\mathrm{T}} & \boldsymbol{a}_2(\Delta\tau_l)^{\mathrm{T}} & ... & \boldsymbol{a}_{M_a}(\Delta\tau_l)^{\mathrm{T}} \end{bmatrix}^{\mathrm{T}}$$

$$[\boldsymbol{a}_m(\Delta\tau_l)]_i = \exp(-j2\pi(f_i + f_m)\Delta\tau_l), \ \boldsymbol{a}_m(\Delta\tau_l) \in \mathbb{C}^{N\times1}$$

$$\boldsymbol{x} = \begin{bmatrix} x_1 & x_2 & ... & x_L \end{bmatrix}^{\mathrm{T}},$$

(2.28)

$f_i = i\Delta f$ denotes the *subcarrier frequency* of the $i$-th subcarrier ($-N_s/2 \leq i \leq N_s/2 - 1$), $\Delta f$ denotes the subcarrier spacing, $f_m$ denotes the *centre frequency* of the $m$-th activated signal band with respect to $f_c$, $x_l$ denotes the complex gain of the $l$-th path (cf. (2.17)) . The variance of the measurement noise $\sigma^2$ is assumed to be known or can be estimated a priori (cf. (2.25)).

Based on the model (2.27) of the sampled channel frequency response, different types of range information can be computed. Particularly, time delay and carrier phase estimation will be introduced in Chapter 3 and Chapter 4, respectively.

# 3

# Time Delay Estimation

The range between a radio transmitter and a radio receiver can be determined by multiplying the signal travel time with the speed of light. In this chapter, we first analyze the Cramér-Rao lower bound (CRLB) of time delay estimation in both a single-path channel and two-path channel, and discuss the impact of signal spectrum pattern and multipath on the CRLB. Then, based on the maximum likelihood (ML) principle, we analyze the performance of time delay estimation in a multipath channel [82]. Particularly, we analyze the bias if a reflection is not considered in the estimation model, and we analyze the precision if a reflection is considered in the model. Lastly, from the ML prospective, we review other techniques that are commonly used for time delay estimation, and present the similarities between these techniques and the ML method.

## 3.1. Cramer-Rao Lower Bound

The Cramer-Rao lower bound (CRLB) is a lower bound on the variance of any *unbiased* estimator [62]. Given the probability density function (PDF) $f_{\underline{r}}(r|u)$ of the received samples $r$,

$$\sigma_{\hat{u}_i}^2 \geq \left[ F^{-1}(u) \right]_{i,i}, \quad u \in \mathbb{C}^{N_u \times 1}, \tag{3.1}$$

where $F(u)$ is an $N_u$-by-$N_u$ Fisher information matrix (FIM), and $N_u$ is the number of unknown parameters in $u$. The FIM is defined by

$$[F(u)]_{i,j} = -\mathbb{E} \left\{ \frac{\partial^2 \ln f_{\underline{r}}(r|u)}{\partial u_i \partial u_j} \right\}, \quad i = 1, 2, \dots, N_u, \ j = 1, 2, \dots, N_u, \tag{3.2}$$

where $u_i$ and $u_j$ denote the $i$-th and $j$-th unknown parameter in $u$, respectively.

### 3.1.1. Single Path Channel

To provide a clear insight on how time-based ranging accuracy is linked to the signal spectrum, only a simple LoS single-path channel (2.10) is considered in this

**3**

subsection. Considering the baseband ranging signal $s_b(t)$ generated in the transmitter, the received baseband signal is given by

$$\underline{r}_b(t) = \alpha s_b(t - \tau) \exp(-j\tilde{\phi}) + \underline{e}(t), \tag{3.3}$$

where $\tilde{\phi}$ denotes the carrier phase as shown in (2.11). Furthermore, the noise $\underline{e}(t)$ is assumed to be complex Gaussian distributed as

$$\Re\left\{\underline{e}(t)\right\} \sim \mathcal{N}\left(0, \sigma_n^2/2\right), \quad \Im\left\{\underline{e}(t)\right\} \sim \mathcal{N}\left(0, \sigma_n^2/2\right). \tag{3.4}$$

For time delay estimation, $N_s$ samples with a sample interval of $T_s$ are taken from $\underline{r}_b(t)$, as an $N_s$ dimensional vector $\boldsymbol{r}$. Hence, the distribution of the received samples is given as

$$\underline{\boldsymbol{r}} \sim \mathcal{CN}\left(\bar{\boldsymbol{r}}_b(\tau), \boldsymbol{Q_r}\right), \quad \boldsymbol{Q_r} = \sigma_n^2 \boldsymbol{I}_{N_s}. \tag{3.5}$$

Then, the CRLB of time delay estimation, in which the time delay of the LoS path is the only unknown parameter in $\boldsymbol{u}$, is given by

$$\sigma_\tau^2 \geq \frac{1}{\text{SNR}4\pi^2 N_s \beta^2}, \tag{3.6}$$

where SNR stands for the signal-to-noise ratio (SNR), $\beta^2$ is a measure of the signal bandwidth as

$$\beta^2 = \frac{\int_{-\infty}^{+\infty} f^2 |S(f)|^2 df}{\int_{-\infty}^{+\infty} |S(f)|^2 df}, \tag{3.7}$$

and $S(f)$ denotes the spectrum of the ranging signal $s_b(t)$. The details on this derivation can be found in Appendix A.2.1.

Furthermore, multiplying by the speed of light $c$, the CRLB of a time-based range estimator in unit of length is given as

$$\sigma_d^2 \geq \frac{c^2}{\text{SNR}4\pi^2 N_s \beta^2}. \tag{3.8}$$

### Discussion
As an example, to illustrate the impact of the signal bandwidth on the CRLB, Fig. 3.1 shows the square-root CRLB in unit of length, when the number of subcarriers is fixed to $N_s = 64$ (i.e., number of samples), the SNR is set to be 20 dB, 10 dB and 0 dB. Clearly, a large signal bandwidth leads to a better ranging accuracy. To achieve a centimeter level ranging accuracy when SNR is 20 dB, at least a 200 MHz of signal bandwidth is required for time delay estimation.

As shown in (3.6), the CRLB is determined by the measure of bandwidth $\beta^2$ instead of the actual signal bandwidth. Therefore, one can place different signal power on different subcarriers, or only select a few subcarriers for ranging. As an example, shown in Fig. 3.2(b), we can select only two edge subcarriers, and mute other subcarriers for ranging. Such a signal does not occupy all available
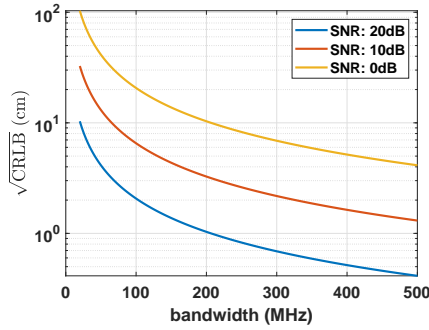
Figure 3.1: Square root of CRLB in unit of length, when an OFDM signal with $N_s = 64$ subcarriers is used for time delay estimation, and all subcarriers have the same power.

signal spectrum, and the frequency difference between these two edge subcarriers is defined as the *virtual signal bandwidth*. One can use two center subcarriers for ranging, which results in a smaller (virtual) signal bandwidth, and hence a larger CRLB. In addition, to maintain the total signal power, when only using two edge subcarriers for ranging, more signal power can also be placed on these two edge subcarriers. For comparison, the signal that uses all subcarriers is also considered, in which the actual signal bandwidth is the same as the virtual signal bandwidth.

Based on the signal spectrum pattern shown in Fig. 3.2(b), the corresponding square-root CRLBs are illustrated in Fig. 3.2(a). The CRLB is mainly determined by the virtual signal bandwidth, as the CRLB of using two edge subcarriers is close to the one using all subcarriers. The CRLB of using two edge subcarriers with more signal power on each, is smaller than using all subcarriers with equivalent total signal power, where each subcarrier has the identical power. Hence, placing more signal power towards the edge of the signal spectrum can improve the CRLB, and the accuracy of time delay estimation.

So far, only a single-path channel is considered in the CRLB (3.6), which means that the time delay is estimated only for one path. Hence, in a practical multi-path channel, if these reflections are not considered in the time delay estimation model, the resulting time delay estimator will become biased, and the derived CRLB (3.6) only presents the precision instead of the accuracy.

### 3.1.2. Two-Path Channel

In multipath conditions, to maintain the unbiasedness of the time delay estimator, one needs to jointly estimate the time delay for both the LoS path and the reflections. For the purpose of ranging and positioning, although we are only interested in the propagation delay of the LoS path, the gain of each path is also useful to help selecting the LoS path in a multipath channel. Hence, the unknown parameters include the time delay and the gain for both the LoS path and the reflections. To be mathematically manageable and derive a closed-from expression, a two-path channel is considered in this subsection, which contains a LoS path
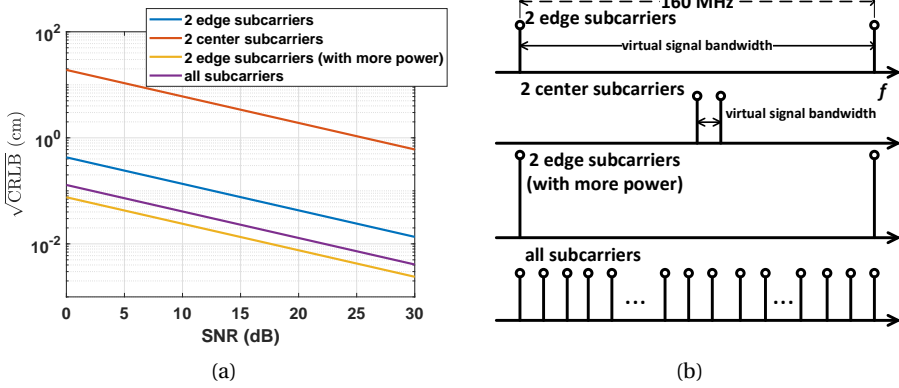
Figure 3.2: (a) Square root of CRLB in unit of length, when OFDM signal with $N_s$ = 64 subcarriers is used for time delay estimation, and subcarriers can have different power as shown in (b).

and one reflection.

The received multiband OFDM signal, in which each signal bands contains $N_s$ subcarriers, is only perturbed by complex Gaussian noise. The distribution of the received samples is given by (3.5). As the variance matrix $\boldsymbol{Q_r}$ in (3.5) is not a function of the unknown parameters, the FIM is given by [62]

$$[\boldsymbol{F}(\boldsymbol{u})]_{i,j} = 2\Re \left\{ \frac{\partial \bar{\boldsymbol{r}}^{\mathrm{H}}(\boldsymbol{u})}{\partial u_i} \boldsymbol{Q_r}^{-1} \frac{\partial \bar{\boldsymbol{r}}(\boldsymbol{u})}{\partial u_j} \right\}, \tag{3.9}$$

and a set of unknown parameters is defined by $\boldsymbol{u}$,

$$\boldsymbol{u} = \begin{bmatrix} \tau_1 & \tau_2 & \alpha_1 & \alpha_2 \end{bmatrix}^{\mathrm{T}} = \begin{bmatrix} \boldsymbol{\tau} \\ \boldsymbol{\alpha} \end{bmatrix}, \tag{3.10}$$

where $\tau_1, \alpha_1$ and $\tau_2, \alpha_2$ denote the delay and the gain of the LoS path and the reflection, respectively. We only consider a two path channel as an example, but this can be expanded to multiple reflections.

Although $M$ OFDM signal bands are assumed to be available for time delay estimation, as shown in Fig. 2.4, we first derive the CRLB in a two-path channel based on a single band OFDM signal $\underline{r}_m[n;\boldsymbol{\theta}]$ (i.e., obtained from the $m$-th band), which is written by

$$\underline{r}_m[n;\boldsymbol{u}] = \alpha_1 \sum_{i=-N_s/2}^{N_s/2-1} c_i \exp\left(j2\pi\frac{i}{N_s}n\right) \exp\left(-j2\pi(f_m + f_i)\tau_1\right) \exp\left(-j\tilde{\phi}_1\right)$$

$$+ \alpha_2 \sum_{i=-N_s/2}^{N_s/2-1} c_i \exp\left(j2\pi\frac{i}{N_s}n\right) \exp\left(-j2\pi(f_m + f_i)\tau_2\right) \exp\left(-j\tilde{\phi}_2\right) \tag{3.11}$$

$$+ \underline{e}_m[n], \quad n = 0, 1, \ldots, N_s - 1; \quad m = 1, 2, \ldots, M,$$

where $n$ denotes the sample index, $i$ and $N_s$ respectively denote the index of the subcarrier and the total number of subcarriers in each band, $c_i$ denotes the data modulated on the $i$-th subcarrier, $f_m$ denotes the central carrier frequency of the $m$-th band with respect to $f_c$ (see Fig.2.4), and $\tilde{\phi}_1$ and $\tilde{\phi}_2$ denote the phase of the LoS path and the reflection on the central carrier $f_c$. If each signal band is treated independently for time delay estimation, the precision does not dependent on the carrier phase introduced by $f_m$ and $f_c$, as shown in (3.6).

Given multiple signal bands that are modulated on different carrier frequencies $f_m$ (see Fig. 2.5), the received baseband signals from the different bands contain different phase rotations by the same propagation delay. In order to benefit from its virtual signal bandwidth, we should consider these phase rotations, so that we can maintain their frequency relation across multiple signal bands.

To simplify the notation, here we first define

$$
\tilde{\boldsymbol{f}}_m = \begin{bmatrix} f_{i=-N_s/2} \\ f_{i=-N_s/2+1} \\ \vdots \\ f_{i=N_s/2-1} \end{bmatrix} + f_m, \quad \tilde{\boldsymbol{f}}_m^2 = \tilde{\boldsymbol{f}}_m \odot \tilde{\boldsymbol{f}}_m, \tag{3.12}
$$

where the vector $\tilde{\boldsymbol{f}}_m$ contains $N_s$ subcarrier frequencies with respect to the central frequency $f_m$ of the $m$-th signal band, $\odot$ denotes the element-wise dot product. In addition, we define

$$
\boldsymbol{q}_m(\tau) = \cos(2\pi \tilde{\boldsymbol{f}}_m \tau), \quad \boldsymbol{p}_m(\tau) = \sin(2\pi \tilde{\boldsymbol{f}}_m \tau).
$$

Then, letting the relative delay as $\tau_{2,1} = \tau_2 - \tau_1$, the FIM based on a single band OFDM signal in a two-path channel be derived as

$$
F_m(\boldsymbol{u}) = \frac{2}{\sigma_n^2} \begin{bmatrix} \boldsymbol{A}_m & \boldsymbol{B}_m \\ \boldsymbol{C}_m & \boldsymbol{D}_m \end{bmatrix}, \tag{3.13}
$$

where

$$
\begin{aligned}
\boldsymbol{A}_m &= \alpha_1^2 4\pi^2 \begin{bmatrix} \tilde{\boldsymbol{f}}_m^T \tilde{\boldsymbol{f}}_m & \frac{\alpha_2}{\alpha_1} \boldsymbol{q}_m^T(\tau_{2,1}) \tilde{\boldsymbol{f}}_m^2 \\ \frac{\alpha_2}{\alpha_1} \boldsymbol{q}_m^T(\tau_{2,1}) \tilde{\boldsymbol{f}}_m^2 & \frac{\alpha_2^2}{\alpha_1^2} \tilde{\boldsymbol{f}}_m^T \tilde{\boldsymbol{f}}_m \end{bmatrix}, \\
\boldsymbol{B}_m &= \alpha_1 2\pi \begin{bmatrix} 0 & \boldsymbol{p}_m^T(\tau_{2,1}) \tilde{\boldsymbol{f}}_m \\ -\frac{\alpha_2}{\alpha_1} \boldsymbol{p}_m^T(\tau_{2,1}) \tilde{\boldsymbol{f}}_m & 0 \end{bmatrix} = \boldsymbol{C}_m^T, \\
\boldsymbol{D}_m &= \begin{bmatrix} N_s & \boldsymbol{1}_N^T \boldsymbol{q}_m(\tau_{2,1}) \\ \boldsymbol{1}_N^T \boldsymbol{q}_m(\tau_{2,1}) & N_s \end{bmatrix}.
\end{aligned} \tag{3.14}
$$

The FIM depends on the relative delay $\tau_{2,1}$, but not on the absolute delay $\tau_1$. The derivation of (3.14) can be found in appendix A.2.2.

Now we consider using multiple signal bands, as shown in Fig. 2.4, for time delay estimation. At the receiver, the signals from different bands can be received

simultaneously and be stacked together for time delay estimation. For convenience, here we assume that each band contains $N_s$ subcarriers for ranging. Thus, there will be $N_s$ samples acquired in $\boldsymbol{r}_m(\boldsymbol{u})$. The expectation of the received signals from $M$ different bands is now written by

$$\mathbb{E}\{\underline{\boldsymbol{r}}\} = \mathbb{E}\left\{\begin{bmatrix} \underline{\boldsymbol{r}}_1(\boldsymbol{u}) \\ \underline{\boldsymbol{r}}_2(\boldsymbol{u}) \\ \vdots \\ \underline{\boldsymbol{r}}_M(\boldsymbol{u}) \end{bmatrix}\right\} = \bar{\boldsymbol{r}}(\boldsymbol{u}) \in \mathbb{C}^{N_s M \times 1}. \tag{3.15}$$

Here, the noise from different bands is assumed to be independent and statistically identical. Then, the FIM based on multiple signal bands is just the sum of the FIM of each single band, which is written by

$$\boldsymbol{F}(\boldsymbol{u}) = \sum_{m=1}^M \boldsymbol{F}_m(\boldsymbol{u}) = \frac{2}{\sigma_n^2} \begin{bmatrix} \sum_m \boldsymbol{A}_m & \sum_m \boldsymbol{B}_m \\ \sum_m \boldsymbol{C}_m & \sum_m \boldsymbol{D}_m \end{bmatrix} = \begin{bmatrix} \boldsymbol{A} & \boldsymbol{B} \\ \boldsymbol{C} & \boldsymbol{D} \end{bmatrix}, \tag{3.16}$$

in which $\boldsymbol{F}_m(\boldsymbol{u})$ denotes the FIM from the $m$-th band in a two-path channel (see (3.13)). Eventually, the CRLB of the estimators, with among them the unknown propagation delay of the LoS path, can be derived from (3.1).

As the inverse of a full block-partitioned matrix can be obtained by

$$\begin{bmatrix} \boldsymbol{A} & \boldsymbol{B} \\ \boldsymbol{C} & \boldsymbol{D} \end{bmatrix}^{-1} = \begin{bmatrix} (\boldsymbol{A} - \boldsymbol{B}\boldsymbol{D}^{-1}\boldsymbol{C})^{-1} & -(\boldsymbol{A} - \boldsymbol{B}\boldsymbol{D}^{-1}\boldsymbol{C})^{-1}\boldsymbol{B}\boldsymbol{D}^{-1} \\ -\boldsymbol{D}^{-1}\boldsymbol{C}(\boldsymbol{A} - \boldsymbol{B}\boldsymbol{D}^{-1}\boldsymbol{C})^{-1} & \boldsymbol{D}^{-1} + \boldsymbol{D}^{-1}\boldsymbol{C}(\boldsymbol{A} - \boldsymbol{B}\boldsymbol{D}^{-1}\boldsymbol{C})^{-1}\boldsymbol{B}\boldsymbol{D}^{-1} \end{bmatrix}, \tag{3.17}$$

the CRLB for time delay estimator can be given by

$$\boldsymbol{F}_\tau(\boldsymbol{u}) = (\boldsymbol{A} - \boldsymbol{B}\boldsymbol{D}^{-1}\boldsymbol{C})^{-1}. \tag{3.18}$$

According to (3.14), the elements in $\boldsymbol{A}$, which are determined by the square of the frequency, is numerically much larger than the ones in $\boldsymbol{B}$, $\boldsymbol{C}$ and $\boldsymbol{D}$. Hence, the CRLB of the variance of time delay estimator can be approximated by

$$\boldsymbol{F}_\tau(\boldsymbol{u}) \approx \boldsymbol{A}^{-1}. \tag{3.19}$$

If all $M$ signal bands are used for ranging, one can have the following vectors

$$\boldsymbol{f} = \begin{bmatrix} \tilde{\boldsymbol{f}}_1 & \tilde{\boldsymbol{f}}_2 & \cdots & \tilde{\boldsymbol{f}}_m & \cdots & \tilde{\boldsymbol{f}}_M \end{bmatrix}^\mathsf{T}$$
$$\boldsymbol{q}(\tau) = \begin{bmatrix} \boldsymbol{q}_1(\tau) & \boldsymbol{q}_2(\tau) & \cdots & \boldsymbol{q}_m(\tau) & \cdots & \boldsymbol{q}_M(\tau) \end{bmatrix}^\mathsf{T}, \tag{3.20}$$

and the FIM (3.16) can be rewritten by

$$\boldsymbol{F}_\tau(\boldsymbol{u}) \approx \boldsymbol{A} = \frac{2\alpha_1^2 4\pi^2}{\sigma_n^2} \begin{bmatrix} \boldsymbol{f}^\mathsf{T}\boldsymbol{f} & \alpha_{2,1}\boldsymbol{q}(\tau_{2,1})^\mathsf{T}\boldsymbol{f} \odot \boldsymbol{f} \\ \alpha_{2,1}\boldsymbol{q}(\tau_{2,1})^\mathsf{T}\boldsymbol{f} \odot \boldsymbol{f} & \alpha_{2,1}^2 \boldsymbol{f}^\mathsf{T}\boldsymbol{f} \end{bmatrix}. \tag{3.21}$$

Then, the variance of the LoS time delay estimator can be obtained as

$$
\sigma_{\tau_1}^2 \geq \frac{\sigma_n^2}{2\alpha_1^2 4\pi^2} \frac{\alpha_{2,1}^2 \boldsymbol{f}^T \boldsymbol{f}}{\alpha_{2,1}^2 \left( \boldsymbol{f}^T \boldsymbol{f} \right)^2 - \alpha_{2,1}^2 \left( \boldsymbol{q}(\tau_{2,1})^T \boldsymbol{f} \odot \boldsymbol{f} \right)^2}
$$
$$
= \frac{1}{4\pi^2 \operatorname{SNR} \boldsymbol{f}^T \boldsymbol{f}} \frac{1}{1 - \left( \frac{\boldsymbol{q}(\tau_{2,1})^T \boldsymbol{f} \odot \boldsymbol{f}}{\boldsymbol{f}^T \boldsymbol{f}} \right)^2}.
$$
(3.22)

### Discussion

As an example, Fig. 3.3(a) shows the impact of the relative delay $\tau_{2,1}$ and the signal spectrum patterns (see Fig. 3.3(b)) on the CRLB, when SNR is set to be 20 dB. In a two-path channel, a close-in reflection with a relative delay less than the inverse of the virtual signal bandwidth (e.g., 6.25 ns, when the virtual signal bandwidth is 160 MHz), deteriorates the accuracy of the time delay estimator of the LoS path. Hence, compared to the CRLB derived from 2 central bands, creating a large virtual signal bandwidth (e.g., using only two edge signal bands) can largely improve ranging accuracy. Within the same virtual signal bandwidth, using more signal bands (e.g., all signal bands) can improve the overall resistance against multipath, so that the accuracy is less affected by the reflection.
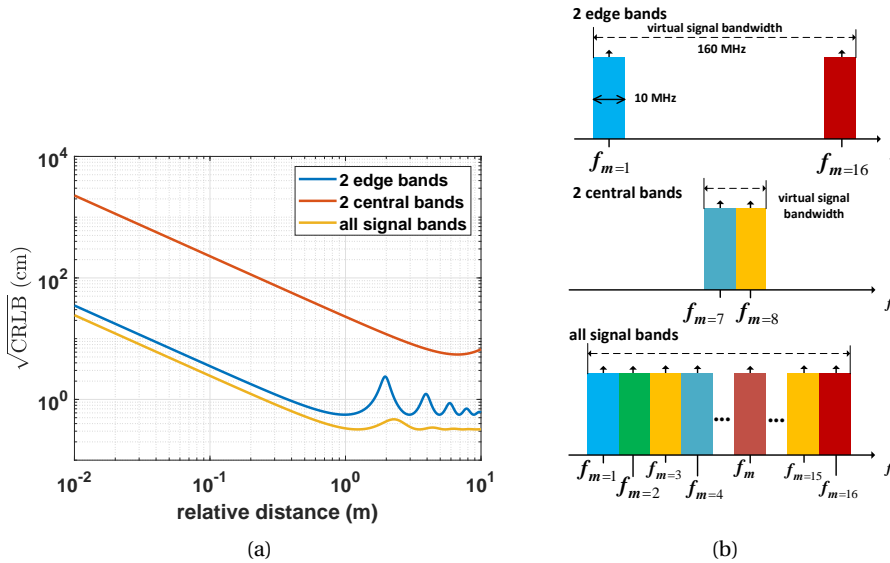


Figure 3.3: (a) Square-root CRLB in unit of length, when a multiband signal, as shown in (b), is used for time delay estimation. Each signal band contains $N_s = 64$ subcarriers, and SNR is set to be 20 dB.

The CRLB derived in a two path channel (cf. (3.22)) considers not only the accuracy of the estimators but also the correlation between the estimators which

indicates the robustness against multipath. In practice, in order to use this CRLB as an indication of the accuracy for time delay estimation, one needs to estimate the time delay for both the LoS path and the reflection.

On the other hand, the correlation between the LoS path and the reflection is not taken into account in the CRLB derived for a single-path channel (cf. (3.6)). In a multipath channel, as the reflection is not considered in the time delay estimation model, the resulting estimator will be biased, and the CRLB (3.6) only indicates the precision instead of the accuracy.

## 3.2. Maximum Likelihood Estimation

In an OFDM-based system, one can estimate the time delay based on the sampled channel frequency response $H$ (cf. (2.26)), as an offset in time will cause a phase rotation in frequency. According to the measurement model presented in (2.27), one can estimate the time delay based on a maximum likelihood (ML) principle. Given the distribution of the channel frequency response (2.27), to simply the notation in the following derivations, the residual time delay after synchronization $\Delta\tau$, will be replaced by $\tau$.

Since the unknown parameters are present not only in $x$ but also in $A(\tau)$, we jointly estimate the time delay and complex gain from the channel estimates through the following minimization

$$\hat{\tau}, \hat{x} = \arg\min_{\tau, x} \|H - A(\tau)x\|^2_{Q_H^{-1}}, \tag{3.23}$$

where $H$ contains the sampled channel frequency response obtained from $M_a$ signal bands and $N_s$ subcarriers in each band. The unknown propagation time delay $\tau$ and the unknown complex gain $x$ are assumed to be two completely disjoint sets. Although there are unknown parameters in $A(\tau)$, its dimension is known a priori. In our case, the number of rows of the design matrix $A(\tau)$ is determined by the number of the subcarriers in each signal band and the number of signal bands. The number of paths (i.e., the number of columns in $A(\tau)$) should be specified, and the impact of selecting different number of paths for parameter estimation will also be discussed in this section.

It has been proven in [112] that if $\hat{\tau}$ and $\hat{x}$ are the global minimizers of (3.23), $\hat{x}$ must satisfy

$$\hat{x} = \left(A(\hat{\tau})^H Q_H^{-1} A(\hat{\tau})\right)^{-1} A(\hat{\tau})^H Q_H^{-1} H, \tag{3.24}$$

when the variance matrix $Q_H$ is a diagonal matrix with identical elements on the main diagonal, as defined in (2.26). Therefore, using the solution $\hat{x}$ to rewrite the cost function (3.23), we can first estimate the propagation delay, then compute the complex gain and its corresponding carrier phase.

Time delay estimation, which is is the first step to obtain the solution from the ML-based cost function (3.23), is discussed in this section. Complex gain estimation and the determination of the resulting carrier phase will be addressed in Chapter 4.

First, assuming that the number of paths is known a priori, all reflections are considered in the design matrix $A(\tau)$, which is referred to as the *full model*. We define a measure of dependence between the LoS component and a reflection for delay estimation, and analyse how this dependence influences the accuracy (i.e., the variance) of the delay estimator of the LoS path.

A low-complexity *simplified model* is also proposed in this section, in which not all reflections are considered in the design matrix. Although we may determine the number of paths in a multipath channel through model order estimation techniques, such as minimum description length (MDL)[113] and generalized Akaike information criterion (GAIC) [114, 115], they generally require a large number of data snapshots and may not provide the exact number of paths. The simplified model seems more practical than the full model to implement in practice. As less unknown parameters are estimated, the computational efficiency and possibly the precision can be improved, but the resulting delay estimator for the LoS path likely will be biased. Therefore, we define a measure of bias, and analyse how an unconsidered reflection in the simplified model impacts delay estimation, with the goal of verifying that the simplified model will eventually meet the requirements.

### 3.2.1. Full Model

In this subsection, we analyse how the accuracy of the delay estimator for the LoS path deteriorates when a reflection is considered in the full model for time delay estimation in an attempt to achieve unbiasedness.

Since the design matrix is partially unknown, combined with (3.24), and considering white Gaussian noise, the delay estimates can be equivalently derived from the minimization of the following nonlinear cost function [116, 88, 112]

$$\hat{\boldsymbol{\tau}} = \arg\min_{\boldsymbol{\tau}} \|P_{A(\tau)}^{\perp}\boldsymbol{H}\|_{Q_H^{-1}}^2 = \arg\min_{\boldsymbol{\tau}} \frac{1}{\sigma^2}\mathrm{tr}\left\{P_{A(\tau)}^{\perp}\boldsymbol{H}\boldsymbol{H}^{\mathrm{H}}\right\}, \tag{3.25}$$

where the variance matrix $Q_H = \sigma^2 \boldsymbol{I}_{NM_a}$, as defined in (2.26), and the complementary projection matrix is defined by

$$\begin{aligned}
P_{A(\tau)}^{\perp} &= \boldsymbol{I}_{N_sM_a} - P_{A(\tau)}, \\
P_{A(\tau)} &= A(\tau)\left(A(\tau)^{\mathrm{H}}Q_H^{-1}A(\tau)\right)^{-1}A(\tau)^{\mathrm{H}}Q_H^{-1}.
\end{aligned} \tag{3.26}$$

Therefore, the propagation delay can be equivalently estimated through the following cost function, with the projection matrix $P_{A(\tau)}$ defined in (3.26),

$$\hat{\boldsymbol{\tau}} = \arg\max_{\boldsymbol{\tau}} \mathrm{tr}\{P_{A(\tau)}\boldsymbol{H}\boldsymbol{H}^{\mathrm{H}}\}. \tag{3.27}$$

In order to find the maximizer of this non-linear cost function, there are generally two different approaches [117]: direct search methods and gradient methods. The direct search methods do not require any evaluation of derivatives of the non-linear cost function, but it can be time consuming to find the solution for the

cost function when it contains multiple variables. The gradient methods require derivatives to determine the direction of each iteration. For a cost function, like (3.25), with a projector, the reader can refer to [112]. However, the additional approximation effect, introduced by ignoring higher order derivatives of the latter, should be properly diagnosed and associated biases should be carefully dealt with (see e.g., [118, 119]). More details on solving a non-linear problem based on gradient methods can be found in [120], which extensively discussed different iterative gradient methods.

Here we consider the direct-search approach to obtain the time delay estimates. Given a multivariate cost function, a significant computation time is required to obtain the optimal solution. One may consider using the alternating projection (AP) [90] to iteratively compute the solution, which is computationally attractive for solving multivariate non-linear MLE.

To simplify the notation and derive a closed-form expression, a two-path channel is considered here as an example to analyse how a reflection deteriorates the accuracy. Considering white Gaussian noise, the uncertainty of unbiased ML-estimation can be derived from the CRLB [62]. Based on (3.22), the variance of the unbiased delay estimator $\sigma^2_{\hat{\tau}_1}$ for the LoS path when the full model is used, is given by

$$
\begin{aligned}
\sigma^2_{\hat{\tau}_1} &= \frac{\sigma^2_n}{8\pi^2\alpha^2_1} \frac{\alpha^2_{2,1}\boldsymbol{f}^{\mathrm{T}}\boldsymbol{f}}{\alpha^2_{2,1}(\boldsymbol{f}^{\mathrm{T}}\boldsymbol{f})^2 - \alpha^2_{2,1}(\boldsymbol{q}(\tau_{2,1})^{\mathrm{T}}\boldsymbol{f}\odot\boldsymbol{f})^2} \\
&= \frac{\sigma^2_n}{8\pi^2\alpha^2_1} \frac{1}{\left(1 - \left(\frac{\boldsymbol{q}(\tau_{2,1})^{\mathrm{T}}\boldsymbol{f}\odot\boldsymbol{f}}{\boldsymbol{f}^{\mathrm{T}}\boldsymbol{f}}\right)^2\right)\boldsymbol{f}^{\mathrm{T}}\boldsymbol{f}}.
\end{aligned}
\tag{3.28}
$$

In addition, for comparison, the variance of the unbiased delay estimator derived for a single path channel is given by

$$
\sigma^2_{\tilde{\tau}_1} = \frac{\sigma^2_n}{8\pi^2\alpha^2_1\boldsymbol{f}^{\mathrm{T}}\boldsymbol{f}}.
\tag{3.29}
$$

It presents the accuracy when the propagation channel only contains the LoS path, or the precision of time delay estimation when there are more paths, but only the LoS path is considered in the model. As $\boldsymbol{q}(\tau_{2,1})^{\mathrm{T}}\boldsymbol{f}\odot\boldsymbol{f} \le \boldsymbol{f}^{\mathrm{T}}\boldsymbol{f}$, we have

$$
\sigma^2_{\hat{\tau}_1} \ge \sigma^2_{\tilde{\tau}_1}.
\tag{3.30}
$$

To simplify notation, we first define

$$
s(\tau_{2,1}) = \frac{\boldsymbol{a}(\tau_1)^{\mathrm{H}}\boldsymbol{a}(\tau_2)}{N_s M_a},
\tag{3.31}
$$

and the real part of its second derivative is given by

$$
\Re\{s''(\tau_{2,1})\} = \Re\left\{\frac{\partial^2 s(\tau_{2,1})}{\partial\tau^2_{2,1}}\right\} = -\frac{4\pi^2\boldsymbol{q}(\tau_{2,1})^{\mathrm{T}}\boldsymbol{f}\odot\boldsymbol{f}}{N_s M_a}.
$$

Therefore, the variance of the unbiased delay estimator in a two path channel is rewritten as

$$\sigma_{\hat{\tau}_1}^2 = \frac{\sigma_n^2}{8\pi^2 \alpha_1^2 \boldsymbol{f}^{\mathsf{T}} \boldsymbol{f}} \frac{1}{1 - \left(\frac{N_s M_a \Re\{s''(\tau_{2,1})\}}{4\pi^2 \boldsymbol{f}^{\mathsf{T}} \boldsymbol{f}}\right)^2}. \tag{3.32}$$

By

$$\varsigma(\tau_{2,1}) = \left| \frac{N_s M_a \Re\{s''(\tau_{2,1})\}}{4\pi^2 \boldsymbol{f}^{\mathsf{T}} \boldsymbol{f}} \right|, \tag{3.33}$$

we define $\varsigma(\tau_{2,1})$ as a *measure of dependence for delay estimation*, which indicates the dependence level between the LoS component and the reflected component. According to Parseval's theorem, $s(\tau_{2,1})$ can also be treated as the auto-correlation function of the ranging signal, and a narrow correlation peak, which is associated with a large second derivative, can improve the resolvability of the reflection in a multipath channel.

Throughout this thesis, a reflection with a non-zero measure of dependence for delay estimation is referred to as a *dependent reflection* for delay estimation. Comparing (3.32) with (3.29), the accuracy of the estimator in a two-path channel and in a single-path channel are identical if $\varsigma(\tau_{2,1})$ is zero.

By using the full model for time delay estimation in a practical multipath channel, the accuracy of the delay estimator for the LoS path will become poorer when more dependent reflections need to be considered in the design matrix $\boldsymbol{A}(\boldsymbol{\tau})$. It should be mentioned that considering more reflections in the model requires a considerably large computation time to obtain the optimal solutions.

On the other hand, one may not consider all reflections in the design matrix $\boldsymbol{A}(\boldsymbol{\tau})$, or in the extreme case no reflection is considered, which is referred to as the *simplified model* for time delay estimation. Based on the simplified model, the computational burden can be largely relaxed, and the precision of the delay estimator can be also improved as shown in (3.30). However, the estimator becomes biased. The resulting bias will be analysed in the following subsection.

### 3.2.2. Simplified Model

Using the simplified model, in which not all reflections are taken into account to determine the time delay, requires less computational time and can provide a higher precision than when using the cost function based on the full model (3.27), but the resulting delay estimate of the LoS path could include a bias. Again, in order to provide a closed-form expression and to keep the derivations mathematically manageable, we consider a two path channel to analyse the bias in the estimated delay with the simplified model. Hence, the measurement model (2.27) is changed to

$$\mathbb{E}\left\{\underline{\boldsymbol{H}}\right\} = \boldsymbol{a}(\tau_1)x_1 + \boldsymbol{a}(\tau_2)x_2. \tag{3.34}$$

In addition, only for the purpose of bias analysis in delay estimation, the complex gains are assumed to be known.

The propagation delay based on the ML method in the simplified model can be determined by the following minimization

$$\check{\tau}_1 = \arg\min_{\tau} \|H - a(\tau)x_1\|^2_{Q_H^{-1}}, \tag{3.35}$$

where only one path is considered, i.e., in a two-path channel scenario. However, it is still difficult to obtain a closed-form expression for the bias based on the non-linear cost function (3.35). Therefore, only for the purpose of bias analysis, we linearise (3.35) through Taylor expansion at $\tau_1$ which is the true time delay of the LoS path, and ignore second and higher order terms. The linearised cost function is given by

$$\check{\tau}_1 \approx \arg\min_{\tau} \left\| H - a(\tau_1)x_1 - \frac{\partial a(\tau_1)}{\partial \tau_1}x_1(\tau - \tau_1) \right\|^2_{Q_H^{-1}}, \tag{3.36}$$

where $Q_H = \sigma^2 I_{N_s M_a}$ as defined in (2.26). Consequently, the linear model is given by

$$H - a(\tau_1)x_1 = \underbrace{\frac{\partial a(\tau_1)}{\partial \tau_1}x_1}_{\tilde{a}(\tau_1)} \underbrace{(\tau - \tau_1)}_{\tau_b}, \tag{3.37}$$

and

$$\tilde{a}(\tau_1) = \frac{\partial a(\tau_1)}{\partial \tau_1}x_1 = -j2\pi f \odot a(\tau_1)x_1. \tag{3.38}$$

As higher order remainders in the Taylor expansion have been neglected in the linearisation, the estimator becomes biased even when the measurements are un-biased [119, 118]. Given the complex non-linear design matrix defined in (2.28), the second order remainder will contribute to the bias in the imaginary part due to non-linearity, and the third order remainder will cause a bias in the real part. Typically, the higher than second order remainders are very small and can be ignored, and the bias introduced by the second order remainder due to non-linearity is jointly determined by the signal structure (i.e., the design matrix $a(\tau)$ itself) and the quality of the estimator [119]. Given a reasonable SNR, for example larger than -10 dB, the bias will be relatively small and will not dominate the accuracy of the estimation.

A bias $\tau_b$ introduced due to an unconsidered reflection in a two-path channel (3.34) is determined by

$$\tau_b = \Re\left\{ \left(\tilde{a}(\tau_1)^H \tilde{a}(\tau_1)\right)^{-1} \tilde{a}(\tau_1)^H (H - x_1 a(\tau_1)) \right\}$$
$$= \Re\left\{ \frac{-j2\pi x_1^H x_2 (f \odot a(\tau_1))^H a(\tau_2)}{-4\pi^2 x_1^2 f^T f} \right\} = \Re\left\{ \frac{j\alpha_1\alpha_2 \exp(j\varphi)f^T a(\tau_2 - \tau_1)}{2\pi\alpha_1^2 f^T f} \right\}, \tag{3.39}$$

where $\varphi$ denotes the phase from $x_1^H x_2$. The estimator obtained from a complex estimation problem is complex, and the imaginary part is introduced mainly due to the non-linearity of $a(\tau)$, which is relatively small. As the time delay estimator

should be a real number, we simply take the real part of the estimator to indicate the delay bias.

As an example, Fig. 3.4 shows the bias derived from the closed-form expression (3.39) and the one derived from the nonlinear ML cost function (3.35), when all $M = 16$ signal bands are used for ranging. The bias derived from (3.39) is slightly different from the one obtained from (3.35), only when a reflection has a large signal power and is close to the LoS path.
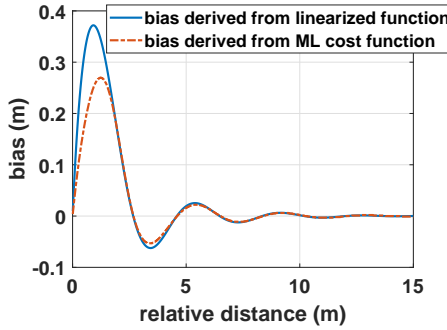


Figure 3.4: Bias derived from linearized function (3.39) and the nonlinear ML cost function (3.35).

The actual bias of delay estimation also depends on whether the reflection is constructive or destructive to the LoS component, as well as the non-linearity of $a(\tau)$. Without loss of generality, we analyse the *envelope* of the bias, or the maximum delay bias. Combined with

$$\Re\{s'(\tau_{2,1})\} = \Re\left\{\frac{\partial s(\tau_{2,1})}{\partial \tau_{2,1}}\right\} = -\frac{2\pi f^{\mathrm{T}} p(\tau_{2,1})}{N_s M_a}, \tag{3.40}$$

where $p(\tau_{2,1}) = \sin(2\pi f \tau_{2,1})$, the maximum of the delay bias $\tau_b$ as a function of the relative propagation delay $\tau_{2,1}$ is given by

$$\begin{aligned}
\tau_b &\leq \left| \Re\left\{\frac{j\alpha_1\alpha_2 f^{\mathrm{T}} a(\tau_{2,1})}{2\pi\alpha_1^2 f^{\mathrm{T}} f}\right\}\right| = \left|\frac{\alpha_{2,1} f^{\mathrm{T}} p(\tau_{2,1})}{2\pi f^{\mathrm{T}} f}\right| \\
&= \left|\frac{N_s M_a \alpha_{2,1} \Re\{s'(\tau_{2,1})\}}{4\pi^2 f^{\mathrm{T}} f}\right|.
\end{aligned} \tag{3.41}$$

Afterwards, we define the *measure of bias* as

$$\varrho(\alpha_{2,1}, \tau_{2,1}) = \left|\frac{N_s M_a \alpha_{2,1} \Re\{s'(\tau_{2,1})\}}{4\pi^2 f^{\mathrm{T}} f}\right|. \tag{3.42}$$

The measure of bias $\varrho(\alpha_{2,1}, \tau_{2,1}) = 0$ means that the reflection will not cause a bias in the estimate $\check{\tau}_1$, even if this reflection is not considered in the estimation model. As we can see, the measure of bias depends on the signal pattern through $s'(\tau_{2,1})$,

but also on the relative gain $\alpha_{2,1}$. Therefore, a reflected signal component, which is largely attenuated compared to the LoS component, will only cause a small bias when it is not considered in the simplified model.

If the channel impulse response (3.34) contains more than two paths (i.e., $L \geq$ 2), the bias due to the unconsidered reflections can be derived as

$$\tau_b = \sum_{l=2}^{L} \Re \left\{ \frac{-j2\pi x_1^H x_l (\boldsymbol{f} \odot \boldsymbol{a}(\tau_1))^H \boldsymbol{a}(\tau_l)}{-4\pi^2 x_1^2 \boldsymbol{f}^T \boldsymbol{f}} \right\} \leq \sum_{l=2}^{L} \left| \frac{N_s M_a \alpha_{l,1} \Re\{s'(\tau_{l,1})\}}{4\pi^2 \boldsymbol{f}^T \boldsymbol{f}} \right| \qquad (3.43)$$

Hence, when more reflections are neglected in the model, the resulting bias in the worst case will be the superposition of the biases derived from multiple two-path channels with the fixed LoS path, in which the reflections are treated separately.

### 3.2.3. Flop Count

A numerical operation (e.g., addition, multiplication, square-root, etc.) can be defined as a flop, and the number of required flops can be used to evaluate the computational complexity [121]. As the direct search method is applied here to determine the time delay, the cost function (3.27) should be computed for each value in a search grid that contains all possible delay values. Here we only derive the required number of flops for a single grid-point, and the size of the search grid is not considered.

Considering $M_a$ signal bands, $N_s$ subcarriers per band, and an $L$-path channel in the estimation model, then the number of required flops is derived as follows,

$$\text{flops}_{\text{tde}} = \begin{cases} (1 + 4L)(M_a N_s)^2 + 2(L^2 + L)(M_a N_s) + L^3/3 + L^2 - L - 1, & L > 1; \\ 5(M_a N_s)^2 + 4 M_a N_s - 1, & L = 1. \end{cases} \qquad (3.44)$$

For more details, the reader is referred to [121], as well as Appendix A.3. The required flops in (3.44) is dominated by the term $(1 + 4L)(M_a N_s)^2$. As the number of measurements $M_a N_s$ is generally larger than the number of paths $L$ considered in the model to avoid rank-deficiency, considering less paths can largely reduce the computational complexity. Given a fixed number of paths $L$, using less signal bands $M_a$ can also reduce the computational complexity considerably. Therefore, we aim to design a ranging signal which provides a good balance between computational complexity and ranging performance. This signal design will be introduced in Chapter 5.

### 3.2.4. Examples

In this subsection, we first provide an example to illustrate impact of the signal spectrum pattern and the reflection on the measure of dependence and the measure of bias. Then, the computational complexity of the ML-based time delay estimation is presented, with regard to the number of signal bands used for time delay estimation, and the number of path considered in the estimation model.

In a multipath channel, the relative propagation distance between the LoS path and the reflected path is expected to be from 0 to 10 m. To derive the measure of dependence, the propagation gain of each path is assumed to be known.

The received signal power for the LoS path and the reflection, within the different propagation distance $d_1$ and $d_2$, can respectively be computed using a free-space path loss (FSPL) model [7],

$$P_{r_1} = P_t \left[ \frac{\lambda \sqrt{G_l}}{2\pi d_1} \right]^2 , \quad P_{r_2} = P_t \left[ \frac{\lambda \sqrt{G_l}}{2\pi d_2} \right]^2 , \tag{3.45}$$

where $\lambda$ denotes the wavelength of the central carrier $f_c$, $\sqrt{G_l}$ denotes the product of the antenna gain for both the transmitter and the receiver. Then, the relative gain $\alpha_{2,1}$ can be derived by

$$\alpha_{2,1} = \frac{\alpha_2}{\alpha_1} = \sqrt{\frac{P_{r_2}}{P_{r_1}}} = \frac{d_1}{d_2} . \tag{3.46}$$

Considering the signal spectrum patterns shown in Fig. 3.5, Fig. 3.6 shows the
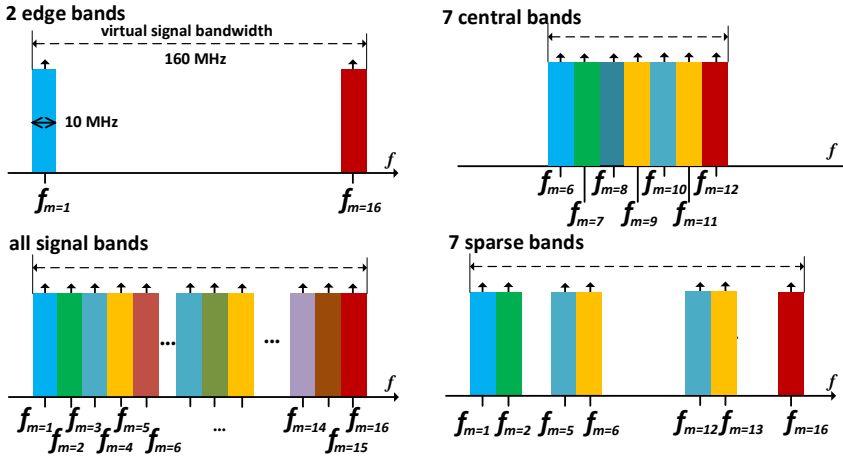


Figure 3.5: Examples of multiband signals, where $M = 16$ signal bands are available for time delay estimation, and each signal band contains $N_s = 64$ subcarriers within a bandwidth of 10 MHz.

measure of dependence and the measure of bias. A reflection with a zero measure of dependence does not correspond to a zero measure of bias. Therefore, an independent but unconsidered reflection can still cause a delay bias in the simplified model. Compared to the measure of dependence and the measure of bias derived based on 7 contiguous bands, the indicators derived for all $M = 16$ bands become smaller due a larger signal bandwidth, especially for close-in reflections. Within the same virtual signal bandwidth, using more signal bands can improve the resistance against multipath, so that the measure of dependence and the measure of bias are not largely affected by having to estimate also the reflection.

Then, Fig. 3.7 presents the accuracy of time delay estimation for the aforementioned signal patterns. The performance of an unbiased estimator in the full
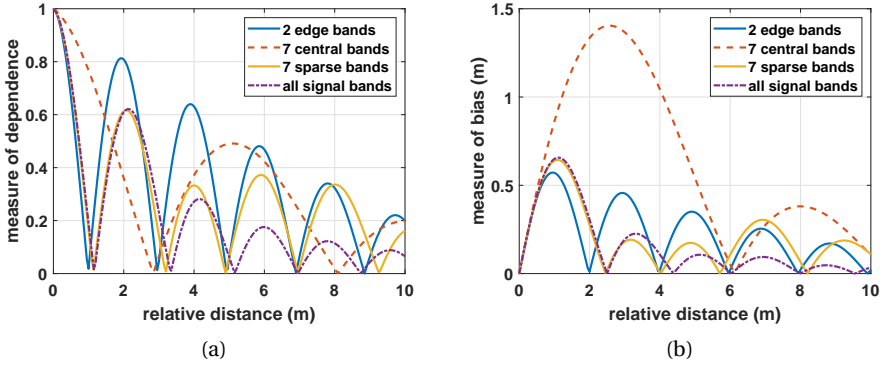
Figure 3.6: (a) Measure of dependence for delay estimation $\varsigma(\tau_{2,1})$ (cf. (3.33)), (b) measure of bias $\varrho(\alpha_{2,1}, \tau_{2,1})$ (cf. (3.42)).

model is evaluated by the CRLB. The accuracy of a biased estimator in the simplified model is quantified by the mean-square-error (MSE), which can be decomposed in a variance-plus-bias-square. Given a fixed virtual signal bandwidth (i.e, 160 MHz), using more signal bands in the full model improves the accuracy of the delay estimator. Although the overall improvement is relatively limited (e.g., a few centimetres) as shown in Fig. 3.7(a), using more signal bands can increase the robustness against multipath, as the root-CRLB is less affected by the reflections. In addition, as shown in Fig. 3.7(b), using the simplified model, the root-MSE is dominated by the bias. Similarly, using more signal bands can generally reduce the bias resulting from not considering the reflection in the model.
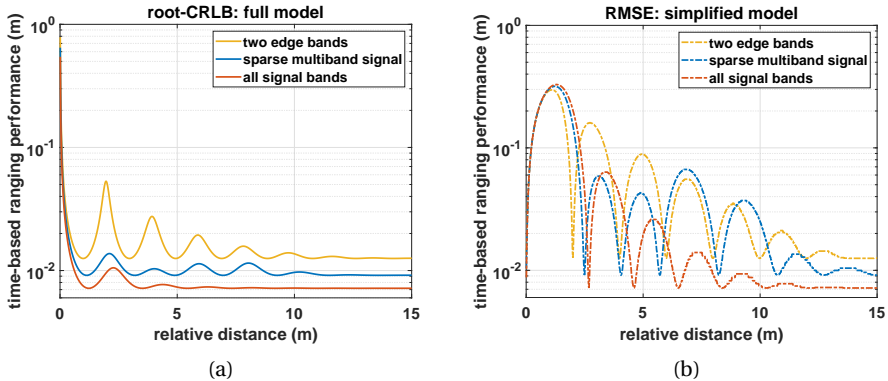


Figure 3.7: Ranging accuracy for different signal patterns. (a) The root-CRLB to evaluate the accuracy of the delay estimator obtained by the full model, and (b) the RMSE for the simplified model. In total, $M = 16$ signal bands with 10 MHz of bandwidth each are available for ranging. The relative gain is computed based on the FSPL model.

Additionally, in Fig. 3.7, one can notice that when a reflection with a very small relative distance (e.g., less than a few decimetres), the simplified model can outperform the full model. A very close-in multipath normally complies with a large measure of dependence. Considering it in the full model leads to a poorly estimated LoS path time delay. On the other hand, close-in multipath only leads to a relatively small measure of bias as shown in Fig. 3.6. Therefore, using the simplified model, only a small bias will be introduced to the time delay estimator, and the precision will not be deteriorated by the close-in reflection.

Furthermore, using the simplified model, Fig. 3.8 shows the envelope of the multipath error as a function of relative distance $c\tau_{2,1}$ in a two-path channel, with the assumption of infinite signal bandwidth, and the relative gain $\alpha_{2,1}$ set to 0.6. Four types of signals are considered in the Fig. 3.8: two contiguous OFDM signal bands occupying a total bandwidth of 20 MHz (i.e., two bands of 10 MHz each), the GPS L5 signal with a chip rate of 10.23 Mchips/s acquired with a sampling frequency of 20.46 MHz, 7 sparsely placed OFDM signal bands (see Fig. 3.5 at the bottom-right) with a virtual signal bandwidth of 160 MHz, and 16 contiguous signal OFDM bands (see Fig. 3.5 at the bottom-left) occupying a total bandwidth of 160 MHz. As shown in Fig. 3.8, a large signal bandwidth effectively improves the separability of multipath reflections and mitigates the multipath error. The maximum multipath error is about 4.0 m when using a bandwidth of 20 MHz for ranging, while the maximum multipath error can be reduced to 0.5 m when increasing the bandwidth of the ranging signal to 160 MHz. Additionally, sparsely occupying 7 bands within a 160 MHz for ranging will not significantly increase the multipath error, compared to using all 160 MHz bandwidth for ranging.
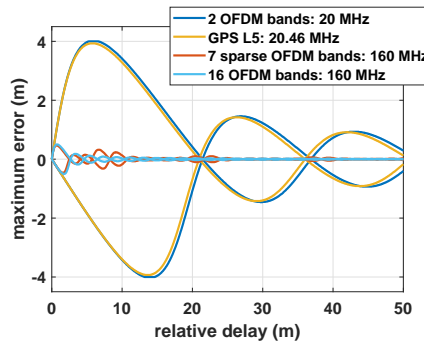


Figure 3.8: Infinite-bandwidth multipath error envelopes for two contiguous OFDM signal bands (20 MHz), GPS L5 signal (20.46 MHz), seven sparsely placed OFDM signal bands (virtual bandwidth: 160 MHz, see Fig. 3.5 at the bottom-right), and 16 contiguous OFDM signal bandwidth (160 MHz, see Fig. 3.5 at the bottom-left) , with the relative path gain $\alpha_{2,1} = 0.6$.

As presented in section 3.2.3, the computational complexity for time delay estimation is evaluated by the number of required flops. Here. the number of paths $L$ considered in the estimation model is set to be 1, 2, and 5, and the number of activated signal bands $M_a$ is varied from 6 to 16. Using the direct search method to solve the cost function (3.27), Fig. 3.9 shows the number of the required flops

for time delay estimation for a single element in the search grid.
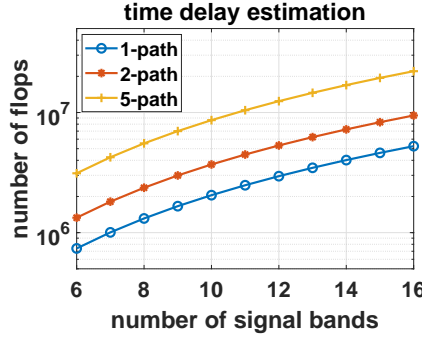


Figure 3.9: Required flops for time delay estimation in computing cost function (3.27) for each element in search grid

Given a fixed amount of signal bands, considering one path less in the time delay estimation model reduces the amount of required flops by about 49%. On the other hand, considering a fixed amount of paths in the model, using one less signal band reduces the number of the required flops by about 27%.

## 3.3. Other methods

Apart from the original ML method, other commonly used time delay estimation methods are introduced in this section, like matched filter, subspace based methods, and the ML method with modified forms. Although these methods use different cost functions to determine the time delay, they can still be linked to the one of the ML-based method as presented in section 3.2.

### 3.3.1. Matched Filter

The matched filter (MF) [122] is the most common approach to determine the time delay, by matching the received signal to the locally generated reference signal. Therefore, the matched filter method is typically implemented based on the cross correlation between the received signal and the locally generated reference signal. Using $M_a$ signal bands and $N_s$ subcarriers in each band, the cost function is obtained by [123]

$$
\begin{aligned}
g(\theta) &= \frac{1}{M_a} \sum_m \frac{1}{N_s} \sum_{n=0}^{N_s-1} r_{b,m}^*[n;\tau] s_{b,m}[n;\theta] \\
&= \frac{1}{N_s M_a} \mathscr{F}\left\{\boldsymbol{r}_b^H[\tau]\right\} \mathscr{F}\left\{\boldsymbol{s}_b[n;\theta]\right\} = \frac{1}{\boldsymbol{a}(\theta)^H \boldsymbol{a}(\theta)} \boldsymbol{H}^H \boldsymbol{a}(\theta).
\end{aligned}
$$
(3.47)

As shown in the cost function of the MF method, one can determine the time delay directly in time domain, by shifting the locally generated reference signal with different time offsets, until it most likely matches the received signal. Without

oversampling or interpolation, the time resolution is limited by the sample interval. Alternatively, one can also the time delay in the frequency domain, by adding an extra phase rotation on the frequency spectrum of the locally generated reference signal. The cost function (3.47) is equivalent to the ML-based cost function (3.35) of the simplified model, in which only one path is considered.

Then, the time delay can be derived by

$$\hat{\tau} = \arg\max_{\theta} \ |g(\theta)|. \tag{3.48}$$

Generally, multipath is not considered in the locally generated reference ranging signal. Hence, in practice, the time delay estimator derived from the MF method will become biased in a multipath channel. However, the MF method is attractive for low-cost applications, as shown in section 3.2.3, as the MF method by default only considers one path in the ML-based simplified mode, and does not require enormous computational resources.

### 3.3.2. Subspace-based Method

In this section, the subspace-based method is introduced, which reduces the bias compared with the MF method, and introduces less computational complexity than the multivariate ML method. The *sample covariance matrix* is the core of the subspace-based methods, of which the eigenvalues and the associated eigenvectors indicate the signal space and noise space.

Using the sampled channel frequency response (2.26), one can compute the sample covariance matrix based on the forward-backward (FB) approach [124, 125]

$$Q = \frac{1}{2K} \left( \mathscr{H} \mathscr{H}^H + J \left( \mathscr{H} \mathscr{H}^H \right)^* J \right) \tag{3.49}$$

where $\mathscr{H}$ denotes a Hankel matrix with $K$ columns

$$\mathscr{H} = \begin{bmatrix} [H]_1 & [H]_2 & \cdots & [H]_K \\ [H]_2 & [H]_3 & \cdots & [H]_{K+1} \\ \vdots & \vdots & & \vdots \\ [H]_{N_s M_a - K} & [H]_{N_s M_a - K+1} & \cdots & [H]_{N_s M_a} \end{bmatrix},$$

and $J$ denotes a matrix that all anti-diagonal elements are 1, and the others are 0. Alternatively, if the propagation delay is constant across $P$ symbols, the sample covariance matrix can be constructed from multiple OFDM symbols [126] as follows

$$Q = \sum_{p=1}^{P} H_p H_p^H, \tag{3.50}$$

where $H_p$ denotes the sampled channel frequency response measured at the $p$-th symbol from $M_a$ signal bands. Mind that the dimension of the sample covariance matrix shown in (3.50) is different from the one in (3.49), due to the offset of $K$ elements in the Hankel matrix.

Considering an $L$-path channel, its eigenvalues and the corresponding eigenvectors of the sample covariance matrix $Q$, can be obtained by [127]

$$Q = \begin{bmatrix} U_s & U_n \end{bmatrix} \left[ \begin{array}{c|c} \Sigma_s + \sigma^2 I_L & 0 \\ \hline 0 & \sigma^2 I_{N_s M_a - K - L} \end{array} \right] \begin{bmatrix} U_s^H \\ U_n^H \end{bmatrix}, \tag{3.51}$$

where $U_s$ contains $L$ orthonormal columns which span the column space of $A$, $\Sigma_s$ denotes a $L \times L$ diagonal matrix containing the nonzero singular values of $A$.

Based on the model of the sampled channel frequency response (2.27), to describe the column span of matrix $A$ in (2.27) with rank $L$, a singular value decomposition of $A$ can be described as

$$A = U_s \Sigma_s V_s^H. \tag{3.52}$$

Then, we elaborate on the subspaced-based MUSIC and ESPRIT method in the following subsections to determine the propagation time delay.

### MUSIC Method
As the columns of $U_s$ should span the same subspace of the columns of $A$, one has

$$U_n^H A = 0, \tag{3.53}$$

and the signal components in $A$ can be determined by exploiting the orthogonality to the noise space.

In practice, the number of paths $L$ in a multipath channel (i.e., the dimension of the matrix $A$) is unknown, but it can be determined, for example, by using minimum description length (MDL) criteria [113]. With the subspace basis derived from the singular value decomposition (SVD) of the sample covariance matrix (3.50), the cost function for the MUSIC (Multiple SIgnal Classification) method is obtained by

$$\hat{\tau} = \arg\min_{\tau} \frac{a^H(\tau) \hat{U}_n \hat{U}_n^H a(\tau)}{a^H(\tau) a(\tau)}. \tag{3.54}$$

Based on the direct search method, one can estimate the time delay for both the LoS path and the reflections, by choosing the $L$ lowest local minima of the cost function (3.54).

It is also worth to mention that if the LoS path and the reflection are *uncorrelated* (i.e., $P_{a_1 a_2} = 0$), though likely not realistic in practice, the ML method is equivalent to the MUSIC method [92], when the noise space $U_n$ can be accurately determined from the sample covariance matrix. So that $L$-dimensional search problem (3.23) can be reduced to $L$ one-dimensional problems.

### ESPRIT Method
To avoid computing the cost function for each value in the search-grid when using the MUSIC method, and further reduce the computational complexity, the ESPRIT (Estimation of Signal Parameters via Rotational Invariance Technique) method

can also be applied for time delay estimation [126], if the design matrix $A(\tau)$ in (2.27) has a shift-invariant structure.

If comb-type pilot subcarriers are used in the OFDM training symbols for ranging, and the spacing between two pilot subcarriers is the same across all pilots (i.e., $\Delta f_p$) for all signal bands, then one can obtain an rotational invariance matrix. For example, here we simply assume that all $N_s$ subcarriers in each of the $M$ signal bands are used for ranging. Then, $\Delta f_p = \Delta f$, and we can select the first $N_s M - 1$ rows from $A$ defined as $A^{(1)}$, also let the last $N_s M - 1$ rows of $A$ be denoted as $A^{(2)}$, and further have

$$A^{(2)} = A^{(1)}\Theta, \tag{3.55}$$

where $\Theta$ denotes the rotation invariant matrix of $A$, which is a diagonal matrix and can be written as

$$\Theta = \text{diag}\left(\left[\exp(-j2\pi\Delta f \tau_1), \; ... \;, \exp(-j2\pi\Delta f \tau_{L-1})), \; \exp(-j2\pi\Delta f \tau_L)\right]\right). \tag{3.56}$$

In addition, there should be an $L \times L$ invertible projection matrix $T$ that maps one basis to the other, and one has

$$U_s^{(1)} = A^{(1)}T, \;\; U_s^{(2)} = A^{(2)}T = A^{(1)}\Theta T, \tag{3.57}$$

where $U_s^{(1)}$ and $U_s^{(2)}$, respectively, denote the first $N_s M - 1$ rows and the last $N_s M - 1$ rows of $U_s$. Based on (3.57), one can also have

$$U_s^{(2)} = U_s^{(1)}\left(T^{-1}\Theta T\right). \tag{3.58}$$

Hence, the solution of (3.58) can be obtained based on a total least squares (TLS) algorithm [127] as

$$\underbrace{\left(U_s^{(1)H}U_s^{(1)}\right)^{-1} U_s^{(1)H}U_s^{(2)}}_{D} = T^{-1}\Theta T, \tag{3.59}$$

which indicates that the eigenvalues of the matrix $D$ will be the diagonal elements of the rotational invariant matrix $\Theta$. Then, the propagation time delays of each path can be derived from the phases of the eigenvalues (cf. (3.56)).

The rotational invariant matrix $\Theta$ is related to the column space of $A$, so the central frequency $f_c$ is captured in an $L$ dimensional vector $x$ instead (cf. 2.28). Therefore, the phase of the diagonal elements in $\Theta$ are determined by the propagation delay and the pilot spacing (i.e., $\Delta f_p$) which is much smaller than the actual central carrier frequency $f_c$. Consequently, the performance of the solution only relies on the spacing of the pilot sub-carriers $\Delta f_p$ instead of the central carrier frequency $f_c$.

For an OFDM system with $N_s = 64$ sub-carriers and a 10 MHz bandwidth in each signal band, the spacing $\Delta f$ is 156.25 kHz in (3.56). When all subcarriers are allocated as pilots (i.e., $\Delta f_p = \Delta f$), and the propagation delay of each path is less

than the period $1/\Delta f$, which is equivalent to 1920 m in distance, we can derive the propagation delay unambiguously from the phase. Similarly, if we only use $N_p = 16$ comb-type pilots with $\Delta f_p = 4\Delta f$ for positioning, we can unambiguously determine the propagation delay when the propagation distance is less than 480 m. Therefore, as long as the propagation delay is less than $1/(\Delta f_p)$, no phase cycle ambiguity problem will be encountered in the ESPRIT method.

### 3.3.3. Modified Maximum Likelihood Method

The cost function of the ML method (3.23) is determined not only by the time delay but also by the complex gain, and the propagation time delay is nonlinearly present in the design matrix $A(\tau)$. Hence, it is not straightforward to obtain a closed-form solution. In this subsection, instead of directly estimating the propagation time delay, one estimates the channel impulse response based on the ML method, in which the design matrix $A(\tau)$ is predefined by the user. By matching the sampled channel frequency response with the predefined $A(\tau)$, one can determine the resulting complex gain as the channel impulse response (CIR), from which one can determine the time delay of the LoS path. As example, inverse Fourier transformation and sparsity-promoting de-convolution approaches are introduced as the modified ML method for time delay estimation.

Inverse Fourier Transformation
Based on the sampled channel frequency response $H$, and the cost function of MLE as shown in (3.23), instead of estimating both the time delay $\tau$ and gain $x$, one can simply assume that the number of paths in a multipath channel is the same as the total number of subcarriers [128]. For example, if all $N_s$ subcarriers in each of the $M$ signal bands are used for ranging, one can assume an $L = N_s M$-path channel, in which the time delay of each path is fixed with a time resolution of the sample interval $T_s$, and the time delay spreads are less than the symbol time (i.e., inverse of the subcarrier spacing). Then, instead of using the design matrix $A(\tau)$ with unknown time delay, the cost function (3.23) can be rewritten by

$$\hat{x} = \arg\min_{x} \|H - Bx\|^2_{Q_H^{-1}}, \quad x \in \mathbb{C}^{N_s M}, \tag{3.60}$$

where $B$ is an $N_s M$-by-$N_s M$ Fourier transformation matrix, and

$$[B]_{i,k} = \exp\left(-j2\pi(i\Delta f)(kT_s)\right).$$

If the variance matrix $Q_H$ is a diagonal and scaled identity matrix as shown in (2.27), then the complex gain can be easily obtained by [129]

$$\hat{x} = (B^H B)^{-1} B^H H = B^{-1} H, \tag{3.61}$$

where $B^{-1}$ can also be treated as an inverse Fourier transformation matrix. Hence, the CIR can be obtained by taking the inverse Fourier transform of the sampled channel frequency response, and the time delay of the LoS path can be taken from the strongest path in the CIR.

Note that if only a few signal bands, which are sparsely placed in the spectrum, are used for time delay estimation, $\boldsymbol{B}$ in (3.61) is no longer an equally spaced symmetric Fourier transformation matrix.

### Sparsity-promoting De-convolution

In a practical multipath channel, the number of resolvable paths is generally less than the size of the sampled channel frequency response (e.g., $L \leq N_s M$). Hence, the CIR $\boldsymbol{x}$ obtained from (3.61) should contain some zeros. To exploit the sparsity, an $l_1$-norm-based regularization can be added to the cost function (3.60).

Furthermore, instead of using a square Fourier transformation matrix for $\boldsymbol{B}$, one can create a wide matrix $\boldsymbol{D}$ (i.e., the number of columns in $\boldsymbol{D}$ is even larger than the number of rows) as a *dictionary*, which contains phasors with a constant amplitude but different propagation delays. Based on the dictionary, we can estimate the channel profile and further obtain the propagation time delay of the direct-LoS path.

For example, one can use a search vector $\boldsymbol{d}$ that contains the time delay for all possible paths, given by

$$\boldsymbol{d} = \begin{bmatrix} 0 & T_d & \dots & (N_d - 1)T_d \end{bmatrix},$$

to create the dictionary $\boldsymbol{D}$, where $T_d$ denotes the time resolution of the dictionary which can be smaller than the sample interval $T_s$, and $N_d$ denotes the number of delays in the dictionary. Considering $M$ signal bands, and based on the search vector $\boldsymbol{d}$, the dictionary $\boldsymbol{D}$ is formulated into a $MN_s$-by-$N_d$ matrix, the $i$-th column of the dictionary is given by

$$[\boldsymbol{D}]_i = \begin{bmatrix} \exp\left(-j2\pi \tilde{\boldsymbol{f}}_1 (i-1)T_d\right) \\ \vdots \\ \exp\left(-j2\pi \tilde{\boldsymbol{f}}_m (i-1)T_d\right) \\ \vdots \\ \exp\left(-j2\pi \tilde{\boldsymbol{f}}_M (i-1)T_d\right) \end{bmatrix}, \tag{3.62}$$

where $\tilde{\boldsymbol{f}}_m$, defined in (3.12), contains the subcarrier frequency in the $m$-th signal band.

Then, the problem of computing the CIR becomes to solve the following optimization [130]

$$\hat{\boldsymbol{x}} = \arg\min_{\boldsymbol{x}} \parallel \boldsymbol{H} - \boldsymbol{D}\boldsymbol{x} \parallel_{Q_H^{-1}}^2 + \rho \parallel \boldsymbol{x} \parallel_1, \quad \boldsymbol{x} \in \mathbb{C}^{N_d \times 1}, \tag{3.63}$$

where the user specified $\rho$ determines the level of sparsity of the estimation result. Generally, the size of the search vector $\boldsymbol{d}$ (i.e., $N_d$) is much larger than the number of the sample channel frequency response $\boldsymbol{H}$ (i.e., $N_s M$), while the actual number of paths $L$ in a multipath channel is much smaller than $N_d$, and the estimates in $\boldsymbol{x}$ should be sparse. Thus, an $l_1$ norm is used as a penalty for $\boldsymbol{x}$ to produce a sparse solution. If the direct LoS path always exists in a multipath channel, its propagation delay can be determined from the propagation gain of the first path in $\boldsymbol{x}$.

### **3.3.4.** Examples

As an example, considering a two-path channel, the cost function of the time delay estimation methods presented in section 3.2 and section 3.3 are shown in this subsection. Here, all $M = 16$ contiguous signal bands are used for time delay estimation, and each signal band has a bandwidth of 10 MHz. Fig. 3.10(a) shows the cost function in the following two path channel

$$h(t) = \delta\left(t - \frac{3\ [m]}{c}\right) + 0.8\delta\left(t - \frac{4.15\ [m]}{c}\right), \tag{3.64}$$

where the propagation distance of the LoS path is set to be 3 m, and the relative distance between the LoS path and the reflection is 1.15 m. Then, in Fig. 3.10(b), the following two-path channel is considered

$$h(t) = \delta\left(t - \frac{3\ [m]}{c}\right) + 0.8\delta\left(t - \frac{5.5\ [m]}{c}\right). \tag{3.65}$$

Note that, as shown in Fig. 3.6(b), using all $M = 16$ signal bands, the measure of bias $\varrho(\tau_{2,1})$ (cf. (3.42)) for a reflection with a relative propagation distance of 2.5 m is zero.
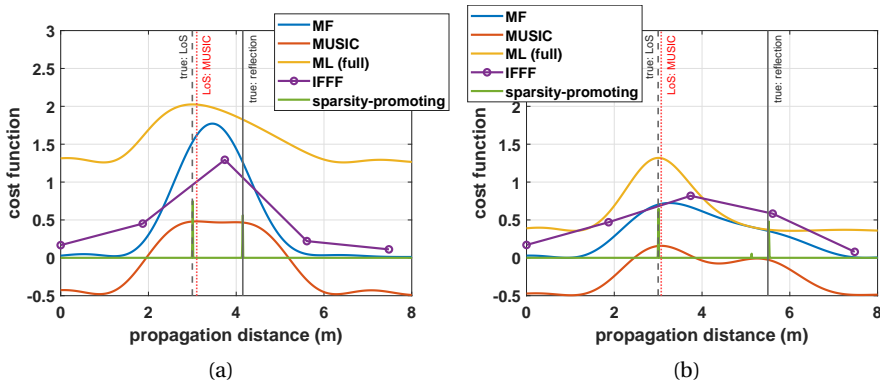


Figure 3.10: Cost function of MLE, matched filter, subspace-based MUSIC method, modified ML method (i.e., both inverse Fourier transform and regularization with $l_1$ norm (sparsity-promoting)), the propagation distance of the LoS path is fixed to 3 m, the relative distance between the LoS path and the reflection is 1.15 m (a), and 2.5 m (b). The SNR is 20 dB, and 16 signal bands with 10 MHz bandwidth of each signal band are used for time delay estimation. A minus sign is added to cost function of MUSIC method, so that a minimization problem (cf. (3.54)) can be changed to a maximization problem, and then the cost function is offset intentionally by 0.5 for better visualization. The LoS time delay estimated derived from MUSIC method is shown in red-dashed line.

The cost function of the ML method with the full model should be a two dimensional surface, but Fig. 3.10 only presents the cross-section (in yellow) when the time delay of the reflection is correctly determined according to the channel. As two paths are jointly considered in the model, the resulting time delay estimator is unbiased.

Using the MF method for time delay estimation, the resulting estimator is likely to be biased (e.g., see Fig. 3.10(a) in blue), unless the measure of bias $\varrho(\tau_{2,1})$ is zero (see Fig. 3.10(b) in blue). If the measure of bias is zero, the corresponding reflection will not cause a bias in the estimator, even it is not considered in the estimation model.

Compared with the cost function of the MF method, the LoS path and the reflection are more distinguishable in the cost function of the MUSIC method. However, if the paths are correlated, the resulting estimator will be still biased.

Based on the inverse Fourier transform of the sampled channel frequency response, and without oversampling, the time resolution of the obtained CIR is equal to the sample interval. Based on a sampling frequency of 160 MHz, the resulting resolution in distance is about 1.87 m. Hence, as shown in Fig. 3.10 (in violet), if the time delay is not an integer multiple of the sample interval, the resulting time delay estimator will be biased due to quantization. While based on a large dimensional dictionary with a search grid with a finer time interval (e.g. 1 cm as shown in Fig.3.10 in green) than the inverse Fourier transform, and sparsity-promoting $l_1$ norm based regularization, the time delay of the LoS path can be determined from the CIR. With the hard constraint of the $l_1$ norm, the precision of the time delay estimator is improved, but at the cost of a bias, and also an enormous computational complexity due to the very large dictionary.

## **3.4.** Time-based ranging and Sampling Frequency Offset

As stated already in section 3.2, we only estimate the *residual* time delay $\Delta\tau$ after symbol synchronization, instead of the absolute time delay $\tau$. Hence, to retrieve the absolute range information, one needs to reconstruct the propagation time by adding the time delay estimate $\Delta\hat{\tau}$ to the symbol synchronization time $\tau_{\text{sym}}$,

$$\underline{\hat{\tau}}[q] = \tau_{\text{sym}}[q] + \Delta\underline{\hat{\tau}}[q]. \tag{3.66}$$

Here, the time delay derived from symbol synchronization is assumed to deterministic, and its random error is lumped into $\Delta\tau[q]$.

In practice, the receiver is generally not synchronized to the transmitters, and runs on its own clock. An extra timing offset will be introduced by the sampling clock offset that is originated from the normalized frequency offset $\eta$. As shown in (2.14) in section 2.2, the clock error due to the receiver sampling frequency offset in the $q$-th symbol is given by

$$\tau_\eta[q] = -\sum_{u=0}^{q}(N_s + N_g)\eta[u]T_s - N_g\eta[q]T_s. \tag{3.67}$$

By estimating $\tau_\eta[q]$, the normalized frequency offset can be obtained for receiver frequency synchronization, which will be introduced in Chapter 6.

In addition, if the reflections are not properly identified and considered in the model, a bias of $\nabla\tau[q]$ will be introduced in the time delay estimator. Now, com-

bined with the actual propagation delay $\tau[q]$, the mean of the time delay estimator is given by

$$\mathbb{E}\left\{\hat{\underline{t}}[q]\right\} = \tau_\eta[q] + \tau[q] + \nabla\tau[q]. \tag{3.68}$$

Then, multiplying the time delay estimate by the speed of light $c$, the time-based range observable can be obtained by

$$\underline{\rho}[q] = \hat{\underline{t}}[q]c. \tag{3.69}$$

As the range measurement $\rho$ contains not only the actual range, but also other errors, $\rho$ is generally referred to as the *pseudo-range* measurement.

Finally, depending on the particular time delay estimation method, one can determine the variance of the time-based range measurement. For example, using the ML method in the full model, the variance of the pseudo-range measurement can be derived from (3.28), and (3.29) in the simplified model.

## 3.5. Summary

In this chapter, time delay estimation particularly for the LoS path in a multipath channel is presented.

Based on OFDM modulation, the CRLB has been derived for both the single band signal and the multiband signal. Using a large signal bandwidth can improve the precision of the time delay estimator. According to the measure of signal bandwidth $\beta^2$ (cf. (3.6)), based on the same amount of total signal power and the signal bandwidth, moving more signal power towards the edge of the signal spectrum can improve the precision of the time delay estimator. On the other hand, considering an additional unknown parameter for the reflection in a multipath channel, the precision of the LoS time delay estimator will also be determined by the relative delay between the LoS path and the reflection.

In order to obtain an unbiased time delay estimator in a multipath channel for ranging, a maximum likelihood (ML) method that considers not only the LoS, but also the reflections, can be applied for time delay estimation. As shown in the CRLB, considering an additional reflection in the model (i.e., the full model), and depending on the relative delay, the accuracy of the time delay estimator can become poor. Hence, a measure of dependence $\varsigma(\tau_{2,1})$ (cf. (3.33)) is defined between the LoS path and a reflection, and indicates how the accuracy gets worse by considering such an additional reflection in the time delay estimation model.

On the other hand, to reduce the computational complexity of multivariate ML-based time delay estimation, one can neglect some of the reflected paths in the simplified model, which can lead to a better precision than using the full model. However, the time delay estimator can become biased. To evaluate the resulting bias in the simplified model, a measure of bias $\varrho(\tau_{2,1})$ (cf. (3.42)) is defined, which indicates how large the bias can be, when such a reflected path is not taken into consideration for time delay estimation.

In practice, as a compromise between computational efficiency and overall ranging performance, one can jointly estimate the time delays only for a few strong

reflections (i.e., keep $L$ limited). Consequently, the resulting bias will be small when other reflections are not considered in the simplified model. In addition, not all signal bands are needed to achieve the user specified threshold for the measure of dependence and the measure of bias. Therefore, one can use less spectral resources and samples (i.e., keep $M_a$ small) to even further reduce the computational complexity. Sparsely selection of the signal bands in an optimal way will be presented in chapter 5.

In addition, other time delay estimation methods have been reviewed in this chapter. The matched filter (MF) is very simple to be implemented, however, the resulting the time delay estimator becomes biased in a multipath channel. The MF method is equivalent to a simplified ML method when only one path is considered. The subspace-based methods pose less computational complexity than the original full ML method. For example, the MUSIC method reduces an $L$-dimensional search problem (in an $L$-path channel) to $L$ one-dimensional search problems [92]. Nevertheless, the estimator can also become biased in a multipath scenario, if the paths are correlated, and a large amount of samples are needed to determine a relatively precise subspace basis. Inverse Fourier transform and sparsity-promoting de-convolution are presented as the modified ML methods in this chapter, which compute the channel impulse response (CIR), instead of directly estimating the time delay. Based on the estimated CIR, one can obtain the time delay of the LoS path for ranging.

**3**

# 4

# Carrier Phase Estimation

Compared with time delay, carrier phase provides range information with much better precision, due to the small wavelength of the center carrier $f_c$, though the involved carrier phase cycle ambiguity should be properly resolved. Carrier phase estimation, for purpose of ranging, is introduced in this chapter. Without considering multipath effects, one can simply reconstruct the carrier phase by combining the sampled channel frequency response of symmetrically placed subcarriers. On the other hand, the carrier phase can be estimated using the maximum likelihood method, in which both the LoS path and the reflections in a multipath channel are considered in the model.

As one can only obtain a fractional part of the carrier phase, which varies from $-\pi$ to $\pi$, each carrier phase estimate in principle carries its own carrier phase cycle ambiguity, which will consequently lead to a rank defect in a positioning model (see Chapter 6), because of too many unknown parameters. Hence, carrier phase tracking (i.e., unwrapping) is needed for a series of carrier phase estimates, so that only one initial integer carrier phase cycle ambiguity remains. Additionally, when using burst-like signal packets for ranging, the receiver frequency offset needs to be considered to avoid cycle slips in carrier phase tracking.

## 4.1. Subcarrier Combination

Based on the measurement model (2.27), and only considering a single path channel, the expectation of the sampled channel frequency response from the $i$-th subcarrier in the $m$-th signal band, is given by

$$\mathbb{E}\left\{\underline{H}_{i,m}\right\} = \underbrace{\exp\left(-j2\pi(f_i + f_m)\Delta\tau\right)}_{[\boldsymbol{a}_m(\Delta\tau)]_{i+N_s/2+1}} \alpha \underbrace{\exp\left(-j\left(\pi\Delta\tilde{f}_c/\Delta f + \tilde{\phi}\right)\right)}_{x}$$

$$f_i = i\Delta f, \quad i = -N_s/2, \ -N_s/2, \ \dots, \ N_s/2 - 1$$

$$f_m = (m - M/2)\Delta f_G, \quad m = 1, \ 2, \ \dots, \ M,$$

(4.1)

where $\Delta\tilde{f}_c$ and $\tilde{\phi}$ have been defined in (2.14), and denote the frequency offset and the accumulated carrier phase offset, respectively; $\Delta f_G$ denotes the frequency hopping basis for generating the multiband signal (cf. (2.19)), the phase in $x$ is determined by the receiver frequency offset and the Doppler frequency offset with respect to $f_c$, and is referred to as the carrier phase. Note that the element index in the vector $\boldsymbol{a}_m(\Delta\tau)$ should be a positive integer number, which is corresponding to the subcarrier index $i$ offset by $N_s/2 + 1$.

Hence, one can use symmetrically located subcarriers to cancel the term $[\boldsymbol{a}_m(\Delta\tau)]_{i+N_s/2+1}$ in (4.1) [107], with

$$f_{-i} = -f_i, \quad i = 0, 1, \dots, N_s/2,$$
$$f_{-m+M} = -f_m, \quad m = 1, 2, \dots, M/2,$$

one has

$$\begin{aligned}
H_{i,m}H_{-i,-m+M} &= \exp\left(-j2\pi(f_i + f_m)\Delta\tau\right)\alpha\exp\left(-j\left(\pi\Delta\tilde{f}_c/\Delta f + \tilde{\phi}\right)\right) \\
&\quad \times \exp\left(-j2\pi(f_{-i} + f_{-m+M})\Delta\tau\right)\alpha\exp\left(-j\left(\pi\Delta\tilde{f}_c/\Delta f + \tilde{\phi}\right)\right) \quad (4.2) \\
&= \alpha^2\exp\left(-j2\Phi\right),
\end{aligned}$$

where $\Phi$ denotes the carrier phase

$$\Phi = \pi\Delta\tilde{f}_c/\Delta f + \tilde{\phi}. \tag{4.3}$$

Then, if all $M$ signal bands and $N_s$ subcarriers in each signal band are used to compute the carrier phase, one can have,

$$\hat{\Phi} = \frac{1}{2}\arg\left\{\sum_{m=1}^{M/2}\sum_{i=0}^{N_s/2-1} H_{i,m}H_{-i,-m+M}\right\}. \tag{4.4}$$

If $f_i + f_m = 0$ (i.e., central subcarrier) is used, then one can simply obtain the carrier phase from this subcarrier directly [51], as $[\boldsymbol{a}_m(\Delta\tau)]_{i+N_s/2+1}$ is no longer present in the sampled channel frequency response (4.1). However, in a zero-IF ( intermediate frequency) receiver, the central subcarrier is generally not activated, in order to avoid the interference from the DC (direct current) component [131].

Equation (4.2) only holds true in a single path channel. However, a practical channel generally contains several or many reflections. In an $L$-path channel, with

$\Delta\tau_{z,l} = \tau_z - \tau_l$, (4.2) is rewritten by

$$
\begin{aligned}
H_{i,m}H_{-i,-m+M} &= \left(\sum_{l=1}^{L} x_l[\boldsymbol{a}_m(\Delta\tau_l)]_{i+N_s/2+1}\right)\left(\sum_{l=1}^{L} x_l[\boldsymbol{a}_{-m+M}(\Delta\tau_l)]_{-i+N_s/2+1}\right) \\
&= \sum_{l=1}^{L} x_l x_l + \sum_{l=1}^{L}\sum_{z=1,z\neq l}^{L} x_i x_z \left(\exp(-j2\pi(f_i+f_m)\Delta\tau_{z,l}) + \exp(j2\pi(f_i+f_m)\Delta\tau_{z,l})\right) \\
&= \underbrace{\alpha_1^2 \exp\left(j2\Phi\right)}_{(1)} + \underbrace{\sum_{l=2}^{L} x_l x_l + \sum_{l=1}^{L}\sum_{z=1,z\neq l}^{L} 2x_i x_z \cos\left(2\pi(f_i+f_m)\Delta\tau_{z,l}\right)}_{(2)}.
\end{aligned}
\tag{4.5}
$$

Therefore, in a multipath channel, the carrier phase obtained by combining symmetrically located subcarriers, being a simple method, is easily affected by multipath due to term (2) in (4.5).

## 4.2. Maximum Likelihood Estimation

To account for multipath effects, one can consider both the LoS path and the reflections in the model when estimating the carrier phase, for instance, based on the maximum likelihood (ML) method. As shown in (3.24), once the propagation time delays are determined by MLE, we can reconstruct the design matrix $\boldsymbol{A}(\hat{\boldsymbol{t}})$, and continue to estimate the complex gains. In a similar way, as discussed in the previous section, one may use the simplified model that only contains the LoS path (i.e., using a vector $\boldsymbol{a}(\tau)$ instead of a matrix $\boldsymbol{A}(\boldsymbol{\tau})$), to estimate the complex gain of the LoS path and its corresponding carrier phase, if a biased solution for the carrier phase is acceptable. Otherwise, one needs to construct a full model based on the delays from the different paths and jointly estimate their corresponding complex gains and carrier phases. Similarly, we will analyse the accuracy of complex gain estimation based on the full model and the bias introduced in the simplified model.

### 4.2.1. Full Model

In this subsection, we analyse the accuracy of the unbiased gain estimator. Again, a 2-path channel (3.34) is considered as an example here. To construct the *full model*, the design matrix $\boldsymbol{A}(\boldsymbol{\tau})$ in (2.28) contains both the LoS component $\boldsymbol{a}(\tau_1)$ and a reflected component $\boldsymbol{a}(\tau_2)$, and they are constructed based on the unbiased propagation delay estimates from section 3.2.1. To simplify notation in the following derivations, $\boldsymbol{a}(\tau_1)$ and $\boldsymbol{a}(\tau_2)$ are replaced by $\boldsymbol{a}_1$ and $\boldsymbol{a}_2$, respectively. It should be mentioned that when there are more reflections in a multipath channel, $\boldsymbol{a}_2$ will be extended from a vector into a matrix that contains all reflected components.

Although the design matrix $\boldsymbol{A}(\boldsymbol{\tau})$ should contain all possible paths in a channel, and the complex gain can be estimated for all paths, only the complex gain of the LoS path is of interest for ranging and positioning. The carrier phase of the LoS

path $\hat{\Phi}$ can be derived from the complex gain $\hat{x}_1$, see (4.14) later on. Based on the partitioned model (3.34) and the MLE solution shown in (3.24), using $M_a$ signal bands and $N_s$ subcarriers in each signal band, the complex gain of the LoS path is given by

$$\hat{x}_1 = \left(\bar{\boldsymbol{a}}_1^{\mathrm{H}} \boldsymbol{Q}_H^{-1} \bar{\boldsymbol{a}}_1\right)^{-1} \bar{\boldsymbol{a}}_1^{\mathrm{H}} \boldsymbol{Q}_H^{-1} \boldsymbol{H}, \tag{4.6}$$

where

$$\begin{aligned}
\bar{\boldsymbol{a}}_1 &= P_{\bar{\boldsymbol{a}}_2}^{\perp} \boldsymbol{a}_1 \\
P_{\bar{\boldsymbol{a}}_2}^{\perp} &= \boldsymbol{I}_{N_s M_a} - \boldsymbol{a}_2 (\boldsymbol{a}_2^{\mathrm{H}} \boldsymbol{Q}_H^{-1} \boldsymbol{a}_2)^{-1} \boldsymbol{a}_2^{\mathrm{H}} \boldsymbol{Q}_H^{-1},
\end{aligned} \tag{4.7}$$

and the variance of the complex gain $x_1$ is computed by

$$\sigma_{\hat{x}_1}^2 = \left(\bar{\boldsymbol{a}}_1^{\mathrm{H}} \boldsymbol{Q}_H^{-1} \bar{\boldsymbol{a}}_1\right)^{-1}. \tag{4.8}$$

If the channel only contains a single path, the variance is given by

$$\sigma_{\check{x}_1}^2 = \left(\boldsymbol{a}_1^{\mathrm{H}} \boldsymbol{Q}_H^{-1} \boldsymbol{a}_1\right)^{-1}, \tag{4.9}$$

where the 'check'-symbol on $x$ explicitly refers to a single path channel, or the estimation model that only contains a single path.

Now we analyse how the accuracy changes when a reflection is taken into consideration in the model for complex gain estimation. The variance of gain estimation in a 2-path channel (4.8) is rewritten as

$$\begin{aligned}
\sigma_{\hat{x}_1}^2 &= (\bar{\boldsymbol{a}}_1^{\mathrm{H}} \boldsymbol{Q}_H^{-1} \bar{\boldsymbol{a}}_1)^{-1} \\
&= \underbrace{(\boldsymbol{a}_1^{\mathrm{H}} \boldsymbol{Q}_H^{-1} \boldsymbol{a}_1)^{-1}}_{\sigma_{\check{x}_1}^2} \underbrace{(\boldsymbol{a}_1^{\mathrm{H}} \boldsymbol{Q}_H^{-1} \boldsymbol{a}_1)(\bar{\boldsymbol{a}}_1^{\mathrm{H}} \boldsymbol{Q}_H^{-1} \bar{\boldsymbol{a}}_1)^{-1}}_{\sin^{-2}(\vartheta)},
\end{aligned} \tag{4.10}$$

where $\sin^{-2}(\vartheta)$ is a scalar in a 2-path channel. The angle $\vartheta$ measures the degree of dependence [132] between the LoS component $\boldsymbol{a}_1$ and a reflection $\boldsymbol{a}_2$ in $\boldsymbol{A}(\boldsymbol{\tau})$, which is written as follows

$$\begin{aligned}
\sin^2(\vartheta) &= \frac{1}{\sin^{-2}(\vartheta)} = \frac{\bar{\boldsymbol{a}}_1^{\mathrm{H}} \boldsymbol{Q}_H^{-1} \bar{\boldsymbol{a}}_1}{\boldsymbol{a}_1^{\mathrm{H}} \boldsymbol{Q}_H^{-1} \boldsymbol{a}_1} = \frac{\boldsymbol{a}_1^{\mathrm{H}} \boldsymbol{a}_1 - \boldsymbol{a}_1^{\mathrm{H}} P_{\boldsymbol{a}_2} \boldsymbol{a}_1}{\boldsymbol{a}_1^{\mathrm{H}} \boldsymbol{a}_1} \\
&= 1 - \frac{\sum_m \sum_i \exp(-j2\pi(f_i + f_m)\tau_{2,1}) \sum_m \sum_i \exp(+j2\pi(f_i + f_m)\tau_{2,1})}{N_s M_a} \cdot \frac{}{N_s M_a},
\end{aligned} \tag{4.11}$$

where the variance matrix of the sampled channel frequency response $\boldsymbol{Q}_H$ is defined in (2.27).

Combined with (3.31), the variance $\sigma_{\hat{x}_1}^2$ in (4.10) is inversely deteriorated by

$$\sin^2(\vartheta) = 1 - s(\tau_{2,1}) s^*(\tau_{2,1}). \tag{4.12}$$

When $|s(\tau_{2,1})|$ approaches zero, the LoS component $\boldsymbol{a}_1$ and the reflection $\boldsymbol{a}_2$ become linearly independent in $\boldsymbol{A}(\boldsymbol{\tau})$, and the variance $\sigma_{\hat{x}_1}^2$ will be the same as $\sigma_{\check{x}_1}^2$. Hence,

$|s(\tau_{2,1})|$ is defined as the *measure of dependence for gain estimation* in this thesis, and a reflection with a non-zero measure of dependence for gain estimation is defined as a dependent reflection in gain estimation. Equivalently, if the angle $\vartheta$ as shown in Fig. 4.1 equals $\pm\pi/2$, $\boldsymbol{a}_1$ and $\boldsymbol{a}_2$ are orthogonal, and if $\vartheta$ is zero, $\boldsymbol{a}_1$ and $\boldsymbol{a}_2$ are fully dependent.
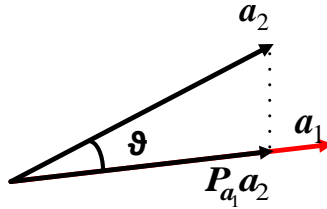


Figure 4.1: The angle $\vartheta$ measures the degree of dependence between $\boldsymbol{a}_1$ and $\boldsymbol{a}_2$, here visualized in the $N_s M_a$ dimensional space of the measured frequency response $\boldsymbol{H}$.

Considering both the LoS path and a reflection in $\boldsymbol{A}(\boldsymbol{\tau})$, the variance of the complex gain of the LoS component (4.10) can be rewritten by

$$\sigma_{\hat{x}_1}^2 = \frac{\sigma^2}{N_s M_a} \frac{1}{1 - s(\tau_{2,1})s^*(\tau_{2,1})} = \frac{\sigma^2}{N_s M_a} \frac{1}{\sin^2(\vartheta)}. \tag{4.13}$$

As we can see, the accuracy of the estimator for the LoS path gets poor if a dependent path is added to the model, because $\sin^2(\vartheta)$ becomes smaller than 1 in (4.13).

### Carrier Phase Estimator
Based on the complex gain of the LoS path, one can determine the carrier phase by

$$\hat{\underline{\Phi}} = \arg\left\{\hat{\underline{x}}_1\right\}. \tag{4.14}$$

As the full model is used to compute the complex gain, the LoS gain estimator $\hat{\underline{x}}_1$ is unbiased, and has the following distribution,

$$\hat{\underline{x}}_1 \sim \mathscr{CN}\left(x_1,\ \sigma_{\hat{x}_1}^2\right), \tag{4.15}$$

where the variance $\sigma_{\hat{x}_1}^2$ has been defined in (4.13).

In order to derive the variance of the resulting carrier phase estimator, we rewrite (4.14) as

$$\begin{aligned}
\hat{\underline{\Phi}} &= \arg\{x_1 + \underline{\nu}\} \\
&= \underbrace{\arctan\left\{\frac{\Im\{x_1\}}{\Re\{x_1\}}\right\}}_{\Phi} + \arctan\left\{\frac{|P_{x_1}^{\perp}\underline{\nu}|}{|x_1| + |P_{x_1}\underline{\nu}|}\right\}
\end{aligned} \tag{4.16}$$

where $\underline{v}$ denotes the random measurement error caused by noise in the complex gain estimator. The illustration of (4.16) is shown in Fig. 4.2.
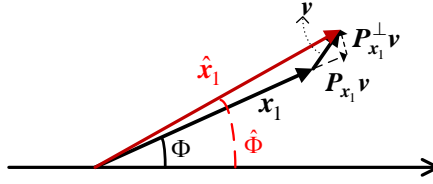


Figure 4.2: Composition of complex gain estimate $\hat{x}_1$, to determine $\Phi$, and measurement error $v$.

The mean of the carrier phase is given by

$$\Phi = \arctan\left\{\frac{\Im\{x_1\}}{\Re\{x_1\}}\right\} = \left(\tilde{\phi} \quad \mathrm{mod}\ (-\pi,\ \pi]\right), \tag{4.17}$$

where $\tilde{\phi}$ denotes the accumulated phase offset introduced by receiver frequency offset and Doppler, defined in (2.14).

Now, we can analyze the second term with the argument function in (4.16). Given a reasonable SNR, one can assume

$$|x_1|^2 \gg |v|^2,$$

and has the following approximation

$$|x_1| + |P_{x_1}\underline{v}| \approx |x_1| = \alpha_1.$$

Additionally, if $|P_{\hat{x}_1}^{\perp}\underline{v}|/|x_1| \ll 1$, with

$$\begin{bmatrix} P_{x_1}\underline{v} \\ P_{\hat{x}_1}^{\perp}\underline{v} \end{bmatrix} = \begin{bmatrix} \cos(\Phi) & \sin(\Phi) \\ -\sin(\Phi) & \cos(\Phi) \end{bmatrix} \begin{bmatrix} \Re\{\underline{v}\} \\ \Im\{\underline{v}\} \end{bmatrix}, \tag{4.18}$$

the carrier phase estimator (4.14) can be simplified by

$$\underline{\hat{\Phi}} \approx \Phi + \frac{|P_{\hat{x}_1}^{\perp}\underline{v}|}{\alpha_1} = \Phi - \frac{\sin(\Phi)}{\alpha_1}\Re\{\underline{v}\} + \frac{\cos(\Phi)}{\alpha_1}\Im\{\underline{v}\}. \tag{4.19}$$

Therefore, with (4.13), the variance of the carrier phase estimator can be derived by

$$\begin{aligned} \sigma_{\Phi}^2 &\approx \frac{\cos^2(\Phi)}{\alpha_1^2}\frac{\sigma_{\hat{x}_1}^2}{2} + \frac{\sin^2(\Phi)}{\alpha_1^2}\frac{\sigma_{\hat{x}_1}^2}{2} = \frac{\sigma_{\hat{x}_1}^2}{2\alpha_1^2} \\ &= \frac{\sigma^2}{2\alpha_1^2 N_s M_a \sin^2(\vartheta)}. \end{aligned} \tag{4.20}$$

## **4.2.2.** Simplified Model

Instead of jointly estimating the complex gain for all paths in a multipath channel, which could provide a poor accuracy when dependent columns are involved in the design matrix $A(\tau)$, one can estimate the complex gain for only a few paths, i.e., $A(\tau)$ contains only a few reflected components, with better precision and lower computational load, but at the cost of a bias. Since the design matrix $A(\tau)$ is not fully reconstructed, it is referred to as the *simplified model*. We analyse the bias and the precision of the complex gain and its corresponding phase using the simplified model in this subsection.

The design matrix $A(\tau)$ is constructed using the time delay estimates obtained from section 3.2. These time delays could be biased due to unconsidered reflections in the simplified model as presented in section 3.2.2, and thus the computational complexity could be lower there. Here, we consider a biased delay estimate to construct the design matrix, and also analyse how the time delay bias impacts carrier phase estimation using the simplified model.

In order to derive a closed-form expression for the resulting bias, we again use a simple 2-path channel (3.34) here, resulting in the same stochastic model as shown in (2.28). The simplified model for gain estimation is constructed as

$$\check{a}_1 = a(\tau_1 + \tau_b). \tag{4.21}$$

Then, the complex gain is derived by

$$\check{x}_1 = \left(\check{a}_1^H Q_H^{-1} \check{a}_1\right)^{-1} \check{a}_1 Q_H^{-1} H. \tag{4.22}$$

As a special case, if the propagation time delay is unbiasedly estimated through a full model in (3.27), $\tau_b$ will be zero. Additionally, if $\tau_1$ (i.e., $\Delta\tau_1$ in (2.28)) also equals to zero, which indicates a perfect symbol synchronization, and without considering multipath effects, the complex gain will be derived by

$$\check{x}_1 = \mathbf{1}_{N_s M_a}^T H, \tag{4.23}$$

if all subcarriers in $M_a$ signal bands are used for ranging. Otherwise, the gain will be derived from the summation of all available sampled channel frequency response [95]. It should be noted that, in practice, it is unlikely to have perfect symbol synchronization to extract the received samples for computing the sampled channel frequency response, due to multipath effects and the receiver sampling frequency offset. Hence, $\Delta\tau$, which could be different for different ranging signal packets, should be considered when estimating the complex gain and the associated carrier phase.

With (4.22) and (3.34), the complex gain of the LoS path is given by

$$\check{x}_1 = \frac{\check{a}_1^H a_1 x_1 + \check{a}_1^H a_2 x_2}{\check{a}_1^H \check{a}_1} = s(\tau_b)x_1 + s(\tau_{2,1} + \tau_b)x_2. \tag{4.24}$$

Once the complex gain of the LoS component is determined, the corresponding carrier phase can be obtained from its arc-tangent. However, the carrier phase

estimate could become biased, because of the delay bias $\tau_b$, and also because of the unconsidered dependent reflection $s(\tau_{2,1} + \tau_b)x_2$. The bias in the carrier phase varies with the number of paths and their propagation delays and gains. Then, the carrier phase derived from the simplified model is given by

$$\check{\Phi} = \arg\{\check{x}_1\} = \Phi + \Phi_b. \tag{4.25}$$

### Bias

To analyse how the bias in the time delay and an unconsidered reflection in the estimation model influence the carrier phase estimator, the maximum absolute phase bias derived in a 2-path channel is given by

$$|\Phi_b|_{\max} = \left|\arg\left(s(\tau_b)\right)\right| + \left|\arg\left(\frac{\alpha_2|s(\tau_{2,1} + \tau_b)|}{\alpha_1|s(\tau_b)|}\right)\right|$$

$$= |\Phi_{b1}|_{\max} + |\Phi_{b2}|_{\max}, \tag{4.26}$$

where $|\Phi_{b1}|_{\max}$ denotes the maximum bias introduced by the biased delay estimate, and $|\Phi_{b2}|_{\max}$ denotes the maximum phase bias introduced by one unconsidered reflection. The geometric interpretation is shown in Fig. 4.3 when considering a 2-path channel.
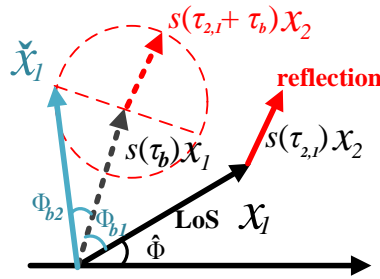


Figure 4.3: Composition of the received phasor with a maximum phase bias because of a reflection (in red) and a delay bias $\tau_b$, in which the solid black arrow denotes the actual LoS complex gain $x_1$, and the dashed black arrow denotes the constructed LoS complex gain from a biased delay estimate. $\check{x}_1$ denotes the complex gain estimate obtained from the simplified model. The phase bias $\Phi_{b1}$ is caused by the delay bias $\tau_b$, and $\Phi_{b2}$ is mainly caused by the unconsidered reflection in the simplified model.

First, to analyse the impact of time delay biased, we can first analyze the phase bias $\Phi_{b1}$. To derive a close form expression, all subcarriers in all signal bands are assumed to be used for ranging. Using

$$\sum_{n=-N/2}^{N/2-1} \exp(jnx) = \sum_{n=0}^{N-1} \exp(jnx) \exp\left(-j\frac{N}{2}X\right)$$

$$= \frac{\sin(Nx/2)}{\sin(x/2)} \exp\left(jx\frac{N-1}{2}\right) \exp\left(-j\frac{N}{2}X\right) = \frac{\sin(Nx/2)}{\sin(x/2)} \exp\left(-jx\frac{1}{2}\right) \tag{4.27}$$

the phase bias $\Phi_{b1}$ is derived by

$$\Phi_{b1} = \arg\{s(\tau_b)\} = \arg\left\{\frac{1}{N_s M_a}\sum_m \sum_i \exp\left(-j2\pi(f_i + f_m)\tau_b\right)\right\}$$

$$= -2\pi\frac{\Delta f}{2}\tau_b \quad \text{mod } (-\pi, \pi]. \tag{4.28}$$

If the subcarrier spacing $\Delta f$ is set to be 156.25 kHz (with 64 subcarriers in 10 MHz), any time variation or bias $\tau_b$ that is far less than the half of the subcarrier spacing (i.e., 12.8 $\mu$s, or 3840 m in distance) will only cause a very small bias in the carrier phase estimate. In a terrestrial system, the receiver generally moves not very fast, and the change of the propagation delay due to the displacement of the receiver is small. For example, assuming the receiver moves with a speed of 30 km/h, a displacement within 1 second interval is about 8.3 m, which is much smaller than 3840m. Then, the change of the time delay within 1 second period can be treated as a bias in $\tau_b$, and the resulting phase bias $\Phi_{b1}$ still remains small. Therefore, instead of updating the time delay estimate in the vector $\check{\boldsymbol{a}}_1$ for every OFDM symbol for computing the complex gain, one can only update the vector $\check{\boldsymbol{a}}_1$ regularly, when the propagation distance has changed significantly.

Now we analyze the second term $\Phi_{b2}$ in (4.26). Except for extremely close-in multipath (e.g., the relative delay is much less than the inverse of the virtual signal bandwidth), reflected components in a multipath channel are weaker than the LoS component. Considering a 2-path channel, the phase bias $\Phi_{b2}$ due to an unconsidered reflection, can be approximated by the first order term of its Taylor expansion,

$$|\Phi_{b2}|_{\max} \approx \frac{\alpha_2 |s(\tau_{2,1} + \tau_b)|}{\alpha_1 |s(\tau_b)|}. \tag{4.29}$$

As $|s(\tau_b)| < 1$ when $\tau_b \neq 0$, the time delay bias will enlarge the phase bias in the simplified model. Therefore, the ranging signal, which can improve the performance of time delay estimation and offer an accurate time delay estimator (i.e., keep $\tau_b$ small), will consequently reduce the bias in estimating the carrier phase.

### Precision
If only a single path is considered in the simplified model, the precision of the gain estimator is given by

$$\sigma_{\check{x}_1}^2 = \left(\check{\boldsymbol{a}}_1^H \boldsymbol{Q}_H^{-1} \check{\boldsymbol{a}}_1\right)^{-1} = (\boldsymbol{a}_1^H \boldsymbol{Q}_H^{-1} \boldsymbol{a}_1)^{-1}. \tag{4.30}$$

Since $\check{\boldsymbol{a}}_1$ in (4.21) is a complex vector which has the same structure as the one defined in (2.28), the precision of $\check{x}_1$ will only be determined by the signal structure itself.

By taking the argument of the complex gain, one can obtain the carrier phase. Similarly, as presented in section 4.2.1, the variance of the carrier phase estimator derived from a simplified model that only considers a single path, is given by

$$\sigma_{\check{\Phi}}^2 \approx \frac{\sigma^2}{2\alpha_1^2 N_s M_a}, \tag{4.31}$$

when $M_a$ signal bands and $N_s$ subcarriers in each band are used for carrier phase estimation.

### **4.2.3.** Flop Count

The number of required flops is computed as an indication of computational complexity for complex gain estimation (cge), from which the carrier phase of the LoS path is obtained. When the propagation time delays for both the LoS path and the reflections have been estimated through the multivariate ML method in section 3.2, the number of required flops for complex gain estimation are given by

$$\text{flops}_{\text{cge}} = \begin{cases} 4L(M_aN_s)^2 + 2L^2(M_aN_s) + L^2 - L + L^3/3, & L > 1; \\ 4(M_aN_s)^2 + 2(M_aN_s), & L = 1, \end{cases} \tag{4.32}$$

where $L$ denotes the number of path considered in the model, $M_a$ denotes the number of signal bands, each containing $N_s$ subcarriers. The derivations can be found in Appendix A.3. The computational complexity is dominated by $4L(M_aN_s)^2$. As $M_aN_s$ is generally much larger than the number of considered path $L$, using the simplified model that considers less paths will largely reduce the computational complexity.

It should be noted that as the design matrix $A(\tau)$ in (3.24) for carrier phase estimation is constructed based on the time delay estimates, the actual computational complexity to compute the carrier phase should include the one for time delay estimation as well (cf. section 3.2.3).

### **4.2.4.** Examples

The performance of carrier phase estimation is presented in this subsection. First, the precision and the bias of the carrier phase estimator are analyzed for both the full and simplified model. Then, based on simulated multipath channels, and using the simplified models, the accuracy of carrier phase estimation is evaluated. Finally, the number of required flops is provided by considering different number of paths and different number of activated signal bands in the model for carrier phase estimation.

#### Precision and Bias

The same signal patterns as shown in Fig. 3.5 are used in the following analysis. The complex gain, and the corresponding carrier phase, for the LoS path is estimated based on a reconstructed design matrix, in which the time delay estimates are initially assumed to be unbiased (i.e., $\tau_b = 0$).

Using the full model (4.6), Fig. 4.4(a) shows the scaling factor $\sin^{-1}(\vartheta)$ in the standard deviation of the LoS gain estimator, which is derived from (4.10). When the measure of dependence $|s(\tau_{2,1})| = 1$, the LoS component $a_1$ and the reflection component $a_2$ will be fully dependent, and $\sin(\vartheta) = 0$ (see (4.12)), then the complex gain estimate will be very poor. Comparing the case of using 7 contiguous bands with the others, a larger virtual signal bandwidth can reduce the measure
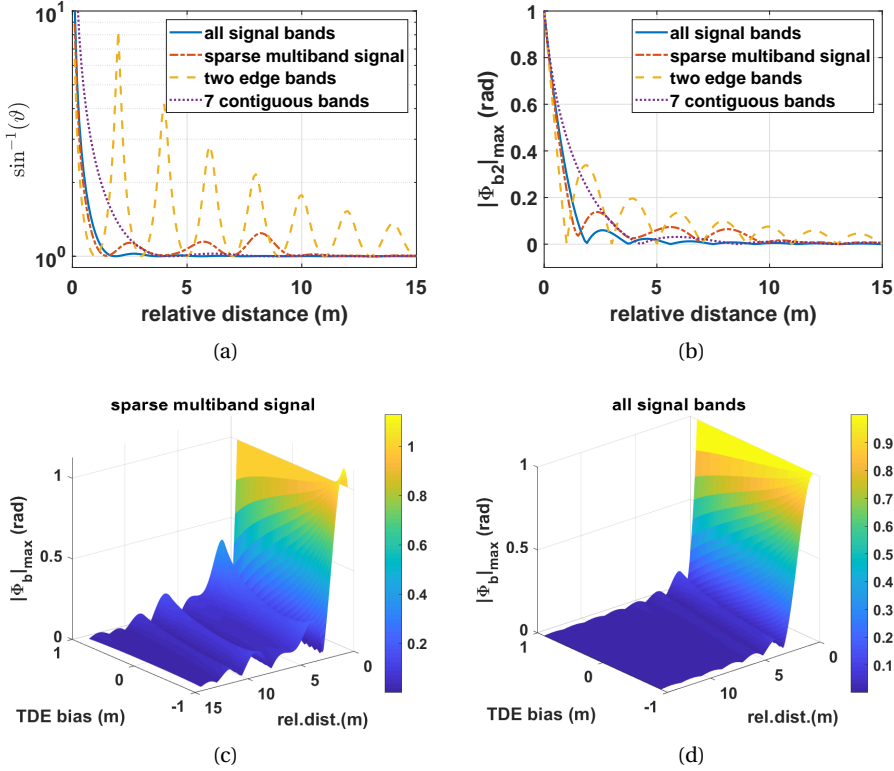
Figure 4.4: (a) The scaling factor $\sin^{-1}(\vartheta)$ of the standard deviation of gain estimation for the LoS component in the full model, given different ranging signal patterns and a 2-path channel, (b) maximum carrier phase bias in the simplified model with an unbiased time estimate, (c, d) maximum phase bias $|\Phi_b|_{\max}$ introduced by the biased time delay estimate (TDE) in the simplified model for different relative distances (rel.dist.).

of dependence for a close-in reflection with a relative distance less than 3 m. However, with less signal bands (e.g., using only two edge signal bands), the accuracy of complex gain estimation becomes sensitive to non-close-in reflections.

Alternatively, the simplified model can be applied to estimate the carrier phase, and consequently it becomes biased. Fig. 4.4(b) shows the maximum carrier phase bias $|\Phi_{b2}|_{\max}$ in (4.26) for the simplified model with an unbiased time delay estimate. Given a fixed virtual signal bandwidth, using more signal bands will improve the robustness against multipath, as less bias will be introduced when using the simplified model without considering non-close-in reflections. With 7 contiguous bands which cover a smaller virtual signal bandwidth than the other ranging signals, the resulting bias will be dominated by the close-in reflections due to a reduced time resolution. In addition, as shown in Fig. 3.6, due to the large measure of dependence and the large measure of bias, the unbiasedness of

the delay estimator becomes difficult to achieve.

The low complexity simplified model can also be applied for time delay estimation (section 3.2.2), and consequently the design matrix for complex gain estimation will be reconstructed using a biased time delay estimate. Although the biased delay estimate of the LoS path will introduce an extra bias $\Phi_{b1}$, as shown in Fig. 4.4(c,d), the phase bias $\Phi_b$ is dominated by $\Phi_{b2}$, which is introduced as the reflections are not considered in the model for carrier phase estimation. Although the integer phase cycle ambiguity should be correctly estimated in order to retrieve the geometric information, the ultimate bias is small in distance and likely acceptable to the user, even if only a few bands are used within the virtual signal bandwidth (comparing (c) against (d)). In such a condition, positioning based on the carrier phase will still largely outperform the one based on the propagation time delay, which will be demonstrated in Chapter 7.

### Simulation

In order to further evaluate performance of carrier phase estimation in mulitpath conditions, multipath channels are generated using the Saleh-Valenzuela (SV) model as that rays arrive in clusters [133, 134]. Here, we only consider the multipath channels which contain the direct LoS path, and the LoS path is always fixed as the first path in the channel impulse response, at $\tau_1 = 0$ ns. As indicated in [133], the arrival time of the clusters and the paths satisfy Poisson distributions. Specifically, the cluster rate $\Lambda$ is set to be 0.023, and the ray arrival rate $\lambda$ is set to be 0.25, the cluster-decay time constant $\Gamma$ is 7.4, and the ray power-decay time constant $\gamma$ is 0.5. Based on these parameters, 1000 channel impulse responses are generated, of which Fig. 4.5 shows an example.
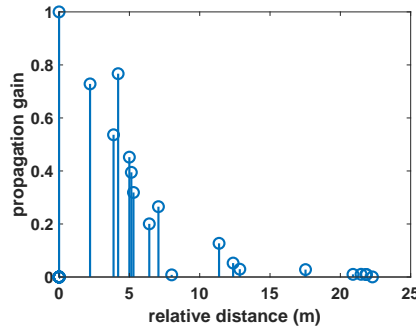


Figure 4.5: Example of generated channel impulse response according to the SV-model, and the LoS path component is set to have a magnitude of 1, and propagation distance of 0 m.

Based on 1000 generated channel impulse responses and 30 dB of SNR, one can obtain the sampled channel frequency response $H$, which can be assumed to be retrieved from 1000 ranging OFDM symbols (or ranging signal packets), although the channel may not change rapidly in practice. Hence, the carrier phase error shown in the following figures will be mainly caused by multipath.

Using all $M = 16$ signal bands and $N_s = 64$ in each signal band to estimate carrier phase, Fig. 4.6 shows the empirical cumulative distribution function (CDF) of the carrier phase error. On the one hand, one can consider only a single path when estimating the complex gain and the associated carrier phase. The time delay estimate in the reconstructed vector $\boldsymbol{a}(\tau)$ (cf. (4.21)) can be determined by the matched filter (MF) method for every OFDM symbol. As presented in section 4.2.2, one may not need to update the time delay in $\boldsymbol{a}(\tau)$ for every symbol. Hence, as an example, the time delay in $\boldsymbol{a}(\tau)$ is fixed to 0 ns (i.e, very accurate time delay estimate), or 1 ns (a biased time delay estimate) for all 1000 symbols. In addition, the MUSIC method is applied to determine the time delay, and one can use the resulting LoS time delay to reconstruct $\boldsymbol{a}(\tau)$, and determine the carrier phase. On the other hand, one can also consider both the LoS path and the reflections when estimating the carrier phase (cf. (4.6)). The time delays of the LoS path and the reflections in $\boldsymbol{A}(\boldsymbol{\tau})$ are determined by the MUSIC method.
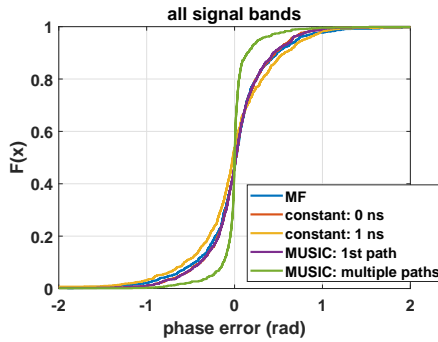


Figure 4.6: Empirical cumulative distribution function of carrier phase error, using all $M = 16$ signal bands and $N_s = 64$ subcarriers in each signal band. When only considering a single path for carrier phase estimation, the time delay in vector $\boldsymbol{a}(\tau)$ (cf. (4.21)) is determined by using the matched filter (MF) method, and is updated for every OFDM symbol. Also, the time delay in $\boldsymbol{a}(\tau)$ can be fixed to a constant value (i.e., 0 ns or 1 ns) for all 1000 OFDM symbols. Alternatively, the time delay in $\boldsymbol{a}(\tau)$ can be determined by the MUSIC method (cf. (3.54)). Finally, both LoS path and reflections can be considered for carrier phase estimation (cf. (4.6)), the time delay of these paths are determined by the MUSIC method.

According to the results shown in Fig. 4.6, considering not only the LoS path but also the reflections in carrier phase estimation, there will be less error in the carrier phase estimates than considering only a single path. When using a wideband signal (i.e., all signal bands), and considering only a single path in carrier phase estimation, the CDF of resulting carrier phase error when time delay in $\boldsymbol{a}(\tau)$ is derived from the MF method, is similar to the one derived from the MUSIC method. In addition, using a fixed $\boldsymbol{a}(\tau)$ with a biased time delay estimate of 1 ns in (4.22), and will not significantly increase the phase error $\Phi_{b2}$ (cf. (4.29)).

Now, only considering one path in carrier phase estimation, Fig. 4.7 shows the empirical CDF of the carrier phase error, when using different signal spectrum patterns that have been presented in Fig. 3.5: all $M = 16$ signal bands, sparse multiband signal ($M_a = 7$), and two edge signal bands ($M_a = 2$). Particularly,
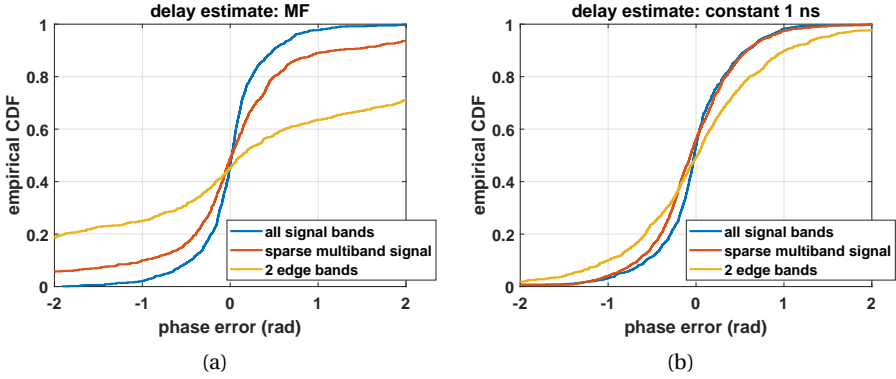
Figure 4.7: Empirical CDF of carrier phase error, when using all signal bands, sparse multiband signal and two edge signal bands as shown in Fig. 3.5, and only considering a single path in carrier phase estimation, time delay in $\boldsymbol{a}(\tau)$ (a) is derived from MF method for every OFDM symbol, (b) is fixed to 1 ns (i.e., biased time delay) for all symbols.

in Fig. 4.7(a), the time delay in the reconstructed vector $\boldsymbol{a}(\tau)$ is determined independently for each symbol using the MF method, and Fig. 4.7(b), the time delay is fixed to 1 ns (i.e., a biased time delay) for all symbols. As shown in Fig. 4.7(a), within the same virtual signal bandwidth, occupying more signal bands for carrier phase estimation can improve the resistance against multipath, which reduces the multipath error in the time delay estimates and consequently leads to a small carrier phase error.

Instead of updating the time delay in $\boldsymbol{a}(\tau)$ for each symbol, one can use a fixed time delay estimate to compute the carrier phase. As presented in section 4.2.2, any change of the time delay will be lumped into $\tau_b$, and will propagate into the phase bias (4.26). A time delay bias $\tau_b$ will not significantly increase $\Phi_{b1}$, while it may enlarge $\Phi_{b2}$ due to $|s(\tau_b)| < 1$ (see Fig. 4.8) in (4.29). Using a constant time delay estimate with a bias of 1 ns, the empirical CDF of the carrier phase error is shown in Fig. 4.7(b). Using only a few sparsely placed signal bands can offer a similar performance of carrier phase estimation as using all signal bands.

According to Fig. 3.7 and Fig. 4.4, the impact of the signal pattern on time delay estimation and carrier phase estimation is similar. A large virtual signal bandwidth helps to distinguish the LoS from relatively close-in multipath, and more signal bands improve the overall robustness against multipath (i.e., less bias in the simplified model, higher precision in the full model). Moreover, not all signal bands are needed to achieve a certain ranging performance.

### Flops

Fig. 4.9 shows the number of required flops for complex gain estimation, in which the number of paths $L$ considered in the estimation model is set to be 1, 2, and 5, and the number of signal bands that are used for ranging is varied from 6 to 16. Compared with the number of the required flops for time delay estimation shown
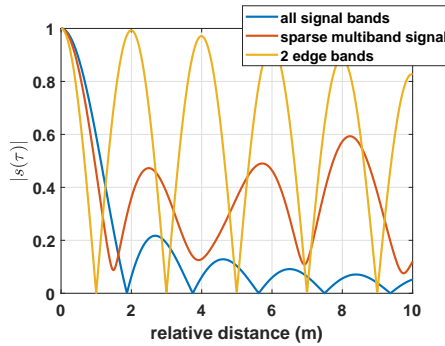
Figure 4.8: $|s(\tau)|$ (cf.(3.31)), based on signal spectrum pattern shown in Fig. 3.5: all signal bands ($M = 16$), sparse multiband signal ($M_a = 7$), and 2 edge bands ($M_a = 2$).

in Fig. 3.9, a similar behaviour can also be observed for complex gain estimation, considering less paths in the estimation model can largely reduce the computational complexity. Using one less signal band, the number of required flops can reduce by about 27%.
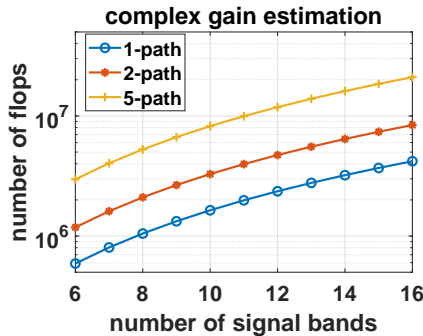


Figure 4.9: Required number of flops for complex gain estimation, when considering 1 path, 2 and 5 paths are considered in the estimation model.

## **4.3.** Phase Tracking and Frequency Offset

As carrier phase estimates are ambiguous as shown in (4.17), the geometric range information cannot be directly obtained from a single estimate. In this section, carrier phase tracking is presented, so that only the initial carrier phase cycle ambiguity is preserved in a series of carrier phase measurements [108]. Additionally, when using the burst-like ranging signal, the carrier phase is not continuously measured, and the receiver frequency offset can cause cycle-slips in a series of carrier phase measurements. Hence, the receiver frequency offset should be dealt with in carrier phase tracking [135].

Due to the arc-tangent operator, the fractional carrier phase obtained from

(4.17) is always from $-\pi$ to $\pi$, which thus introduces an ambiguity. The carrier phase obtained from the $q$-th symbol can be rewritten by

$$\Phi[q] = \mathrm{frac}\left\{\tilde{\phi}[q]\right\} = \tilde{\phi}[q] - \underbrace{2\pi N[q]}_{\mathrm{int}\{\tilde{\phi}\}}, \quad \Phi[q] \in (-\pi,\ \pi],$$

$\Phi$ denotes the *fractional* part of the carrier phase $\tilde{\phi}$ in (2.14), and $N$ denotes the unknown *integer* carrier phase cycle ambiguity. Each carrier phase estimate carries its own carrier phase cycle ambiguity.

Fig. 4.10 illustrates the relation among integer phase ambiguity $N[q]$, and the ambiguous carrier phase measurements $\Phi[q]$, where the receiver is assumed to be synchronized to the transmitter, and continuously moves with a constant speed.
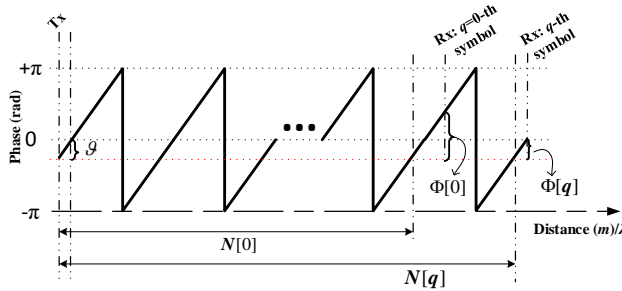


Figure 4.10: Phase ambiguities and wrapped phase estimates, in which the horizontal direction indicates the propagation distance in terms of wavelength of the central carrier frequency $\lambda$, $\vartheta$ is the initial phase offset (cf. (2.4)). $\Phi[0]$ indicates the carrier phase estimate at the first epoch (i.e., from the 0-th symbol), which is ambiguous and contains only the fractional part of the physical carrier phase. $\Phi[q]$ denotes the ambiguous carrier phase estimate from the $q$-th symbol. $N[q]$ indicates integer carrier phase cycle ambiguity of the $q$-th symbol.

## **4.3.1.** Carrier Phase Tracking

In a non-static positioning scenario, the unknown phase ambiguity $N[q]$ is time variant (i.e., depends on the symbol index $q$), due to the Doppler frequency offset (and also the receiver frequency offset between the transmitter and receiver, to be addressed separately in section 4.3.2 ). Consequently, it will lead to a rank defect in the positioning model because of too many unknown parameters, which will be introduced in Chapter 6. Alternatively, we only preserve one *initial* time-invariant integer carrier phase ambiguity in the observation model, and absorb the change of the carrier phase cycle into the observations, namely by unwrapping a sequence of carrier phase estimates.

Hence, a series of *carrier phase estimates* should be tracked continuously, so that only the initial carrier phase ambiguity remains in the resulting *unwrapped carrier phase measurements*. By absorbing the change of the carrier phase cycle

in the carrier phase estimate, the unwrapped carrier phase $\tilde{\Phi}$ is written by

$$\tilde{\Phi}[q] = \tilde{\phi}[q] - 2\pi N, \quad \tilde{\Phi}[q] \in (-\infty, +\infty] \tag{4.33}$$

where $N$ becomes time-independent, and denotes the initial carrier phase cycle ambiguity.

The tracking procedure can be achieved by a phase-locked-loop (PLL) [122, 9, 136], shown in Fig. 4.11. As the carrier phase is derived from the complex gain, the carrier phase tracking is also based on the complex gain. By combining the locally generated phasor, in which the phase is provided by the numerically controlled oscillator (NCO), with the LoS complex gain, one can determine the phase error $\delta\Phi$ through the discriminator (or arc-tangent). The phase error $\delta\Phi$ is obtained by

$$\delta\Phi[q] = \tilde{\phi}[q] - \hat{\tilde{\Phi}}[q-1]. \tag{4.34}$$
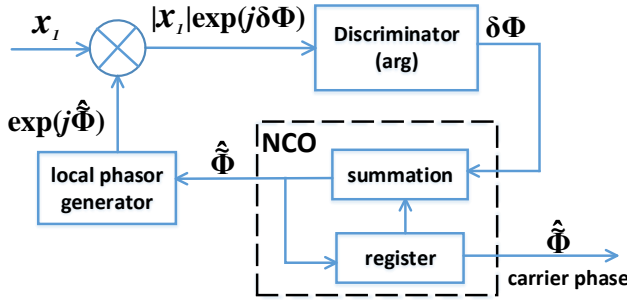


Figure 4.11: Carrier phase tracking based on phase-locked loop.

Also presented in Fig. 4.11, the NCO produces the phase for the local phasor generator. In practice, the NCO increases or decreases the output phase by successively adding a series of phase errors $\delta\Phi$ over time from the discriminator. By tracking the change of the carrier phase, one can obtain the unwrapped carrier phase by

$$\hat{\tilde{\Phi}}[q] = \hat{\tilde{\Phi}}[q-1] + \delta\Phi[q], \tag{4.35}$$

and any change of the carrier phase cycle ambiguity $N[q]$ in $\Phi[q]$ will be absorbed in $\hat{\tilde{\Phi}}[q]$.

As an example, Fig. 4.12 shows the unwrapped carrier phase obtained from the PLL, in which the complex gain is obtained from the simplified model where only one path is considered. Similar to Fig. 4.7(b), 200 sampled channel frequency responses are generated from the 200 CIRs, and the time delay in $\boldsymbol{a}(\tau)$ is fixed to 1 ns (i.e., a biased time delay estimate). The receiver is assumed to be continuously moving at a constant speed. Hence, the propagation distance of the LoS path increases linearly across 1000 symbols.
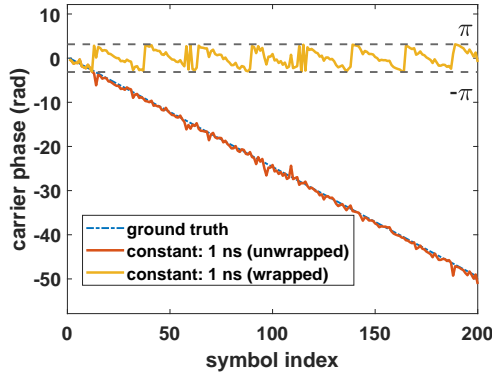
Figure 4.12: Example of unwrapped carrier phase measurements obtained from PLL.

In practice, as shown in Fig. 4.13, a loop filter can also be applied to the discriminator output, so that a certain error introduced by multipath and the clock jitters can be effectively filtered out [9]. However, a loop filter is not applied in our work, and thus the variance of the unwrapped carrier phase measurement can be obtained by (4.20) or (4.31).
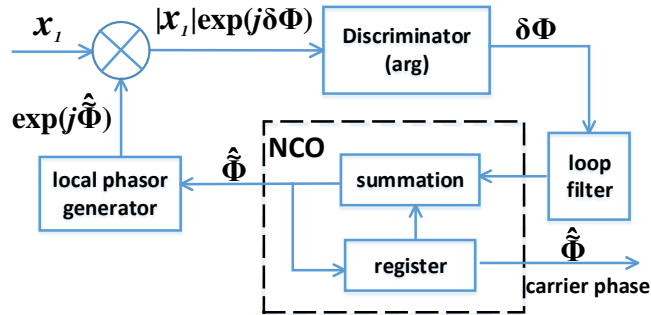


Figure 4.13: carrier phase tracking based on phase-locked loop with loop filter.

When the phase estimation error is relatively small, and the rate of change of the phase is also small, one can simply compute differences between consecutive phase estimates $\hat{\Phi}$ and compare these with a phase jump threshold, and determine whether a jump has occurred or not.

The relation among the initial integer phase ambiguity $N$ and unwrapped carrier phase estimates $\tilde{\Phi}$ is illustrated in Fig.4.14, where the receiver is assumed to be synchronized to the transmitters, and moving with a constant speed.
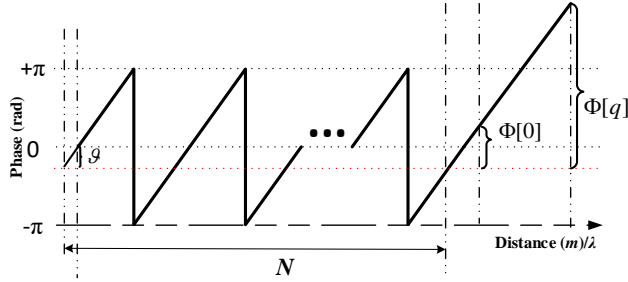
Figure 4.14: Phase ambiguities and unwrapped phase $\tilde{\Phi}$, in which only the initial phase ambiguity $N$ is preserved (cf. Fig. 4.10).

### 4.3.2. Carrier Frequency Offset and Cycle Slips

Generally, the receiver is not synchronized to the transmitters, and runs on its own clock. Thereby the phase will change as time elapses, even in a static set-up (with constant propagation time delays). Due to the receiver frequency offset $\Delta \tilde{f}_c$ (cf. (2.14)), the phase rotation can become larger than one cycle during the transmission period $T_D$. However, the phase obtained from the discriminator is ambiguous, and the integer part of the rotation will not be reflected. If the phase rotation is larger than one cycle during the transmission period, one has

$$\delta \hat{\Phi} = (\delta \Phi \quad \mathrm{mod}\ (-\pi, \pi]) \neq \delta \Phi. \tag{4.36}$$

in which $\delta \hat{\Phi}$ obtained from discriminator will not represent the actual phase change $\delta \Phi$, and consequently leads to *cycle slips* in the unwrapped carrier phase measurements $\hat{\tilde{\Phi}}$, without using any loop filters. To avoid such an issue, one can estimate the receiver frequency offset $\Delta f_c$ a priori, and compensate it when unwrapping the carrier phase (i.e., to obtain phase-of-arrival (PoA)). So that the phase rotation is determined by the Doppler frequency offset $\Delta f_D$ and the residual receiver frequency offset. Alternatively, if all transmitters are frequency synchronized (as in our SuperGPS system), and one is less interested in analysing the receiver clock error, the difference of the carrier phase between two Tx-Rx pairs (i.e., phase-difference-of-arrival (PDoA)) can be computed for positioning, which effectively eliminates the receiver frequency offset $\Delta f_c$.

#### Compensate CFO in PoA Measurement

As shown in Fig. 2.2, the shortened Moose's symbol can be used for receiver frequency offset estimation. The CFO and SFO are assumed to be invariant at least within one OFDM symbol, with a duration typically in the order of microseconds. Hence, the sample interval $T_s' \approx (1-\eta)T_s$ is presented without argument $t$ in the following derivations. After the ADC, the discrete received baseband OFDM symbol

from the $k$-th packet with $N_s M$ samples is given by

$$r_b[\Delta t_k; n] = \underbrace{s_b(nT'_s - \Delta \tau(\Delta t_k))}_{r_b^{(1)}[n; \Delta t_k]} \underbrace{\alpha \exp\left(-j\left(2\pi\Delta f_c nT'_s + \tilde{\phi}(\Delta t_k)\right)\right)}_{r_b^{(2)}[n; \Delta t_k]} \tag{4.37}$$

$$n = N_g, \ldots, N_g + N_s M - 1,$$

where $\Delta t_k$ is the elapsed time between the 1-st received packet and the $k$-th packet, and

$$r_b^{(1)}[\Delta t_k; n] = \sum_m \sum_i c_{i,m} \exp(-j2\pi(f_i + f_m)\Delta \tau(\Delta t_k)) \exp\left(-j2\pi(f_i + f_m)(n - N_g)T'_s\right),$$
$$\tag{4.38}$$

and $N_s$ is assumed to be an even number, $f_i = i\Delta f$ denotes the frequency of the $i$-th subcarrier in each band, $n$ denotes the sample index in the current symbol, $c_{i,m}$ denotes the pilot data modulated on the $i$-th subcarrier in the $m$-th band, $N_g$ denotes the number of samples in the cyclic prefix and $\Delta \tau(\Delta t_k)$ denotes the residual time offset after symbol synchronization (cf.(2.14)).

In (4.37), the discrete received signal has been split into two parts (i.e., $r_b^{(1)}[\Delta t_k; n]$ and $r_b^{(2)}[\Delta t_k; n]$). We first analyse the term $r_b^{(1)}[\Delta t_k; n]$ in (4.37), and show that the first half of the shortened Moose's symbol will be approximately the same as the second half, and the impact of CFO will be reflected in the term $r_b^{(2)}[\Delta t_k; n]$. Finally, based on the correlation between the first half of the symbol and the second half, the CFO is estimated [137].

Using the second half of the shortened Moose's symbol with $n = N_g, \ldots, N_g + N_s M/2 - 1$, we have

$$r_b^{(1)}[\Delta t_k; n + N_s M/2] = \sum_m \sum_{i=\text{even}} c_{i,m} \exp(-j2\pi(f_i + f_m)\Delta \tau(\Delta t_k))$$

$$\exp\left(-j2\pi(f_i + f_m)(n - N_g)T'_s\right) \exp\left(-j2\pi(f_i + f_m)(N_s M/2)(1 - \eta)T_s\right)$$

$$= \sum_m \sum_{i=\text{even}} c_{i,m} \exp(-j2\pi(f_i + f_m)\Delta \tau(\Delta t_k)) \exp\left(-j2\pi(f_i + f_m)(n - N_g)T'_s\right)$$

$$\exp\left(-j(i + mN_s)\pi(1 - \eta)\right) \tag{4.39}$$

$$\approx \sum_m \sum_{i=\text{even}} c_{i,m} \exp(-j2\pi(f_i + f_m)\Delta \tau(\Delta t_k)) \exp\left(-j2\pi(f_i + f_m)(n - N_g)T'_s\right)$$

$$= r_b^{(1)}[\Delta t_k; n].$$

As only every other subcarrier is used in the shortened Moose's symbol, $i$ is an even number in (4.39). Also because the normalized frequency offset $\eta$ is typically small and $i + mN_s$ is an even number, the term $r_b^{(1)}[\Delta t_k; n]$ is approximately equal to $r_b^{(1)}[\Delta t_k; n + N_s M/2]$. To remove the common phase offset in $r_b^{(2)}[\Delta t_k; n]$ and

$r_b^{(2)}[\Delta t_k; n + N_s M/2]$, one has

$$
\begin{aligned}
r_b^*[\Delta t_k; n] r_{bb}[\Delta t_k; n + N_s/2] &= |r_b[\Delta t_k; n]|^2 \exp\left(-j2\pi\Delta f_c \frac{N_s M}{2}(1 - \eta)T_s\right) \\
&\approx |r_b[\Delta t_k; n]|^2 \exp\left(-j2\pi\Delta f_c \frac{N_s M}{2}T_s\right) \\
&= |r_b[\Delta t_k; n]|^2 \exp\left(-j\pi\Delta f_c N_s M T_s\right).
\end{aligned}
\tag{4.40}
$$

Therefore, using the shortened Moose's symbol, the CFO can be estimated by

$$
\Delta\check{f}_c(\Delta t_k) = -\frac{\check{\psi}}{\pi N_s M T_s}, \quad \check{\psi} = \arg\left\{\sum_{n=N_g}^{N_s M/2 + N_g - 1} r_b^*[\Delta t_k; n] r_b[\Delta t_k; n + N_s M/2]\right\}, \tag{4.41}
$$

where the check-symbol (i.e., ˇ) is used to denote the coarse estimate.

The CFO will cause a change in carrier phase as time elapses, even when the receiver is static. As a burst signal is used for ranging and positioning, if the carrier phase rotates more than one cycle within the transmission period of the burst ranging signal, a cycle-slip will be introduced in the carrier phase measurement. To reduce the extra phase rotation due to CFO, one can estimate and compensate the CFO based on the shortened Moose's symbol with (4.41),

$$
\begin{aligned}
\check{r}_b[n; \Delta t_k] &= r_b[\Delta t_k; n] \exp(j\check{\phi}_\eta(\Delta t_k)) \\
&= \alpha s_b[nT_s' - \Delta\tau(\Delta t_k)] \exp\left(-j\left(2\pi\Delta\tilde{f}_c n(1 - \eta)T_s + \tilde{\phi}(\Delta t_k) - \check{\phi}_\eta(\Delta t_k)\right)\right)
\end{aligned}
\tag{4.42}
$$

where

$$
\tilde{\phi}_\eta(\Delta t_k) = \phi_\eta(\Delta t_k) - \check{\phi}_\eta(\Delta t_k) = 2\pi\int_{\nu=0}^{\nu=\Delta t_k}\left(\Delta f_c(\nu) - \Delta\check{f}_c(\nu)\right)d\nu, \tag{4.43}
$$

and $\phi_\eta$ denotes the accumulated receiver phase offset due to the CFO (cf. (2.12)). The extra rotation of the carrier phase $\tilde{\phi}_\eta(\Delta t_k)$ caused by the residual CFO, is referred to as the *clock offset* in this thesis, and will be estimated along with the position coordinates in a positioning model introduced in Chapter 6.

As shown in (4.41), the CFO is estimated in the range of $\pm\Delta f$ (over a period of $MN_s T_s/2$). Later, the clock offset $\tilde{\Phi}_\eta(\Delta t_k)$, computed along with the position solution in a positioning model, can also be used for CFO estimation within a range of $\pm1/2T_D$ (i.e., over a period of $T_D$). As the transmission period $T_D$ is much longer than the OFDM symbol time, the CFO estimated based on the clock offset can provide a much finer frequency range than the one based on the shortened Moose's symbol. Therefore, in this thesis, CFO estimation based on the shortened Moose's symbol is referred to as *coarse* CFO estimation ( the estimate is denoted by $\Delta\check{f}_c$), and the one based on the positioning model is referred to as *fine* CFO estimation (the estimate will be denoted by $\Delta\hat{\tilde{f}}_c$).
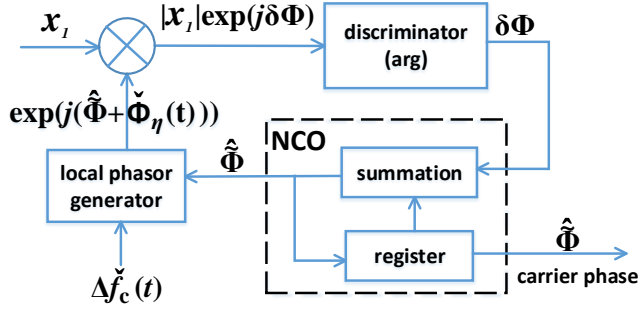
Figure 4.15: Carrier frequency offset aided phase tracking loop.

**4**

Finally, by considering the receiver frequency offset, the carrier phase tracking can be achieved through the carrier-frequency-offset-aided phase tracking loop shown in Fig. 4.15. Generally, the CFO can be assumed to be relatively stable for a certain period (e.g., for a few seconds), and the CFO estimate for the compensation does not need to be updated for every ranging signal packet (i.e., with an update rate of $T_D$). As long as the carrier phase can be properly tracked without cycle slips, the error caused by the residual frequency offset will be estimated through the positioning model. If the carrier frequency offset is continuously updated and compensated in Fig. 4.15, the phase rotation due to the Doppler frequency offset will be removed, which however is of interest for positioning. Then, the carrier phase should be derived by integrating the carrier frequency offset over time [138].

### PDoA Measurement

If all radio transmitters are frequency synchronized, the accumulated phase rotation $\phi_\eta(t)$ (cf. (2.12)) becomes identical among all Tx-Rx pairs. Without considering multipath effects, and based on (2.13), the complex gain obtained from the $\text{Tx}_i$ (the $i$-th transmitter)-Rx and the $\text{Tx}_p$ (the pivot transmitter)-Rx pair, can be written by

$$
\begin{aligned}
\hat{x}_1^i(\Delta t_k) &= \alpha \exp\left(-j\left(2\pi f_c \tau^i(t_0) + \phi_D^i(\Delta t_k) + \phi_\eta(\Delta t_k) + \vartheta^i - \vartheta_r\right)\right) \\
\hat{x}_1^p(\Delta t_k) &= \alpha \exp\left(-j\left(2\pi f_c \tau^p(t_0) + \phi_D^p(\Delta t_k) + \phi_\eta(\Delta t_k) + \vartheta^p - \vartheta_r\right)\right),
\end{aligned}
\tag{4.44}
$$

where $\vartheta^i$, $\vartheta^p$ and $\vartheta_r$ denote the initial carrier phase offset at the $i$-th transmitter, pivot transmitter and the receiver, respectively.

To avoid the extra phase rotation due to the receiver frequency offset during the transmission period $T_D$, one can compute the phase difference between two Tx-Rx pairs (i.e., the $i$-th transmitter and the $p$-th transmitter), which is given by

$$
\Phi_r^{i,p} = \arg\left\{x_1^i \left(x_1^p\right)^*\right\}.
\tag{4.45}
$$

Then, by tracking the carrier phase $\Phi_r^{i,p}$ through the PLL shown in Fig. 4.11, one can have the so-called phase-difference-of-arrival (PDoA) measurements for positioning, and no cycle-slip will be introduced by the receiver frequency offset.

In order to derive the mean and the variance of the PDoA estimator, one has

$$
\begin{aligned}
\underline{x}_1^i \left(\underline{x}_1^p\right)^* &= \left(x_1^i + \underline{v}_i\right)\left(x_1^p + \underline{v}_p\right)^* \\
&= x_1^i \left(x_1^p\right)^* + x_1^i \underline{v}_p^* + \left(x_1^p\right)^* \underline{v}_i + \underline{v}_i \underline{v}_p^*,
\end{aligned}
\tag{4.46}
$$

where $\underline{v}_i$ and $\underline{v}_p$ are assumed to independent, and are zero-mean Gaussian distributed (cf. (4.15)),

$$
\underline{v}_i,\ \underline{v}_p \sim \mathscr{CN}\left(0,\ \sigma_{\hat{x}_1}^2\right).
\tag{4.47}
$$

Then,

$$
\underline{v}\,\underline{v}^*/\sigma_{\hat{x}_1}^2 \sim \chi^2\left(1,0\right),
\tag{4.48}
$$

and the mean and variance of $\underline{v}\underline{v}^*$ are given as

$$
\mathbb{E}\left\{\underline{v}\underline{v}^*\right\} = \sigma_{\hat{x}_1}^2;\quad \mathbb{D}\left\{\underline{v}\underline{v}^*\right\} = 2\sigma_{\hat{x}_1}^4.
\tag{4.49}
$$

In an LoS condition and a reasonable SNR, one can safely assume that $\sigma_{\hat{x}_1} \gg |x_1|$ in (4.13).

The mean of the combination of the complex gain from two Tx-Rx pairs can be obtained by

$$
\begin{aligned}
\mathbb{E}\left\{\underline{x}_1^i \left(\underline{x}_1^p\right)^*\right\} &= x_1^i \left(x_1^p\right)^* + \mathbb{E}\left\{\underline{v}_i \underline{v}_p^*\right\} \\
&= x_1^i \left(x_1^p\right)^* + \sigma_{\hat{x}_1}^2 \\
&\approx x_1^i \left(x_1^p\right)^*,
\end{aligned}
\tag{4.50}
$$

and

$$
\begin{aligned}
\mathbb{D}\left\{\underline{x}_1^i \left(\underline{x}_1^p\right)^*\right\} &= \mathbb{D}\left\{x_1^i \underline{v}_p^*\right\} + \mathbb{D}\left\{\left(x_1^p\right)^* \underline{v}_i\right\} + \mathbb{D}\left\{\underline{v}_i \underline{v}_p^*\right\} \\
&= \left(\alpha_1^i\right)^2 \sigma_{\hat{x}_1}^2 + \left(\alpha_1^p\right)^2 \sigma_{\hat{x}_1}^2 + 2\sigma_{\hat{x}_1}^4 \\
&\approx \left(\alpha_1^i\right)^2 \sigma_{\hat{x}_1}^2 + \left(\alpha_1^p\right)^2 \sigma_{\hat{x}_1}^2
\end{aligned}
\tag{4.51}
$$

Hence, without considering multipath effects, the PDoA estimate can be assumed to be approximately unbiased. Similar to the derivation of (4.20), one can derive the variance of the PDoA estimator

$$
\sigma_{\hat{\Phi}_r^{i,p}}^2 \approx \frac{\left(\alpha_1^i\right)^2 \sigma_{\hat{x}_1}^2 + \left(\alpha_1^p\right)^2 \sigma_{\hat{x}_1}^2}{2\left(\alpha_1^i\right)^2 \left(\alpha_1^p\right)^2} = \frac{\sigma_{\hat{x}_1}^2}{2\left(\alpha_1^p\right)^2} + \frac{\sigma_{\hat{x}_1}^2}{2\left(\alpha_1^i\right)^2}.
\tag{4.52}
$$

## **4.4.** Summary

In this chapter, based on the sampled channel frequency response, carrier phase estimation and tracking are introduced for the purpose of positioning.

First, by multiplying the sampled channel frequency response of symmetrically located subcarriers, one can easily reconstruct the phase of the central carrier, as the phases of the subcarriers are eliminated. This approach is very simple to implement, however, the resulting LoS carrier phase estimate can contain a large bias in a multipath channel.

Then, based on the maximum likelihood (ML) method, both the LoS path and the reflections are considered in the model for carrier phase estimation, which is referred to as the full model. Considering the reflections, one can effectively account for multipath effects. The resulting carrier phase estimator becomes unbiased, however the accuracy may get poor, the effect of which is captured by the measure of dependence $|s(\tau_{2,1})|$ between the LoS path and the reflection.

Alternatively, one can consider only a few paths or even only a single path when estimating the complex gain and the resulting carrier phase, the model for which is referred to as the simplified model. The precision of the carrier phase estimator can become better than the one derived from the full model, but generally at the cost of a bias. To estimate the carrier phase, one needs to reconstruct the design matrix based on the time delay estimate. Hence, the phase bias in the simplified model, depends not only on the unconsidered reflections in the carrier phase estimation model, but also on the error of the time delay estimate. Generally, a ranging signal that offers an accurate time delay estimator, also results in an accurate carrier phase estimate.

The bias in the time delay estimate will propagate into the carrier phase estimate. In a time-variant channel, the change of the time delay bias will lead to a large variation in the carrier phase bias. Hence, to practically estimate the complex gain, one may not need to update the time delay estimate in the design matrix for every ranging symbol (or signal packet). So that the resulting carrier phase estimate is less affected by the change of the time delay bias.

The carrier phase obtained from the argument of the complex gain is ambiguous, and each carrier phase estimate in principle carries its own carrier phase cycle ambiguity. Consequently, one cannot determine a unique position solution using a series of carrier phase estimates in a straightforward way, because of too many unknown parameters. Hence, a series of carrier phase estimates need to be tracked (i.e., unwrapped), so that any change in carrier phase cycle in the series can be absorbed by the unwrapped carrier phase measurement, and only an initial carrier phase cycle ambiguity remains. The carrier phase tracking/unwrapping can be achieved by using a phase-locked loop (PLL).

The carrier frequency offset can cause extra phase rotations even when the receiver is static. If such a phase rotation is larger than one cycle during the burst transmission period (e.g., $T_D$ in Fig. 2.2), cycle slips will occur in the unwrapped carrier phase measurement. To avoid such an issue, it is recommended to estimate the carrier frequency offset a priori, and compensate it before estimating the carrier phase (i.e., phase-or-arrival). Alternatively, if all transmitters are

frequency-synchronized, one can compute the carrier phase difference between two Tx-Rx pairs (i.e., phase-difference-of-arrival), so that the phase rotation due to the receiver frequency offset is eliminated, which prevents the occurrence of cycle slips introduced by the receiver frequency offset.

**4**

# 5

# Signal Design for Positioning

In this Chapter, we aim to design a ranging signal, which only occupies limited spectral resources, while still offers a good ranging accuracy based on time delay or carrier phase estimation. Unlike the design of communication signals, where the data transmission rate is of interest, a ranging signal does not need to occupy a large contiguous bandwidth to sustain a high data transmission rate. Hence, for the purpose of ranging, one can use only a few signal bands sparsely placed in the available signal spectrum, which largely improves the spectral efficiency and the reduces the computational complexity to determine the range observation.

First, in section 5.1, we analyze relation between the signal spectrum pattern and the correlation function, from which the propagation time delay can be determined (i.e., the MF method). By selecting different subcarriers in different signal bands for ranging, the precision, the unambiguous ranging distance, and the resistance against multipath are reflected through the associated correlation function.

As introduced in Chapter 3 and 4, one can consider both the LoS path and the reflections in the time delay and carrier phase estimation model, so that the resulting estimator can be less biased than using the MF method in multipath conditions, and ultimately can achieve a better accuracy. Given the same bandwidth and power for each signal band as shown in Fig. 2.4, the design of ranging signal becomes selecting $M_a$ signal bands out of $M$, with the aim of achieving the user-desired ranging accuracy by using as few bands as possible. Sparsely selecting multiple signal bands for ranging and positioning is similar to the problem of sensor selection [139, 140, 141].

Then, in section 5.2, aiming to obtain an unbiased time delay estimator for the LoS path, one can use the multivariate CRLB as criteria to design a ranging signal that occupies as little spectrum resources as possible. By considering not only the LoS path, but also all reflections in a multipath channel, the accuracy of the delay estimators can meet the user-specified requirement, when using the designed ranging signal.

Alternatively, in section 5.3, if one accepts biased estimates through the simplified model, which does not contain all reflections, one can design a sparse multiband signal by considering the ranging precision, the measure of dependence, and the measure of bias, as introduced in chapter 3, as criteria. Using the resulting multiband signal for ranging, the precision of the LoS time delay estimator will not largely decrease by considering the additional reflections in the estimation model, and the bias will remain small when the reflections are neglected in the model.

## 5.1. Ranging Signal and Correlation Function

In this section, we first derive the auto-correlation function (ACF) of the multiband OFDM ranging signal, and the means to analyse the associated ranging precision, the unambiguous ranging distance, and the multipath resistance [123]. In order to derive a closed-form expression of the correlation function, the pilot subcarrier spacing is assumed to be the same for all pilot subcarriers (i.e., one needs to use the comb-type of pilots [142]). In addition, the spacing between two activated signal bands is also assumed to the same.

### 5.1.1. Single-band Signal

First, we start with a single-band OFDM training symbol. Given a fixed subcarrier spacing $\Delta f$ and fixed total signal power, one can select some of the subcarriers as pilots for ranging and mute the others. To have the same amount of signal power, the less pilot subcarriers are used, the more power will be allocated on those pilot subcarriers. Furthermore, the pilot spacing and the power are assumed to be the same for all pilot subcarriers. The baseband OFDM signal in discrete time can be rewritten by

$$s[n] = \frac{1}{\sqrt{N_p}} \sum_{i=-N_p/2}^{N_p/2-1} c_i \exp\left(j2\pi \frac{iP}{N_s} n\right), \quad n = 0, 1, \ldots, N_s - 1, \quad N_p = \lfloor \frac{N_s - 1}{P} \rfloor + 1, \quad (5.1)$$

in which $N_p$ denotes the number of pilots out of the total number of subcarriers $N_s$ for ranging, $P$ denotes the interval between two adjacent pilots, $\lfloor \cdot \rfloor$ denotes rounding down. It should be noted that the signal power is normalized to one by the coefficient $1/\sqrt{N_p}$, hence it is different from the one in (2.1).

For simplicity, we consider a BPSK modulation on every subcarrier (i.e., $|c_i| = 1$). Then, based on one symbol, the correlation function of a single-band signal is derived as follows

$$c_{sb}(\tilde{\tau}) = \frac{\exp(-j2\pi f_c \tau)}{N_p} \exp\left(j\pi N_p P \Delta f(\tau - \tilde{\tau})\right) \exp\left(-j\pi(N_p - 1)P\Delta f(\tau - \tilde{\tau})\right)$$
$$\frac{\sin\left(\pi N_p P \Delta f(\tau - \tilde{\tau})\right)}{\sin\left(\pi P \Delta f(\tau - \tilde{\tau})\right)}, \quad (5.2)$$

where the subscript 'sb' is the abbreviation for 'single-band', $\tau$ denotes the prop-
agation time delay, and $\tilde{\tau}$ denotes the delay variable in the correlation function.
The derivation of (5.2) can be found in Appendix A.4.1.

The correlation function $c_{sb}(\tilde{\tau})$ will reach its maximum, when the time delay
estimate $\hat{\tau}$ is equal to the propagation time delay $\tau$ (also see section 3.3.1). Hence,
one can determine the time delay based on the amplitude of the correlation func-
tion. The modulus of the correlation function in (5.2) is given by

$$|c_{sb}(\tilde{\tau})| = \left| \frac{1}{N_p} \frac{\sin\left(\pi N_p P \Delta f (\tau - \tilde{\tau})\right)}{\sin\left(\pi P \Delta f (\tau - \tilde{\tau})\right)} \right|. \tag{5.3}$$
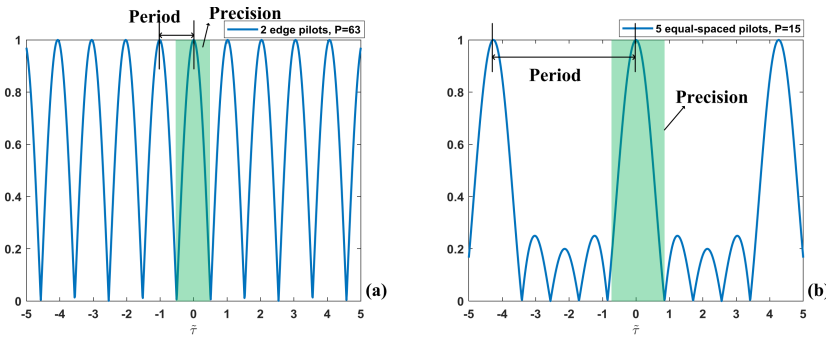


Figure 5.1: The amplitude of the correlation function of (a) a two edge pilot subcarriers, and (b) five
equally spaced pilot subcarriers; all other subcarriers are muted. The overall signal power is identical
in both cases and the signal bandwidth is assumed to be 10 MHz. The horizontal axis shows the time
delay estimate normalized by the sample interval (i.e., $T_s = 10^{-7}$ s). Since the actual propagation delay
is offset to zero for this graph, the main lobe of the correlation function occurs at $\tilde{\tau} = 0$.

For example, considering a single band signal with a bandwidth of 10 MHz
and $N_s = 64$ subcarriers, Fig. 5.1 shows the correlation function $c_{sb}(\tilde{\tau})$, when using
only two edge pilots (i.e., $N_p = 2$, $P = 63$) (see Fig. 5.1(a)), and 5 equally spaced
pilots (i.e., $N_p = 5$, $P = 15$) (see Fig. 5.1(b)). The correlation function contains a
main-lobe and also multiple side-lobes, and we will analyze how the correlation
function is related to the ranging performance, with regard to the precision of the
time delay estimator, the ranging ambiguity, and the resistance against multipath.

### Precision
Theoretically, the precision of the time delay estimator using the MF method, can
be evaluated the CRLB (cf. (3.6)). Practically, the precision is also reflected by the
curvature of the main-lobe of the correlation function [143]. A larger curvature
(i.e., a narrower main-lob) consequently leads to a lower CRLB and a better rang-
ing precision.

Hence, to evaluate the ranging precision, one can compute the width of the
main-lobe of the correlation function as a first indication, or the first zero point

of the correlation function. Based on the correlation function shown in (5.3), the first zero point of the correlation function is given by

$$\tilde{\tau}|_{c_{sb}=0} = \frac{1}{PN_p\Delta f}. \tag{5.4}$$

When the value of the peak in the correlation function is fixed (i.e., the total signal power is fixed), a small first zero point can result in a narrow main-lobe with a large curvature. Such a peaked main lobe in the correlation function leads to a better precision of time delay estimation. Therefore, given a fixed signal bandwidth and a fixed subcarrier spacing $\Delta f$, in order to improve the precision of time delay estimation, we should insert pilots as few as possible, and mute the other subcarriers, so that the pilot spacing $P$ is as large as possible, and more power will be moved to the edges of the signal spectrum. This is also in line with the conclusion derived from the CRLB in (3.6). For example, as shown in Fig. 5.1, the main-lobe of the correlation based on 2 edge pilots (with $PN_p = 63 \times 2 = 126$) is narrower than 5 equally spaced pilots (with $PN_p = 15 \times 5 = 75$).

### Ambiguity
The period of the occurrence of the main-lobe in the correlation function determines the unambiguous ranging distance. Its period $T_{c_{sb}}$ can be derived from the denominator in (5.3), and is given by

$$T_{c_{sb}} = \frac{1}{P\Delta f}. \tag{5.5}$$

Given a fixed signal bandwidth and subcarrier spacing $\Delta f$, the more pilots we insert (i.e., smaller $P$), the larger the period of the correlation function becomes, which consequently results in a longer unambiguous ranging distance.

For example, within a fixed signal bandwidth of 10 MHz, if we use only two edge pilot subcarriers (i.e., the {-32,31}-th subcarriers, when $N_s = 64$, $N_p = 2$, $P = 63$), the main lobe will occur almost every 0.1 $\mu$s, as shown in Fig. 5.1(a). In such a case, the unambiguous ranging distance is about 30 m. In order to increase the period of the occurrence of the main-lobe and the resulting unambiguous ranging distance, one can insert more pilots. As shown in Fig. 5.1(b), based on $N_p = 5$ pilots with an equal spacing (i.e., the {-32,-17,-2,13,28}-th subcarrier, $P = 15$), the period of the correlation function will be 0.427 $\mu$s, and the unambiguous ranging distance is extended to about 128 m. Inserting more pilots increases the unambiguous ranging distance, but sacrifices the ranging precision, because the main lobe becomes wider.

Note that in practice, in the presence of noise, a large side lobe may get even bigger than the actual main lobe, which can lead to an ambiguity problem (also referred to as false or incorrect detection). In addition, if one considers the data $c_i$ modulated on pilot subcarriers, then there is no ambiguity introduced to time delay estimation beyond the OFDM symbol duration. However, ambiguity can still exist within one symbol duration.

## Multipath Resistance

In a multipath channel, the correlation function of the received signal will be the sum of the correlation functions of the signals from all paths (i.e., LoS and reflections). The correlation function of a received multipath signal is an attenuated correlation function of the LoS signal and shifted by the relative delay. Hence, time delay estimation will be affected by the side lobes and the repeated main lobes through the ambiguity. Given a fixed 10 MHz signal bandwidth, based on only two edge subcarriers, time delay estimation can be easily affected by a reflection in a multipath channel. However, ranging based on five equally spaced pilots (i.e., the {-32,-17,-2,13,28}-th subcarrier) can be more robust in multipath conditions, because the amplitude of the side lobes is significantly reduced as shown in Fig. 5.1(b), compared to Fig. 5.1(a). In addition, Fig. 5.2 presents the envelope of time delay estimation error in a two-path multipath channel as a function of the relative delay. Compared with the case that only two edge subcarriers are used for time delay estimation, the impact of a reflection with a relative delay from 0.1 $\mu$s to 0.3 $\mu$s (i.e., 30-90 m in distance) can be largely mitigated, when five equally spaced pilots are used.



(a)                              (b)
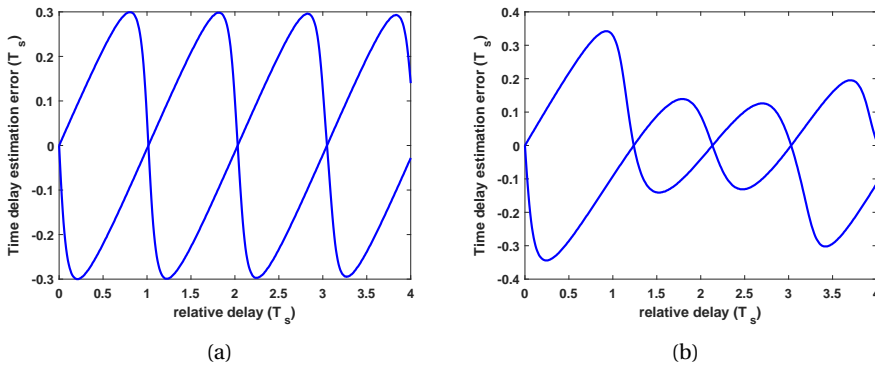
Figure 5.2: The envelope of the multipath time delay estimation error, for a single band OFDM signal with only $N_P = 2$ edge subcarriers (a) and $N_p = 5$ equally spaced pilots are transmitted for time delay estimation and ranging, and the relative attenuation $\alpha_{2,1} = 0.8$.

Given a fixed signal bandwidth, to obtain a better ranging precision, one should let the pilot spacing be as large as possible, which also means that less subcarriers should be used for time delay estimation and ranging. But even so, in practice, the ambiguity and the robustness of time delay estimation in a multipath environment should be taken into account. In accordance to the required unambiguous ranging distance and the typical channel characteristic, we can compute the required period of the correlation function, and further determine the pilot spacing and the minimum number of pilots for the purpose of time delay estimation and ranging.

### **5.1.2.** Multiband Signal

A multiband signal is shown in Fig. 2.4, where the available signal spectrum is sliced into $M$ signal bands, and each band has the same bandwidth. As presented in Chapter 3, using more signal bands, and considering the frequency relations across different bands, the ranging accuracy will be improved by the large total signal bandwidth. In this subsection, we analyze the ranging precision, the range ambiguity, and the resistance against multipath, based on the correlation function derived from a multiband signal. Given the multiband signal scheme presented in Chapter 2 and a fixed frequency basis $\Delta f_G$, the spacing between two adjacent activated signal bands is set to be $S\Delta f_G$. For example, if all signal bands, as shown in Fig. 2.4, are used for ranging, then $S = 1$.

After receiving the signals from different bands, the correlation function can be initially computed independently for each signal band. But eventually we use all signals together to emulate a large virtual signal bandwidth. The phase rotation due to the signal band spacing $S\Delta f_G$ has to be taken into account for time delay estimation. Therefore, the locally generated reference signal for the $m$-th band should contain an extra phase rotation due to the corresponding signal band spacing, and is given by

$$s_m(t - \tilde{\tau}) = s(t - \tilde{\tau}) \exp(-j2\pi(mS - M/2)\Delta f_G \tilde{\tau}), \quad m = 1, 2, \dots, M_a, \quad (5.6)$$

where $M_a$ denotes the total number of activated signal bands with a spacing of $S\Delta f_G$,

$$M_a = \lfloor \frac{M - 1}{S} \rfloor + 1, \quad (5.7)$$

and $s[n]$ denotes the baseband signal defined in (5.1). For simplicity and the ease of derivation, we assume here that $s[n]$ is the same for all bands, but it can be different in practice. The correlation function of the multiband signal can be derived by the sum of the correlation function of all $M_a$ activated bands,

$$c_{mb}(\tilde{\tau}) = \frac{1}{M_a} \sum_{m=1}^{M_a} \left( \frac{1}{N_s} \sum_{n=0}^{N_s-1} r_m[n] s_m^*[n, \tilde{\tau}] \right). \quad (5.8)$$

Then, the amplitude of the correlation function of the multiband signals is given by

$$|c_{mb}(\tilde{\tau})| = \left| \underbrace{\frac{1}{M_a} \frac{\sin\left(2\pi S\Delta f_G \frac{M_a}{2}(\tau - \tilde{\tau})\right)}{\sin\left(2\pi S\Delta f_G \frac{1}{2}(\tau - \tilde{\tau})\right)}}_{c_{mb}^{(2)}(\tilde{\tau})} \underbrace{\frac{1}{N_p} \frac{\sin\left(2\pi P\Delta f \frac{N_p}{2}(\tau - \tilde{\tau})\right)}{\sin\left(2\pi P\Delta f \frac{1}{2}(\tau - \tilde{\tau})\right)}}_{c_{mb}^{(1)}(\tilde{\tau})} \right|, \quad (5.9)$$

where the subscript 'mb' is the abbreviation for 'multi-band'. The derivation of (5.9) can be found in Appendix A.4.2.

The term $c_{mb}^{(1)}(\tilde{\tau})$ in (5.9), is referred to as the primary component of the correlation function, and is identical to (5.3). In a similar way, the central carriers from different bands can be treated as OFDM 'pilot' subcarriers in the virtual signal bandwidth. Thus, the central carriers from different bands (i.e., signal band spacing $S\Delta f_G$) play the role of the secondary part of the correlation function $c_{mb}^{(2)}(\tilde{\tau})$.

The correlation function now relies not only on the pilot spacing $P\Delta f$, but also on the signal band spacing $S\Delta f_G$ between two activated signal bands. As an example of the correlation function $c_{mb}(\tilde{\tau})$ with primary and secondary main lobes is shown in Fig. 5.3. Similarly, we analyze the correlation function derived from a multiband signal, in terms of the ranging precision, the ambiguity, and the resistance against multipath.
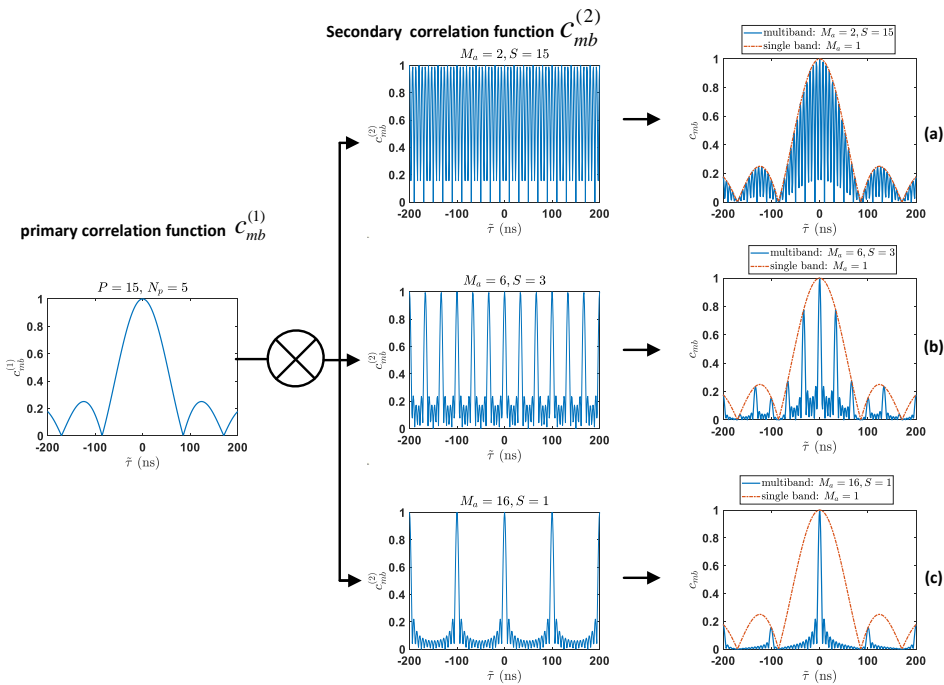


Figure 5.3: Correlation function of $M_a = 2$ bands (a), $M_a = 6$ bands (b) and $M_a = 16$ bands (c), when the baseband signal bandwidth and $\Delta f_G$ are 10 MHz, and $N_p = 5$ pilots with an equal spacing are inserted in each band for time delay estimation and ranging. The primary correlation function is identical to the one in Fig. 5.1(b).

## Precision and Ambiguity

To evaluate the ranging precision, one can again compute the width of the main-lobe. The first zero point of the correlation function of the multiband signal $c_{mb}^{(2)}(\tilde{\tau})$

is defined as the first secondary zero point of $c_{mb}(\tilde{\tau})$, which is given by

$$\tilde{\tau}\big|_{c_{mb}^{(2)}=0} = \frac{1}{S\Delta f_G M_a}. \tag{5.10}$$

Then, the first zero point of $c_{mb}^{(1)}(\tilde{\tau})$ is defined as the first primary zero point of the correlation function $c_{mb}(\tilde{\tau})$. Based on (5.4), as $\Delta f_G$ is generally much larger than $\Delta f$, $\tilde{\tau}\big|_{c_{mb}^{(2)}=0} < \tilde{\tau}\big|_{c_{sb}=0}$. Hence, the width of the main-lobe will be determined by the first secondary zero point.

Since the first secondary zero point $\tilde{\tau}\big|_{c_{mb}^{(2)}=0}$ is linked to the inverse of the virtual signal bandwidth, one can simply increase the virtual signal bandwidth to narrow the main lobe of the correlation function and improve the precision of time delay estimation and ranging.

In the same way, we define the period of the occurrence of the main-lobe in the function $c_{mb}^{(1)}(\tilde{\tau})$ as the primary period of $c_{mb}(\tilde{\tau})$, given by (5.5). The period of the occurrence of the main-lobe in the function $c_{mb}^{(2)}(\tilde{\tau})$ is then defined as the secondary period of $c_{mb}(\tilde{\tau})$, and is given by

$$T_{c_{mb}} = \frac{1}{S\Delta f_G}. \tag{5.11}$$

A larger spacing $S\Delta f_G$ between two adjacent activated bands results in a smaller secondary period of the correlation function $c_{mb}(\tilde{\tau})$.

For example, considering a 10 MHz single band OFDM signal, in which the FFT size is assumed to be $N_s = 64$, and $N_p = 5$ pilots (i.e., the {-32,-17,-2,13,28}-th subcarrier, $P = 15$) are inserted with an equal spacing and equal power for ranging. In addition, the signal band spacing $\Delta f_G$, as shown in Fig. 2.4, is assumed to be 10 MHz. In order to achieve a virtual signal bandwidth of 160 MHz, we can transmit 16 consecutive bands as in Fig. 2.4. Alternatively, we can occupy only $M_a = 6$ bands (i.e., the band {1,4,7,10,13,16}) with $S = 3$, then the carrier spacing of those two bands becomes $S\Delta f_G = 30$ MHz. In an extreme case, $M_a = 2$ edge bands (i.e., the band {1,16}, $S$=15) are used for time delay estimation and ranging. The correlation functions are presented in Fig. 5.3.

A large signal band spacing $S\Delta f_G$ leads to a small secondary period of $T_{c_{mb}}$ of the correlation function $c_{mb}^{(2)}(\tilde{\tau})$, but the amplitude of the secondary main lobe in the product of $c_{mb}(\tilde{\tau})$ still relies on the primary period $T_{c_{sb}}$. Therefore, the unambiguous ranging distance is determined by the primary period of the correlation function, which relies only on the pilot spacing $P\Delta f$, with the assumption that all bands are modulated with the same baseband signal format. In this example, the pilot spacing is 781.3 kHz. Consequently, based on (5.5), the unambiguous ranging distance will be about 128 m, no matter how many signal bands (i.e., $M_a$) are activated for ranging, or how large the spacing between two adjacent bands (i.e., $S\Delta f_G$) is.

In addition, the precision of time delay estimation depends on the width of the secondary main lobe, which is related to the virtual signal bandwidth. As

shown in Fig. 5.3(a), the first secondary zero point of the correlation function of the two edge signal bands (i.e., 160 MHz virtual signal bandwidth, and 20 MHz occupied bandwidth) is about 5 ns, corresponding to 1.5 m in distance which is much smaller than the one from a single band signal (i.e., 10 MHz (virtual) signal bandwidth). Hence, a multiband signal sparsely occupying the available bandwidth can very much improve the ranging precision.

### Multipath Resistance

In a multipath–free or a low multipath environment with a relatively high SNR, one can simply use multiple signal bands which are sparsely placed in the available bandwidth for ranging and positioning. However, considering close-in reflections with a relative delay less than the inverse of the virtual signal bandwidth, since the product of $c_{mb}(\tilde{\tau})$ still relies on the primary main lobe and contains larger side lobes as shown in Fig. 5.3(a), the robustness of time delay estimation will not be significantly improved by using multiband signal sparsely occupying the available signal bandwidth. When the channel contains the reflections with the relative delay less than the width of the primary main lobe, more signal bands should be used for ranging and positioning, so that the amplitude of the secondary main-lobe in the correlation function becomes small (see Fig. 5.3(b,c)). Reducing the spacing between two adjacent activated bands $\Delta f_G$ will increase the period of the secondary main lobe $T_{c_{mb}}$. For instance, when 16 consecutive 10 MHz signal bands with a spacing $\Delta f_G$ of 10 MHz are used, there is only one secondary main lobe inside the primary main lobe (see Fig. 5.3 (c)). Therefore, ranging based on these 16 bands is more robust to close-in reflections compared to only using a two sparse edge bands, as less secondary main lobes appear in the primary main lobe.

### 5.1.3. Discussion

Given a multiband signal shown in Fig. 2.4, and assuming each signal band has the same bandwidth and the same pilot subcarriers, then the unambiguous ranging distance will only be determined by the spacing of the pilot subcarriers $P\Delta f$. Using more signal bands, the ranging precision will be improved by the larger virtual signal bandwidth, as well as the resistance against multipath, as the amplitude of the side-lobes becomes smaller. Therefore, one can design a ranging signal by determining the spacing of the pilots (i.e., $P\Delta f$) and of the signal bands (i.e., $S\Delta f_G$), under the user-specified requirements on the width of the main-lobe (i.e., precision, cf. (5.10)), the period of the main-lobe (i.e., unambiguous ranging distance, cf. (5.5)), and the amplitude of the side-lobes (i.e., multipath resistance, cf. (5.9))

However, the design of the ranging signal, based on the closed-form correlation function (5.9), is with the assumption that any two adjacent activated signal bands will have the same spacing, and that the time delay will be determined by the MF method. If the spacing between two adjacent activated signal bands $S\Delta f_G$ is not the same across all $M_a$ bands, one can no longer obtain a closed-form expression of the correction function. The first secondary zero point of the correlation function will be determined by the Gabor bandwidth, instead of the spacing $S\Delta f_G$. As shown in (5.10), the first zero point varies for different signal patterns. In

addition, if the spacing of any two adjacent bands is no longer a constant number, (5.11) will not be valid. Consequently, the secondary correlation function will not be periodic, thus it will be different from the one shown in Fig. 5.3. Additionally, as presented in Chapter 3, instead of using the MF method which only considers a single path in the model for time delay estimation, one can jointly estimate the time delay for both the LoS path and some reflections.

To avoid the assumption that the spacing between any two adjacent signal bands should be the same, and considering the impact of the multipath on the ultimate ranging accuracy, we will design the ranging signal based on quantitative performance metrics (e.g., accuracy, measure of dependence, and measurement of bias) in the following sections. Moreover, given a fixed and the same pilot pattern for all $M$ signal bands (i.e., a fixed unambiguous ranging distance), the ranging signal design becomes a problem of selecting $M_a$ signal bands out of $M$.

## 5.2. Multiband Signal Design for Unbiased Estimation

Based on the analysis of the correlation function, presented in section 5.1, the precision of time-based ranging estimator is largely improved by a large virtual signal bandwidth, even though only a small amount of spectral resources is used. Instead of using the MF method to obtain a likely biased time delay estimator in multipath conditions, one can apply a ML-based full model to obtain an unbiased estimator, which considers not only the LoS path but also reflections. In this section, we aim to design a multiband signal that can meet the user specified ranging accuracy of an unbiased time delay estimator.

### 5.2.1. Problem Formulation

Considering spectral efficiency, it may not be necessary to occupy an entire wide signal bandwidth for time delay estimation. Similar to [140], we introduce a binary selection vector for $M$ different signal bands,

$$\boldsymbol{w} = \begin{bmatrix} w_1 & w_2 & ... & w_M \end{bmatrix}^{\text{T}} \in \{0,1\}^M, \tag{5.12}$$

where $w_m = 1$ (0) indicates that the $m$-th OFDM signal band is activated (muted), and used (not used) for time delay estimation. The objective is to minimize the total number of activated bands for ranging.

Rather than (3.16), the FIM based on a multiband signal with a selection vector can be obtained by

$$\boldsymbol{F}(\boldsymbol{w}, \boldsymbol{u}) = \sum_{m=1}^{M} w_m \boldsymbol{F}_m(\boldsymbol{u}). \tag{5.13}$$

To design an optimal multiband signal for ranging, we use the CRLB as an inequality constraint in an optimization problem to meet the desired performance, and try to minimize the number of activated signal bands.

However, the propagation time delay and the gain in $\boldsymbol{u}$ have different units. If the uncertainty in one of the estimators is numerically much larger than one of the others, the optimization will be dominated by the estimators with the larger uncertainty. Thus, we also introduce a user-specified compensation weight vector $\boldsymbol{\gamma}$. Then, the modified FIM (MFIM) is defined as

$$\tilde{\boldsymbol{F}}(\boldsymbol{w}, \boldsymbol{u}) = \text{diag}^{-1}\{\boldsymbol{\gamma}\} \boldsymbol{F}(\boldsymbol{w}, \boldsymbol{u}) \text{diag}^{-1}\{\boldsymbol{\gamma}\}. \tag{5.14}$$

Furthermore, for the purpose of ranging and positioning, we only use the time delay estimates to retrieve the geometric information. The gain of each path is also important to help us distinguish whether the propagation channel contains a direct-LoS path or not, however, its required accuracy can be much lower than that of the time delay estimators. Thus, the different requirements for the time estimators and the gain estimators should be also taken into account when we design the compensation vector $\boldsymbol{\gamma}$. In our case, $\gamma_\tau \gg \gamma_\alpha$.

After compensation, all estimators are expected to have approximately the same precision. Because of the presence of multiple unknown parameters, the CRLB is no longer a scalar. In order to employ the CRLB as a constraint in an optimization problem, the minimum eigenvalue constraint (i.e., E-optimality) [141, 140] is chosen here. The errors of the estimators in $\boldsymbol{\epsilon_u}$ are assumed to be constrained in an origin-centered sphere of radius $r_e$, with a probability larger than $p_e$, which can be written by

$$p(\|\boldsymbol{\epsilon_u}\|_2 \leq r_e) \geq p_e. \tag{5.15}$$

To avoid the nonlinear inverse operator, instead of using the CRLB as a constraint, the MFIM is employed in the optimization. The minimum eigenvalue for the MFIM is given in [141] and also derived in appendix A.5,

$$\lambda_{\min}\{\tilde{\boldsymbol{F}}(\boldsymbol{w}, \boldsymbol{u})\} \geq \lambda_{\text{eig}} = \frac{N_u}{r_e^2}\left(\frac{1}{1 - p_e}\right), \tag{5.16}$$

where $N_u$ denotes the number of unknown parameters in $\boldsymbol{u}$. Since here we are using the MFIM which is the inverse of the CRLB, the smallest eigenvalue of the MFIM should be larger than the $\lambda_{\text{eig}}$ derived in (5.16). Thus, considering $M$ available signal bands for time delay estimation, the inequality constraint can be written as

$$\sum_{m=1}^{M} w_m \tilde{\boldsymbol{F}}_m(\boldsymbol{u}) - \lambda_{\text{eig}} \boldsymbol{I}_{N_u} \geq \boldsymbol{0}_{N_u}. \tag{5.17}$$

Based on the actual positioning scenario or the user desired capability of separating certain reflections, a set of $\mathcal{U}$, containing the different potential relative delays and the corresponding gains, is introduced here to compute a numerical value for the MFIM in the optimization, using (3.13) and (5.14).

In order to design a sparse multiband signal for ranging, the objective function is based on the $l_1$ norm, which can produce a sparse selection vector [130]. The

optimization problem is now formulated by

$$\underset{\boldsymbol{g}\in\mathbb{R}^M}{\arg\min} \quad \|\boldsymbol{g}\|_1$$

$$\text{s.t.} \quad \sum_{m=1}^{M} g_m \tilde{\boldsymbol{F}}_m(\boldsymbol{u}) - \lambda_{\text{eig}}\boldsymbol{I}_{N_u} \geq \boldsymbol{0}_{N_u} \quad \forall \boldsymbol{u} \in \mathcal{U} \tag{5.18}$$

$$0 \leq g_m \leq 1, \quad m = 1, 2, , \dots, M.$$

The selection vector $\boldsymbol{w}$ defined in (5.12) with elements being either zero or one, leads to a non-convex function, which is thus relaxed to $\boldsymbol{g}$ with *inequalities*. The value of the elements in a selection vector $\boldsymbol{g}$ can vary from zero to one.

To retrieve a binary selection vector $\boldsymbol{w}$, one can activate the signal band for positioning once the corresponding selection coefficient in $\boldsymbol{g}$ is larger than the user specified threshold $c_t$,

$$w_m = \begin{cases} 1, & \text{if } g_m \geq c_t, \\ 0, & \text{otherwise.} \end{cases} \tag{5.19}$$

if one is satisfied by an approximation to the solution found in (5.19).

### **5.2.2.** Examples
In this subsection, we provide some examples of signal design using the CRLB as criteria. In addition, we aim to only analyse how the signal design is impacted by a reflection, thus the SNR is fixed to 20 dB. The available total bandwidth of 160 MHz is divided into $M = 16$ signal bands as shown in Fig. 2.4, and each signal band has a bandwidth of 10 MHz and $N_s = 64$ subcarriers.

To define the required performance, for 70% of the cases (i.e., $p_e = 0.7$ in (5.15)), the error in the delay estimate $\hat{\tau}$ should be less than 0.1 ns, which is equivalent to 3 cm in distance, and the error in the gain estimate is expected to be less than 0.05. The delay estimate is numerically much smaller than the gain estimate. A compensation vector $\boldsymbol{\gamma}$ should be introduced to numerically adjust the required accuracy for time delay and the gain, so that they are in the same order of magnitude. First, the unit of the propagation time delay is normalized by the inverse of the total signal bandwidth (i.e., 160 MHz). Then, to further balance the performance of the delay and gain estimators, and maintain their error bounds on the same level, a scalar of 0.3 is introduced for the gain. Then the lower bound of the gain estimator will increase by about 11%, so that the performance of the balanced parameters are close. Hence, the compensation weight vector $\boldsymbol{\gamma}$ is written as

$$\boldsymbol{\gamma} = \begin{bmatrix} 160 \times 10^6 & 160 \times 10^6 & 0.3 & 0.3 \end{bmatrix}^{\text{T}}. \tag{5.20}$$

To compute the relative propagation gain in (3.46), the distance of the LoS path $d_1$ is assumed to be 5 m. Then, the relative time delay of the reflection is assumed to range from 6.8 ns to 47 ns (i.e., about 2 m to 14 m). The resulting propagation gain is shown in Fig. 5.4(b).
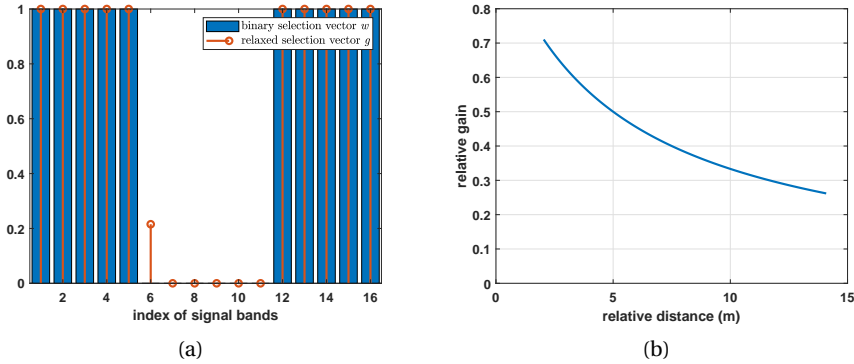
Figure 5.4: (a) Relaxed selection vector $\boldsymbol{g}$ (in red stems) and its binary selection vector $\boldsymbol{w}$ (in blue) to activate the signal bands for positioning, when considering reflections with relative delay from 6.8 ns to 47 ns, and (b) relative gain derived from FSPL model.

After we determine $\tilde{\boldsymbol{F}}_m(\boldsymbol{u})$ and $\lambda_{\text{eig}}$ in (5.18), the optimization problem is solved by the CVX toolbox [144], which contains the solver of SDPT3 [145] employed with a primal-dual interior-point algorithm. To retrieve the binary selection vector $\boldsymbol{w}$ from the relaxed selection vector $\boldsymbol{g}$, the threshold $c_t$ in (5.19) is set to be 0.5.

Fig. 5.4(a) shows the resulting ranging signal, which occupies $M_a = 10$ out of $M = 16$ signal bands. By considering both the LoS path and the reflections, the unbiased time delay estimator can achieve a centimeter level accuracy, when using the designed multiband signal.

In order to obtain an unbiased time delay estimator, all reflections will be considered in the model for time delay estimation. As the estimator for the LoS path and other reflections are treated equally in (5.18), one needs to use more signal bands for ranging, so that the time delay estimator of the weakest reflection considered in the model, can still achieve the user specified ranging accuracy (i.e., $\lambda_{\text{eig}}$).

For comparison, Fig. 5.5 shows the case, in which the channel only contains the reflections with the relative delay from 6.8 ns to 37 ns. Compared with the example shown in Fig. 5.4, if the channel contains less weak reflections, the model for unbiased time delay estimation only needs to consider the reflections associated with large propagation gain. Consequently, to meet the requirement on ranging accuracy, less signal bands are needed. If the channel contains the reflections only with the relative delay from 6.8 ns to 17 ns (i.e., 2~5 m), as shown in Fig. 5.6, only $M_a = 4$ signal bands out of $M = 16$ are needed for ranging, in order to achieve a centimeter level ranging accuracy.

If the design of a ranging signal is based on the goal of obtaining an unbiased time delay estimator of the LoS path for ranging, more signal bands will be used, so that the time delays of the reflections can be accurately resolved.

On the other hand, as presented in chapter 3 one can apply a simplified model, in which not all reflections are considered, if a biased estimator is acceptable for
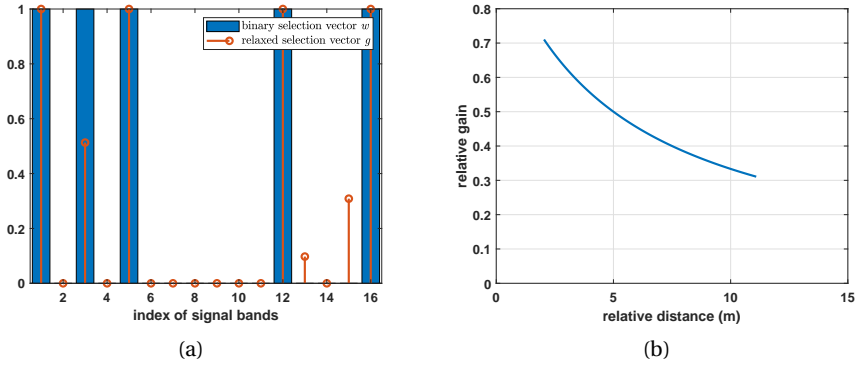
Figure 5.5: (a) Relaxed selection vector $\boldsymbol{g}$ (in red stems) and its approximated binary selection vector $\boldsymbol{w}$ (in blue) to activate the signal bands for positioning, when considering reflections with relative delay from 6.8 ns to 37 ns, and (b) relative gain derived from FSPL model.

**5**
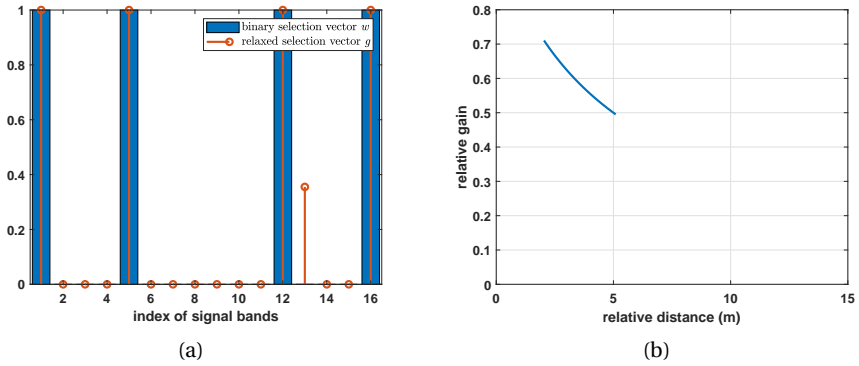


Figure 5.6: (a) Relaxed selection vector $\boldsymbol{g}$ (in red stems) and its binary selection vector $\boldsymbol{w}$ (in blue) to activate the signal bands for positioning, when considering reflections with relative delay from 6.8 ns to 17 ns, and (b) relative gain derived from FSPL model.

the user. Consequently, there is less computational complexity to estimate the time delay. In the following section, to allow for possibly biased estimation, we use the measure of dependence and the measure of bias as ranging performance metrics to design a multiband ranging signal.

## 5.3. Multiband Signal Design for Biased Estimation

In this section, we aim to design a sparse multiband ranging signal, which uses limited spectrum resources (e.g., $M_a$ signal bands out of $M$), reduces the computational complexity, and in a multipath channel still achieves a user-specified precision for time delay estimation and keeps the bias small. As we determine

the carrier phase based on the time delay estimate(s), in return, the bias in carrier phase estimation will also remain small.

### 5.3.1. Problem Formulation

Instead of using the CRLB derived in a 2-path channel as a criterion as in the previous section, we employ constraints on the precision of time delay estimation (i.e., the CRLB derived in a single path channel), on the measure of dependence for delay estimation, and on the measure of bias, to formulate an optimization problem. As discussed in section 3.2, the measure of dependence for delay estimation indicates how the precision deteriorates when an additional reflection is considered in the model, and the measure of bias indicates how large the bias is, if we do not consider such a reflection in the simplified model.

To simplify the discussion, the signal power in each signal band is assumed to be the same, i.e., the more signal bands are used for positioning, the larger the total signal power becomes. Similarly, we consider $M$ signal bands and introduce a binary selection vector for these bands as in (5.12).

We first give a constraint on the precision of the time delay estimator. Similar to (3.29), but considering the frequency relation of the different signal bands and the binary selection vector, the variance of the delay estimator needs to be smaller than a user-specified threshold $\sigma_\tau^2$. Hence, the constraint is given by

$$\frac{\sigma_n^2}{\alpha_1^2 8\pi^2 \ddot{\boldsymbol{f}}^{\mathrm{T}} \boldsymbol{w}} \le \sigma_\tau^2, \quad \left[\ddot{\boldsymbol{f}}\right]_m = \sum_i (f_m + f_i)^2, \tag{5.21}$$

where the frequency $f_m + f_i$, the measurement noise variance $\sigma_n^2$ (cf. (3.4)) and the propagation gain $\alpha_1$ (or SNR) are assumed to be known to the user.

Then, to consider the impact of multipath on time delay estimation, we put constraints on the measure of dependence and on the measure of bias. Without obtaining the channel information a priori, we simply consider a set of reflections that cover a certain range (e.g., with a relative propagation distance from 0.6 m to 15 m). The relative delay is derived from the relative propagation distance, and the relative propagation gains can be derived from the free-space path-loss (FSPL) model.

As shown in (3.42), a reflection that is close to the LoS path may have a strong relative signal power and is likely to cause a large bias when such a reflection is not considered in the model. Therefore, some reflections with strong signal power can be considered in the simplified model to mitigate the bias. One can place a constraint on the measure of dependence for time delay estimation, so that the precision of the LoS estimator will not deteriorate when such a reflection is considered for delay estimation. Combined with the binary selection vector $\boldsymbol{w}$, the measure of dependence for time delay estimation (3.33), which is required to be smaller than a user-specified threshold $c_\varsigma$, is rewritten as

$$\varsigma(\tau) = \frac{\left|\boldsymbol{q}(\tau)^{\mathrm{T}} \mathrm{diag}(\boldsymbol{w}) \boldsymbol{f} \odot \boldsymbol{f}\right|}{\boldsymbol{f}^{\mathrm{T}} \mathrm{diag}(\boldsymbol{w}) \boldsymbol{f}} = \frac{\left|\ddot{\boldsymbol{\varkappa}}(\tau)^{\mathrm{T}} \boldsymbol{w}\right|}{\ddot{\boldsymbol{f}}^{\mathrm{T}} \boldsymbol{w}} \le c_\varsigma, \quad \tau \in \mathcal{U}_I \tag{5.22}$$

where

$$[\ddot{\boldsymbol{\varkappa}}(\tau)]_m = \sum_i (f_m + f_i)^2 \cos\left(2\pi(f_m + f_i)\tau\right),$$

and the user-specified set $\mathcal{U}_I$ contains relative delays of the to-be-considered reflections in the model for time delay estimation.

Other weak reflections could be neglected in the simplified model, so that the computational complexity will not be increased significantly. Therefore, we place a constraint on the measure of bias, so that the bias of delay estimation still remains small, even though those reflections are not considered in the model. Similar to (3.41), the measure of bias with a binary selection vector $\boldsymbol{w}$, which is required to be smaller than the user-specified threshold $c_\varrho$, is given by

$$\varrho(\alpha, \tau) = \frac{\alpha|\boldsymbol{f}^{\mathrm{T}}\mathrm{diag}(\boldsymbol{w})\boldsymbol{p}(\tau)|}{2\pi\boldsymbol{f}^{\mathrm{T}}\mathrm{diag}(\boldsymbol{w})\boldsymbol{f}} = \frac{\alpha\left|\dot{\boldsymbol{\varkappa}}(\tau)^{\mathrm{T}}\boldsymbol{w}\right|}{2\pi\ddot{\boldsymbol{f}}^{\mathrm{T}}\boldsymbol{w}} \leq c_\varrho, \quad (\alpha, \tau) \in \mathcal{U}_{II}, \tag{5.23}$$

where

$$[\dot{\boldsymbol{\varkappa}}(\tau)]_m = \sum_i (f_m + f_i) \sin\left(2\pi(f_m + f_i)\tau\right).$$

The user-specified set $\mathcal{U}_{II}$ contains the relative delays and relative gains of the reflections that would not need to be considered in the model for time delay estimation.

However, due to the binary nature of the selection vector $\boldsymbol{w}$, convexity cannot be guaranteed. Thus, we relax the binary selection vector $\boldsymbol{w}$ to $\boldsymbol{g}$ with inequalities (i.e., $0 \leq g_i \leq 1$), so that each signal band is activated with a weight.

Given $M$ available signal bands with frequency vector $\boldsymbol{f}$ and the signal condition (i.e., $\alpha_1$ and $\sigma^2$), the optimization problem to sparsely select multiple signal bands for ranging, with the user-specified thresholds (i.e., $\sigma_\tau^2$, $c_\varsigma$ and $c_\varrho$) and the user-specified set (i.e., $\mathcal{U}_I$ and $\mathcal{U}_{II}$), can be formulated as follows [82],

$$
\begin{aligned}
&\text{minimize} \quad \|\boldsymbol{g}\|_1 \\
&\text{subject to} \\
&\quad 8\pi^2\alpha_1^2\boldsymbol{f}^{\mathrm{T}}\boldsymbol{g} \geq \frac{\sigma^2}{\sigma_\tau^2}; \\
&\quad \left|\ddot{\boldsymbol{\varkappa}}(\tau)^{\mathrm{T}}\boldsymbol{w}\right| \leq c_\varsigma\ddot{\boldsymbol{f}}^{\mathrm{T}}\boldsymbol{w}, \ \forall \ \tau \in \mathcal{U}_I; \\
&\quad \alpha\left|\dot{\boldsymbol{\varkappa}}(\tau)^{\mathrm{T}}\boldsymbol{w}\right| \leq c_\varrho 2\pi\ddot{\boldsymbol{f}}^{\mathrm{T}}\boldsymbol{w}, \ \forall \ (\alpha, \tau) \in \mathcal{U}_{II}; \\
&\quad g_m \leq 1, \ m = 1, 2, \dots, M; \\
&\quad g_m \geq 0, \ m = 1, 2, \dots, M; \\
&\quad \boldsymbol{1}_M^{\mathrm{T}}\boldsymbol{g} \leq M,
\end{aligned}
\tag{5.24}
$$

in which the $l_1$ norm is used in the objective function to produce a sparse selection vector. It should be mentioned that the required precision for the propagation delay, the measure of dependence for delay estimation, and the measure of bias

should not be exceeded the ones when using all $M$ available signal bands, which determines the lower bound of these performance metrics.

Finally, after solving the optimization problem (5.24), one can retrieve a binary selection vector $\boldsymbol{w}$ based on (5.19), if one can accept the approximation. Some examples of designing a sparse multiband signal will be presented in following subsection.

### 5.3.2. Examples

It is assumed that there are $M = 16$ contiguous signal bands potentially available for positioning, and each signal band has the same signal power and the same bandwidth of 10 MHz.

In order to provide numerical values for the constraints in (5.24), we first anal-yse the measure of dependence for delay estimation $\varsigma(\tau_{2,1})$ (cf. (3.33)) and the measure of bias $\varrho(\alpha_{2,1}, \tau_{2,1})$ (cf. (3.42)) as a function of the relative propagation distance when $M = 16$ bands are activated for positioning. These results were pre-sented in Fig. 3.6 (see the violet dashed line). There will be a strong dependence between the LoS component and the reflections when the relative propagation distance is less than 0.8 m (i.e., $\varsigma(\tau_{2,1}) \geq 0.7$). Therefore, it is infeasible to further decrease the measure of dependence based on the existing signal bandwidth to improve robustness against multipath, other than creating an even larger virtual signal bandwidth. Given 16 signal bands each with 10 MHz bandwidth, we only consider the reflections that are 0.8 m or further away from the LoS path.

First, the standard deviation of the time based ranging error is fixed to 0.003 m, which only indicates the lower bound for time delay estimation in an ideal situation where the channel only contains a LoS path.

Then, we set $c_\varsigma$ to 0.7 as the maximum threshold for the measure of depen-dence when the relative propagation distance ranges from 0.8 m to 3.5 m in set $\mathscr{U}_I$, so that the precision will not decrease significantly when a reflection is taken into consideration in the model for time delay estimation. According to (3.32), the variance is doubled when the measure of dependence $\varsigma(\tau_{2,1})$ is 0.7.

Finally, we may simply neglect reflections that have a relative propagation dis-tance from 3.5 m to 15 m in set $\mathscr{U}_{II}$ with the relative gain shown in Fig. 5.7(b), and expect that the bias in the LoS time delay estimate will remain small. Hence, we set the threshold $c_\varrho$ for the bias to 0.1 m, assuming we can accept a 0.1 m bias in time-based ranging.

The solution of the optimization problem (5.24) is obtained by the CVX toolbox [144]. Fig. 5.7(a) shows the relaxed selection vector $\boldsymbol{g}$, and its binary selection vector $\boldsymbol{w}$ when $c_t = 0.5$. In order to achieve a decimetre level time-based ranging accuracy and guarantee robustness against multipath according to the threshold $c_\varsigma$ and $c_\varrho$, only $M_a = 7$ out of $M = 16$ signal bands are needed for positioning.

Based on the sparsely activated signal bands, as shown in Fig. 5.7(a), Fig. 5.7(c) presents the value of the measure of dependence $\varsigma(\tau)$ and of the measure of bias $\varrho(\alpha, \tau)$, cf. (3.33) and (3.42). Using a few sparse signal bands, the measure of dependence becomes somewhat larger than when using all 16 signal bands, as shown in Fig. 3.6(a). However, as indicated by the measure of bias, a decime-
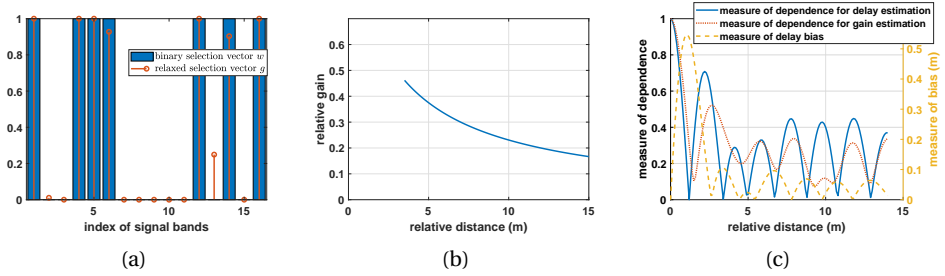
Figure 5.7: (a) Relaxed selection vector $\boldsymbol{g}$ (as red stems) and its binary selection vector $\boldsymbol{w}$ (in blue) to activate the signal bands for positioning from $M = 16$ available signal bands. (b) Relative gain of reflections considered in set $\mathscr{U}_{II}$. (c) Value of measures of dependence for time delay estimation $\varsigma(\tau_{2,1})$ (blue solid line, cf. (3.33)), measure of dependence for complex gain estimation $|s(\tau_{2,1})|$ (red dotted line, cf. (4.12)), measure of bias $\varrho(\alpha_{2,1}, \tau_{2,1})$ (yellow dashed line, cf.(3.42)), as function of relative propagation distance, based on the designed sparse multiband signal.

ter level bias will be introduced in the time delay estimate, if the reflection is not considered in the simplified model. Using the designed signal, the user can apply the simplified model for time delay estimation, in which not all reflections are considered, or no reflection at all.

The carrier phase can also be estimated with the simplified model for precise positioning. The measure of dependence for complex gain estimation based on the designed signal is also presented in Fig. 5.7(c) by the red dotted line, which also links to the phase bias in the simplified model as shown in (4.29).

The performance of parameter estimation using the designed sparse multiband signal can also be found in Fig. 3.7 and Fig. 4.4, in which the so-called 'sparse multiband signal' is the one shown in Fig. 5.8(a).

In addition, for comparison, we also consider different relative gain in set $\mathscr{U}_{II}$ when designing the multiband ranging signal. As shown in (3.42), the measure of bias in time delay estimation depends not only on the relative delay, but also on the relative gain. Without considering the reflection with a large gain in the model, a large bias will be introduced in the resulting estimate. Here, assuming that the reflections in the multipath channel has smaller gain (see Fig. 5.8(b)) than the one shown in Fig. 5.7(b), Fig. 5.8 shows the resulting selection vector for ranging, and the associated measure of dependence for time delay and carrier phase estimation, and measure of time delay bias. As the reflections are assumed to have smaller gain than the ones shown in Fig. 5.7(b), less bias will be introduced in the estimate, when these reflections are not considered in the estimation model. Consequently, as shown in Fig. 5.8(a), less signal bands are needed, in order keep the measure of bias $\varrho(\alpha_{2,1}, \tau_{2,1})$ small.

In Fig. 5.9, assuming that the reflections in the multipath channel are slightly stronger than in the example shown in Fig. 5.7, consequently more signal bands will be needed, in order to meet the user-specified requirement on the measure of bias. As shown in Fig. 5.9(a), at least $M_a = 8$ out of $M = 16$ are needed to be used for ranging.
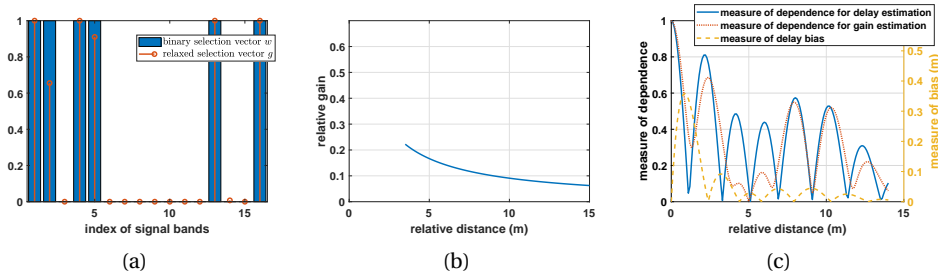
Figure 5.8: (a) Relaxed selection vector $g$ (in red stem) and its binary selection vector $w$ (in blue) to activate the signal bands for positioning from $M = 16$ available signal bands. (b) Relative gain of reflections considered in set $\mathcal{U}_{II}$, which is smaller than the one in Fig. 5.7. (c) Value of measures of dependence for time delay estimation $\varsigma(\tau_{2,1})$ (blue solid line, cf. (3.33)), measure of dependence for complex gain estimation $|s(\tau_{2,1})|$ (red dotted line, cf. (4.12)), measure of delay bias $\varrho(\alpha_{2,1}, \tau_{2,1})$ (yellow dashed line, cf. (3.42)), as a function of relative propagation distance.
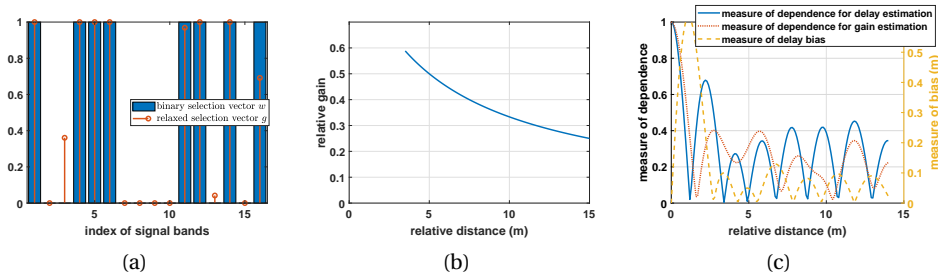


Figure 5.9: (a) Relaxed selection vector $g$ and its binary selection vector $w$ to activate the signal bands for positioning from $M = 16$ available signal bands. (b) Relative gain of reflections considered in set $\mathcal{U}_{II}$, which is larger than the one in Fig. 5.7. (c) value of measures of dependence for time delay estimation $\varsigma(\tau_{2,1})$ (blue solid line, cf. (3.33)), measure of dependence for complex gain estimation $|s(\tau_{2,1})|$ (red dotted line, cf. (4.12)), measure of delay bias $\varrho(\alpha_{2,1}, \tau_{2,1})$ (yellow dashed line, cf. (3.42)), as function of relative propagation distance.

In addition, although we aim to design a multiband ranging signal for biased estimation in this section, one can use only the ranging precision and the measure of dependence as criteria to design a ranging signal, so that the designed signal can be applied for unbiased estimation.

Here, the precision of the LoS time delay estimator is set be 0.003 m. Then, we only consider set $\mathcal{U}_I$ which contains reflections with a relative distance between 0.8 m to 30 m, and set $\mathcal{U}_{II}$ will be empty. The maximum threshold for the measure of dependence $c_\varsigma$ is set to be 0.8, which is larger than the one used in the previous examples. By solving the optimization problem, the resulting sparse multiband ranging signal and the associated measure of dependence for both time delay and carrier phase estimation are shown in Fig. 5.10.

One can also reduce the threshold for the measure of dependence $c_\varsigma$ to 0.6, which allows for a more accurate time delay estimation, compared to the exam-

(a)                                        (b)

Figure 5.10: Only considering measure of dependence with set $\mathscr{U}_I$ that contains reflections with relative distance from 1 m to 30 m, and the user specified threshold $c_\varsigma$ is set to be 0.8, (a) relaxed selection vector $\boldsymbol{g}$ and its binary selection vector $\boldsymbol{w}$ to activate the signal bands for positioning from $M = 16$ available signal bands, (b) value of measures of dependence $\varsigma(\tau_{2,1})$, $|s(\tau_{2,1})|$ (with relative gain shown in Fig. 5.7(b)), and measure of bias $\varrho(\alpha_{2,1}, \tau_{2,1})$, as a function of relative propagation distance.

ple shown in Fig. 5.10. As presented in section 3.2, a small measure of dependence will slightly reduce the ranging accuracy, when the corresponding reflection is considered in the model for time delay estimation. Fig. 5.11 shows the resulting sparse multiband signal. In order to reduce the measure of dependence, and eventually meet the user-specified requirement, more signal bands will be needed for ranging.
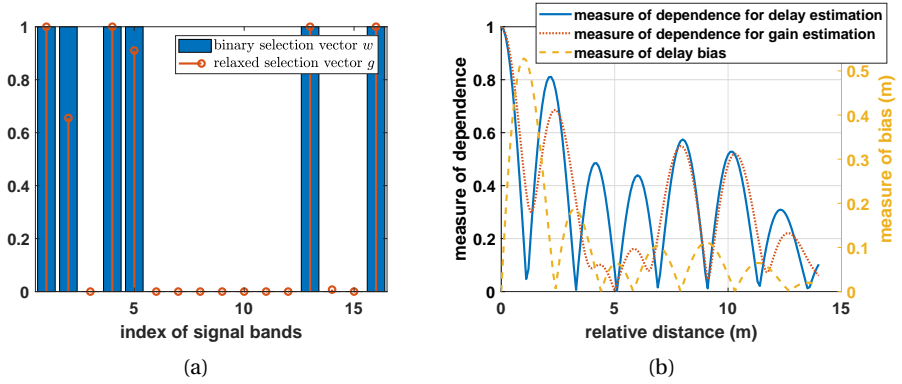


(a)                                        (b)
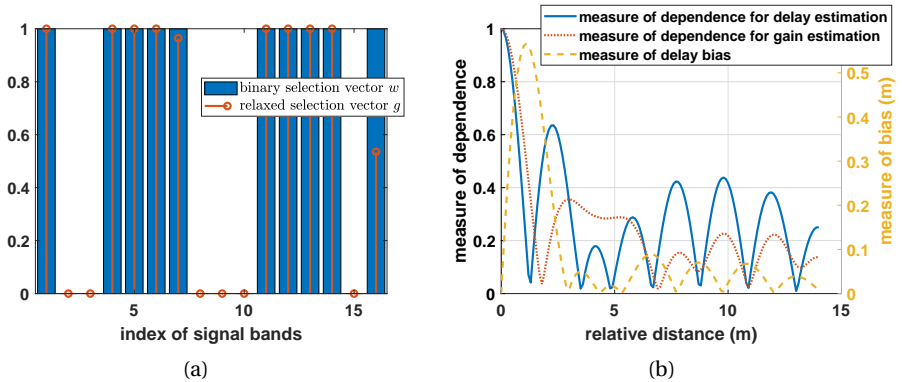
Figure 5.11: Only considering measure of dependence with set $\mathscr{U}_I$ that contains reflections with relative distance from 1 m to 30 m, and the user specified threshold $c_\varsigma$ is set to be 0.6, (a) relaxed selection vector $\boldsymbol{g}$ and its binary selection vector $\boldsymbol{w}$ to activate the signal bands for positioning from $M = 16$ available signal bands, (b) value of measures of dependence $\varsigma(\tau_{2,1})$, $|s(\tau_{2,1})|$ (with relative gain shown in Fig. 5.7(b)), and measure of bias $\varrho(\alpha_{2,1}, \tau_{2,1})$, as a function of relative propagation distance.

## 5.4. Summary

With the aim of occupying as few spectral resources as possible, and to meet user-specified ranging performance, the design of a multiband ranging signal is presented in this chapter.

Under the assumption that the spacing of any two adjacent pilot subcarriers and the spacing of any two activated signal bands are fixed, and using the same amount of total signal power, one can derive a closed-form expression for the correlation function of the multiband ranging signal. By placing constrains on the width (or curvature) of the main-lobe of the correlation function (i.e., precision, cf. (5.10)), the period of the occurrence of the main-lobe (i.e., unambiguous ranging distance, cf. (5.5)), and the amplitude of the side-lobes (i.e., resistance against multipath, cf. (5.9)), one can determine the spacing of the pilot subcarriers and the spacing of the activated signal bands for ranging. This approach of designing a multiband signal is simple and straightforward, but neither the precision nor the bias of the time delay estimator are rigorously considered. In addition, the ranging signal is designed based on the characteristics of the correlation function, which is the realization of the MF method, and the resulting ranging signal could become less optimal when reflections are considered in the model for time delay estimation.

In a multipath channel, one can jointly estimate the time delays for both the LoS path and the reflections. Assuming each signal band has the same signal bandwidth and the same pilot-pattern (i.e., a fixed unambiguous ranging distance), the design of the ranging signal becomes a problem of selecting the signal bands for ranging. Hence, one can formulate an optimization problem with an objective of using as few signal bands as possible and yet meeting the constraints of the user -specified ranging accuracy.

For purpose of unbiased estimation, the ranging signal design can be guided by the CRLB derived from multiple two-path channels with a fixed LoS path, in which the unknown parameters contain the time delay and the propagation gain for both the LoS path and the reflection. The estimator for the LoS path and the reflections are treated equally, and expected to achieve the same accuracy in the optimization (5.18). More signal bands are needed, in order to let the accuracy of the delay estimator for the weakest reflection also meet the user specified requirement.

Alternatively, if biased estimation can be accepted by the user, one can estimate the time delay for the LoS path and only a few reflections, or no reflection at all. Thereby the precision of the LoS delay estimator can be improved, and the resulting computational complexity can be reduced, compared to using the full model that considers all reflections. Then, one can design a sparse multiband ranging signal, by considering the measure of dependence and the measure of bias as the performance criteria, so that the precision will not deteriorate by considering some additional reflections in the model, and the bias can remain small when other reflections are neglected in the model.

The design is guided by the quantitative performance metrics of time delay estimation in this chapter. As shown in chapter 4, we propose to compute the car-

rier phase based on the model reconstructed by the time delay estimates. Most likely, one will use a simplified model in practice, due to computational complexity considerations and the actual number of paths in a multipath channel being unknown. If the ranging signal can offer a time delay estimator with less delay bias, it can also reduce the associated bias in the carrier phase.

**5**

# 6

# Positioning Models

Based on the designed ranging signal presented in Chapter 5, one can obtain time delay estimates (Chapter 3) and carrier phase estimates (Chapter 4) as range observables to determine the receiver position solution. In this chapter, the transmitters are assumed to be synchronized in time and frequency via the commonly distributed reference signals (i.e., 1 PPS and 10 MHz), but the receiver is not synchronized to the transmitters and runs on its own clock. Therefore, the receiver clock offset should be accommodated, in order to determine the receiver position coordinates. We presents positioning models based on the time delay estimates, and the models based on the carrier phase estimates. The time delay estimates and the carrier phase estimates are used separately for positioning. The clock offset, which is introduced by the receiver frequency offset, obtained from a time-delay-based positioning model can be used for coarse frequency offset estimation, and the one obtained from a carrier-phase-based positioning model can be used for fine frequency synchronization.

Because of the small wavelength of the central carrier, carrier phase can provide much more precise range information than time delay, but the carrier phase cycle ambiguity should be properly resolved. One can estimate the carrier phase cycle ambiguity together with the receiver position coordinates. Due to different hardware delays and initial phase offsets among transmitters, the carrier phase cycle ambiguities will no longer be integer numbers. Without calibration, one can only obtain the so-called *float* solution.

If all transmitters are frequency synchronized (hence, syntonized), one can obtain a snapshot of carrier phase measurements for all transmitters at a known location, and save them as ' corrections'. Then by taking the difference between carrier phase measurements at locations of interest and the previously acquired corrections, the integer nature of the carrier phase cycle ambiguities can be preserved, and this effectively allows for integer estimation of the ambiguities. Consequently, one can obtain the so-called *fixed* solution, which delivers high precision position solutions, and requires less receiver displacement to let the position

precision converge to centimeter level as needed with the float solution.

The carrier phase cycle ambiguity problem can be avoided, if one can accurately determine the starting position of the receiver. Then, a *relative* positioning model can be applied to determine the receiver position with respect to the known starting positioning, then the receiver displacement is effectely determined, rather than the absolute position.

Finally, we present a practical solution to determine the antenna phase center, which is essential for precise positioning. If all transmitters are equipped with the same type of antenna, in which the antenna phase center is vertically aligned with the known antenna reference point (ARP), one only needs to determine the phase center offset (PCO) in vertical direction. Based on a series of carrier phase measurements, one can estimate the vertical PCO through the relative positioning model.

## **6.1.** Positioning based on Time Delay Estimates

As presented in (3.68) and (3.69), the time-based pseudo range (i.e., based on time-of-arrival (ToA) measurements) is written by

$$
\begin{aligned}
\underline{\rho}_r^i(t) &= c\tau_r^i(t) + c\tau_{\eta,r}^i(t) + c\nabla\tau_r^i(t) + \underline{e}_r^i(t) \\
&= d_r^i + \rho_\eta(t) + \nabla\rho_r^i(t) + \underline{e}_r^i(t)
\end{aligned}
\tag{6.1}
$$

where $c$ denotes the speed of light, the superscript $i$ denotes the transmitter (Tx) index, the subscript $r$ denotes the receiver (Rx), $\underline{e}_r^i(t)$ denotes the measurement error introduced by the noise. Depending on the model for time delay estimation, the variance of $\underline{e}_r^i$ can be derived from (3.28), or (3.29). In addition, in (6.1), $\nabla\tau_r^i(t)$ contains the hardware delay in both the transmitter and the receiver and the error introduced by multipath, $\rho_\eta(t)$ denotes the accumulated clock offset (in the unit of length) over the observation period $[t_0, t]$, introduced by the frequency offset $\eta$ (cf. (2.5) and (3.67)), and is given by

$$
\rho_\eta(t) = c\int_{t_0}^t \eta(\zeta)\zeta d\zeta,
\tag{6.2}
$$

and $d_r^i$ denotes the propagation distance between the $i$-th transmitter and the receiver. In a terrestrial positioning system, as the atmospheric delays are generally negligible, the propagation distance equals to the geometric distance. By default, $\rho_\eta(t_0)$ is assumed to be 0, otherwise, the initial offset can be lumped into the time-invariant hardware delay.

Assuming that the position of the $i$-th transmitter $(x^i, y^i, z^i)$ is known a priori to the receiver, the propagation distance $d_r^i$ is written by

$$
d_r^i(t) = \sqrt{(x_r(t) - x^i)^2 + (y_r(t) - y^i)^2 + (z_r(t) - z^i)^2},
\tag{6.3}
$$

where $x_r(t)$, $y_r(t)$ and $z_r(t)$ are the unknown coordinates of the receiver at time instant $t$.

### **6.1.1.** Joint Positioning and Coarse Frequency Offset Estimation

If all transmitters are implemented by the same type of hardware, the hardware delay can be assumed to be the same for all Tx-Rx pairs. However, the error introduced by multipath, which is transmitter-dependent, will not be considered in the positioning model, and will go into the measurement error $\underline{e}_r^i$. By replacing $\nabla \tau_r^i$ in (6.1) by $\tau_h$, the pseudo-range is rewritten by

$$\underline{\rho}_r^i(t) = d_r^i(t) + \underbrace{\rho_\eta(t) + c\tau_h}_{\epsilon_r(t)} + \underline{e}_r^i(t), \tag{6.4}$$

where $\tau_h$ denotes the sum of the hardware delay in the transmitter and the receiver and is identical for all Tx-Rx pairs. In addition, as the accumulated clock offset $\rho_\eta(t)$ and the hardware delay $\tau_h$ cannot be separated in (6.4), one can only estimate their combination as $\epsilon_r(t)$ in the positioning model, which is referred to as the *pseudo-range clock offset* in this thesis.

Because the receiver coordinates are non-linearly involved in the Tx-Rx propagation distance $d_r^i(t)$ (6.3), one can determine the receiver position based on the non-linear least-squares (LS) principle. The propagation distance $d_r^i(t)$ can be linearised by the Taylor expansion with respect to the approximated receiver position $\boldsymbol{x}(t)|_0$, and given by

$$\begin{aligned} d_r^i(t) &\approx d_r^i(t)|_0 + \partial_{\boldsymbol{x}^\mathrm{T}} d_r^i(t)|_0 (\boldsymbol{x}(t) - \boldsymbol{x}(t)|_0) \\ &= d_r^i(t)|_0 + \boldsymbol{g}_r^i(t)^\mathrm{T} \Delta \boldsymbol{x}(t), \end{aligned} \tag{6.5}$$

where $\boldsymbol{x}$ contains the unknown $N_d$ dimensional coordinates of the receiver (e.g., $N_d = 2$ or 3), $(\cdot)|_0$ denotes the initial or updated approximate value in the Gauss-Newton iteration, $\boldsymbol{g}_r^i(t)$ is the transmitter-receiver geometric unit direction vector.

Considering that the system contains $K$ transmitters, and the nonlinear geometry range is linearised by the Taylor expansion, the ToA-based positioning model is given by

$$\mathbb{E}\left\{\begin{bmatrix} \Delta\underline{\rho}_r^1(t) \\ \vdots \\ \Delta\underline{\rho}_r^K(t) \end{bmatrix}\right\} = \underbrace{\begin{bmatrix} \boldsymbol{g}_r^1(t)^\mathrm{T} & 1 \\ \vdots & \vdots \\ \boldsymbol{g}_r^K(t)^\mathrm{T} & 1 \end{bmatrix}}_{\begin{bmatrix} \boldsymbol{A}_1 & \boldsymbol{A}_2 \end{bmatrix}} \begin{bmatrix} \Delta\boldsymbol{x}(t) \\ \epsilon_r(t) \end{bmatrix}, \quad \mathbb{D}\left\{\begin{bmatrix} \Delta\underline{\rho}_r^1(t) \\ \vdots \\ \Delta\underline{\rho}_r^K(t) \end{bmatrix}\right\} = \boldsymbol{Q}_{\boldsymbol{\rho}}(t)$$

$$\mathbb{E}\left\{\Delta\underline{\boldsymbol{\rho}}_r(t)\right\} = \boldsymbol{A}(t)\boldsymbol{u}(t), \tag{6.6}$$

where

$$\Delta\rho_r^i(t) = \rho_r^i(t) - d_r^i(t)|_0.$$

A good initial estimate is necessary. Otherwise, the iterative estimation process may not converge to the correct value. One can obtain an initial value to start

the iteration, for example, by the direct method which provides the a closed-form solution without any iterations [120].

Then, the unknown parameters in $\boldsymbol{u}(t)$ can be determined by

$$\hat{\boldsymbol{u}}(t) = \left(\boldsymbol{A}(t)^{\mathrm{T}}\boldsymbol{Q}_{\boldsymbol{\rho}}^{-1}(t)\boldsymbol{A}(t)\right)^{-1}\boldsymbol{A}(t)^{\mathrm{T}}\boldsymbol{Q}_{\boldsymbol{\rho}}^{-1}(t)\Delta\boldsymbol{\rho}_r(t),$$

$$\boldsymbol{Q}_{\hat{\boldsymbol{u}}(t)} = \left(\boldsymbol{A}(t)^{\mathrm{T}}\boldsymbol{Q}_{\boldsymbol{\rho}}^{-1}(t)\boldsymbol{A}(t)\right)^{-1}, \tag{6.7}$$

where $\boldsymbol{Q}_{\boldsymbol{\rho}}$ denotes the variance matrix of the ToA-based range measurement, and is assumed to be a $K$-by-$K$ diagonal matrix. For example, if the time delay is derived from the simplified model, where only a single path is considered, the variance matrix is given by

$$\left[\boldsymbol{Q}_{\boldsymbol{\rho}}\right]_{i,i} = \frac{c^2\sigma_n^2}{8\pi^2\left(\alpha_{1,r}^i\right)^2\boldsymbol{f}^{\mathrm{T}}\boldsymbol{f}}, \tag{6.8}$$

where $\boldsymbol{f}$ denotes the frequency vector that contains the frequencies of the pilot subcarriers in the activated signal bands (cf. (3.20)), $\alpha_{1,r}^i$ denotes the LoS propagation gain of the link between the $i$-th transmitter and the receiver.

Though we have assumed that all Tx-Rx pairs have the same hardware delay, in practice, these hardware delays could be different among the transmitters. As only a single receiver is used in the system, one should either carefully calibrate the hardware delay for all transmitters, or simply accept the resulting bias due to the unmodelled transmitter-dependent hardware delay. In addition, a time-invariant offset could also be introduced in the distributed reference signals (i.e., 1 PPS and 10 MHz) among the transmitters due to the different cable length, which will also be lumped into the hardware delay.

### Coarse Frequency Offset

As the change of the pseudo-range clock offset $\hat{\epsilon}_r(t)$ in (6.4) is introduced by the sampling frequency offset (SFO) originating from the normalized frequency offset (NFO). One can coarsely determine the NFO based on the pseudo-range clock offset estimates. Given a $T_D = 1\,\mathrm{ms}$ update period of the position solution (i.e., the transmission period of the ranging signal shown in Fig. 2.2), the frequency offset is assumed to be constant not only within one OFDM symbol, but also during the transmission period $T_D$ for the following analysis. Therefore, according to (6.2) and (6.4), one has

$$\hat{\epsilon}_r(nT_D)-\hat{\epsilon}_r\left((n-1)T_D\right) = \hat{\rho}_\eta(nT_D) - \hat{\rho}_\eta\left((n-1)T_D\right) = c\check{\eta}[n]T_D, \tag{6.9}$$

where the check-symbol (i.e., ˇ) is used to particularly denote the coarse estimate, $n$ denotes the index of the received ranging packet. The NFO estimate follows as the first divided difference of the pseudo-range clock offset estimates.

As the variance of the clock offset estimator $\check{\epsilon}_r[nT_D]$ is given by

$$\sigma_{\check{\epsilon}_r}^2[nT_D] = \left(\bar{\boldsymbol{A}}_2^{\mathrm{T}}[nT_D]\boldsymbol{Q}_{\boldsymbol{\rho}}^{-1}[nT_D]\bar{\boldsymbol{A}}_2[nT_D]\right)^{-1},$$

$$\bar{\boldsymbol{A}}_2 = P_{\boldsymbol{A}_1}^{\perp}\boldsymbol{A}_2 = \left(I_K - \boldsymbol{A}_2\left(\boldsymbol{A}_1^{\mathrm{T}}\boldsymbol{Q}_{\boldsymbol{\rho}}^{-1}\boldsymbol{A}_1\right)^{-1}\boldsymbol{A}_1^{\mathrm{T}}\boldsymbol{Q}_{\boldsymbol{\rho}}^{-1}\right)\boldsymbol{A}_2, \tag{6.10}$$

the variance of the coarse NFO estimator can be derived by applying the propagation law of variance,

$$\sigma_{\breve{\eta}}^2 = \frac{2\sigma_{\hat{\epsilon}_r}^2}{(cT_D)^2}. \tag{6.11}$$

As the precision of NFO estimator depends on the precision of the ToA-based ranging measurement, which is generally far worse than the one of the carrier-phase-based measurement, the estimate $\breve{\eta}$ obtained from (6.9) is referred to as the *coarse* frequency offset estimate.

As presented in section 4.3.2, one can compensate the carrier frequency offset (e.g., in Fig. 4.15) based on the coarse NFO estimate,

$$\Delta \breve{f}_c = f_c \breve{\eta}. \tag{6.12}$$

The precision of the NFO estimator can be improved by increasing the transmission period $T_D$. However, in practice, to select the transmission period $T_D$ when estimating the NFO, one should consider the stability of the clock, so that the NFO $\eta$ can be assumed to be constant during the transmission period $T_D$.

### 6.1.2. Single Differencing between Transmitters

By taking the difference between the measurements taken from the $i$-th transmitter and a pivot/reference transmitter (the $p$-th transmitter), with (6.4), one can obtain the time-difference-of-arrival (TDoA) measurement,

$$\begin{aligned} \underline{\tilde{\rho}}_r^{i,p}(t) &= \underline{\rho}_r^i(t) - \underline{\rho}_r^p(t) \\ &= d_r^i(t) - d_r^p(t) + \underline{\tilde{e}}_r^{i,p}(t), \end{aligned} \tag{6.13}$$

where

$$\underline{\tilde{e}}_r^{i,p}(t) = \underline{e}_r^i(t) - \underline{e}_r^p(t), \tag{6.14}$$

and the receiver-dependent parameter will be effectively eliminated.

For example, if one selects the first transmitter as the pivot transmitter ($p = 1$), the linearized TDoA-based positioning model becomes

$$\mathbb{E}\left\{ \begin{bmatrix} \Delta\underline{\tilde{\rho}}_r^{2,p}(t) \\ \vdots \\ \Delta\underline{\tilde{\rho}}_r^{K,p}(t) \end{bmatrix} \right\} = \begin{bmatrix} \tilde{g}_r^{2,p}(t)^{\mathrm{T}} \\ \vdots \\ \tilde{g}_r^{K,p}(t)^{\mathrm{T}} \end{bmatrix} \Delta x(t), \quad \mathbb{E}\left\{ \begin{bmatrix} \Delta\underline{\rho}_r^{2,p}(t) \\ \vdots \\ \Delta\underline{\rho}_r^{K,p}(t) \end{bmatrix} \right\} = Q_{\tilde{\rho}}, \tag{6.15}$$

where

$$\begin{aligned} \Delta\tilde{\rho}_r^{i,p}(t) &= \rho_r^i(t) - \rho_r^p(t) - d_r^i(t)|_0 + d_r^p(t)|_0, \quad i \neq p, \\ \tilde{g}_r^{i,p} &= g_r^i(t) - g_r^p(t), \quad i \neq p, \end{aligned} \tag{6.16}$$

and the variance matrix is propagated from the $Q_\rho$ in (6.6) by

$$Q_{\tilde{\rho}} = BQ_\rho B^{\mathrm{T}}, \quad B = \begin{bmatrix} -1 & 1 & 0 & \dots & 0 \\ -1 & 0 & 1 & \dots & 0 \\ \vdots & & & \vdots & \vdots \\ -1 & 0 & 0 & \dots & 1 \end{bmatrix} \in \mathbb{R}^{(K-1)\times K}.$$

Compared with the ToA-based positioning model (6.6), the total number of the available measurements in the TDoA-based positioning model (6.15) is reduced by 1, but the unknown pseudo-range clock offset is eliminated. Hence, the redundancy of (6.15) remains the same as of (6.6).

The theoretical positioning performance of using the TDoA-based model is equivalent to using the ToA-based positioning mode. However, using the TDoA-based positioning model yields less computational complexity, as less unknown parameters need to be estimated. It should be noted that if the hardware delays among the transmitters are not the same, which cannot be effectively eliminated in TDoA measurement, the solution will consequently become biased.

## 6.2. Positioning based on Carrier Phase Estimates

The properly unwrapped carrier phase measurement (i.e., phase-of-arrival (PoA) measurement) $\tilde{\Phi}$ (cf. (4.33)), obtained from an asynchronous system, is presented in unit of length as

$$\underline{\varphi}_r^i(t) = \lambda \tilde{\Phi}_r^i(t) = d_r^i(t) + c\tau_{h,r}^i + \lambda \left( \frac{\tilde{\phi}_\eta(t) + \vartheta^i - \vartheta_r}{2\pi} - N_r^i \right) + \underline{e}_r^i(t), \qquad (6.17)$$

where $\lambda$ denotes the wavelength of the central carrier $f_c$, and the hardware delay $\tau_{h,r}^i$ can be decomposed as

$$\tau_{h,r}^i = \Delta\tau_h^i + \Delta\tau_{h,r} + \frac{\lambda}{c} N_{h,r}^i, \qquad (6.18)$$

$\Delta\tau_h^i$, $\Delta\tau_{h,r}$ and $\lambda N_{h,r}^i/c$ denote the fractional part of the hardware delay in the transmitter and the receiver, and the integer part of the hardware delay, respectively. $\tilde{\phi}_\eta(t)$ (cf. (4.43)) denotes the residual accumulated carrier phase offset after coarsely compensating the CFO and is referred to as the *residual clock offset* in the carrier phase measurements, $\vartheta^i$ and $\vartheta_r$ denote the initial phase offsets from the $i$-th transmitter and the receiver, respectively. $N_r^i$ denotes the integer carrier phase cycle ambiguity of the propagation distance, and $e_r^i(t)$ contains the noise and also includes the additional error due to multipath, as not all reflections are considered in the model (4.22).

Generally, there are two approaches to tackle the phase ambiguity problem. The first approach is the so-called known-point-initialization (KPI) [20] which can be referred to as *relative positioning*. The initial position of the receiver should be accurately determined, and one only measures the displacement of the receiver with respect to this initial position, so that the carrier phase cycle ambiguity problem is avoided. Due to the strict requirement on the receiver starting position, the KPI method is less attractive in practice. The other approach is the so-called on-the-fly (OTF) approach [146, 147, 148] which can be referred to as *absolute positioning*, and one should jointly estimate the position of the receiver and the carrier phase cycle ambiguities based on a change of the positioning geometry, when only using the carrier phase measurements for positioning.

## 6.2.1. Absolute Positioning and Ambiguity-float Solution

Similar to section 6.1.2, here we first present a positioning model based on the differenced carrier phase measurement (i.e., phase-difference-of-arrival (PDoA) measurement).

By taking the so-called single difference between the measurements from two transmitters, all receiver-dependent parameters are eliminated (i.e., accumulated clock offset $\tilde{\phi}_\eta(t)$, initial receiver phase offset $\vartheta_r$, and the fractional receiver hardware delay $\Delta\tau_{h,r}$). However, the transmitter-dependent parameters, such as, the initial phase offset of the transmitter $\vartheta^i$ and the fractional transmitter hardware delay $\Delta\tau^i_{h,r}$, are still present in single differenced observables. One can arbitrarily select one of the $K$ transmitters as the *pivot transmitter* (i.e., reference transmitter), and then compute the single difference between the PoA measurement associated to the pivot transmitter $\underline{\varphi}^p_r(t)$ and the one from the $i$-th transmitter $\underline{\varphi}^i_r(t)$. In practice, one can directly compute the PDoA measurement from (4.45), so that cycle-slips will not be introduced by the receiver frequency offset in the carrier phase tracking. The PDoA measurement is given by

$$
\begin{aligned}
\underline{\tilde{\varphi}}^{i,p}_r(t) &= \underline{\varphi}^i_r(t) - \underline{\varphi}^p_r(t) \\
&= d^i_r(t) - d^p_r(t) + \lambda\left(\tilde{\mathfrak{I}}^{i,p} - \tilde{N}^{i,p}_r\right) + \underline{\tilde{e}}^{i,p}_r(t),
\end{aligned}
\tag{6.19}
$$

where $i \neq p$ and

$$
\tilde{N}^{i,p}_r = N^i_r - N^p_r - N^i_{h,r} + N^p_{h,r},
$$

$$
\tilde{\mathfrak{I}}^{i,p} = \frac{\vartheta^i - \vartheta^p}{2\pi} + f_c\left(\Delta\tau^i_h - \Delta\tau^p_h\right),
$$

$$
\underline{\tilde{e}}^{i,p}_r(t) = \underline{e}^i_r(t) - \underline{e}^p_r(t).
$$

where $\underline{\tilde{e}}^{i,p}_r$ is assumed to be complex white Gaussian distributed with the variance shown in (4.52). In addition, it should be noted that although the same symbol $\underline{\tilde{e}}^{i,p}_r$ is used to denote the TDoA (cf. (6.14)) and PDoA measurement error, they are numerically very different, and the variance of the PDoA measurement error should be much smaller than the one of the TDoA measurement error, if no cycle-slips occur.

The PDoA measurement from each transmitter-receiver pair carries its own unknown carrier phase cycle ambiguity in (6.19), and therefore a position solution cannot be obtained based on a single epoch of just carrier phase measurements, as too many unknown parameters need to be estimated. This can be overcome by stacking the carrier phase estimates from multiple time epochs, with a change of the positioning geometry in the mean time.

The transmitter-receiver range $d^i_r(t)$ can be linearized with respect to the approximated receiver position, as shown in (6.5). A good initial guess $\boldsymbol{x}(t)|_0$ is necessary, otherwise, the solution may not converge to the global minimum, when

there are multiple minima in the objective function for positioning. One can obtain an initial value based on time-delay-based range estimates, to start the iteration. First, one can use a so-called direct method [149, 80] which provides a closed-form solution without any iteration. Then, based on the position solution derived from the direct method, one can iteratively compute the position solution with a better precision based on the linearized time-delay-based positioning model (cf. (6.6) or (6.15)).

In addition, as shown in [149, 120], convergence of the iteration (e.g., Gauss-Newton) and also the bias in the position estimator depend on the quality of the observables (e.g., time delay and carrier phase). Using a large signal bandwidth, which improves the resolvability of reflections and the precision of the observables, convergence can be guaranteed and the bias introduced by linearization will be small enough for the user to accept.

To simplify notations in the positioning model, we first introduce the following definitions,

$$
\begin{aligned}
\Delta\tilde{\varphi}_r^{i,p}(t) &= \tilde{\varphi}_r^{i,p}(t) - (d_r^i(t)|_0 - d_r^p(t)|_0) \\
\tilde{N}_{r,f}^{i,p} &= \tilde{\vartheta}^{i,p} - \tilde{N}_r^{i,p}, \quad i \neq p, \quad \tilde{N}_{r,f} \in \mathbb{R}.
\end{aligned}
\tag{6.20}
$$

As the integer carrier phase cycle ambiguity $\tilde{N}_r^{i,p}$ cannot be separated from the time-invariant phase offset $\tilde{\vartheta}^{i,p}$ (they always occur pairwise), only the float and real-valued carrier phase cycle ambiguity $\tilde{N}_{r,f}^{i,p}$ can be estimated, where the subscript '$f$' indicates the float nature of the ambiguity.

Assuming that the first transmitter is selected to be the pivot transmitter ($p = 1$), the linearized positioning model based on the carrier phase estimates obtained from $K$ transmitters at two epochs $t_1$ and $t_2$ is given by

$$
\mathbb{E}\left\{\begin{bmatrix}\Delta\tilde{\boldsymbol{\varphi}}_r(t_1) \\ \Delta\tilde{\boldsymbol{\varphi}}_r(t_2)\end{bmatrix}\right\} = \begin{bmatrix}\tilde{\boldsymbol{G}}_r(t_1) & \boldsymbol{0} & \boldsymbol{\Lambda} \\ \boldsymbol{0} & \tilde{\boldsymbol{G}}_r(t_2) & \boldsymbol{\Lambda}\end{bmatrix}\begin{bmatrix}\Delta\boldsymbol{x}(t_1) \\ \Delta\boldsymbol{x}(t_2) \\ \hline \tilde{\boldsymbol{N}}_{r,f}\end{bmatrix}, \quad \mathbb{D}\left\{\begin{bmatrix}\Delta\tilde{\boldsymbol{\varphi}}_r(t_1) \\ \Delta\tilde{\boldsymbol{\varphi}}_r(t_2)\end{bmatrix}\right\} = \boldsymbol{Q}_{\tilde{\boldsymbol{\varphi}}_r} \tag{6.21}
$$

where $\boldsymbol{\Lambda} = -\lambda\boldsymbol{I}_{K-1}$, $\Delta\boldsymbol{x}(t)$ denotes the position increment vector ($\Delta\boldsymbol{x}(t) = \boldsymbol{x}(t) - \boldsymbol{x}(t)|_0$) and

$$
\begin{aligned}
\Delta\tilde{\boldsymbol{\varphi}}_r(t) &= \begin{bmatrix}\Delta\tilde{\varphi}_r^{2,p}(t) & \cdots & \Delta\tilde{\varphi}_r^{K,p}(t)\end{bmatrix}^{\mathrm{T}} \\
\tilde{\boldsymbol{G}}_r(t) &= \begin{bmatrix}\boldsymbol{g}_r^2(t)^{\mathrm{T}} - \boldsymbol{g}_r^p(t)^{\mathrm{T}} & \cdots & \boldsymbol{g}_r^K(t)^{\mathrm{T}} - \boldsymbol{g}_r^p(t)^{\mathrm{T}}\end{bmatrix}^{\mathrm{T}} \\
\tilde{\boldsymbol{N}}_{r,f} &= \begin{bmatrix}\tilde{N}_{r,f}^{2,p} & \cdots & \tilde{N}_{r,f}^{K,p}\end{bmatrix}^{\mathrm{T}}, p = 1.
\end{aligned}
$$

This positioning model is referred to as the *PDoA-based positioning model* in this thesis. The carrier phase cycle ambiguity in $\tilde{N}_{r,f}^{i,p}$ is no longer an integer number as shown in (6.20), therefore, one can only obtain the so-called ambiguity-float solution based on least-squares estimation (LSE).

With $K$ transmitters, there are $(K-1)$ PDoA measurements available at each epoch. The redundancy of the positioning model (6.21) is $r = 2(K-1)-2N_d-(K-1)$. To avoid rank-deficiency, at least $2N_d + 1$ transmitters are required to be used, so that $r \geq 0$. For example, in a 2D positioning scenario (i.e., $N_d = 2$), based on the carrier phase estimates obtained from $K = 6$ transmitters, the redundancy of the positioning model (6.21) is $r = 1$.

The PDoA-based positioning model (6.21) can be rewritten as the following partitioned model

$$\mathbb{E}\left\{\Delta\underline{\tilde{\varphi}}_r\right\} = \begin{bmatrix} A_1 & | & A_2 \end{bmatrix}\begin{bmatrix} u_1 \\ u_2 \end{bmatrix} = Au, \tag{6.22}$$

and the formal variance matrix of the estimator can be derived from

$$Q_{\hat{u}} = \left(A^{\mathrm{T}}Q_{\tilde{\varphi}_r}^{-1}A\right)^{-1} = \begin{bmatrix} Q_{\hat{u}_1} & Q_{\hat{u}_1\hat{u}_2} \\ Q_{\hat{u}_2\hat{u}_1} & Q_{\hat{u}_2} \end{bmatrix}, \tag{6.23}$$

where $Q_{\tilde{\varphi}_r}$ denotes the variance matrix of the PDoA measurements (cf. (4.52)). Particularly, the ambiguity-float position solution (with $\Delta x(t_1)$ and $\Delta x(t_2)$ in $u_1$) is given by

$$\hat{u}_1 = \left(\bar{A}_1^{\mathrm{T}}Q_{\tilde{\varphi}_r}^{-1}\bar{A}_1\right)^{-1}\bar{A}_1^{\mathrm{T}}Q_{\tilde{\varphi}_r}^{-1}\Delta\tilde{\varphi}_r, \tag{6.24}$$

where

$$\begin{aligned} \bar{A}_1 &= \mathrm{P}_{A_2}^{\perp}A_1 \\ &= \left(I_{K-1} - A_2\left(A_2^{\mathrm{T}}Q_{\tilde{\varphi}_r}^{-1}A_2\right)^{-1}A_2^{\mathrm{T}}Q_{\tilde{\varphi}_r}^{-1}\right)A_1. \end{aligned} \tag{6.25}$$

With the projector on the orthogonal complement of $A_2$ (i.e., $P_{A_2}^{\perp}$), the variance of the position solution is given by

$$Q_{\hat{u}_1} = \left(\bar{A}_1^{\mathrm{T}}Q_{\tilde{\varphi}_r}^{-1}\bar{A}_1\right)^{-1}. \tag{6.26}$$

As the precision of the position solution depends on the geometry reflected in $\bar{A}_1$ ($A_1$ contains both $\tilde{G}_r(t_1)$ and $\tilde{G}_r(t_2)$ in (6.21)), a large displacement of the receiver between $t_1$ and $t_2$ is required in order to achieve an acceptable precision. If $\tilde{G}_r(t_1) = \tilde{G}_r(t_2)$, then the design matrix in (6.21) only has a rank of $N_d + (K-1)$ rather than $2N_d + (K-1)$, and it becomes infeasible to compute a unique position solution.

As presented in (6.18) and (6.20), the hardware delay among different Tx-Rx pairs can be different. As long as the hardware delay is time invariant, it can be lumped into the constant float ambiguity $\tilde{N}_{r,f}$.

Given the PDoA-based positioning model, any unmodelled error $\nabla\tilde{\varphi}_r$ (e.g., multipath error) in the carrier phase measurement will be propagated into the ambiguity-float position solution with (6.24), through

$$\begin{aligned} \nabla\hat{u}_1 &= \left(\bar{A}_1^{\mathrm{T}}Q_{\tilde{\varphi}_r}^{-1}\bar{A}_1\right)^{-1}\bar{A}_1^{\mathrm{T}}Q_{\tilde{\varphi}_r}^{-1}\nabla\tilde{\varphi}_r \\ &= \Xi_{\mathrm{ft}}\nabla\tilde{\varphi}_r. \end{aligned} \tag{6.27}$$

In this thesis, matrix $\Xi_{\text{ft}}$ is defined as the *LSE coefficient* for the *float solution*. If the entries in $\Xi_{\text{ft}}$ are large, it gives a large amplification of noise and unmodelled errors.

### 6.2.2. Absolute Positioning and Ambiguity-fixed Solution

Generally, in a terrestrial system, the carrier phase ambiguity of the transmitter-receiver link is not an integer number, because of, among others, hardware delays and the carrier phase offsets. Without an accurate calibration, the ambiguity should be treated as a constant, real-valued, hence float number, and one can only obtain the so-called float solution. In a terrestrial positioning system, unlike the continuously moving satellites in GNSS, which automatically leads to a change of geometry, the geometry based on ground-based transmitters is generally fixed and static. Therefore, for the OTF approach, a moving receiver is needed to create a change of geometry so that the precision of the ambiguity-float solution can converge to an acceptable level. Given a certain terrestrial positioning geometry, the receiver may be required to move over a large distance in order to obtain a reasonable precision of the float solution. To relax the requirement on the change of the positioning geometry, so that the precision of the receiver position solution can quickly converge to centimeter-level, we explore the possibilities to treat the phase cycle ambiguities as integer numbers, and compute the resulting fixed solution.

To be able to exploit the integer nature of the carrier phase cycle ambiguities, the transmitter-dependent float offset should be eliminated or calibrated. Therefore, one may use the idea of PPP-RTK [2, 150], in which some offsets are provided as corrections to the user receiver. In GNSS, atmospheric errors are time and position dependent, but such error sources can be neglected in a terrestrial positioning system. As long as all transmitters are well frequency synchronized (e.g., based on WR-PTP in our SuperGPS system), and the radio transmitters are not restarted, the transmitter dependent initial phase offset $\vartheta^i$ and the fractional transmitter hardware delay $\Delta\tau_h^i$ are time-invariant.

Corrections can be taken from a single snapshot measurements set of all transmitters, and do not need to be updated in real-time, unless the transmitters are restarted or the operation condition (e.g., temperature) has changed significantly. Therefore, over a certain period, the snapshot correction file can be applied to all measurements taken from the to-be-positioned receiver. The error of the correction is neglected in this thesis, and is generally treated as a constant minor systematic effect.

#### PDoA-based Positioning Model

Here, using the ambiguous PDoA measurement $\Phi_c^{i,p}(t_c)$ (cf. (4.45)), obtained at a reference point with a known position $\boldsymbol{x}_c$ for all transmitters at time instant $t_c$, a snapshot correction file for the PDoA absolute positioning model (6.21) can be created by

$$\frac{\lambda}{2\pi}\Phi_c^{i,p}(t_c) - d_c^i(t_c) + d_c^p(t_c), \quad i \neq p. \tag{6.28}$$

As a different receiver can be used to generate the snapshot correction file, the subscript '$c$' is used in (6.28).

Next, by taking the difference between the current carrier phase estimates and the corrections, the transmitter-dependent parameters in (6.19) are eliminated. Therefore, the double difference carrier phase with the correction is given by

$$
\begin{aligned}
\underline{\varphi}^{i,p}_{r,c}(t) =& \underline{\varphi}^{i,p}_r(t) - \left(\frac{\lambda}{2\pi}\Phi^{i,p}_c(t_c) - d^i_c(t_c) + d^p_c(t_c)\right) \\
=& d^i_r(t) - d^p_r(t) + \lambda(\tilde{\mathcal{Y}^{i,p}} - \tilde{N}^{i,p}_r) - \lambda(\tilde{\mathcal{Y}^{i,p}} - \tilde{N}^{i,p}_c) + \underline{\tilde{e}}^{i,p}_r(t) \\
=& d^i_r(t) - d^p_r(t) - \lambda\tilde{\tilde{N}}^{i,p}_{r,c} + \underline{\tilde{e}}^{i,p}_r(t), \quad i \neq p,
\end{aligned}
\tag{6.29}
$$

where

$$
\begin{aligned}
\tilde{\tilde{N}}^{i,p}_{r,c} =& \tilde{N}^{i,p}_r - \tilde{N}^{i,p}_c, \quad \tilde{\tilde{N}}^{i,p}_{r,c} \in \mathbb{Z}, \\
\tilde{N}^{i,p}_c =& N^i_c - N^p_c - N^i_{h,c} + N^p_{h,c}.
\end{aligned}
$$

Now, in (6.29), the carrier phase cycle phase ambiguity $\tilde{\tilde{N}}^{i,p}_{r,c}$ remains as an integer number.

Similar to (6.21), the position solution can be obtained through the model based on the carrier phase obtained from $K$ transmitters at two different epochs with a change in geometry. The double differenced positioning model (between the transmitters, and between the measurements and the corrections) is now given by

$$
\mathbb{E}\left\{\begin{bmatrix}\Delta\underline{\tilde{\boldsymbol{\varphi}}}_{r,c}(t_1) \\ \Delta\underline{\tilde{\boldsymbol{\varphi}}}_{r,c}(t_2)\end{bmatrix}\right\} = \begin{bmatrix}\tilde{\boldsymbol{G}}_r(t_1) & \boldsymbol{0} & \boldsymbol{\Lambda} \\ \boldsymbol{0} & \tilde{\boldsymbol{G}}_r(t_2) & \boldsymbol{\Lambda}\end{bmatrix}'\begin{bmatrix}\Delta\boldsymbol{x}(t_1) \\ \Delta\boldsymbol{x}(t_2) \\ \tilde{\tilde{\boldsymbol{N}}}_{r,c}\end{bmatrix} \quad \mathbb{D}\left\{\begin{bmatrix}\Delta\underline{\tilde{\boldsymbol{\varphi}}}_{r,c}(t_1) \\ \Delta\underline{\tilde{\boldsymbol{\varphi}}}_{r,c}(t_2)\end{bmatrix}\right\} = \boldsymbol{Q}_{\tilde{\boldsymbol{\varphi}}_r}, \tag{6.30}
$$

where the first transmitter is selected as the pivot transmitter (i.e., $p = 1$), and

$$
\begin{aligned}
\Delta\tilde{\boldsymbol{\varphi}}_{r,c}(t) =& \begin{bmatrix}\Delta\tilde{\varphi}^{2,p}_{r,c}(t) & \dots & \Delta\tilde{\varphi}^{K,p}_{r,c}(t)\end{bmatrix}^{\mathrm{T}} \\
\Delta\tilde{\varphi}^{i,p}_{r,c}(t) =& \tilde{\varphi}^{i,p}_{r,c}(t) - (d^i_r(t)|_0 - d^p_r(t)|_0) \\
\tilde{\tilde{\boldsymbol{N}}}_{r,c} =& \begin{bmatrix}\tilde{\tilde{N}}^{2,p}_{r,c} & \dots & \tilde{\tilde{N}}^{K,p}_{r,c}\end{bmatrix}^{\mathrm{T}}.
\end{aligned}
$$

Now, the carrier phase cycle ambiguities in $\tilde{\tilde{\boldsymbol{N}}}_{r,c}$ with integer nature can be fixed (i.e., estimated specifically as integers) using the LAMBDA method [146, 151]. With carrier phase integer ambiguity resolution, one can obtain high-precision ambiguity-fixed position solutions.

Similarly, positioning model (6.30) can be rewritten as the following partitioned model,

$$
\mathbb{E}\left\{\Delta\underline{\tilde{\boldsymbol{\varphi}}}_{r,c}\right\} = \begin{bmatrix}\boldsymbol{A}_1 & | & \boldsymbol{A}_2\end{bmatrix}\begin{bmatrix}\boldsymbol{u}_1 \\ \boldsymbol{u}_2\end{bmatrix} = \boldsymbol{A}\boldsymbol{u}, \tag{6.31}
$$

where $\boldsymbol{u}_1$ contains the unknown receiver positions at $t_1$ and $t_2$, and $\boldsymbol{u}_2$ contains the unknown integer phase cycle ambiguities. If the ambiguities in $\tilde{\boldsymbol{N}}_{r,c}$ are properly and reliably fixed into integer numbers $\check{\boldsymbol{u}}_2$[1], they can be practically set into a known vector in (6.31). The position solution is then determined under the condition of the ambiguities being known, and the conditioned position solution (i.e., the fixed solution) is given by [152]

$$\check{\boldsymbol{u}}_{1|\boldsymbol{u}_2=\check{\boldsymbol{u}}_2} = \hat{\boldsymbol{u}}_1 - \boldsymbol{Q}_{\hat{\boldsymbol{u}}_1\hat{\boldsymbol{u}}_2}\boldsymbol{Q}_{\hat{\boldsymbol{u}}_2}^{-1}(\hat{\boldsymbol{u}}_2 - \check{\boldsymbol{u}}_2),\tag{6.32}$$

By neglecting the randomness of $\check{\boldsymbol{u}}_2$, the variance matrix of the conditioned position solution is given by

$$\boldsymbol{Q}_{\hat{\boldsymbol{u}}_1|\hat{\boldsymbol{u}}_2} = \boldsymbol{Q}_{\hat{\boldsymbol{u}}_1} - \boldsymbol{Q}_{\hat{\boldsymbol{u}}_1\hat{\boldsymbol{u}}_2}\boldsymbol{Q}_{\hat{\boldsymbol{u}}_2}^{-1}\boldsymbol{Q}_{\hat{\boldsymbol{u}}_2\hat{\boldsymbol{u}}_1}.\tag{6.33}$$

Note that strictly speaking, $\check{\boldsymbol{u}}_2$ is random and not deterministic, and the conditioned variance, given in (6.33), provides an optimistic description of the performance of the ambiguity-fixed solution. For the correct description of the probability density function (PDF) of the ambiguity-fixed solution, the reader is referred to [152, 153].

Based on (6.33), any unmodelled error in the carrier phase measurement $\nabla\tilde{\boldsymbol{\varphi}}_{r,c}$ will propagate into the fixed solution through

$$\begin{aligned}\nabla\check{\boldsymbol{u}}_{1|\boldsymbol{u}_2=\check{\boldsymbol{u}}_2} &= \left(\left(\bar{\boldsymbol{A}}_1^{\mathrm{T}}\boldsymbol{Q}_{\tilde{\boldsymbol{\varphi}}_r}^{-1}\bar{\boldsymbol{A}}_1\right)^{-1}\bar{\boldsymbol{A}}_1^{\mathrm{T}}\boldsymbol{Q}_{\tilde{\boldsymbol{\varphi}}_r}^{-1} - \boldsymbol{Q}_{\hat{\boldsymbol{u}}_1\hat{\boldsymbol{u}}_2}\boldsymbol{Q}_{\hat{\boldsymbol{u}}_2}^{-1}\left(\bar{\boldsymbol{A}}_2^{\mathrm{T}}\boldsymbol{Q}_{\tilde{\boldsymbol{\varphi}}_r}^{-1}\bar{\boldsymbol{A}}_2\right)^{-1}\bar{\boldsymbol{A}}_2^{\mathrm{T}}\boldsymbol{Q}_{\tilde{\boldsymbol{\varphi}}_r}^{-1}\right)\nabla\tilde{\boldsymbol{\varphi}}_{r,c} \\ &= \boldsymbol{\Xi}_{\mathrm{fx}}\nabla\tilde{\boldsymbol{\varphi}}_{r,c},\end{aligned}\tag{6.34}$$

where

$$\bar{\boldsymbol{A}}_2 = \mathrm{P}_{\boldsymbol{A}_1}^{\perp}\boldsymbol{A}_2,\tag{6.35}$$

and the complementary projection matrix has been defined in (6.25). It should be noted that the error $\nabla\tilde{\boldsymbol{\varphi}}_{r,c}$ propagated into $\hat{\boldsymbol{u}}_2$ is assumed here to stay within the pull-in region of integer least-squares estimate $\check{\boldsymbol{u}}_2$, and will not cause an incorrect integer fixing [150].

The conditioned positioning model with the fixed ambiguities has a redundancy of $r = 2(K-1) - 2N_d$, and is larger than the one from the unconditioned model (6.21) with the float solution (i.e., $r = 2(K-1) - 2N_d - (K-1)$). Consequently, with the fixed ambiguities, the model becomes stronger.

## PoA-based Positioning Model
In this subsection, instead of taking the single difference between the carrier phase measurements from two transmitters to eliminate the clock offset, one can jointly

---

[1]Note that the check-symbol ( $\check{}$ ) now denotes the estimate with integer nature, which is no longer used to denote the coarse estimate for the frequency offset as in section 6.1. But the hat-symbol will again be used to denote the coarse estimate in section 7.4.4, when frequency offset estimation is again introduced.

estimate the position coordinates and the clock offset using the PoA measurements. Therefore, the positioning model proposed in this subsection is referred to as the *PoA-based positioning model*. Additionally, we apply the corrections to preserve the integer nature of the carrier phase cycle ambiguities, which is generated by

$$\frac{\lambda}{2\pi}\Phi_c^i(t_c) - d_c^i(t_c), \quad i = 1, \dots, K, \tag{6.36}$$

it is the carrier phase observed at time $t_c$, corrected for the known distance between the transmitter-$i$ and the receiver-$c$ at that time.

By taking the difference between the PoA measurement (6.17) and the corrections (6.36), one will have

$$
\begin{aligned}
\underline{\varphi}_{r,c}^i(t) &= \underline{\varphi}_r^i(t) - \left(\frac{\lambda}{2\pi}\Phi_c^i(t_c) + d_c^i(t_c)\right) \\
&= d_r^i(t) + \lambda\frac{\tilde{\phi}_\eta(t) - \tilde{\phi}_\eta(t_c) - \vartheta_r + \vartheta_c}{2\pi} + c\left(\tau_{h,r}^i - \tau_{h,c}^i\right) - \lambda(N_r^i - N_c^i) + \underline{e}_r^i(t) \\
&= d_r^i(t) + \lambda\tilde{\vartheta}_{r,c}(t)/2\pi - \lambda\tilde{N}_{r,c}^i + \underline{e}_r^i(t),
\end{aligned}
\tag{6.37}
$$

where, with (6.18)

$$
\begin{aligned}
\tilde{\vartheta}_{r,c}(t) &= \tilde{\phi}_\eta(t) - \tilde{\phi}_\eta(t_c) - \vartheta_r + \vartheta_c + \frac{2\pi c}{\lambda}\left(\Delta\tau_{h,r} - \Delta\tau_{h,c}\right) \\
\tilde{N}_{r,c}^i &= N_r^i - N_c^i + N_{h,r}^i - N_{h,c}^i,
\end{aligned}
$$

$\vartheta_c$ denotes the receiver initial phase offset in the correction file,and the randomness of the corrections is neglected. $\vartheta_c$ can be different from $\vartheta_r$, as a different type of receiver can be used to produce the correction file, or the same receiver but which has been restarted in the meantime.

According to (6.37), every transmitter-receiver link carries its own phase ambiguity, therefore, the PoA measurements taken from at least two epochs, with a change in geometry, are required. Moreover, the phase ambiguity $\tilde{N}_{r,c}^i$ cannot be separated from $\tilde{\vartheta}_{r,c}(t)$, which is a receiver-dependent and time-variant parameter. The positioning model will be rank-defect, if all ambiguities and the clock offset are to be estimated at the same time. However, rank-deficiencies can be identified and removed by defining a singularity-basis (i.e., $S$-basis) according to the $S$-theory [154, 155].

One can select one of the transmitters as the pivot transmitter, and combine $\tilde{\vartheta}_{r,c}(t)$ and the phase ambiguity of the pivot transmitter into one unknown parameter. Then, the carrier phase ambiguities for the other transmitters are estimated as the difference with respect to the ambiguity of the pivot transmitter.

Similarly, based on the Taylor expansion, the observable in the following linearized positioning model is given by

$$\Delta\varphi_{r,c}^i(t) = \varphi_{r,c}^i(t) - d_r^i(t)|_0.$$

The PoA-based positioning model, in which the first transmitter is selected as the pivot transmitter (i.e., $p = 1$), is now given by

$$
\mathbb{E}\left\{\begin{bmatrix}\Delta\underline{\boldsymbol{\varphi}}_{r,c}(t_1)\\\Delta\underline{\boldsymbol{\varphi}}_{r,c}(t_2)\end{bmatrix}\right\} = \begin{bmatrix}\boldsymbol{G}_r(t_1) & \boldsymbol{0} & -\lambda\boldsymbol{1}_K & \boldsymbol{0} & | & \boldsymbol{\Omega}\\\boldsymbol{0} & \boldsymbol{G}_r(t_2) & \boldsymbol{0} & -\lambda\boldsymbol{1}_K & | & \boldsymbol{\Omega}\end{bmatrix}\begin{bmatrix}\Delta\boldsymbol{x}(t_1)\\\Delta\boldsymbol{x}(t_2)\\\tilde{\delta}_r^{p=1}(t_1)\\\tilde{\delta}_r^{p=1}(t_2)\\\hline\tilde{\tilde{\boldsymbol{N}}}_r\end{bmatrix}
$$
(6.38)

$$
\mathbb{D}\left\{\begin{bmatrix}\Delta\underline{\boldsymbol{\varphi}}_{r,c}(t_1)\\\Delta\underline{\boldsymbol{\varphi}}_{r,c}(t_2)\end{bmatrix}\right\} = \boldsymbol{Q}_{\boldsymbol{\varphi}_r},
$$

where $K$-by-$(K-1)$ matrix $\boldsymbol{\Omega}$ is derived from matrix $-\lambda\boldsymbol{I}_K$ with its first column removed,

$$
\begin{aligned}
\Delta\boldsymbol{\varphi}_{r,c}(t) &= \begin{bmatrix}\Delta\varphi_{r,c}^1(t) & \cdots & \Delta\varphi_{r,c}^K(t)\end{bmatrix}^{\mathrm{T}}\\
\boldsymbol{G}_r(t) &= \begin{bmatrix}\boldsymbol{g}_r^1(t)^{\mathrm{T}} & \cdots & \boldsymbol{g}_r^K(t)^{\mathrm{T}}\end{bmatrix}^{\mathrm{T}}\\
\tilde{\delta}_r^p(t) &= \tilde{N}_{r,c}^p - \tilde{\vartheta}_{r,c}(t)/2\pi, \quad p = 1\\
\tilde{\tilde{\boldsymbol{N}}}_r &= \begin{bmatrix}\tilde{\tilde{N}}_r^2 & \cdots & \tilde{\tilde{N}}_r^K\end{bmatrix}^{\mathrm{T}}\\
\tilde{\tilde{N}}_r^i &= \tilde{N}_{r,c}^i - \tilde{N}_{r,c}^p, \quad i \neq p.
\end{aligned}
$$
(6.39)

Both the accumulated clock offset $\tilde{\vartheta}_{r,c}(t)$ (cf. (6.4)) in the PoA measurement and the pseudo-range clock offset $\epsilon_r(t)$ in the ToA measure are caused by the NFO (cf. (2.5)). However, $\tilde{\vartheta}_{r,c}(t)$ is different from $\epsilon_r(t)$, , as part of the frequency offset can have been compensated in $\tilde{\vartheta}_{r,c}(t)$. As one can only compute the residual frequency offset from $\tilde{\delta}_r^p(t)$, $\tilde{\delta}_r^p(t)$ is referred to as the *residual clock offset* in this thesis. To avoid rank deficiency, a change of geometry is required, so that $\boldsymbol{G}_r(t_1)$ and $\boldsymbol{G}_r(t_2)$ in (6.38) are different.

The positioning model (6.38) can be rewritten as the following partitioned model

$$
\mathbb{E}\left\{\Delta\underline{\boldsymbol{\varphi}}_{r,c}\right\} = \begin{bmatrix}\boldsymbol{A}_1 & | & \boldsymbol{A}_2\end{bmatrix}\begin{bmatrix}\boldsymbol{u}_1\\\boldsymbol{u}_2\end{bmatrix} = \boldsymbol{A}\boldsymbol{u}.
$$
(6.40)

Note that $\boldsymbol{A}_1, \boldsymbol{A}_2, \boldsymbol{u}_1$ and $\boldsymbol{u}_2$ are different from the ones used in section 6.2.1. Here, $\boldsymbol{u}_1$ contains the unknown receiver position and the residual clock offset at $t_1$ and $t_2$, and $\boldsymbol{u}_2$ contains the carrier phase cycle ambiguities with integer nature. Consequently, the float solution can be computed by

$$
\hat{\boldsymbol{u}} = \left(\boldsymbol{A}^{\mathrm{T}}\boldsymbol{Q}_{\boldsymbol{\varphi}_r}^{-1}\boldsymbol{A}\right)^{-1}\boldsymbol{A}^{\mathrm{T}}\boldsymbol{Q}_{\boldsymbol{\varphi}_r}^{-1}\Delta\boldsymbol{\varphi}_{r,c},
$$
(6.41)

with the formal variance matrix

$$
\boldsymbol{Q}_{\hat{\boldsymbol{u}}} = \left(\boldsymbol{A}^{\mathrm{T}}\boldsymbol{Q}_{\boldsymbol{\varphi}_r}^{-1}\boldsymbol{A}\right)^{-1},
$$
(6.42)

where $Q_{\varphi_r}$ denotes the variance matrix of the PoA measurements (cf. (4.20) or (4.31)).

Using the correction, as shown in (6.37), the integer nature of the carrier phase ambiguity is preserved, and the LAMBDA method can be used to compute the integer carrier phase ambiguities $\check{u}_2$. Then, the fixed position solution can be computed through (6.32).

Similar to (6.33), one can derive an optimistic variance matrix to describe the precision of the ambiguity fixed solution,

$$
\begin{aligned}
Q_{\hat{u}_1|\hat{u}_2} &= Q_{\hat{u}_1} - Q_{\hat{u}_1\hat{u}_2}Q_{\hat{u}_2}^{-1}Q_{\hat{u}_2\hat{u}_1} \\
&= \left(A_1^{\mathrm{T}}Q_{\varphi_{r,c}}^{-1}A_1\right)^{-1}.
\end{aligned}
\tag{6.43}
$$

Then, the variance of the position solution follows as

$$
\begin{aligned}
Q_{\Delta\hat{x}(t_1)} &= \left[Q_{\hat{u}_1|\hat{u}_2}\right]_{1:N_d,1:N_d} \\
Q_{\Delta\hat{x}(t_2)} &= \left[Q_{\hat{u}_1|\hat{u}_2}\right]_{(N_d+1):2N_d,(N_d+1):2N_d} \\
\sigma^2_{\hat{\delta}_r^p(t_1)} &= \left[Q_{\hat{u}_1|\hat{u}_2}\right]_{(2N_d+1),(2N_d+1)} \\
\sigma^2_{\hat{\delta}_r^p(t_2)} &= \left[Q_{\hat{u}_1|\hat{u}_2}\right]_{(2N_d+2),(2N_d+2)},
\end{aligned}
\tag{6.44}
$$

where $N_d$ denotes the dimension of the receiver solution (i.e., $N_d = 2$ or 3).

In addition, one can use the LSE coefficient $\Xi_{\mathrm{ft}}$ and $\Xi_{\mathrm{fx}}$, which can be found in a similar way as (6.27) and (6.34), to analyze the sensitivity of the positioning model to the unmodelled error.

### 6.2.3. Relative Positioning

Using the carrier phase measurements for positioning, the highest accuracy of the solution can be achieved when the carrier phase cycle ambiguities are correctly fixed to integer numbers. By computing the difference between the current PoA measurement and the PoA measured at a known starting position (i.e., the KPI method), time-invariant parameters (such as carrier phase cycle ambiguity, initial phase offset, and hardware delay) can be eliminated. Then, we effectively measure a *change* in position and clock offset. Hence, we can only obtain a *relative* position solution, with respect to the known starting position.

Compared to the positioning models introduced in the previous subsections, the phase ambiguity problem is avoided in the relative positioning model, and less unknown parameters need to be estimated. Consequently, the relative positioning model has more redundancy. The position error of using the relative positioning model can be used to verify the quality of the ground truth of the receiver position as it evolves during the experiment, which will be introduced in chapter 7.

Based on (6.17), the observable for the PoA-based relative positioning model

is given by

$$
\begin{aligned}
\underline{\tilde{\varphi}}_r^i(t) &= \underline{\varphi}_r^i(t) - \underline{\varphi}_r^i(t_0) \\
&= d_r^i(t) - d_r^i(t_0) + \lambda \frac{\tilde{\phi}_\eta(t) - \tilde{\phi}_\eta(t_0)}{2\pi} + \underline{e}_r^i(t) - \underline{e}_r^i(t_0),
\end{aligned}
\tag{6.45}
$$

where $\tilde{\phi}_\eta(t)$ (cf. (4.43)) denotes the residual accumulated carrier phase offset after coarsely compensating the CFO, and $d_r^i(t_0)$ denotes the known distance between the $i$-th transmitter and the receiver at the starting epoch $t_0$.

Consequently, the relative positioning model for an asynchronous receiver is now given by

$$
\mathbb{E}\left\{\Delta \underline{\tilde{\boldsymbol{\varphi}}}_r\right\} = \begin{bmatrix} \Delta \tilde{\varphi}_r^1(t) \\ \vdots \\ \Delta \tilde{\varphi}_r^M(t) \end{bmatrix} = \begin{bmatrix} \boldsymbol{G}_r(t) & \lambda \mathbf{1}_K \end{bmatrix} \begin{bmatrix} \Delta \boldsymbol{x}(t) \\ \delta_r(t) \end{bmatrix}, \quad \mathbb{D}\left\{\Delta \underline{\tilde{\boldsymbol{\varphi}}}_r\right\} = \boldsymbol{Q}_{\tilde{\boldsymbol{\varphi}}_r},
\tag{6.46}
$$

where

$$
\begin{aligned}
\Delta \tilde{\varphi}_r^i(t) &= \tilde{\varphi}_r^i(t) + d_r^i(t_0) - d_r^i(t)|_0 \\
\delta_r(t) &= \frac{\tilde{\phi}_\eta(t) - \tilde{\phi}_\eta(t_0)}{2\pi},
\end{aligned}
$$

and $\delta_r(t)$ represents the *change* of the residual clock offset from epoch $t_0$ onward, expressed in cycles.

Let $\boldsymbol{a} = \lambda \mathbf{1}_K$, the variance of the receiver position solution and the residual clock offset are given by

$$
\begin{aligned}
\boldsymbol{Q}_{\Delta \hat{\boldsymbol{x}}} &= \left(\bar{\boldsymbol{G}}_r^{\mathrm{T}} \boldsymbol{Q}_{\tilde{\boldsymbol{\varphi}}_r}^{-1} \bar{\boldsymbol{G}}_r\right)^{-1}, \quad \bar{\boldsymbol{G}}_r = P_{\boldsymbol{a}}^{\perp} \boldsymbol{G}_r, \\
\sigma_{\hat{\delta}_r}^2 &= \left(\bar{\boldsymbol{a}}^{\mathrm{T}} \boldsymbol{Q}_{\tilde{\boldsymbol{\varphi}}_r}^{-1} \bar{\boldsymbol{a}}\right)^{-1}, \quad \bar{\boldsymbol{a}} = P_{\boldsymbol{G}_r}^{\perp} \boldsymbol{a}.
\end{aligned}
\tag{6.47}
$$

### 6.2.4. Fine Frequency Offset Estimation

Similarly, one can estimate the frequency offset based on the change of the clock offset. Based on the PoA-based positioning model (6.38), one can keep the measurement $\Delta \underline{\tilde{\boldsymbol{\varphi}}}_{r,c}(t_1)$ constant in the model, and update the measurement $\Delta \underline{\tilde{\boldsymbol{\varphi}}}_{r,c}(t_2)$ as time elapses. Then, $\hat{\tilde{\delta}}_r^p(t_1)$ in (6.38) contains the clock offset at the starting epoch $t_1$, while $\hat{\tilde{\delta}}_r^p(t_2)$ contains the *change* of the clock offset from $t_1$ onward. Hence, one can estimate the residual CFO based on a series of $\hat{\tilde{\delta}}_r^p(t_2)$ obtained from the PoA-based positioning model. Alternatively, the residual CFO can be determined based on a series of residual clock offset estimates $\hat{\delta}_r(t)$ obtained from the relative positioning model (cf. (6.46)).

Given a $T_D = 1$ ms update interval of the position solution, we assume that the CFO is constant not only within one OFDM symbol, but also during the transmission period in the following analysis. Therefore, according to (6.38) and (4.43),

one has

$$\overset{\approx p}{\delta}_r[nT_D] - \overset{\approx p}{\delta}_r[(n-1)T_D] = \frac{1}{2\pi}\left(\hat{\bar{\phi}}_\eta[nT_D] - \hat{\bar{\phi}}_\eta[(n-1)T_D]\right) \approx \Delta\hat{\bar{f}}_c[nT_D]T_D, \quad (6.48)$$

where

$$\Delta\tilde{f}_c[nT_D] = \Delta f_c[nT_D] - \Delta\check{f}_c[nT_D], \quad (6.49)$$

the check-symbol ( $\check{}$ ) is again used to denote the coarse frequency offset estimate, and $\Delta\check{f}_c[nT_D]$ denotes the coarse carrier frequency offset (cf. (6.12)), which is treated as a deterministic value in compensating the phase rotation due to the carrier frequency offset (e.g., see Fig. 4.15).

Based on the propagation law of variances, the variance of the fine carrier frequency offset is given by

$$\sigma^2_{\Delta\hat{\bar{f}}_c} = \frac{\sigma^2_{\overset{\approx p}{\delta}_r[nT_D]} + \sigma^2_{\overset{\approx p}{\delta}_r[(n-1)T_D]}}{(T_D)^2}, \quad (6.50)$$

where $\sigma^2_{\overset{\approx p}{\delta}_r}$ denotes the optimistic variance of the ambiguity-fixed residual offset obtained from the PoA-based positioning model (cf. (6.44)). Noted that if the residual clock offset is derived based the relative positioning model, its variance in (6.50) should then be replaced by $\sigma^2_{\hat{\bar{\delta}}_r}$ (cf. (6.47)). As the variance $\sigma^2_{\overset{\approx p}{\delta}_r}$ is much smaller than $\sigma^2_{\hat{\epsilon}_r}$ (cf. (6.10)), the resulting $\Delta\hat{\bar{f}}_c$ is referred to as the *fine* carrier frequency estimate.

The residual CFO is estimated based on $\overset{\approx p}{\delta}_r(t_2)$ through the carrier-phase-based positioning model. The frequency range of the residual CFO that can be estimated, is determined by the update rate of the clock offset $\overset{\approx p}{\delta}_r[nT_D]$ (i.e., $\pm 1/2T_D$), which is much finer than the one using the shortened Moose's symbol (see section 4.3.2) that depends on the subcarrier spacing (i.e., $\pm\Delta f$).

Finally, combining the coarsely estimated CFO $\Delta\check{f}_c$, which can be based on the shortened Moose's symbol or the ToA-based positioning model, with the fine CFO estimate $\Delta\hat{\bar{f}}_c$, the ultimate CFO is given by

$$\Delta\hat{f}_c[nT_D] = \Delta\check{f}_c[nT_D] + \Delta\hat{\bar{f}}_c[nT_D]. \quad (6.51)$$

## 6.3. Determination of Antenna Phase Center

In order to accurately compute the receiver position solution, the position of the transmitter antennas should be properly measured. In addition, to determine the receiver position of interest, the electro-magnetic (EM) phase center of the receiver antenna should also be measured. However, the actual phase center of the antenna is generally unknown and should be therefore accurately determined. In practice, one could only measure a specific physical antenna reference point (ARP) marked a priori by the user on the antenna, as shown in Fig. 6.1. The ARP

is marked along the $z$-direction and central to the horizontal plate of the antenna. We assume that the actual phase center of the antenna is at the center and along the $z$-direction (i.e., the antenna is assumed to be rotationally symmetric). Therefore, we should determine the phase center offset (PCO) $\Delta z_p$ between the ARP and the actual phase center. Due to the different elevation angles, given the dimension of the physical product, a sub-centimeter offset may still occurs, which is referred to as the phase center variation (PCV). As the PCV is generally much smaller than the unknown phase center offset $\Delta z_p$, typically at mm-level [156]), it is neglected in our system.

Here, the same type antenna [157] is used for both the transmitters and receiver, so their PCOs can be assumed to be the same. The receiver and the transmitters are fully synchronized in time and frequency. In addition, as shown in Fig. 6.1, the antenna for the transmitter is facing down to the ground, and the antenna of the receiver is facing up to the ceiling/sky. The ARP position of each transmitter will be determined through a professional land-surveying total station. Then, an offset of $\Delta z_p$ in the vertical direction should be estimated and calibrated.
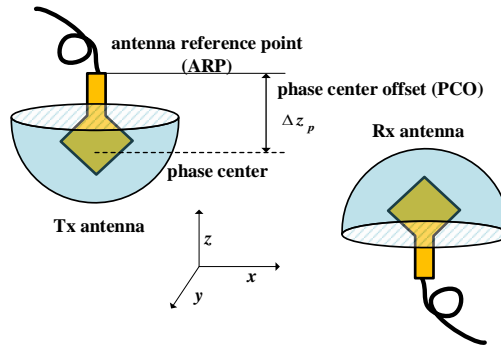


Figure 6.1: Antenna set-up for determination of phase center offset (PCO): the transmitter (Tx) antenna is facing down to the ground, the receiver (Rx) antenna is facing up to the ceiling/sky. The locations of the antennas are determined through a total station by measuring the antenna reference point (ARP). Therefore,after accounting for these positions, there is an offset of $\Delta z_p$ in the vertical (i.e., $z$) direction.

The position of the ARP on the $i$-th Tx-antenna $(x^i, y^i, z^i)$ is known a priori to the user, and the staring position of the ARP on the Rx antenna $(x_r(t_0), y_r(t_0), z_r(t_0))$ is also known a priori based on measurements from the total station. Additionally, the Rx antenna height and $z_r$ are assumed to be constant throughout an experiment. Then, the propagation distance $d_r^i(t)$ should be written by

$$d_r^i(t) = \sqrt{\left(x_r(t) - x^i\right)^2 + \left(y_r(t) - y^i\right)^2 + \left(z_r(t) + \Delta z_p - \left(z^i - \Delta z_p\right)\right)^2}, \qquad (6.52)$$

in which the unknown parameters are the PCO $\Delta z_p$, and the 2D receiver position (i.e., $x_r(t)$ and $y_r(t)$).

As the carrier phase can provide much more precise range information than the time delay, we use the carrier phase here to estimate both the 2D position of the receiver (i.e., $x$ and $y$ coordinates) and the antenna PCO $\Delta z_p$ in $z$-direction. To avoid having to solve for carrier phase cycle ambiguities, a relative positioning model is applied for PCO estimation. Hence, we only measure a *change* of the receiver position in the relative positioning model, with the a priori measured starting position of the ARP on the receiver at $t_0$. Hence, the difference between two carrier phase estimates $\tilde{\varphi}_r^i$ (cf. (6.45)), obtained from the same transmitter at two different epochs in time with a change in geometry, becomes the observation for the relative positioning model.

It is assumed that the receiver is synchronized to the transmitters, otherwise, the clock offset need to be estimated. Now, the relative positioning model based on $K$ transmitters, in which the PCO $\Delta z_p$ is jointly estimated along with the 2D receiver position, is given by

$$\mathbb{E}\left\{\Delta\underline{\tilde{\varphi}}(t)\right\} = \begin{bmatrix} \tilde{\varphi}_r^1(t) + d_r^1(t_0) - d_r^1(t)|_0 \\ \vdots \\ \tilde{\varphi}_r^K(t) + d_r^K(t_0) - d_r^K(t)|_0 \end{bmatrix} = \boldsymbol{G}(t)\boldsymbol{u}(t)$$

$$= \begin{bmatrix} \partial_{x_r}d_r^1(t)|_0 & \partial_{y_r}d_r^1(t)|_0 & \partial_{\Delta z_p}d_r^1(t)|_0 - \partial_{\Delta z_p}d_r^1(t_0)|_0 \\ \vdots & \vdots & \vdots \\ \partial_{x_r}d_r^K(t)|_0 & \partial_{y_r}d_r^K(t)|_0 & \partial_{\Delta z_p}d_r^K(t)|_0 - \partial_{\Delta z_p}d_r^K(t_0)|_0 \end{bmatrix} \begin{bmatrix} \Delta x_r(t) \\ \Delta y_r(t) \\ \Delta \tilde{z}_p \end{bmatrix} \qquad (6.53)$$

$$\mathbb{D}\left\{\Delta\underline{\tilde{\varphi}}(t)\right\} = \boldsymbol{Q}_{\tilde{\varphi}},$$

where

$$\begin{aligned} \Delta x_r &= x_r - x_r|_0 \\ \Delta y_r &= x_r - y_r|_0 \\ \Delta \tilde{z}_p &= \Delta z_p - \Delta z_p|_0 \end{aligned} \qquad (6.54)$$

and $(\cdot)|_0$ denotes the initial or updated approximate value in Gauss-Newton iteration, $\Delta x_r(t)$, $\Delta y_r(t)$ and $\Delta \tilde{z}_p$ denotes the increment with respect to the approximate value in the Gauss-Newton iteration; $\tilde{\varphi}_r^i$ denotes the difference of the carrier phase obtained at two different epochs ($t_0$ and $t$) from the same transmitter (cf. (6.45)). In order to estimate the PCO $\Delta z_p$, a change in geometry is required. Otherwise, the rank of the design matrix in (6.53) will be 2, as all elements in the last column are zero.

The variance matrix of the estimators is given by

$$\boldsymbol{Q}_{\hat{\boldsymbol{u}}}(t) = \left(\boldsymbol{G}(t)^\mathrm{T}\boldsymbol{Q}_{\tilde{\varphi}}^{-1}(t)\boldsymbol{G}(t)\right)^{-1}, \qquad (6.55)$$

the variance of the phase center offset $\hat{z}_p$ is derived as follows

$$\sigma_{\Delta\hat{z}_p}^2(t) = [\boldsymbol{Q}_{\hat{\boldsymbol{u}}}(t)]_{3,3}. \qquad (6.56)$$

As the PCO is a time-invariant parameter, it can be recursively averaged based on a series of carrier phase estimates taken at different epochs. Without considering

the co-variance among the PCO estimates, the recursive solution of the ordinary average is given by

$$\Delta\hat{\hat{z}}_p[nT_D] = \Delta\hat{\hat{z}}_p[(n-1)T_D] + \frac{1}{n}\left(\Delta\hat{z}_p[nT_D] - \Delta\hat{\hat{z}}_p[(n-1)T_D]\right), \qquad (6.57)$$

where the double-hat-symbol (i.e., $\hat{\ }$) denotes the recursive estimate.

## **6.4.** Summary

In this chapter, assuming that all transmitters are synchronized in time and frequency, and the receiver runs on its own clock, we present both the time-delay-based and carrier-phase-based positioning models, as well as an approach to determine the antenna phase center offset.

First, as presented in section 6.1, using the time-of-arrival (ToA) measurement, one can jointly estimate the receiver position coordinates and the common clock offset for all Tx-Rx links. With a series of clock offset estimates based on time delay measurements, one can coarsely determine the receiver oscillator frequency offset. Alternatively, one can use the time-difference-of-arrival (TDoA) measurement for positioning, so that the clock offset gets eliminated. The clock offset is assumed to be a receiver-dependent parameter (i.e., identical for all Tx-Rx links). If the transmitters are not well synchronized in time (e.g., due to different hardware delays), which is not considered in the positioning model, the resulting solution will become biased.

Then, the carrier-phase-based positioning model is presented. As the transmitters are fixed and static in a terrestrial system, to create a diversity of geometry, the receiver needs to move during the observation period when only using the carrier phase for positioning. Hence, in section 6.2, the positioning models are developed based on carrier phase measurements obtained from two different epochs, and a change in geometry occurred in between.

On the one hand, one can use phase-of-arrival (PoA) measurements for positioning. However, the receiver frequency offset should be coarsely compensated (for example, based on the coarse frequency estimate using the ToA measurement) to avoid cycle-slips, as presented in section 4.3. Due to different phase biases among the transmitters, the carrier phase ambiguity should be treated as a real-valued float number, and one can only obtain the so-called float solution, which could require a large receiver displacement to let the solution converge to an acceptable precision. Similarly, with a series of clock offset estimates based on carrier phase measurements and obtained along with the receiver position solution and the ambiguities, a fine receiver frequency offset estimate can be obtained with high precision.

On the other hand, if all transmitters are frequency synchronized (i.e., syntonized), one can use phase-difference-of-arrival (PDoA) measurements for positioning. As the clock offset introduced by the receiver frequency offset is eliminated, a large transmission period $T_D$ can be applied in the system.

In order to exploit the integer nature of the carrier phase cycle ambiguity and allow for a fast convergence of the position solution, we propose to use a correc-

tion file, based on snapshot phase measurements for all transmitters taken at a known position. After accounting for the phase biases in this way, one can retrieve the integer nature of the carrier phase ambiguity, and obtain the so-called fixed solutions, which largely relaxes the requirement on receiver displacement. Additionally, a relative positioning model with a known starting position is introduced, which is stronger as the phase ambiguity problem is avoided (the ambiguities are absent from the model, as long as no cycle slips occur), and it can be used to indicate the quality of the ground truth used in the experiment in chapter 7.

Lastly, the determination of the antenna phase center offset (PCO) is presented in section 6.3. Assuming that both the transmitters and the receiver use the same type of antenna, and the PCO occurs along the vertical-axis, one can measure the antenna reference point (ARP) a priori for all transmitters and the receiver at the starting position. In addition, the height of the receiver is assumed to be constant during the experiments. Then, using the carrier-phase-based relative positioning model, in which the carrier phase cycle ambiguities are eliminated, one can estimate the PCO based on a series of carrier phase measurements.

**6**

# 7

# Experimental Results

Experimental results are presented in this chapter. First, an indoor laboratory experiment was carried out to determine the antenna phase center offset. Then, the setup of the SuperGPS prototype system is introduced for outdoor experiments. Afterwards, based on time delay measurement, the performance of positioning and of coarse frequency offset estimation are presented. Finally, using carrier phase measurement, the performance of the ambiguity-float solution, and the ambiguity-fixed solutions when applying corrections are presented to account for different initial phase offsets among the transmitters, as wells as the performance of fine frequency offset estimation.

## 7.1. Antenna Phase Center

In order to determine the antenna phase center offset (PCO), as discussed in section 6.3, an experiment was conducted in the lab. The associated experimental setup and the experimental results are presented in this section. As shown in Fig. 7.1, the experimental system contained 6 transmitters (Txs), which were placed in a 5 m-by-5 m area. A receiver was placed on a rail, and operated in a stop-and-go mode, so that the receiver moved and stopped at each of the reference points on the rail for a few seconds. The position of the transmitter antenna reference point (ARP) , the receiver ARP at the starting point, and the position of the reference points were determined by the total station (see Fig. 7.2(a)). The height of the receiver is assumed to be constant and is known for this experiment.

In addition, all transmitters and the receiver are synchronized in time and frequency through the common reference signal (i.e., 1 PPS and 10 MHz) from OctoClock [158], which is a clock distribution module from Ettus Research™. Each transmitter transmits its ranging signal, as shown in Fig. 2.2, in a time-division scheme on a central carrier of 3500 MHz. As the receiver moved very slowly in this experiment (a few centimeters per second), the transmission period $T_D$ was set to be 250 ms.
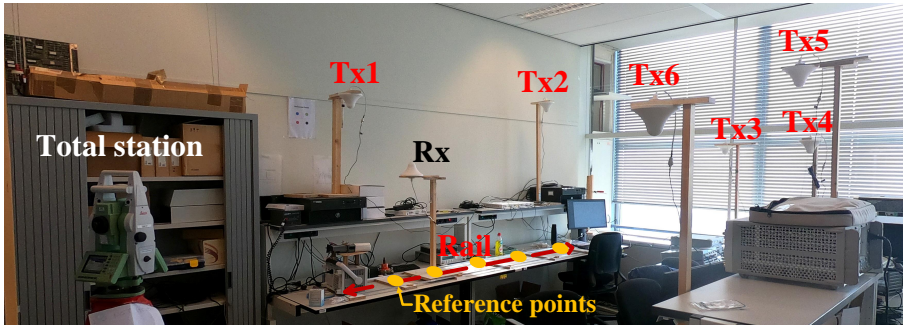
Figure 7.1: Experimental setup for determination of antenna phase center in lab (TU Delft, EEMCS), which contains six transmitters and one receiver. The receiver was moved on a rail, and was operated in stop-and-go mode. Positions of transmitter antennas and 5 reference points on the rail were determined by a total station.
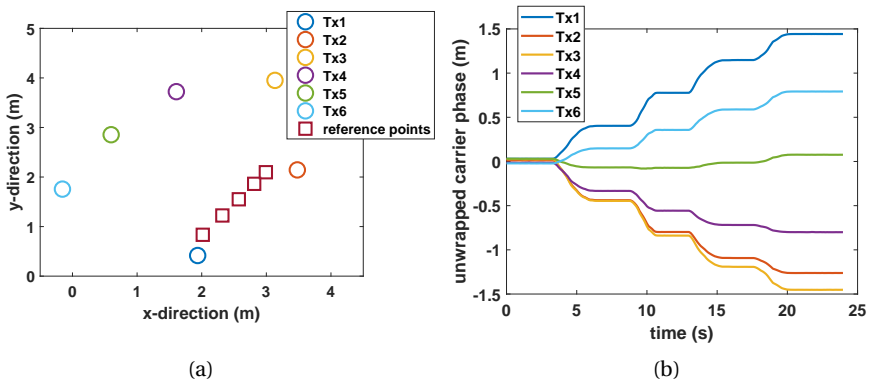


(a)                                                                (b)

Figure 7.2: (a) Geometry of experimental setup shown in Fig. 7.1. (b) Unwrapped carrier phase (in unit of length) obtained from six transmitters, in which receiver was synchronized to transmitters, and was operated in stop-and-go mode.

Based on the received ranging signal, a simplified model (cf. (3.35) and (4.22)) is used, in which only a single path is considered for both time delay and carrier phase estimation. In addition, the time delay estimate in the reconstruction design matrix (4.21) for carrier phase estimation was updated only every 1 second. The unwrapped carrier phase measurements (in unit of length) are shown in Fig. 7.2(b). As the receiver operated in stop-and-go mode, the figure of the resulting unwrapped carrier phase measurements, as a function of time, looks like a series of steps.

Fig. 7.3 shows the 2D receiver position solutions, based on the relative positioning model (6.53), in which a change in the positioning geometry is needed, in order to estimate the PCO. Hence, we only present the position solution based on the measurements taken from the 4-th second onward, as before the receiver
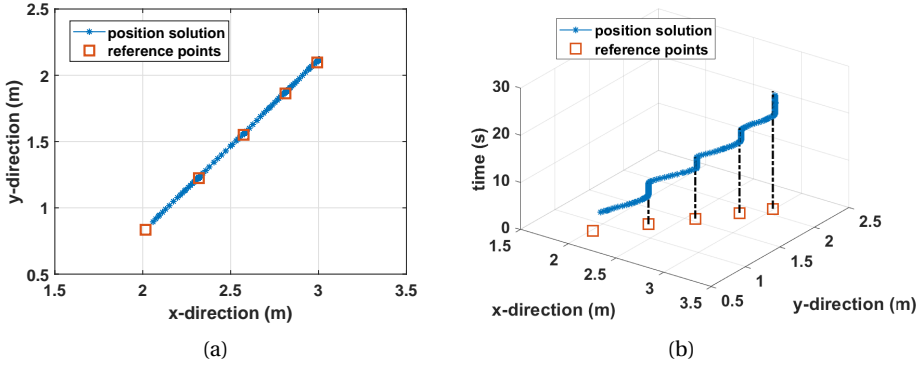
Figure 7.3: (a) Horizontal relative position solution based on (6.53). (b) Horizontal position solution versus measurement time.

stayed at the first reference point (also see Fig. 7.2(b)). According to the results shown in Fig. 7.3(b) and Table. 7.1, when the receiver stopped at the reference points, the position solutions are generally aligned with the ground truth, and the root-mean-square-error (RMSE) of the position solution is less than 2.08 cm.

Table 7.1: Root-mean-square-error (RMSE) of position solutions at reference point 2,3,4 and 5 (see Fig. 7.1, and Fig. 7.3(b)), based on relative positioning model (6.53). The receiver stopped at each of points for a few second, and the measurement update rate is 4 Hz.

| point | 2 | 3 | 4 | 5 |
|---|---|---|---|---|
| RMSE-x (cm) | 0.03 | 0.59 | 0.60 | 0.94 |
| RMSE-y (cm) | 0.45 | 1.52 | 1.72 | 2.08 |

Within a single run, all time-differenced carrier phase measurements are computed with reference to the starting epoch $t_0$. Therefore, the error in the carrier phase measurement taken at $t_0$ manifests itself as a minor systematic bias. Then, Fig. 7.4 shows the PCO estimate. Here, the PCO can be determined by epoch-by-epoch estimation (cf. (6.53)) and recursive average (cf. (6.57)). In epoch-by-epoch estimation, the PCO is estimated at each epoch, based on the time differenced carrier phase measurements. In recursive average, under the assumption that the PCO $\Delta z_p$ is a time-invariant parameter, the PCO estimate is updated using a time series of measurements. There is a variation of 2 cm in the PCO estimate derived from epoch-by-epoch estimation, which could be introduced by multipath, as only the simplified model is applied here for carrier phase estimation, and could also be introduced by a small change in the receiver antenna height during the movement (as the height was assumed to be constant and known for a 2D positioning scenario). By applying recursive estimation, the precision can be improved. Here, the antenna PCO derived by the estimate resulting at the end of the recursion, is 8.04 cm, which will be used in other experiments that will be introduced in the following sections.
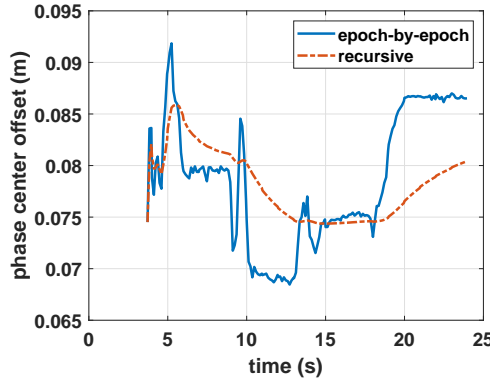
Figure 7.4: Antenna phase center offset (PCO) estimate. In epoch-by-epoch estimation, measurements taken from two epochs are used, and the measurement taken at epoch $t_0$ is kept fixed in (6.53), and will not be updated. Based on epoch-by-epoch estimates, the PCO, assumed to be time invariant, can also be recursively averaged through (6.57).

## 7.2. Setup of SuperGPS Prototype System

In this section, the setup of the SuperGPS prototype system is briefly introduced. For more details, the reader can refer to [159, 160, 161]. In our system, all transmitters and the receiver are implemented based on the Ettus X310 Universal Software Radio Peripheral (USRP), which supports a maximum sampling frequency of 200 MSps with an effective bandwidth of 160 MHz. Time-frequency reference signals (i.e., 1 PPS and 10 MHz) are generated by a central atomic clock, which is located at VSL (the Dutch national metrology institute), a few kilometers away from the test-site, and distributed to the so-called timing nodes over an optical glass fiber connection via WR-PTP (see Fig. 7.5). By connecting the USRPs to the timing nodes, which extract the time and frequency reference signals, all radio transmitters are synchronized at a level of about 100 picoseconds [77].
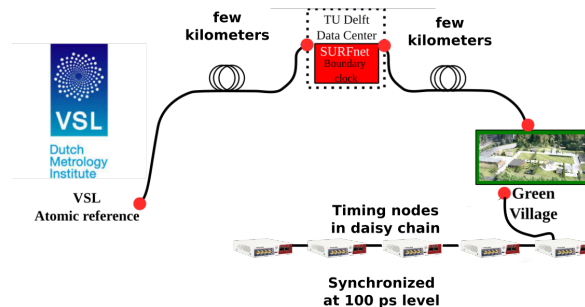


Figure 7.5: Time-frequency reference signals propagate (bidirectionally over a single fiber) from a central atomic clock at VSL, through SURFnet/TU Delft optical infrastructure, to the five timing nodes installed at The Green Village test-site [159].

The transmitters and the receiver were all equipped with the same type of antenna [157], and the phase center offset (PCO) of 8.04 cm (see section 7.1) was calibrated before. The position of the transmitters are determined by a land-surveying total station. The positioning geometry of the experimental terrestrial positioning system is shown in Fig. 7.8, and there are $K = 6$ transmitters installed on lampposts along the road in an area of 20-by-50 meters. Tx-2 and Tx-3 were implemented in one USRP through two different channels, and were synchronized by the second timing node shown in Fig. 7.5. Tx-1, 4, 5 and 6 were implemented independently by 4 USRPs, and were synchronized independently by the remaining 4 timing nodes as shown in Fig. 7.5.
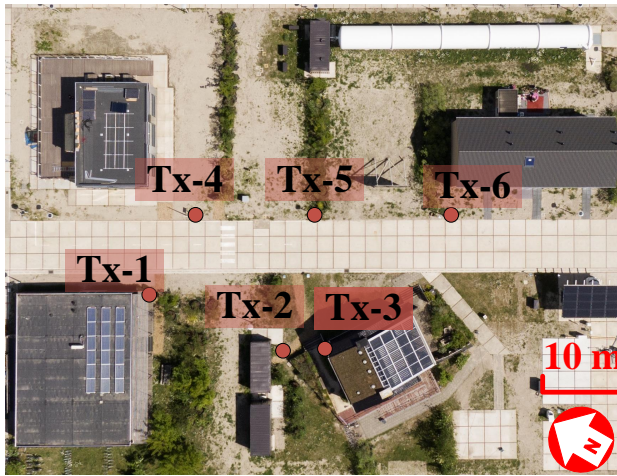


Figure 7.6: Outdoor experimental setup with $K = 6$ transmitters (aerial photo from The Green Village [162]).

The transmitters were installed on lampposts or attached to the roof of building, for example, as shown in Fig. 7.7(a). Additionally, Fig. 7.7(b) shows the antenna height of all six transmitters. As the heights of all six transmitters are very close, within a small area, the elevation angle of the received signal from each transmitter will be similar and small,by which the up-coordinate is very poorly estimable. On the other hand, the area for experiments in The Green Village (see Fig 7.6) is flat, and the receiver moving on this area did not experience a significant change in height. Hence, in the following section, we only consider a 2 dimensional (2D, $N_d$=2) positioning scenario. The height of the receiver is assumed to be known and constant throughout of the experiments, and only the horizontal position coordinates in local East and North directions are estimated.

For experiments and demonstration of the proof-of-concept of the terrestrial positioning system, a frequency band of 160 MHz with a central carrier $f_c$ at 3960 MHz has temporarily been licensed by the Radiocommunications Agency Nether-

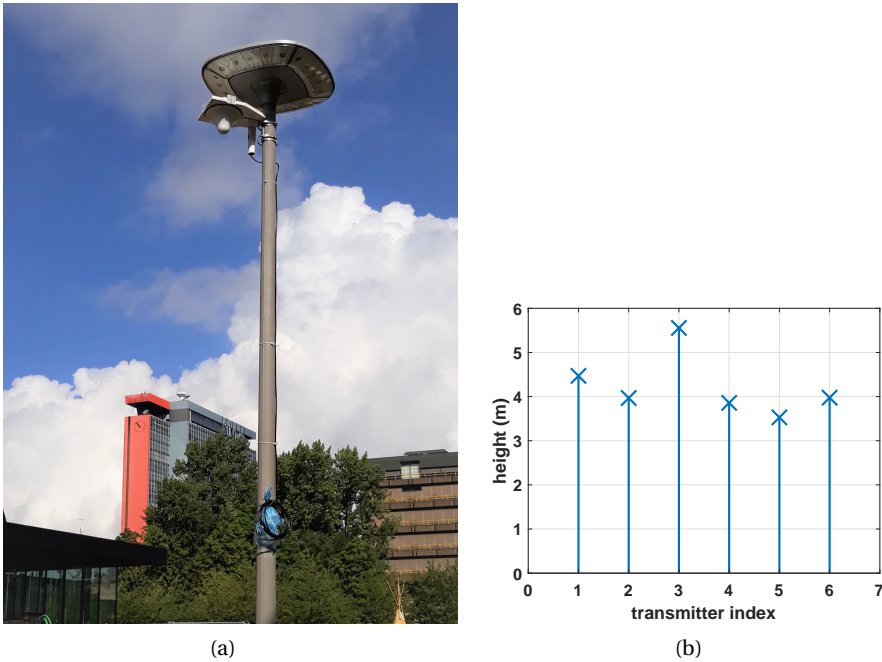(a)                                                                        (b)

Figure 7.7: (a) Example of installation of transmitter antenna in lamppost. (b) Overview of antenna height of all six transmitters.

lands (Agentschap Telecom). The burst-like OFDM packet, as shown in Fig. 2.4, is used as a ranging signal in the current system. By default, $M = 16$ signal bands, each with a 10 MHz bandwidth, are used for ranging, and each signal band contains $N_{\text{sc}} = 64$ subcarriers. In addition, as shown in Fig. 2.2, each transmitter periodically transmits its own ranging signal burst every $T_D = 1$ ms. Therefore, the update frequency of the time delay and carrier phase measurement, and resulting position solution is 1 kHz. The ranging signals from all six transmitters are transmitted within an interval of 142.1 $\mu$s, and the receiver displacement and the change of the frequency offset within this period can be neglected. Some key parameters of the experimental system setup are summarized in Table. 7.2.

Table 7.2: Key parameters of SuperGPS prototype system.

| parameters | value |
|---|---|
| central frequency | 3960 MHz |
| total bandwidth | 160 MHz |
| duration of ranging packet | 142.1 $\mu$s |
| update period of ranging packet | 1 ms |
| modulation of ranging signal | OFDM |
| number of transmitters | 6 |
| multiplexing | TDM |
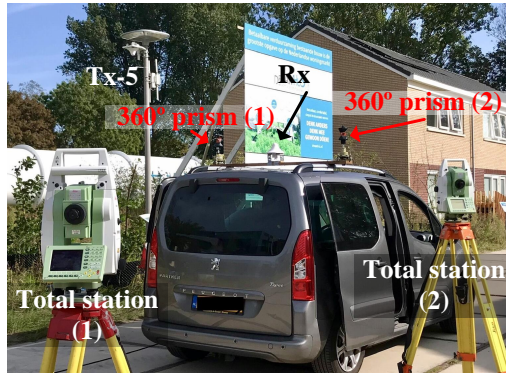
(a)



(b)

Figure 7.8: (a) The receiver antenna is mounted on the roof of a vehicle, and two 360° prisms were mounted sideways. (b) The white receiver antenna is attached to a trolley, and two 360° prisms were also attached to the trolley at different heights. The two prisms were tracked separately by two total stations, and these positions are used as ground-truth of the moving receiver (Rx).

The setup of the receiver and the determination of its ground truth is shown in Fig. 7.8. The receiver antenna was attached to a trolley to realize a (slowly) moving vehicle, or also directly installed on the roof of a vehicle . Two prisms were also attached to the trolley at different heights, and they were tracked independently by two robotized professional land-surveying total stations for determination of the ground truth of the trajectory of the receiver. The total station measures the angles and the distance with an update rate of typically between 1 Hz to 10 Hz. Like in [135], a piece-wise linear LSE with a moving window over 5 points is used, per coordinate direction, to reconstruct the ground truth of the receiver positions. By estimating offset and slope, the positions of the prisms are interpolated at a rate of 1 kHz (for example, as shown in Fig. 7.9(a)). The two total stations are not synchronized. The time lag between the two total stations is retrieved by shifting one of the time series trajectories, until the motion patterns of the two trajectories are best matched (the receiver was operated in a stop-and-go mode). After aligning the trajectories of the two prisms in time, one can estimate the corresponding po-

sition of the receiver antenna by trilateration, as the distances between the prisms and the receiver antenna have been measured a priori.

To justify the quality of the reconstructed ground truth, one can retrieve the distance between the two prisms based on their interpolated trajectories, and compare it with the a priori measured distance (by ruler). Fig. 7.9 shows the difference, from which one can conclude that the error in the reconstructed ground-truth is at the centimeter level. Additionally, to justify the performance of the estimated position solution of the SuperGPS-system, one can compute the position error with respect to the ground-truth. The time lag between the position solution and the interpolated ground-truth should also be best-matched, as the receiver and the total stations are not synchronized.



(a)                                                   (b)
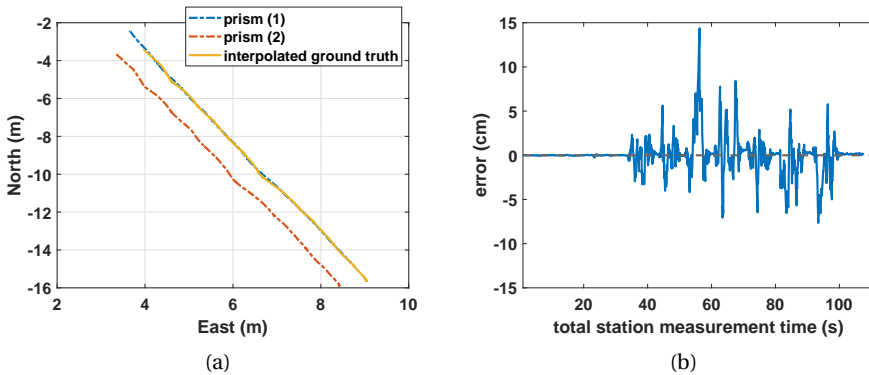
Figure 7.9: Example: interpolated trajectories of two prisms and reconstructed ground truth value for receiver antenna, and update period is the same as transmission period $T_D$ = 1 ms. (a) Receiver antenna was attached to trolley as shown in Fig. 7.8(b). Trajectories of two prisms are shown in dashed-line, and reconstructed receiver trajectory is shown in solid-line (in yellow). (b) Difference between the a priori measured (by ruler) distance between two prisms, and the distance retrieved from the interpolated trajectories. The RMSE is 1.91 cm.

## 7.3. Positioning Performance Based on Time Delay Estimates

In this section, the positioning performance only based on the time delay measurement (i.e., time-of-arrival (ToA) measurement) is presented. We first consider a receiver, which was synchronized (in time and frequency) to the transmitters by using an additional timing node. Hence, we can also analyze the performance of coarse frequency offset estimation, as ideally there should not be any change in the pseudo-range clock offset. In addition, the results of using an asynchronous receiver, which runs on its own clock, is also presented. Finally, as introduced in chapter 5, instead of using all available bandwidth (i.e., 160 MHz), we only occupy a few signal bands within a large virtual signal bandwidth for ranging, and accordingly present the resulting positioning performance.

### 7.3.1. Synchronized Receiver

Here, a synchronized receiver is considered, of which the antenna was attached to the trolley as shown in Fig. 7.8(b). The receiver operated in a stop-and-go mode, thereby stopped at each of a few reference points for a few seconds.

All 160 MHz of bandwidth is used for time delay estimation, and only a single path is considered in the simplified model (3.27). Fig. 7.10 shows the pseudo-range measurements (i.e., ToA measurements) for 6 Tx-Rx pairs. Due to the un-calibrated hardware delay, the pseudo-range distance is much larger than the actual propagation distance (less than 50 m). In addition, as the receiver was synchronized to the transmitters, the pseudo-range measurement is expected to be constant when the receiver stopped at those reference points.
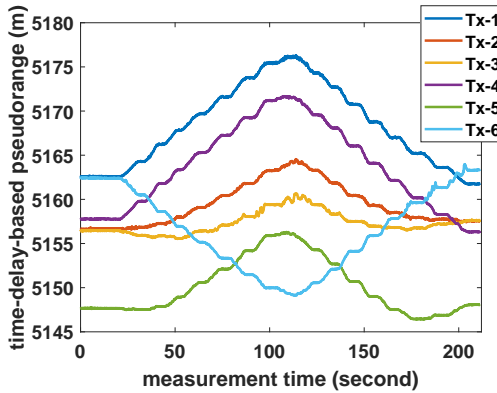


Figure 7.10: Time-delay-based pseudorange measurements for six Tx-Rx pairs, using a synchronized receiver operated in a stop-and-go mode.

By applying the ToA-based positioning model (6.6), and under the assumption that all Tx-Rx pairs have the same hardware delay that is lumped into the receiver pseudo-range clock offset $\epsilon_r(t)$, the receiver position solutions and the ground truth values determined by the total station are shown in Fig. 7.11(a). By computing the difference between the position solutions and the associated ground truth values, the empirical cumulative distribution function (CDF) of the position error is shown in Fig. 7.11(b).

According to the results shown in Fig. 7.11, the position solution is obviously biased mainly in East-direction. As the bias seems approximately time-invariant, it could be that there is a time-invariant bias in the time-delay-based pseudo-range measurement from one or more Tx-Rx pairs. To inspect the potential biases in the measurements, we directly compute the difference between the pseudo-range measurement and the ground truth propagation distance. With (6.1), and assuming that the accumulated clock offset $\rho_\eta(t)$ equals to 0 when using a synchronized receiver, we have

$$\underline{\rho}_r^i(t) - d_r^i(t) = d_r^i(t) + \rho_\eta(t) + \nabla \rho_r^i(t) - d_r^i(t) + \underline{e}_r^i$$
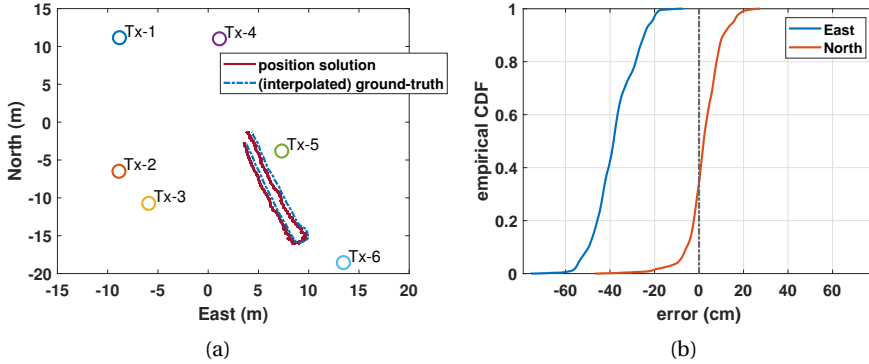$$= \nabla \rho_r^i(t) + \underline{e}_r^i, \tag{7.1}$$

(a)

(b)

Figure 7.11: (a) Positioning geometry, ground truth receiver trajectory (dashed line) and the receiver position solutions (solid line). (b) Empirical cumulative distribution function (CDF) of position error in East and North directions. Root-mean-square-error (RMSE) in East and North direction are 39.07 cm and 8.02 cm, respectively.

where $\nabla \rho_r^i(t)$ contains the hardware delay and the multipath error as no reflection is considered in the model for time delay estimation, and also the error in the ground truth values. Fig. 7.12(a) shows error $\nabla \rho_r^i(t)$ as a function of time, and the errors presented in Fig. 7.12 are offset by

$$\nabla \bar{\rho}_r^{1,2,3,4} = \frac{1}{4} \sum_{i=1}^{4} \text{avg} \left\{ \nabla \rho_r^i(t) \right\}, \tag{7.2}$$

where $\text{avg}\{\cdot\}$ denotes the average operation over a series of measurements. According to the experimental result shown in Fig. 7.12(a), $\nabla \bar{\rho}_r^{1,2,3,4}$ is set to be 17.1562 $\mu$s (5143.3 m in unit of length).

The residuals in the pairs with Tx1, 2, 3 and 4 are relatively close, but the residual errors in the pairs with Tx-5 and Tx-6 are consistently larger than the ones in other pairs, which can be the result of a different hardware delay. One can determine these offsets by

$$\Delta \nabla \bar{\rho}_r^i = \text{avg} \left\{ \nabla \rho_r^i(t) \right\} - \nabla \bar{\rho}_r^{1,2,3,4}, \quad i = 5, 6. \tag{7.3}$$

As shown in Fig. 7.12, the offset $\Delta \nabla \bar{\rho}_r^5$ is 1.4713 ns, and the offset $\Delta \nabla \bar{\rho}_r^6$ is 1.8771 ns. It should be noted that the cause of this offset in pairs with Tx-5 and Tx-6 requires further investigation. Likely it is introduced because the 10 MHz reference signals in the time nodes are not well aligned with 1 PPS reference signal. This offset causes an apparently constant effect as long as the timing nodes and the connected USRPs are not restarted. For comparison, Fig. 7.12(b) shows the residual errors for another run measured at a different time, and the results are similar to the ones shown in Fig. 7.12(a). The timing offsets in the pairs with Tx5 and Tx6 seem quite consistent.
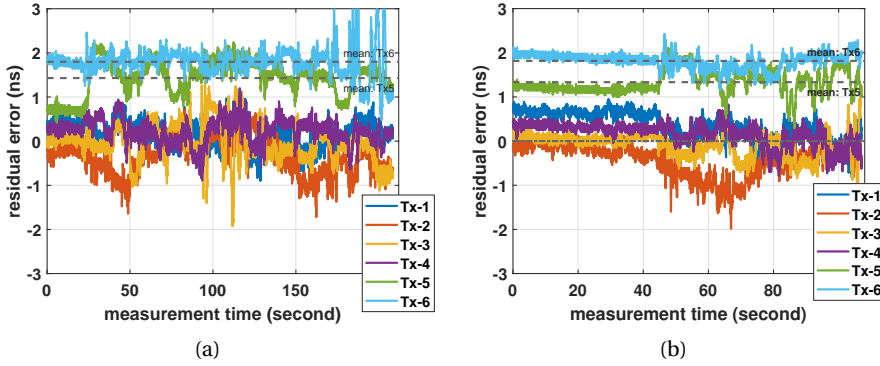
Figure 7.12: (a) Difference between the time-of-arrival measurement and the ground-truth propagation time delay, offset by 17.1562 $\mu$s (the average residual error $\nabla \bar{\rho}_r^{1,2,3,4}$ of Tx-1,2,3 and 4). The residual errors of the link with Tx-5 ($\Delta\nabla\bar{\rho}_r^5$) and Tx-6 ($\Delta\nabla\bar{\rho}_r^6$) are much larger than the others, and averages are 1.4713 ns (44.41 cm) and 1.8771 ns (56.27 cm). (b) Residual errors computed for another run, where $\nabla\bar{\rho}_r^{1,2,3,4}$ is 17.1559 $\mu$s, $\Delta\nabla\bar{\rho}_r^5$ and $\Delta\nabla\bar{\rho}_r^6$ are 1.3342 ns and 1.8157 ns, respectively.

In the following processing, we calibrate the system by removing the offsets $\Delta\nabla\bar{\rho}_r^5$=44.41 cm and $\Delta\nabla\bar{\rho}_r^6$=56.27 cm in the pseudo-range measurements taken from Tx-5 and Tx-6, respectively. Fig. 7.13 shows the receiver position solution after calibration. Compared with the solutions shown in Fig. 7.11(a), the solutions shown in Fig. 7.13(a) are clearly less biased.
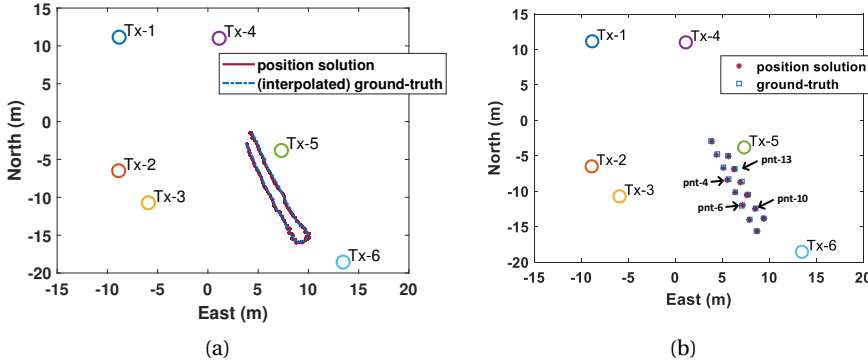


Figure 7.13: (a) Receiver position solution after removing the offsets $\Delta\nabla\bar{\rho}_r^5$ and $\Delta\nabla\bar{\rho}_r^6$ from pseudo-range measurements taken from Tx-5 and Tx-6, respectively. (b) Receiver position solution on 14 static reference points, and associated ground truth values.

Fig. 7.14 shows the position error of the entire trajectory in the East and North direction, and the empirical CDF. After calibration of the timing offsets for the measurements taken from Tx-5 and Tx-6, the receiver position solutions become

less biased, and the RMSE in East and North direction are 9.75 cm and 9.64 cm. The position error is mainly caused by multipath, as only a single path considered in the simplified model for time delay estimation.
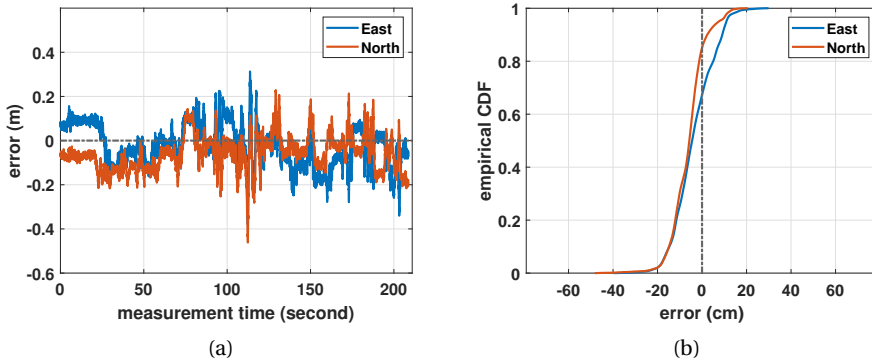


(a)                                                                      (b)

Figure 7.14: (a) Position error in East and North direction, after removing the offsets $\Delta\nabla\bar{\rho}_r^5$ and $\Delta\nabla\bar{\rho}_r^6$ from pseudo-range measurements taken from Tx-5 and Tx-6, respectively. (b) Empirical CDF of the position error in East and North direction. The update rate of the receiver position solution is 1 kHz.

Additionally, as the receiver operated in stop-and-go mode, one can evaluate the positioning performance on the static reference points. The receiver position solutions on the static reference points and the associated ground truth values are shown in Fig. 7.13(b). The ground truth position of the static points can be directly determined based on the measurements obtained from the total station without any interpolation, which is more accurate than the one of the entire trajectory. Using all measurements collected at each static reference point, one can analyze both the precision and accuracy of the receiver position solution. The empirical standard deviation of the position error is shown in Fig. 7.15(a), which is typically at the centimeter level. Due to multipath and using the simplified model for time delay estimation, a centimeter to decimeter bias presents in the position solution, which can be seen at right.

In Fig. 7.16, the precision is visualized by the (biased) 95% ellipse of concentration for the static points 4, 6, 10 and 13 (see Fig. 7.13(b)), which is thereby centered at the mean of receiver position solution instead of the ground truth position. Each time a 20-by-20 cm area is shown. In addition, using all $M = 16$ bands, the variance of the measurement error $\mathbf{Q}_\rho$ in (6.6) introduced by thermal noise can be derived through (3.29). The shape of the ellipse depends on the formal variance matrix $\mathbf{Q}_{\hat{u}}$ given in (6.7), and thereby shows the impact of the positioning geometry on the precision of receiver position solutions. For example, in Fig. 7.16(a), the lengths of the semi-major and semi-minor axes of the 95% ellipse are 1.48 cm and 1.70 cm, respectively. There are 1693 out of the 1920 points (88.18%) lie within the 95% position error ellipse. Hence, the empirical percentages seem to agree with the formal probabilities.

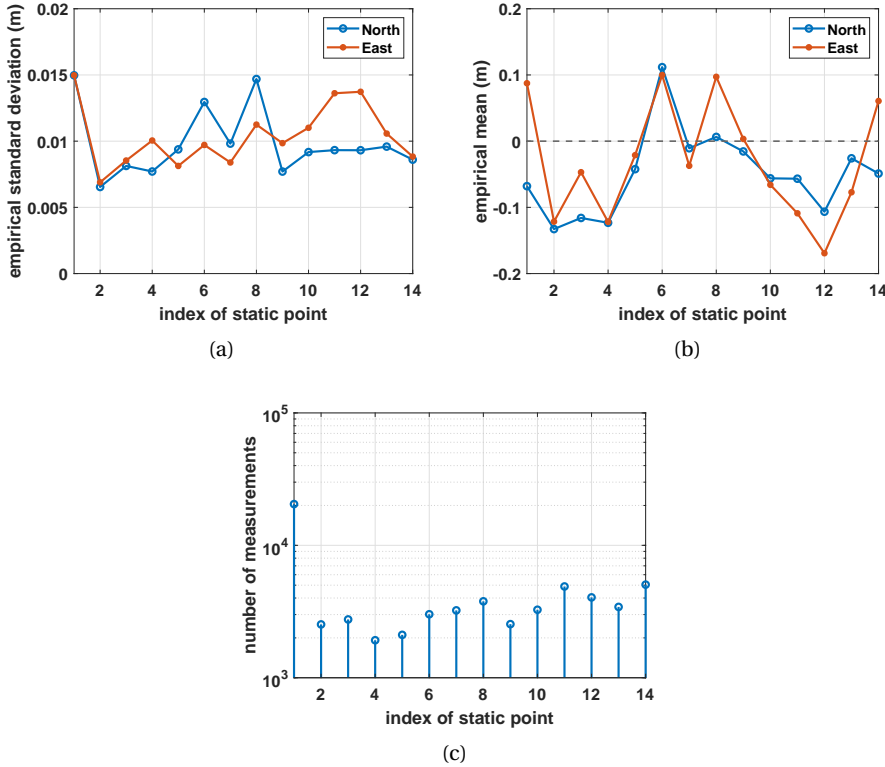In addition, although the receiver was synchronized to the transmitters us-

Figure 7.15: (a) Standard deviation of position error on 14 static reference points, (b) mean of the position error. The ground truth of static reference points is computed directly based on the measurements from total stations, and (c) number of measurements at each of the static reference points.

ing an additional timing node, the pseudo-range clock offset is always estimated along with the receiver position coordinates. The clock offset estimate $\hat{\epsilon}_r(t)$ is shown in Fig. 7.17(a), of which the mean value is 5143.36 m. This offset is mainly caused by the hardware delay, which is equivalent to 17.1564 ns and is close the value of $\nabla \bar{\rho}_r^{1,2,3,4}$ obtained in (7.2). The deviation of the pseudo-range clock offset is mainly caused by multipath, as only a single path is considered for time delay estimation, and the resulting pseudo-range measurements can become slightly biased. The standard deviation of the clock offset is 4.08 cm, and the histogram of the clock offset estimates is shown in Fig. 7.17 at right. It has been overlaid with a normal probability density function (PDF) using the empirical mean and standard deviation.

## 7.3.2. Asynchronous Receiver
In this subsection, an asynchronous receiver is considered. The receiver clock operated independently from the transmitters, and the receiver antenna was in-
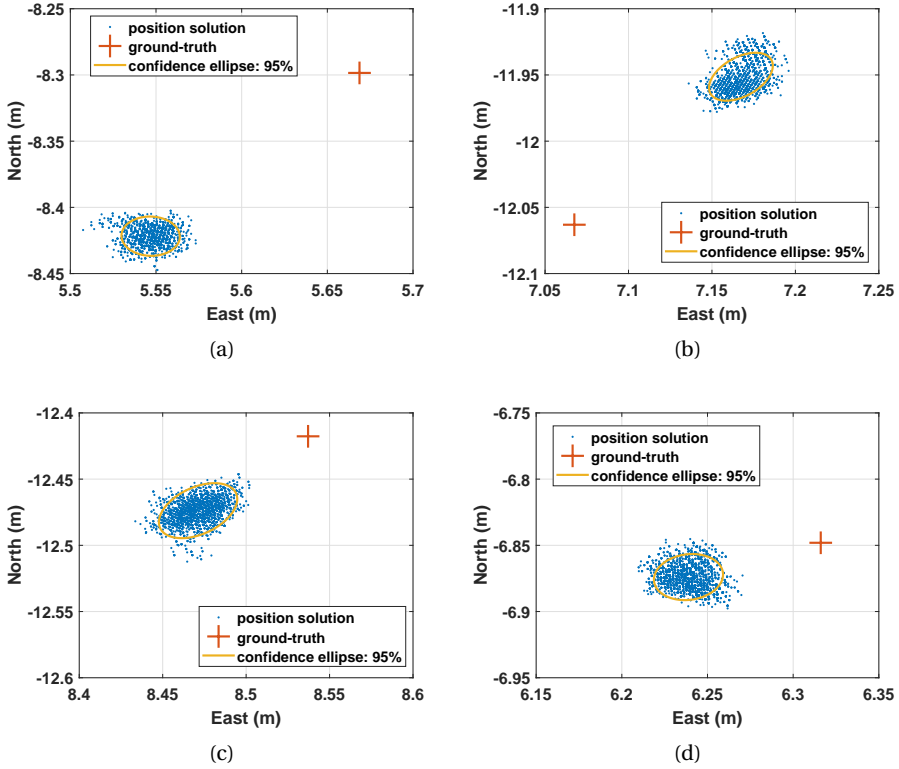
Figure 7.16: 95% ellipse of concentration, scatter of receiver position solution and the associated ground truth. (a) pnt-4 (see Fig. 7.13(b)), standard deviation in East and North direction is (1.01, 0.77) cm, bias: (-9.15, -12,84) cm. (b) pnt-6, standard deviation: (0.98, 1.3) cm, bias: (12.74,11.06) cm. (c) pnt-10, standard deviation (1.11, 0.92) cm, bias: (3.72,-5.62) cm. (d) pnt-13, standard deviation: (1.07,0.96) cm, bias: (-4.80,-3.11) cm.

stalled on the roof of the vehicle as shown in Fig. 7.8(a). The ranging signal and the setup of the transmitters are the same as the one used in the previous subsection. In addition, as the transmitters were not restarted during the experiments, the hardware delays in each Tx-Rx link can be assumed to be time-invariant. Hence, the offset $\Delta \nabla \bar{\rho}_r^5$ of 1.4713 ns, and the offset $\Delta \nabla \bar{\rho}_r^6$ of 1.8771 ns as determined before are removed from the pseudorange measurements.

The pseudo-range measurements obtained by an asynchronous receiver is shown in Fig. 7.18. Although the receiver (mounted on the vehicle) moved forth and back, the movement is not visible in the pseudo-range measurements, as the receiver time-variant clock offset dominates the change of the pseudo-range measurements. By solving the ToA-based positioning model (6.6), the receiver position solutions and the corresponding ground truth trajectory are shown in Fig. 7.19.
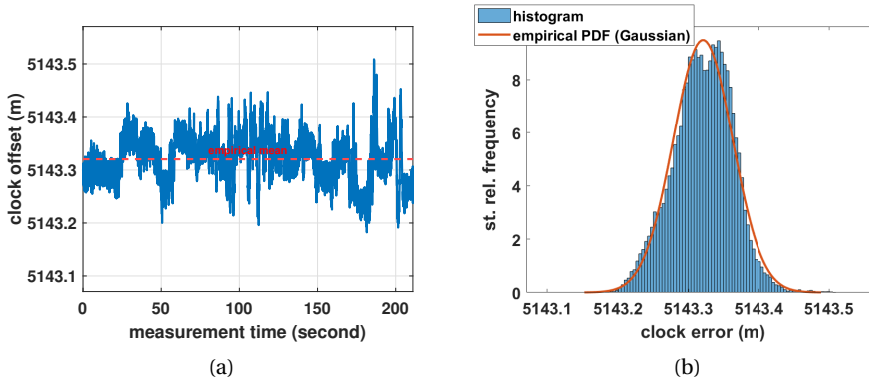
Figure 7.17: (a) Pseudo-range clock offset versus measurement time. Empirical mean and empirical standard deviation are 5143.3596 m, 0.0408 m, respectively. (b) Histogram of pseudo-range clock offset, where the vertical axis gives the standardized relative (st. rel.) frequency [163].
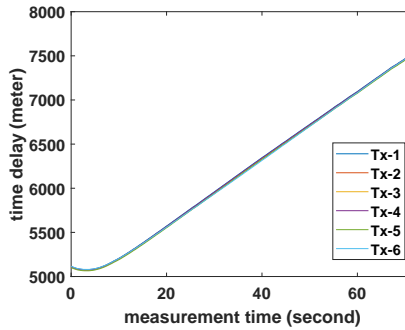


Figure 7.18: Pseudo-range measurement obtained from 6 transmitters by an asynchronous receiver. The change of pseudo-range measurement is dominated by the time-variant clock offset.

To justify the positioning performance, we compute the difference between the ground truth value and the estimated receiver position, which is shown in Fig. 7.20. The RMSEs of the position solutions in the East and North direction are 9.53 cm and 10.72 cm, respectively.

Finally, the pseudo-range clock offset is shown in Fig. 7.21(a), and the behaviour is close to that of the pseudo-range measurements shown in Fig. 7.18. Under the assumption that the frequency offset is constant within the transmission period $T_D$ (1 ms in this experiment), we can also estimate the receiver frequency offset by (6.9). The resulting coarsely estimated normalized frequency offset (NFO) is shown in Fig. 7.21(b) with unit of ppm (part-per-million). According to the NFO estimates shown in Fig. 7.21(b), it seems that the USRP-based receiver requires about 15 seconds to produce a relatively stable clock, after turning the device on.

Based on (6.11), the formal standard deviation of the NFO estimator is shown
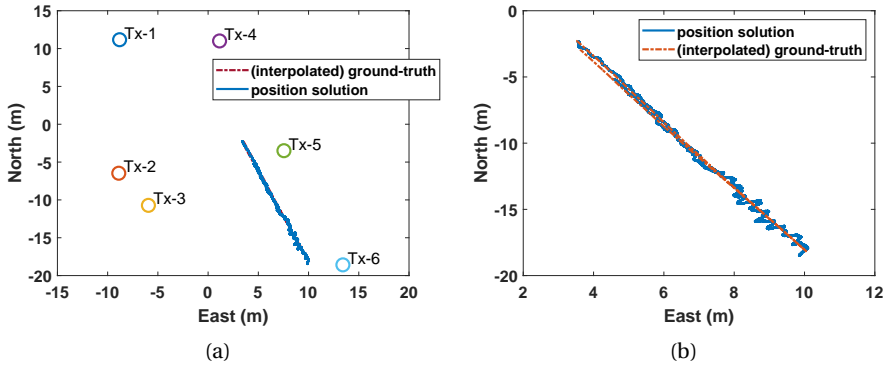
Figure 7.19: (a) Position solution of asynchronous receiver, and the associated ground truth values. (b) Zoom-in view of receiver position solutions.
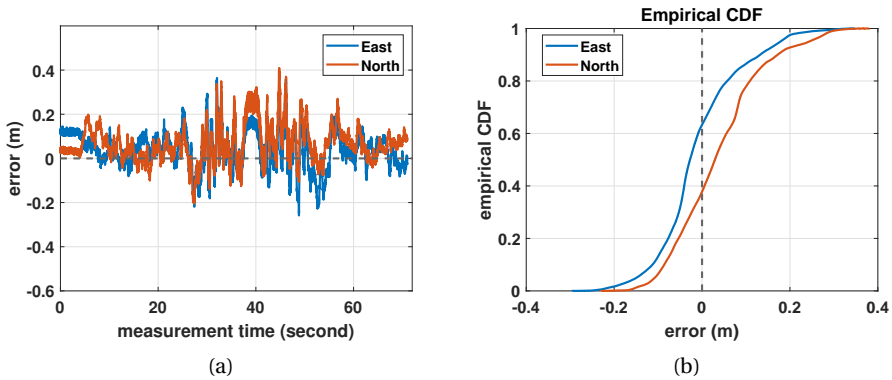


Figure 7.20: (a) Position error versus measurement time, in East and North direction. RMSEs of position error in East and North direction are 9.53 cm and 10.72 cm, respectively. (b) Empirical CDF of position error.

in Fig. 7.22, in which the SNRs for all Tx-Rx pairs are assumed to be identical and set to 10 dB, and all $M = 16$ signal bands are used for ranging. The change of the formal standard deviation depends on the change of the geometry introduced by the receiver motion. At about 40 seconds, the receiver came close to Tx6 as shown in Fig. 7.19, and then started to move back to its starting position. Based on (2.5) and the coarse NFO estimates, one can consequently determine the coarse sampling frequency offset and the coarse carrier frequency offset (CFO).

Particularly, as presented in section 4.3.2, one can compensate this coarse carrier frequency estimate $\Delta \check{f}_c(t)$ before estimating the carrier phase, so that the cycle-slips will not be introduced in phase unwrapping (see Fig. 4.15). Depending on the geometry, the formal standard deviation of the NFO can be smaller than 0.045 ppm. Considering a central frequency of 3960 MHz, the precision of the coarse
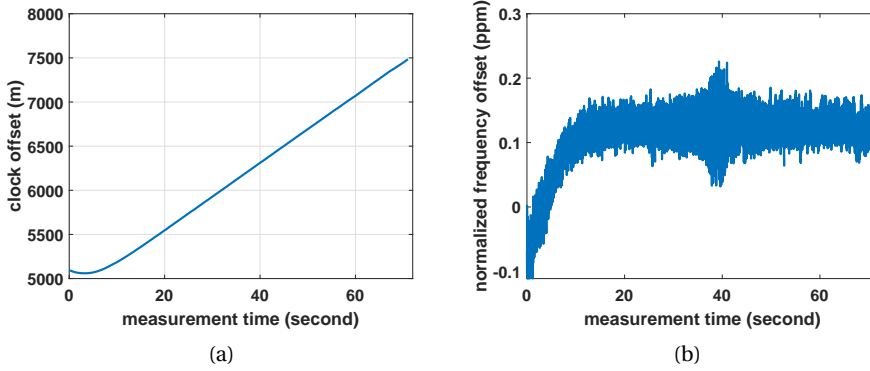
Figure 7.21: Using pseudo-range measurements, (a) pseudo-range clock offset estimated along with the receiver position coordinates, where receiver was not synchronized to transmitters, and (b) coarsely estimated normalized frequency offset (NFO) based on the pseudo-range clock offset (cf. (6.9)).
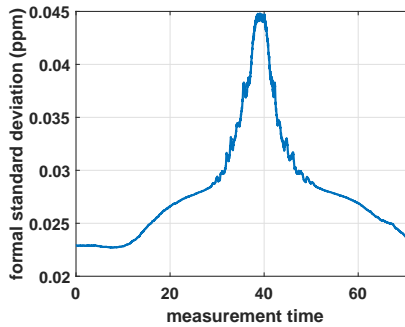


Figure 7.22: Formal standard deviation of coarse normalized frequency offset (NFO) estimator, when SNR of all Tx-Rx pairs are assumed to be 10 dB, and all signal bands $M = 16$ are used for ranging.

CFO estimator will consequently be about 178.2 Hz. Given a transmission period $T_D = 1$ ms, the corresponding phase rotation will be about 0.18 cycle, so that no cycle-slip will occur in the unwrapped carrier phase measurement, because of the receiver frequency offset.

For comparison, Fig. 7.23 shows the coarse carrier frequency estimates derived through both the ToA-based positioning model (cf. (6.9)) and the shortened Moose's symbol (cf. (4.41)). As the transmission period $T_D$ (e.g., 1 ms) is much longer than the duration of the shortened Moose's symbol (e.g., 6.4 $\mu$s, see Fig. 2.2), the resulting precision of the CFO estimator based on a series of pseudo-range clock offset estimates is better than using the single shortened Moose's symbol independently in each signal packet.
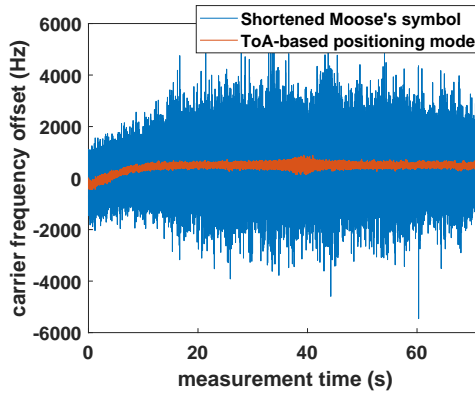
Figure 7.23: Coarse carrier frequency offset $\Delta \check{f}_c(t)$, based on a series of pseudo-range clock offset estimates derived from ToA-based positioning model (cf. (6.9)), and based on the shortened Moose's symbols (cf. (4.41)).

### 7.3.3. Sparse Multiband Signal

In this section, we aim to demonstrate the potential flexibility of using a sparse multiband signal for ranging. Here, the sparse multiband signal shown in Fig. 5.7 was used for ranging, which occupies $M_a = 7$ out of $M = 16$ signal bands. For comparison, in Fig. 7.24 we present the receiver position solutions based on both the sparse multiband signal and all signal bands at the static reference point 7 and 10 shown in Fig. 7.13. In addition, to visualize the formal precision by the ellipse of concentration, the SNRs for all Tx-Rx links are coarsely determined by the ratio between the received signal power and the received noise power.
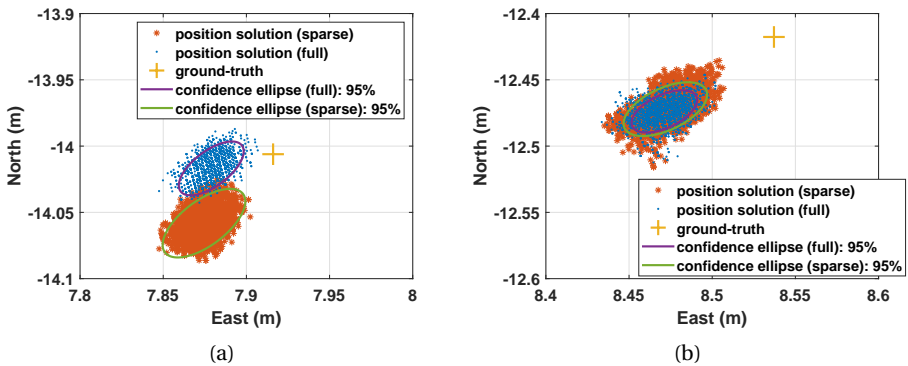


Figure 7.24: 95% ellipse of concentration, scatter of receiver position solution and the associated ground truth, for (a) static reference point 7, and (b) static reference point 10, as shown in Fig. 7.13.

As shown in Fig. 7.24(a), for the static reference point 7, the lengths of the semi-major and semi-minor axes of 95% ellipse are 3.24 cm and 1.53 cm when using

the sparse multiband signal with $M_d = 7$, and 2.55 cm and 1.20 cm when using all $M = 16$ signal bands. There are 3071 out of the 3277 points (95.2 %) lie inside the 95% ellipse when using the sparse multiband signal. The RMSEs in East and North direction are 3.81 cm and 1.45 cm, respectively, when using the all signal bands, and 4.25 cm and 5.32 cm when using the sparse multiband signal.

Similarly, one can also analyze the results for the static reference point 10, as shown in Fig. 7.24(b), there are 3179 out of the 3277 points (98.5 %) lie inside 95% position error ellipse. Generally, the empirical percentages are slightly higher than the theoretical percentage, as the SNR is not accurately computed. The RMSEs in East and North direction are 6.66 cm and 5.56 cm, respectively, when using all signal bands, and 6.68 cm and 6.69 cm when using the sparse multiband signal. Using the sparse multiband signal for ranging, the precision will slightly decrease, and the overall ranging performance is close to using full signal bandwidth.

## 7.4. Positioning Performance Based on Carrier Phase Estimates

In this section, we present the positioning performance only based on the carrier phase measurement (i.e., phase-of-arrival (PoA) measurements) or the differenced carrier phase measurement (i.e., phase-difference-of-arrival (PDoA) measurement). Five runs were carried out to evaluate the positioning performance. The interpolated ground truth receiver trajectory and the starting position for each run are shown in Fig. 7.25. In order to be able to exploit the integer nature of the carrier phase cycle ambiguities, the snapshot correction file, for both the PoA-based positioning model (cf. (6.36)) and for the PDoA-based positioning model (cf. (6.28)), is created at the reference point shown in Fig. 7.25. The position of the reference point is also determined using the total station. Note that the position of the reference point should be carefully selected to avoid severe multipath impact on carrier phase estimation when producing the correction file. Otherwise, additional different phase biases will be introduced, when applying the correction file.

In addition, Table. 7.3 shows the configuration of the receiver. In runs 1-3, the receiver was not synchronized to the transmitters. In runs 4-5, the receiver was synchronized to the transmitters through the commonly distributed time-frequency reference by using an additional timing node. Each run lasted for about 1-3 minutes. All runs and the measurements to produce the correction file are conducted within about 1 hour and 30 minutes. The end time of each measurement is also presented in Table. 7.3, in CEST on September 16, 2020.

To derive the variance of the PoA measurement (cf. (4.31)) and the PDoA measurement (cf. (4.52)), the SNR of each Tx-Rx link is simply computed by the received signal power divided by the received noise power.

In addition, a CFO of 403 Hz is compensated a priori when computing the PoA measurement so that cycle-slips are avoided. This coarse value for the CFO was determined earlier based on an experiment performed in the lab, and is used in section 7.4.1, 7.4.2, and 7.4.3. In section 7.4.4, we compensate the CFO by us-
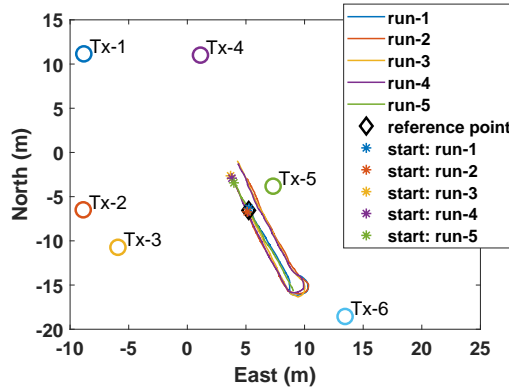
7

Figure 7.25: Positioning geometry and receiver trajectory for 5 runs, and the reference point for acquiring carrier phase measurements to produce corrections.

Table 7.3: Synchronization mode of receiver for each run and producing the correction file, and measurement duration and time.

| run no. | time-frequency synchronization of receiver | duration (s) | end time (hr:min) |
|---|---|---|---|
| 1 | no | 86 | 15:18 |
| 2 | no | 146 | 15:54 |
| 3 | no | 186 | 16:06 |
| 4 | yes | 184 | 16:38 |
| 5 | yes | 118 | 16:47 |
| correction | no | 0.001 | 15:39 |

ing the coarse CFO estimates obtained from the shortened Moose's symbol (cf. (4.41)), or a series of the pseudo-range clock offsets through the ToA-based positioning model (cf. (6.9) and (6.12), and also see section 7.3.2), when estimating the carrier phase. Then, the performance of fine frequency offset estimation is presented by using the residual clock offset obtained through the PoA-based positioning model (cf. (6.38) and (6.48)).

## 7.4.1. Overall Positioning Performance

In this subsection, the overall positioning performance is presented for different positioning models introduced in section 6.2. Given the system setup (i.e., $K = 6$), the carrier phase estimated at two different epochs is used for positioning. Due to the limited redundancy of the positioning model, only a 2D positioning scenario (i.e., $N_d = 2$) is considered, and the height of the receiver antenna throughout the experiment is assumed to be known and constant, and measured once a priori by the total station. The experiment with different runs was carried out on a paved, flat road (see Fig. 7.6), and the variation in the height can be expected to be 5 cm at most.

First, the overall positioning performance is analysed based on the PoA mea-

surements for the entire trajectory of the receiver. Both, the float solution, fixed solution, and the solution derived from the relative positioning model, are used to evaluate the positioning accuracy. During the experiment, the receiver also stopped at a few positions for a few seconds each time. Then, the positioning performance is analysed for these static points based on the fixed solution, using both the PoA-based and PDoA-based positioning model, and the correction files to be able to exploit the integer nature of the carrier phase cycle ambiguity.

Table. 7.4 shows the root mean-squared error (RMSE) of the position solution for each run. As the carrier phase ambiguities are absent in the relative positioning model and assuming a good positioning geometry, the performance of the position solution mainly depends on the quality of the carrier phase measurement. Therefore, the relative position error is jointly determined by the quality of the ground truth, as well as the carrier phase measurements. Relative positioning requires a known starting position, and the starting point of the receiver antenna is measured a priori by the total station in each run. The RMSE of relative positioning in East and North direction is about 1.5 cm and 3 cm.

Table 7.4: Root mean-squared-error (RMSE) of position solution in East (E) and North (N) direction, using PoA relative positioning model and PoA-based positioning model, presented in unit of cm, based on over 100000 position solutions in each run.

| run no. | | 1 | 2 | 3 | 4 | 5 |
|---|---|---|---|---|---|---|
| relative positioning | E | 1.5 | 1.5 | 1.4 | 1.9 | 1.5 |
| | N | 3.2 | 2.7 | 2.2 | 1.8 | 3.0 |
| PoA float | E | 14.6 | 12.2 | 2.9 | 3.2 | 6.9 |
| | N | 18.1 | 14.8 | 2.9 | 4.2 | 3.7 |
| PoA fixed w/ correction | E | 1.7 | 1.8 | 1.3 | 1.8 | 2.4 |
| | N | 2.7 | 3.8 | 2.8 | 3.4 | 3.2 |
| | $n_{fx}/n$ (%) | 92.4 | 97.7 | 100 | 93.4 | 87.7 |
| PoA fixed w/o correction | E | 33.9 | 19.1 | 6.9 | 12.6 | 8.8 |
| | N | 42.4 | 15.0 | 3.0 | 7.1 | 5.1 |
| | $n_{fx}/n$ (%) | 23.8 | 26.7 | 90 | 16.1 | 51.6 |

In addition, Table. 7.4 also presents the performance of using the PoA-based positioning model (cf. (6.38)). As shown in Fig. 7.26, epoch $t_1$ is kept fixed to the starting epoch of the run, and the carrier phase $\varphi_r(t_1)$ is the same all the time. Epoch $t_2$ is varied up to the end of the experiment. In this way a change in geometry can be guaranteed, as long as the receiver does not go back to the starting position. For each solution, only two epochs are used, $t_1$ and $t_2$. The performance of the float solution is determined by both the positioning geometry at $t_1$ and $t_2$. One can notice that the positioning performance of the ambiguity-float solution in runs 1-2 is much poorer than the other runs, as the start point of runs 1-2 at $t_1$ is further away from the center in the given positioning geometry (see Fig. 7.25). Generally, a decimeter to a centimeter level accuracy can be achieved for the ambiguity-float position solution. Alternatively, one can update the measurements for both $t_1$ and $t_2$ (maintaining a fixed time-offset between $t_1$ and $t_2$), and an example will be provided in section 7.4.3.
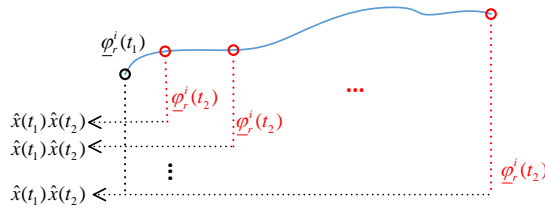
Figure 7.26: Configuration of carrier-phase-based positioning model using two epochs of measurements, of which the first epoch measurement at $t_1$ is kept the same all the time, and epoch $t_2$ is varied up to the end of experiment, so that the time span between $t_1$ and $t_2$ is increasing.

Using the corrections taken at the reference point shown in Fig. 7.25, the integer nature of the carrier phase ambiguities can be exploited, and one can use the LAMBDA toolbox [164] developed at Delft University of Technology to obtain integer ambiguity estimates and next compute fixed position solutions. Once the integer phase ambiguities are computed, one can use, for example, a ratio-test to decide whether the integer solution is sufficiently likely, and hence can be relied on. The reader can refer to [165] for the details of the ambiguity ratio-test and the determination of the critical value. Here, the critical value for the ratio-test is set to 0.7, and the required success rate is set to 99.9%. If the test is not passed, one will only obtain the ambiguity-float solution.

Once the ambiguities are fixed to integer numbers, when using the provided correction file, as shown in Table. 7.4, the RMSE of the fixed solution is generally at the centimeter level and close to the one obtained with relative positioning. Again, these figures contain the error introduced by the interpolated ground truth (see also Fig. 7.39(b) later on). In addition, the ratio of the number of fixed solutions (i.e., $n_{fx}$) and the total number of solutions (i.e., $n$, float and fixed together) is also presented in Table.7.4. By using the correction file, one can obtain fixed solutions for most of the epochs, demonstrating the effectiveness of the correction file.

For comparison, without using the correction file, one can still try to fix the ambiguities, even though the ambiguities are no longer integer numbers. As shown in Table. 7.4, the fixed solution can only be obtained from a small amount of float solutions, given the same critical value for the ambiguity ratio-test as before. And the RMSE of the position solution is still much larger than the one when using the correction files, likely due to incorrectly fixed ambiguities and an incorrect model.

In addition, in each run, the receiver stopped at about 5-13 locations (i.e., static points), each time for a few seconds. As no interpolation is needed to determine the ground truth of the static points, this ground truth will be more precise than the one of the entire trajectory. The accuracy of the position solution, therefore, is analysed at these static points. Using the correction files, Table 7.5 shows the *average* mean value and the *average* standard deviation of the fixed position error at the static points in each run. Both the PoA-based positioning model (cf.

Table 7.5: Average mean, and average standard deviation of fixed position error at static points (positioning at 1 kHz rate), when using positioning model based on PoA and PDoA measurements, with correction file.

| run no. | | unit (cm) | 1 | 2 | 3 | 4 | 5 |
|---|---|---|---|---|---|---|---|
| PoA fixed with correction | average mean | E | -0.5 | -0.0 | -0.2 | -0.1 | -1.2 |
| | | N | -2.5 | -2.2 | -2.1 | -1.9 | -3.8 |
| | average std. | E | 0.5 | 0.6 | 0.5 | 0.5 | 0.6 |
| | | N | 0.2 | 0.2 | 0.1 | 0.3 | 0.3 |
| PDoA fixed with correction | average mean | E | -0.5 | -0.3 | 0.2 | 1.0 | -1.2 |
| | | N | -2.4 | -2.7 | -2.9 | -2.5 | -3.9 |
| | average std. | E | 0.5 | 1.4 | 0.6 | 1.8 | 0.6 |
| | | N | 0.3 | 1.3 | 0.4 | 0.8 | 0.4 |
| number of static points | | | 5 | 12 | 11 | 13 | 7 |

(6.38)) and the PDoA-based positioning model (cf. (6.30)) are used to compute ambiguity-fixed position solutions.

Using the PoA and PDoA-based positioning models, the average mean values, as well as the average standard deviations, are close (Table 7.5). This indicates that the residual clock offset can indeed be effectively canceled by taking the difference of the measurements between two transmitters.

As the RMSE and the empirical standard deviation of the fixed position solution in both East and North direction is at centimeter level, it also indicates that the synchronization among the transmitters is at least at the 100 picosecond level (or better) when using the optically distributed time and frequency reference signals. This seems to correspond to the assumption that all transmitters are synchronized in time and frequency, as made in chapter 6.

## 7.4.2. Synchronized Receiver: Run-4

In this subsection, we evaluate the positioning performance for run-4, in which the receiver is synchronized to the transmitters using the commonly distributed time and frequency reference through an additional timing node.

Measurements

Fig. 7.27 shows the carrier phase measurements obtained from all 6 transmitters (i.e., PoA measurements) as a function of time. As the receiver is assumed to be synchronized to the transmitters, the change of the carrier phase measurements is caused by the movement of the receiver. Hence, the carrier phase measurements look like step-functions, because the receiver was operated in stop-and-go mode, and stopped at each of the static reference points for a few seconds.

At the starting reference point, as the receiver did not move, ideally the PoA measurements should be constant. Fig. 7.28 (a) shows an zoom-in on the PoA measurements of the first second from run-4. The PoA measurements taken from all Tx-Rx pairs oscillate with similar behavior, which is unanticipated and could be caused by the receiver clock jitter, and requires further investigation. Then, by computing the Fourier transform of the PoA measurements of the first 15 seconds (as the receiver was static), Fig. 7.29(a) shows the spectrum of the PoA measure-
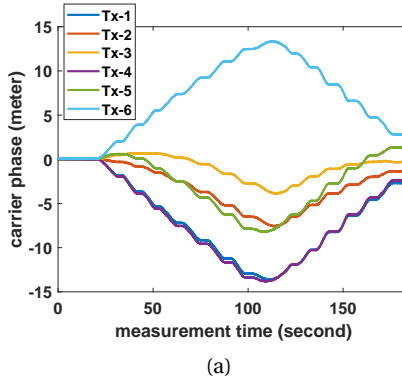
(a)

Figure 7.27: Carrier phase measurement obtained from six transmitters, and the receiver was synchronized to all transmitters.

ments taken from Tx-2, and the oscillation frequency is about 14 Hz. In an ideal case when only considering the white Gaussian noise, the amplitude of the noise spectrum will be flat. As the oscillation in the PoA measurements taken from all transmitters behaves similarly, it can be approximately treated as a receiver dependent clock offset, which will be estimated along with the position solution (cf. (6.38)).



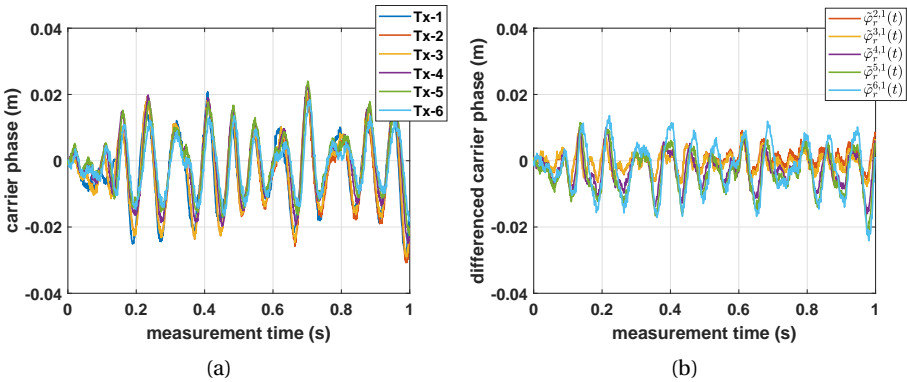(a)                                                    (b)

Figure 7.28: (a) Carrier phase measurements (i.e., PoA) for all transmitters, (b) differenced carrier phase measurements (i.e., PDoA, and Tx1 is selected as pivot transmitter), for a duration of 1 second. For better visualization, the measurements of each Tx-Rx pair are offset by the first measurement, so that they all start from 0.

One the other hand, one can compute the differenced carrier phase measurement (i.e., PDoA measurement) between two transmitters, and evaluate whether such a oscillation behavior in the PoA measurement is receiver-dependent and can be effectively removed or not. As shown in Fig. 7.28(b) and Fig. 7.29(b), where Tx1 is selected as the pivot transmitter, by taking the difference between

two transmitters, most of the oscillations shown in Fig. 7.28(b) can be removed in the PDoA measurement. However, due to the slightly different oscillation amplitudes among different transmitters, the effect cannot completely be removed by taking the difference. When computing the ambiguity-fixed solutions, the different initial offsets in different Tx-Rx links (being time-variant) will be taken into account by using the correction file. However, the different oscillation amplitude in different links will not be considered in the model, and these unmodelled errors propagate into the position solution.
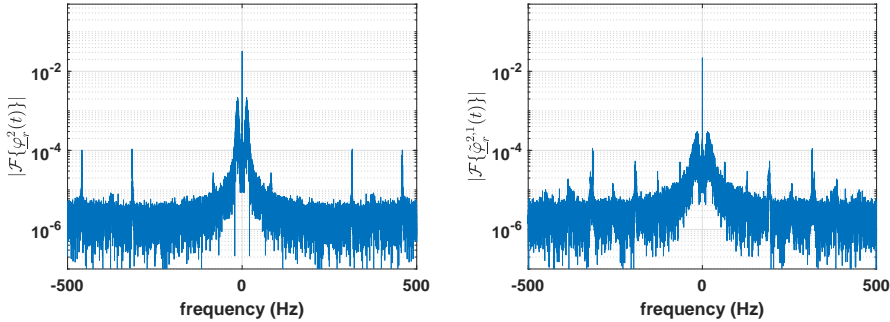


Figure 7.29: (a) Amplitude spectrum of carrier phase measurements (i.e., PoA) of Tx2-Rx pair, (b) amplitude spectrum of differenced carrier phase measurements (between Tx2 and Tx1, i.e., PDoA), for duration of 15 seconds with update period of 1 ms.

Finally, the histogram and the empirical probability density function (PDF) of the PoA (Tx2) and PDoA (between Tx2 and Tx1) measurements, with a duration of 15 seconds, are shown in Fig. 7.30, when the receiver is static. The empirical PDF is computed based on a Gaussian distribution, in which the empirical mean and the empirical standard deviation are derived from the carrier phase measurements. Although oscillations (typically less than 1 cm) are still present in the PDoA measurement, the histogram and the resulting empirical Gaussian PDF seem to match well.

### Ambiguity-float and -fixed solutions

Fig. 7.31 shows the 2D ambiguity-float and ambiguity-fixed position solution, as well as the ground truth versus measurement time. Both the float and fixed position solution are very close to the ground truth, which is also generally in line with the results presented in Table. 7.4.

Compared to the setup of run-1 and run-2, the geometry of run-4 is better, as the location of its starting point is closer to the center of the area covered by the transmitters, shown in Fig. 7.25. One can analyze the LSE coefficients when using the PoA-based positioning model. As an example, Fig. 7.32 shows the LSE coefficients $[\Xi_{\text{ft}}]_8$ (cf. (6.27)) that correspond to the contribution of $\varphi_r^2(t_2)$. As the values are generally about -7 to -3, and much smaller than in run-1 (see Fig. 7.41 in section 7.4.3), the float solution in this case will be less sensitive to noise and errors in the carrier phase measurements.
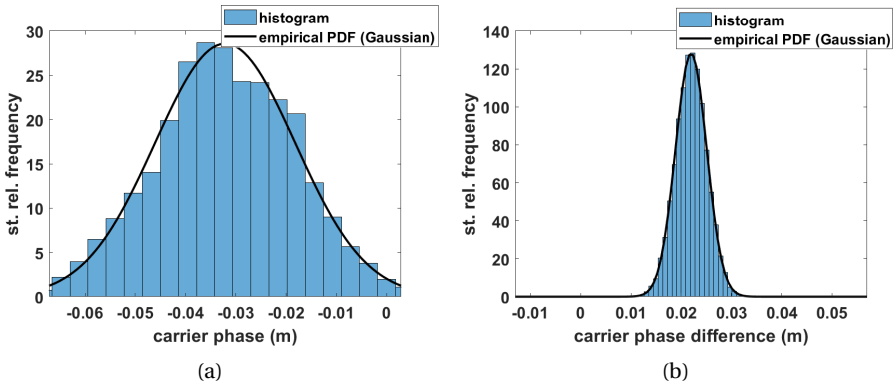
Figure 7.30: Histogram and empirical PDF of (a) carrier phase measurement (empirical standard derivation: 1.4 cm), and (b) differenced carrier phase measurement (empirical standard deviation: 0.31 cm), when receiver is static, and is assumed to be synchronized to transmitters. Measurement duration is 15 seconds with update period of 1 ms (i.e., 15000 measurements). Vertical axis gives the standardized relative (st. rel.) frequency.
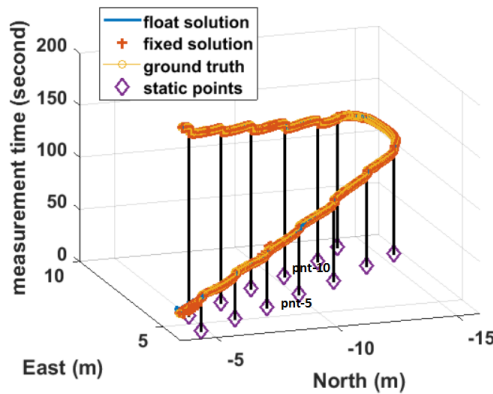


Figure 7.31: Ambiguity-float and ambiguity-fixed position solutions for run-4, ground truth of receiver trajectory versus time, and 13 static points where the receiver stops for a few seconds each time.

Once the carrier phase ambiguities are fixed to integer numbers, they are assumed to be deterministic when computing the LSE coefficients for the fixed solution $\Xi_{fx}$ (cf. (6.34)). The LSE coefficients to compute the fixed solution for both run-1 (see section 7.4.3) and run-4 are quite similar, which is also in line with the positioning performance of the fixed solution presented in Table. 7.4.

Fig. 7.33 presents the ambiguity-float and ambiguity-fixed solution for the residual clock offset $\tilde{\delta}_r^1(t_1)$ and $\tilde{\delta}_r^1(t_2)$. Note that the measurement for epoch $t_1$ is always fixed, while the measurement for epoch $t_2$ varies till the end of the experiment (see Fig. 7.26). By fixing the carrier phase cycle ambiguities to integer numbers, the resulting solution requires less displacement of the receiver, compared

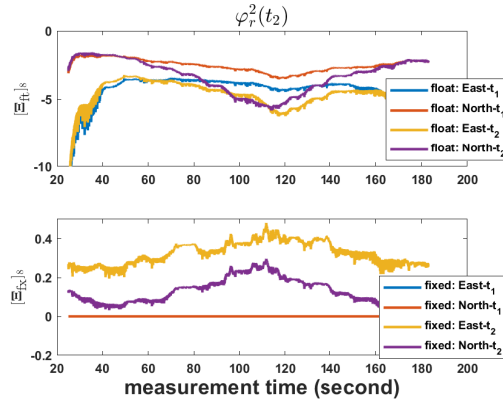Figure 7.32: LSE coefficients of PoA-based positioning model in run-4, for both the float (top) and fixed (bottom) solution. The integer phase ambiguities are assumed to be deterministic and known when computing the coefficients for fixed solutions.

to the float solution in order to achieve a cm-level precision. In Fig. 7.33(a), there are a few solutions with a large offset, because of incorrectly fixed ambiguities.
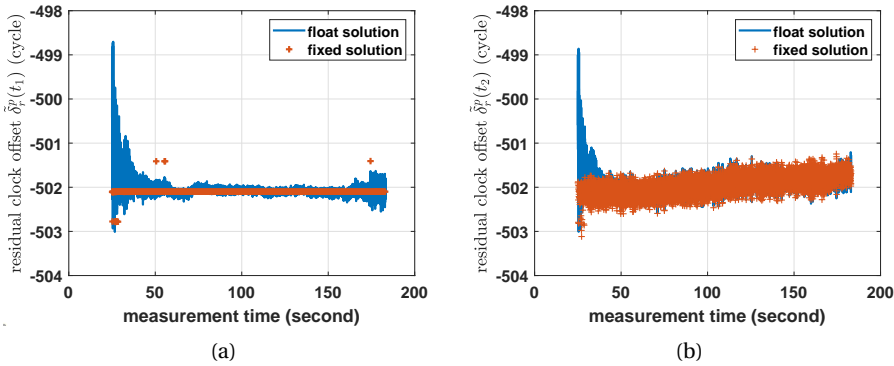


Figure 7.33: Ambiguity-float and ambiguity-fixed residual clock offset (a) $\tilde{\delta}_r^1(t_1)$, and (b) $\tilde{\delta}_r^i(t_2)$, when the receiver was synchronized to the transmitters through commonly distributed time and frequency reference signal. (1 cycle corresponds to 7.57 cm)

Although the receiver was synchronized to the transmitters, there is apparently still a small frequency offset in the receiver, which introduces a change of about 0.5 cycle (i.e., 126.26 ps in time) in the receiver clock offset over a measurement duration of 184 seconds. This could be introduced by temperature variation, and the restart operation of the receiver USRP. For each run, the receiver is restarted, and its PLL requires a certain time to get stably locked, while the transmitters were continuously operating.

If such an offset is a receiver-dependent parameter, one should observe the

similar offset in the measurements taken from all transmitters. To justify this assumption, Fig. 7.34 shows the difference between the PoA measurements and the ground truth propagation distance for all Tx-Rx pairs, which ideally for a synchronized receiver only contains the time-invariant parameter (e.g., carrier phase ambiguities, hardware delay, initial phase offset) and the error introduced in the determination of the ground truth. Note that the results for different transmitters shown in Fig. 7.34, are intentionally offset by different values to have a better visualization. It should also be mentioned that the receiver antenna experienced a U-turn at about 120-130 seconds (also see Fig. 7.31), and the trajectory certainly does not represent a straight line, constant velocity motion. Consequently, based on piece-wise linear LSE, a relatively large error will be introduced in the interpolated ground truth.

The residual errors computed for all transmitters behave similarly in Fig. 7.34, which confirms that there is a small frequency offset only in the receiver, and the transmitters can be assumed to be synchronized. In fact, as the positioning performance with the PoA and PDoA-based positioning model is very similar, this indicates that the frequency offset only occurs in the receiver, and can be eliminated by taking the difference in carrier phase measurement between two transmitters, or be covered by the receiver clock offset parameter in the PoA-based positioning model.
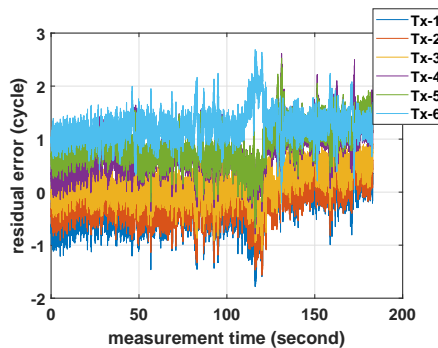


Figure 7.34: Difference between PoA measurement and ground truth propagation distance for different transmitters, presented in unit of cycle (1 cycle corresponds to 252.53 ps). Mind that the results for all Tx-Rx pairs are intentionally offset by different values for a better visualization.

### Distribution of Static Position Solution

As shown in Fig. 7.31, the receiver stopped at each of the static reference points for a few seconds. The ground truth of the static reference points does not require interpolation, and thereby is more accurate than the ground truth of the entire receiver trajectory. As an example, Fig. 7.35 shows the position solutions and the ellipse of concentration of the static reference point 5 (pnt-5), at left, and the static reference point 10 (pnt-10), at right.

For static reference point 5, as shown in Fig. 7.35(a), based on the formal variance (6.42), the lengths of the semi-major and semi-minor axes of the 95% ellipse

Figure 7.35: 95% ellipse of concentration, scatter of receiver position solution and the associated ground truth. (a) pnt-5, standard deviation of ambiguity-float solution in East and North direction is (0.91, 0.48) cm, bias: (-3.27, -5.23) cm; ambiguity-fixed solution, standard deviation in East and North direction is (0.52, 0.13) cm, bias (-0.17, -3.08) cm. (b) pnt-10, standard deviation in East and North direction is (0.87, 0.62) cm, bias: (-0.81, -1.02) cm, ambiguity-fixed solution, standard deviation (0.55, 0.33) cm bias (-0.19, -0.70) cm
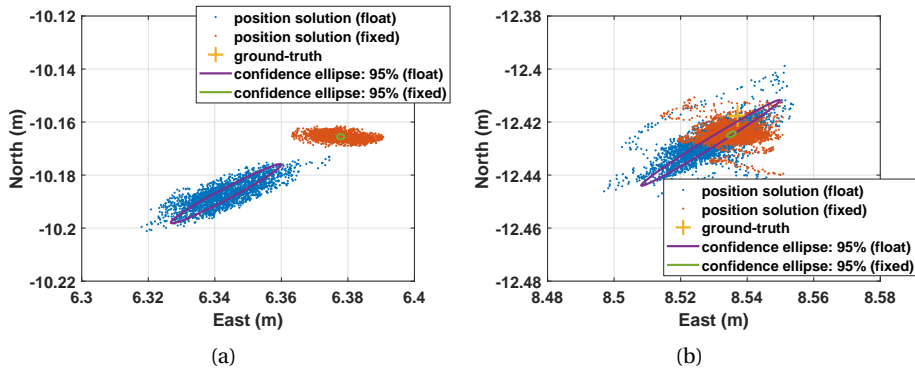
of the ambiguity-float solution are 1.99 cm and 0.20 cm, respectively. There are 1977 out of the 2108 points (93.79%)that lie within the 95% position error ellipse. The empirical percentages of the float solutions approximately agree with the formal probabilities. The position solution scatters of the ambiguity-fixed solutions and the 95% ellipse are also shown in Fig. 7.35(a). Compared with the ambiguity-float solution, the ambiguity-fixed solution achieves higher accuracy. However, the ambiguity-fixed solution scatters are not well matched the ellipse of concentration, which could be caused by an unmodelled error, for example, the oscillations in the carrier phase measurements (see Fig. 7.28 and Fig. 7.29).

For the static reference point 10, as shown Fig. 7.35(b), the lengths of the semi-major and semi-minor axes of the 95% ellipse of the ambiguity-float solutions are 2.64 cm and 0.17 cm, respectively. There are 3156 out of the 3262 points (96.75%) that lie within the 95% position error ellipse. The empirical percentage of the float solution also approximately agrees with the formal probability. The ambiguity-fixed solution achieves higher accuracy than the float solution, however, likely again due to an unmodelled error, the 95% ellipse of the fixed solution does not match the fixed position scatters.

To analyze the distribution of the position solution, one can first examine its spectrum by Fourier transform. Similar to Fig. 7.29, the spectrum of the ambiguity-fixed solution for the static reference point 10 in East and North direction is shown in Fig. 7.36(a) and (b), respectively. One can notice that the error of the fixed solution particularly in the East direction is not white, and a oscillation behavior can also be observed, which is likely caused by the different oscillation amplitudes among different transmitters. On the other hand, the noise level, and the amplitude of the oscillation frequency (of about 14 Hz) in the spectrum of

the ambiguity-fixed solution in North direction are smaller than the ones in East direction. Hence, the fixed solution scatter is larger in East direction than in the North direction. Due to the unmodelled error, the formal precision of the ambiguity-fixed solution is not in line with the empirical precision.
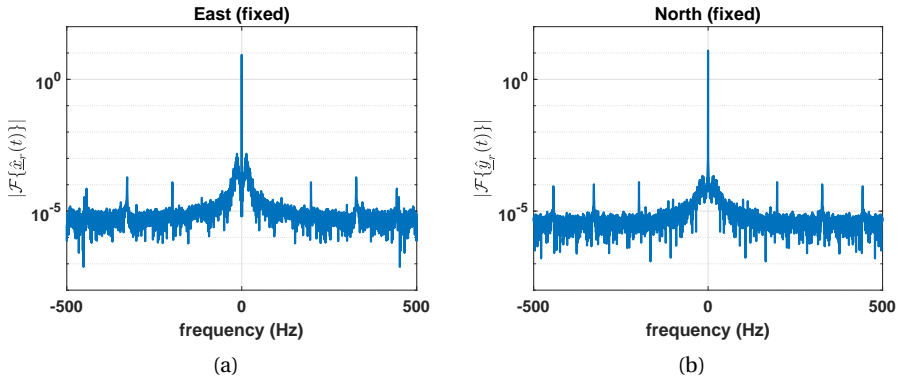


Figure 7.36: Spectrum of position solution at static reference point 10 (i.e., pnt-10 in Fig. 7.31) in East (a) and North direction (b).

Finally, the histogram of both the float and fixed solutions in East and North directions at the static reference point 10, as well as the PDF of a Gaussian distribution, at the empirical mean, one with formal standard deviation and one with empirical standard deviation, are shown in Fig. 7.37. The formal PDFs of the float solutions generally seem to agree with the histogram (see Fig. 7.37(a) and (c)). Hence, the position scatters also matches the 95% ellipse. However, due to the small and time-variant unmodelled error, the empirical precision of the ambiguity-fixed solution is larger than the formal precision, particularly in the East direction (compared Fig. 7.37(b) to Fig. 7.37(d)).

### 7.4.3. Asynchronous Receiver: Run-1

This subsection will closely evaluate the positioning performance of run-1, in which the receiver runs on its own clock. First, the configuration of the PoA-based positioning model (cf. (6.38)) with two epochs of measurements is based on the one shown in Fig. 7.26. The measurement for epoch $t_1$ is kept constant, while the one for $t_2$ is varied from the beginning till the end of the experiment. Then, we also examine the positioning performance using a different configuration, where both epoch $t_1$ and $t_2$ are varied throughout the experiment. To guarantee a sufficient change in geometry, the time difference between $t_1$ and $t_2$ is kept constant at 45 seconds.

#### Varying time span - epoch $t_1$ fixed and epoch $t_2$ varying

Using the PoA-based positioning model and the correction file, Fig. 7.38 shows the 2D position solution and the ground truth versus the measurement time $(t_2 - t_1)$.
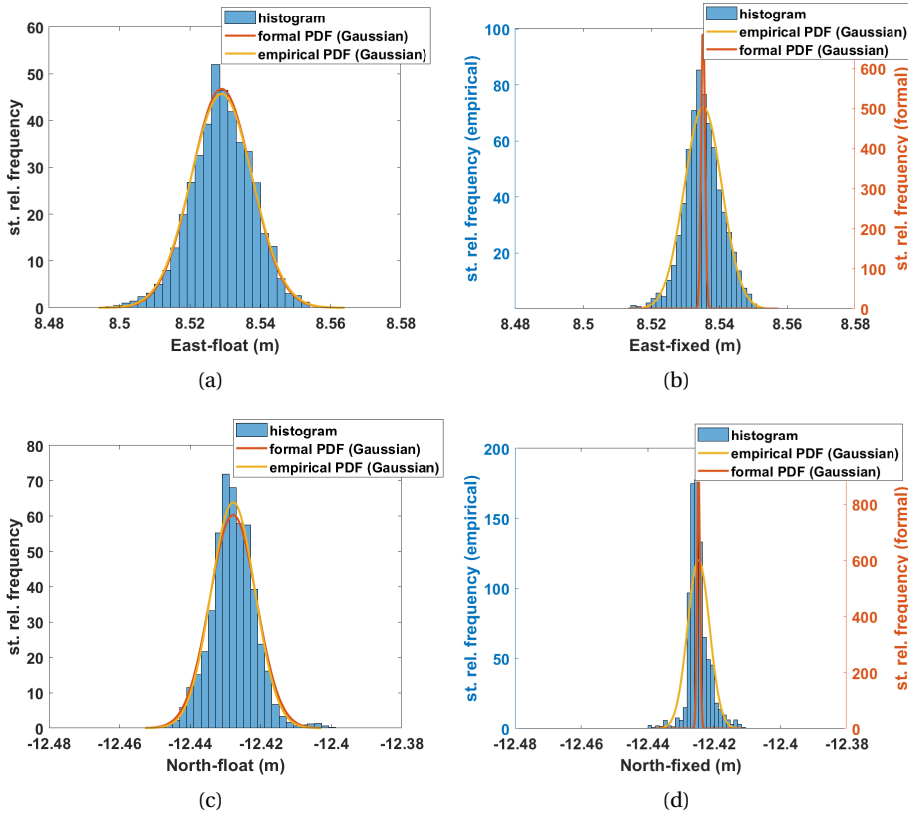
Figure 7.37: Histogram and formal PDF of ambiguity-float solution in (a) East direction (formal standard deviation: 0.82 cm) and (c) North direction (formal standard deviation: 0.64 cm), and of ambiguity-fixed solution in (b) East direction (formal standard deviation: 0.06 cm) and (d) North direction (formal standard deviation: 0.05 cm). The vertical axis gives the standardized relative (st. rel.) frequency.

Generally, the ambiguity-fixed solutions are very close to the ground truth values. In addition, Fig. 7.39(a) shows the position error for the ambiguity-fixed solution and the ambiguity-float solution in both East and North direction. As the receiver rarely moved for the first 21 seconds, the second epoch for $t_2$ in (6.38) was taken from about 21.5 seconds after the start of the run to the end. After these 21.5 seconds, the receiver moved by just 7.1 cm and -15.4 cm in East and North direction from the starting point, respectively, and due to this very limited change in positioning geometry, the float position solution has a poor precision and contains a large error. However, even with such a very small displacement, most of the integer phase ambiguities can apparently still be correctly estimated, and the resulting fixed solution largely reduces the convergence time required to achieve a centimeter level accuracy.

As the position error shown in Fig. 7.39(a) can also be introduced by an er-
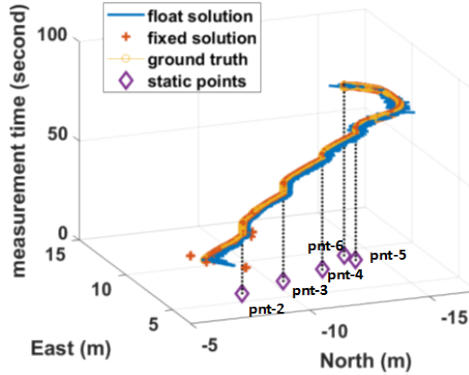
Figure 7.38: Ambiguity-float, ambiguity-fixed solution, ground-truth of the receiver trajectory, and 5 static points in run-1.
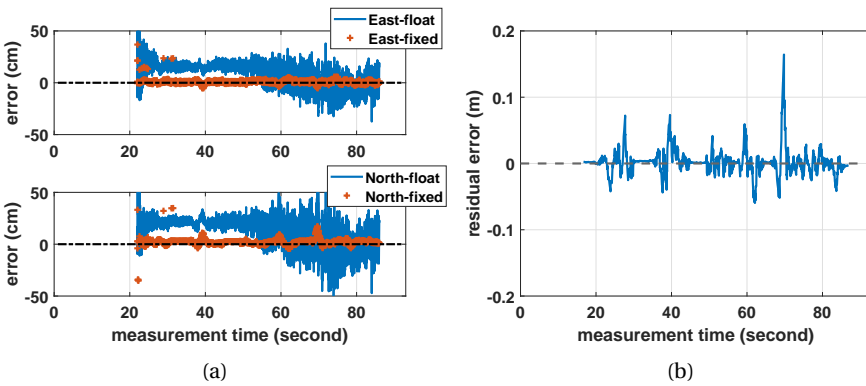


Figure 7.39: (a) Position error of ambiguity-float (in blue) and ambiguity-fixed (in red) solutions in both East direction (top) and North direction (bottom). (b) Residual error of the distance between two prisms based on the interpolated ground truth trajectory of the prisms, with respect to a priori measured distance. RMSE of the residual error is 1.92 cm.

ror of the ground-truth, Fig. 7.39(b) shows the difference between the distance of the two interpolated prism trajectories and the distance measured by the ruler (similar to Fig. 7.9(b)). A large difference in the distance between two prisms may indicate a large error in the ground truth of the receiver position, which explains the occurrence of a few spikes in the fixed position error (in red) for both directions.

In addition, to analyse the precision of the solution, Fig. 7.40 shows the formal standard deviation of the ambiguity-float position solution at epoch $t_2$ and the residual clock offset, based on (6.42). The standard deviation (i.e., the precision) of the solution first comes down a long way with elapsed time, then increases, and then decreases, which is also in line with the variation of the position error

shown in Fig. 7.39(a). The variance matrix is determined by (4.31), and here the SNR is simply determined by the ratio between the received signal power and the received noise power. However, it may be that due to multipath fading, the received signal power and the resulting SNR are determined less accurately, which explains a large variation in Fig. 7.40, even within a small change in distance.
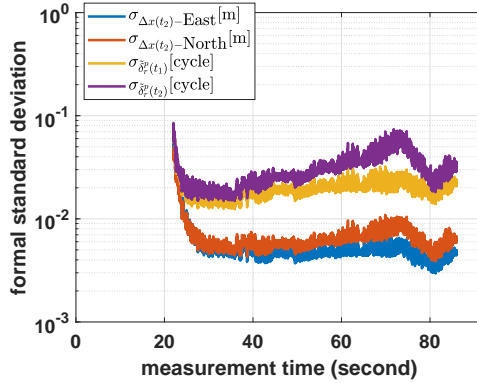


Figure 7.40: Formal standard deviation of the ambiguity-float position solution at epoch $t_2$ (in meter), and residual clock offset (in cycle) at both $t_1$ and $t_2$, when using PoA measurements for positioning.

Although the receiver moves as time elapses, which creates a change in geometry, the positioning model is relatively weak and susceptible to unmodelled errors (e.g., multipath). Hence, the position solution still contains a relatively large error, as shown in Fig. 7.39(a). One can analyse the LSE coefficients $\Xi_{\text{ft}}$ (cf. (6.27)) of using the PoA-based positioning model to compute the float solution, given the geometry of run-1. As an example, Fig. 7.41 shows $[\Xi_{\text{ft}}]_{i,8}$ and $[\Xi_{\text{ft}}]_{i,10}$, which correspond to the contribution of the carrier phase from Tx-2 and Tx-4 at time epoch $t_2$ in (6.38) (i.e., $\varphi_r^2(t_2)$ and $\varphi_r^4(t_2)$)to the solution in East and North direction at $t_1$ and $t_2$ for $i= 1, 2, 3, 4$, respectively. Due to the poor geometry at the starting point and the limited redundancy of the PoA-based positioning model, the elements in $[\Xi_{\text{ft}}]_{i,8}$ and $[\Xi_{\text{ft}}]_{i,10}$ for the 2D position solution are large, about ±10-30, which is much larger than the one shown in Fig. 7.32, and this will consequently amplify noise and errors in these measurements.

As a change in height is not considered in a 2D positioning model (i.e., the height is kept constant to the value determined by the total station at epoch $t_1$), Fig. 7.42 shows the unmodelled error in the measurements $\nabla\varphi_r$ originating from a constant 5 cm height offset in the receiver position. Generally, a 1-2 cm offset will thereby be propagated to the measurements. Given the positioning model and the resulting LSE coefficients in Fig. 7.41(a), such a small offset will be substantially enlarged in the float position solution. Additionally, an unmodelled error could also be introduced by multipath.

Once the carrier phase ambiguities are reliably fixed into the integer numbers, we treat them as deterministic parameters. Consequently, the conditional LSE coefficients for the fixed solution $[\Xi_{\text{fx}}]_{i,8}$ and $[\Xi_{\text{fx}}]_{i,10}$ are shown in Fig. 7.41 (b).

(a)                                                        (b)
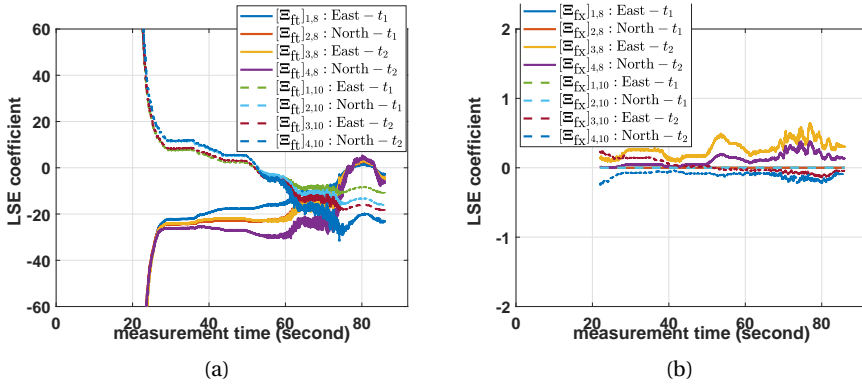
Figure 7.41: LSE coefficients of PoA-based positioning model in run-1 for measurements taken at epoch $t_2$ from Tx-2 and Tx-4, for both (a) ambiguity-float and (b) ambiguity-fixed solution. The integer phase ambiguities are assumed to be known and deterministic when computing coefficients for fixed solution.
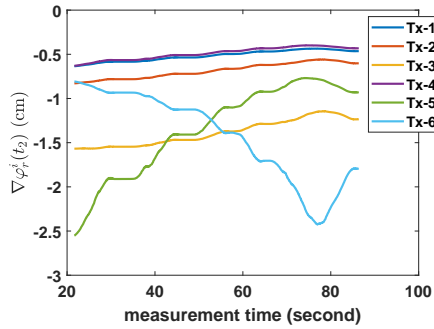


Figure 7.42: Unmodelled error $\nabla \varphi_r^i$ in phase measurement originating from an unaccounted constant 5 cm height offset of the receiver (in 2D positioning), given the positioning geometry of run-1 shown in Fig. 7.25.

Because of a stronger model, the coefficients become much smaller, and therefore the solution is less sensitive to noise and biases in the measurements. In addition, if the ambiguities are fixed, the carrier phase measurements taken at $t_2$ (e.g., $\varphi_r^2(t_2)$) will no longer contribute to the position solution at $t_1$. This explains why there are large errors in the float solution shown in Fig. 7.39(a), while the errors in the fixed solution remain small.

Apart from the position solution, also estimates for the integer phase ambiguities $\tilde{\tilde{\boldsymbol{N}}}_r$ and the residual clock offset $\tilde{\delta}_r^1(t)$ in (6.38) are shown in Fig. 7.43. The residual clock offset $\tilde{\delta}_r^1(t_2)$ in Fig. 7.43(a) as a function of $t_2$ changes by about 1250 cycles in 10 seconds, and therefore the additional phase rotation due to the residual frequency offset, is about 0.125 cycle in the transmission period $T_D = 1$ ms, which should not cause a cycle-slip in phase unwrapping. As shown in Fig. 7.43(a),
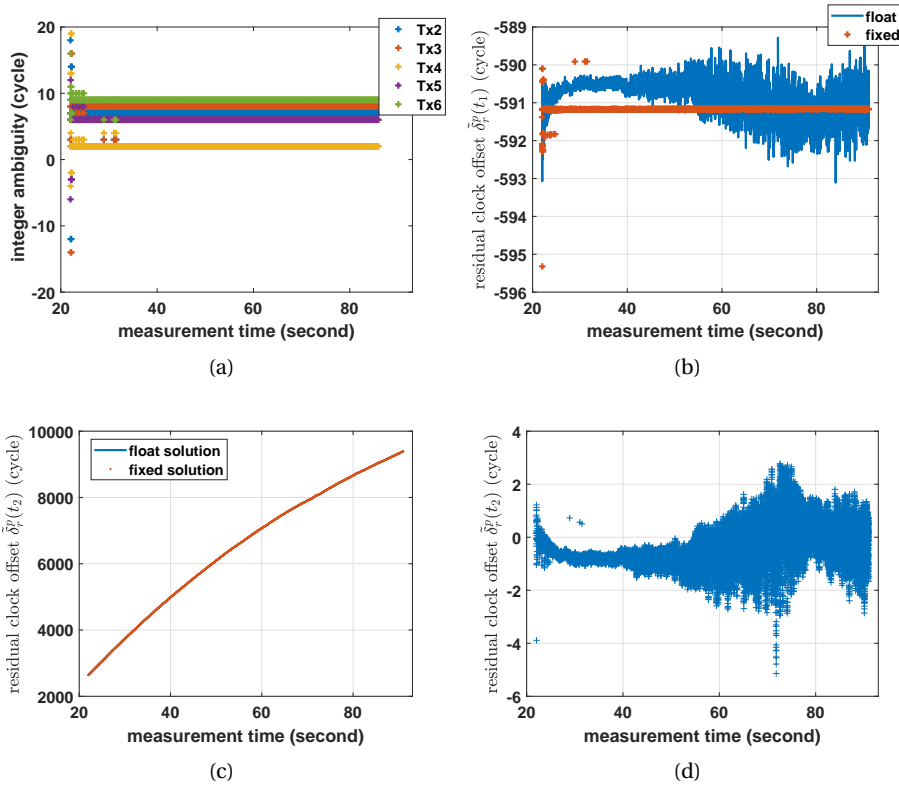
Figure 7.43: (a) Integer carrier phase ambiguity estimates, (b) float and fixed residual clock offset $\tilde{\delta}_r^1(t_1)$, (c) float and fixed residual clock offset $\tilde{\delta}_r^1(t_2)$, (d) difference between the float and fixed residual clock offset $\tilde{\delta}_r^1(t_2)$. Update rate of estimates is 1 kHz.

the carrier phase ambiguities in (6.38) are constant throughout the experiment, though at the beginning, due to a very limited change in geometry, the integer carrier phase ambiguities, though accepted by the ratio-test, are incorrectly fixed.

The residual clock offset $\tilde{\delta}_r^1(t_1)$ is shown in Fig. 7.43(b). As the carrier phase measurements for the first epoch are kept the same as time elapses (i.e., epoch $t_1$ in (6.38) is kept fixed), the residual clock offset $\tilde{\delta}_r^1(t_1)$ should be a constant value. Due to the large LSE coefficient in $\Xi_{ft}$ and the large formal standard deviation as shown in Fig. 7.40, there are large errors in the float solution. However, once the integer phase ambiguities are estimated and accepted, from which the fixed solution is derived, the fixed residual clock offset is approximately constant.

The receiver runs on it own clock in this run, and the change of the clock offset will be reflected in $\tilde{\delta}_r^1(t_2)$, as epoch $t_2$ is varied from 21.5 to 86 seconds, and its float and fixed solution are shown in Fig. 7.43(c). Like in [135], one can use the residual clock offset to estimate the frequency offset of the receiver. For a better visualization, Fig. 7.43(d) shows the difference between the fixed and float resid-

ual clock offset $\tilde{\delta}_r^1(t_2)$. Using the fixed solution for frequency offset estimation will consequently improve its accuracy.

As shown in Fig. 7.38, the receiver stopped at each of the reference points (pnt) for a few seconds. The ground truth of these static reference points can be directly computed by the measurements from the total stations without any interpolation, which will be more accurate than the one of the entire trajectory. As an example, the ambiguity-float and ambiguity-fixed position solution scatters of the static point 2 and 5, and their associated ellipse of concentration is shown in Fig. 7.44(a) and (b), respectively, showing each time a 80-by-80 cm area.



(a)                                                                           (b)
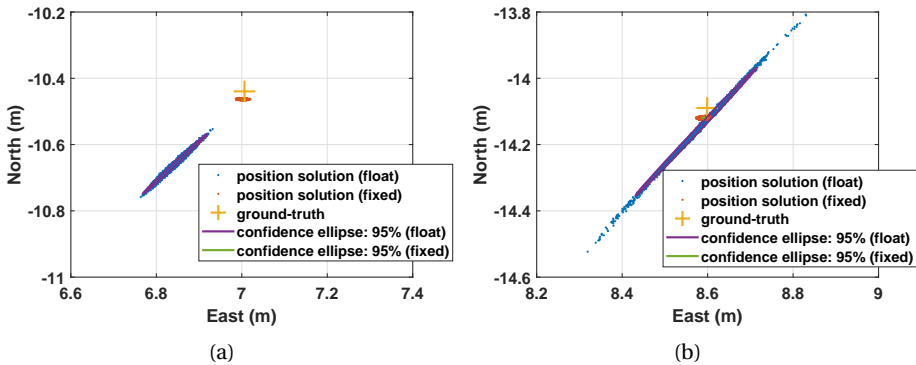
Figure 7.44: 95% ellipse of concentration, receiver position solution and the associated ground truth. (a) pnt-3, standard deviation of ambiguity-float solution in East and North direction is (2.46, 2.95) cm, bias: (-16.26, -21.90) cm; ambiguity-fixed solution, standard deviation in East and North direction is (0.53, 0.11) cm, bias (-0.49, -2.38) cm. (b) pnt-5, standard deviation of ambiguity-float solution in East and North direction is (7.67, 10.69) cm, bias: (-2.61, 7.19) cm; ambiguity-fixed solution, standard deviation in East and North direction is (0.56, 0.21) cm, bias (-0.88, -2.98) cm.

For the static reference point 3 (i.e., 'pnt-3' shown in Fig. 7.38), the lengths of the semi-major and semi-minor axes of the 95% ellipse of the ambiguity-float solution are 11.81 cm and 0.43 cm, respectively. 4129 out of the 4141 points (99.71%) lie within the 95% position error ellipse. Hence, the empirical percentage approximately agrees with the formal probability. However, as shown in Fig. 7.44(a), the 95% ellipse of concentration of the ambiguity-fixed solution does not match the ambiguity-fixed solution scatters. This could be caused by an unmodelled error, such as each of the transmitters experiencing slightly different (time-dependent and transmitter-dependent) clock jitters (e.g., see Fig. 7.28(b)). Due to the unmodelled error, the empirical standard deviation can become larger than the formal standard deviation. The empirical standard deviation of the ambiguity float solution is 2.46 cm and 2.95 cm in East and North direction, respectively, and the 0.53 cm and 0.11 cm for the ambiguity fixed solution. Hence, the ambiguity-fixed solution can ultimately offer higher precision than the ambiguity-float solutions. Compared with the ground truth position, the empirical bias of the ambiguity-float position solution in East and North direction is -16.26 cm and -21.90 cm,

respectively, and -0.49 cm and -2.38 cm for the ambiguity-fixed solutions.

Similarly, in Fig. 7.44(b) for the static reference point 5 (i.e., 'pnt-5' shown in Fig. 7.38) the lengths of the semi-major and semi-minor axes of the 95% ellipse of the ambiguity-float solution are 23.92 cm and 0.55 cm, respectively. 1983 out of the 2151 points (92.19%) lie within the 95% position error ellipse. Hence, the empirical percentage approximately agrees with the formal probability. If the carrier phase cycle ambiguity can be properly fixed into integer numbers, the fixed solution can achieve a higher accuracy than the float solutions.

### Fixed time span - both epoch $t_1$ and $t_2$ varying

Different from the configuration shown in Fig. 7.26, in which the measurements taken at epoch $t_1$ are kept fixed, one can change both the measurements taken at $t_1$ and $t_2$, as shown in Fig. 7.45. As a change in geometry is required, and the receiver was operated in stop-and-go mode, we set the time difference between $t_1$ and $t_2$ constant, shown in Fig. 7.45, to 45 seconds, in order to guarantee a sufficient change in geometry during this period.
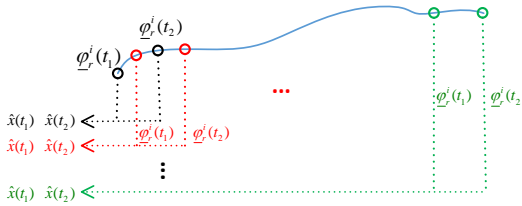


Figure 7.45: Configuration of carrier-phase-based positioning model using measurements taken at two epochs. The measurements taken at $t_1$ and $t_2$ are varied, while the time difference between $t_1$ and $t_2$ is kept constant.

As the total measurement time for this run is 91 seconds, and the time difference between $t_1$ and $t_2$ is set to be 45 seconds, the position solution for $\hat{x}(t_1)$ in (6.38) covers the first 46 seconds of the measurement time, and $\hat{x}(t_2)$ covers the last 46 seconds of the measurement time. Fig. 7.46 shows the ambiguity-float and fixed receiver position solutions, and the ground truth values. Compared with the solutions shown in Fig. 7.38, one can obtain solutions for the starting epochs. However, the first solution will only be available after 45 seconds from the start of the experiment.

To evaluate the positioning performance, we compute the error of the receiver position solution. To reconstruct the position solution for the entire receiver trajectory, we combine the solution $\boldsymbol{x}(t_1)$ for the first 45 seconds, and the solution $\boldsymbol{x}(t_2)$ for the last 46 seconds of the experiment. The position error in East and North direction are shown in Fig. 7.47(a). The RMSEs of the ambiguity-float solution in East and North direction are 12.71 cm and 18.24 cm, respectively, which are close to the performance shown in Table. 7.4 (see 'PoA float' for run-1). 90.8% of the integer carrier phase cycle ambiguities are accepted by the ratio test, which
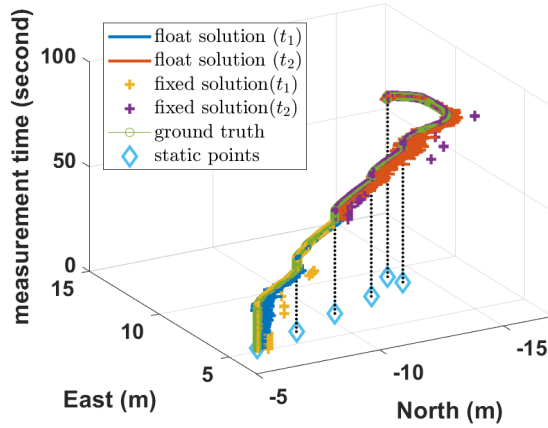
Figure 7.46: Ambiguity-fixed and float position solution for both at $t_1$ and $t_2$ (with a fixed time span of 45 seconds between $t_1$ and $t_2$), and ground truth of the receiver trajectory.

is smaller than the one shown in Table. 7.4, due to a limited change of geometry between $t_1$ and $t_2$. The RMSEs of the resulting ambiguity-fixed solution in East and North direction are 2.86 cm and 4.69 cm. The RMSEs of the ambiguity-fixed solution with both $t_1$ and $t_2$ varying are also slightly larger than the one shown in Table. 7.4, because of wrongly fixed integer carrier phase cycle ambiguities (also see Fig. 7.46).
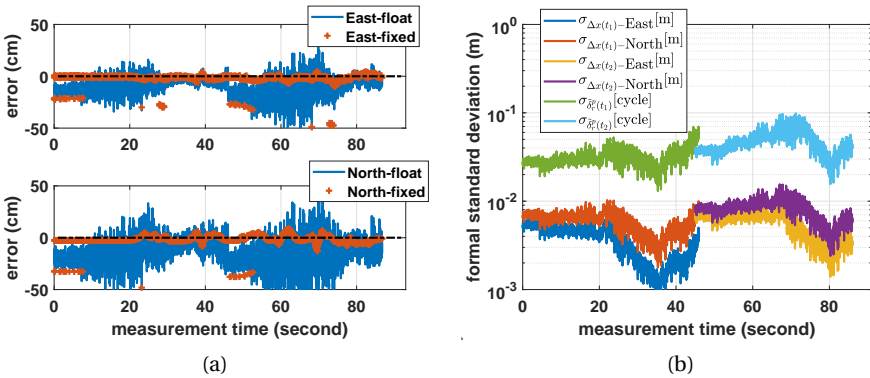


Figure 7.47: (a) Position error of ambiguity-float (in blue) and ambiguity-fixed (in red) solutions in both East and North direction. (b) Formal standard derivation of the estimators of receiver position coordinates and the residual clock offset at both $t_1$ and $t_2$, and the time difference between $t_1$ and $t_2$ is kept constant as shown in Fig. 7.45.

In addition, the formal standard deviation is shown in Fig. 7.47(b), when the time difference between $t_1$ and $t_2$ in the PoA-based positioning model (6.38) is always kept constant. The formal standard deviations shown in Fig. 7.47(b) are

similar to the ones shown in Fig. 7.40 after convergence, as the time difference between epoch $t_1$ and epoch $t_2$ is fixed to 45 seconds which already guarantees a sufficient change in geometry.

### 7.4.4. Fine Frequency Offset Estimation

In this subsection, as a continuation of section 7.3.2, we evaluate the performance of fine frequency offset estimation based on a series of residual clock offset $\hat{\tilde{\delta}}_r^p(t_2)$ obtained from the PoA-based positioning model (cf. (6.38)). Based on the receiver setup shown in Fig. 7.8(a), Fig. 7.48 shows the carrier phase measurements (i.e., PoA) obtained from an asynchronous receiver. The carrier frequency has been coarsely compensated during the carrier phase unwrapping (see Fig. 4.15).
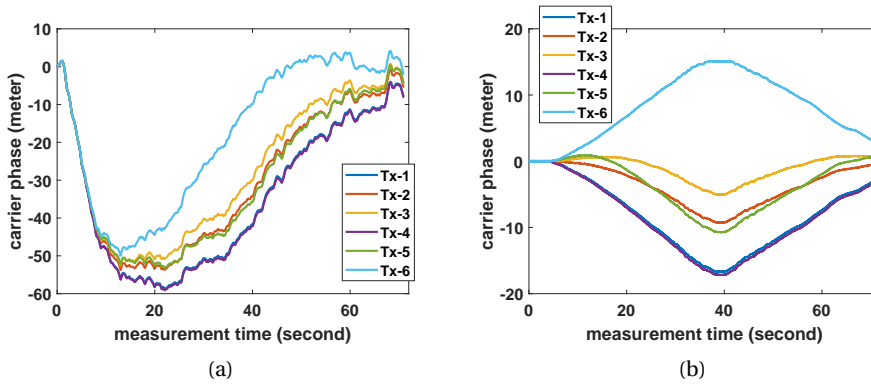


Figure 7.48: Unwrapped carrier phase measurements, in which the carrier frequency offset has been coarsely compensated based on (a) shortened Moose's symbol (shown in Fig. 7.49), (b) pseudo-range clock offset derived from ToA-based positioning model (shown in Fig. 7.23).

Fig. 7.48(a) presents the PoA measurements when the coarse carrier frequency estimate is derived by the shortened Moose's symbol (cf. (4.41)). Using the Moose's symbol for carrier frequency estimation, as the CFO is estimated independently for each of the symbols, no phase tracking is required. Here, as shown in Fig. 7.49, the CFO is estimated for every received Moose's symbol in the received packets within 1 second, and its mean value over this 1 second time span is used to compensate the CFO for the received signal packets in the next second. As the coarse CFO estimate derived from the shortened Moose's symbol is not so accurate, the carrier phase measurements shown in Fig. 7.48(a) are still dominated by the residual clock offset, and the receiver motion pattern cannot be clearly recognized.

On the other hand, the frequency offset can also be coarsely determined by the pseudo-range clock offset through the ToA-based positioning model (see Fig. 7.23). Because the NFO is estimated from a series of clock offset estimates, carrier phase tracking without cycle-slips is required. The precision of the frequency offset estimator obtained through a series of clock offset estimates is inversely proportional to the transmission period $T_D$ (e.g., 1 ms, see Fig. 2.2), as shown in (6.11).
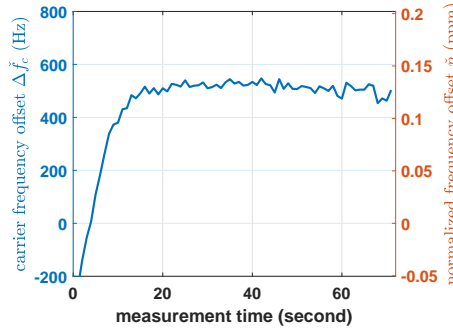
Figure 7.49: Coarse CFO estimates $\Delta \check{f}_c$ based on the shortened Moose's symbol and shown on the left vertical-axis, with an update interval of 1 second. As the transmission period $T_D$ of each transmitter is 1 ms as shown in Fig.2.2(a), and there are 6 transmitters in the current prototype system, 6000 packets are used for coarse CFO estimation. The coarse CFO is determined by averaging over 6000 estimates per second. In addition, based on (2.5), the equivalent normalized frequency offset $\check{\eta}$ is shown on the right vertical-axis with a unit of ppm.

On the other hand, as shown in (4.41), the precision of the frequency offset estimator derived from a shortened Moose's symbol is inversely proportional to the symbol duration (e.g., 6.4 $\mu$s), which is much smaller than the transmission period $T_D$. Hence, the carrier frequency offset derived from the pseudo-range clock offset $\hat{\varepsilon}_r(t)$ (cf. 6.9) through the ToA-based positioning model is more precise than the one derived from the shortened Moose's symbol. By correspondingly compensating the phase rotation due to the CFO, Fig. 7.48(b) shows the PoA measurements. As most of the frequency offset has been removed, the change of the carrier phase measurements is mainly caused by the movement instead of the clock offset, hence the receiver motion pattern (forth-and-back) can be well recognized in the carrier phase measurements.

After coarsely compensating the CFO when estimating the carrier phase, cycle slips due to the receiver frequency offset can be avoided in the unwrapped carrier phase measurement. As long as no cycle slip occurs, the residual CFO can be estimated from the residual clock offset $\tilde{\delta}_r^p(t_2)$ through the PoA-based positioning model (cf. (6.38), and (6.48)), as the fine frequency offset estimate. The carrier phase measurement for epoch $t_1$ in (6.38) is fixed to the measurement taken at the start of this run, and the measurement for $t_2$ changes as time elapses. Consequently, the residual clock offset estimate $\hat{\tilde{\delta}}(t_1)$ will remain constant, and the residual clock offset estimate $\hat{\tilde{\delta}}(t_2)$ shows the change of the clock offset with respect to the one at $t_1$ (i.e., the start of this run).

When the coarse CFO is estimated and compensated by using the shortened Moose's symbol, Fig. 7.50 (a) and (b) shows the ambiguity-float residual clock offset $\hat{\tilde{\delta}}_r^p(t_1)$ and $\hat{\tilde{\delta}}_r^p(t_2)$, respectively. The change of the residual clock offset $\hat{\tilde{\delta}}_r^p(t_2)$ is close the change of the carrier phase measurement shown in Fig. 7.48(a), which is dominated by the residual clock offset.
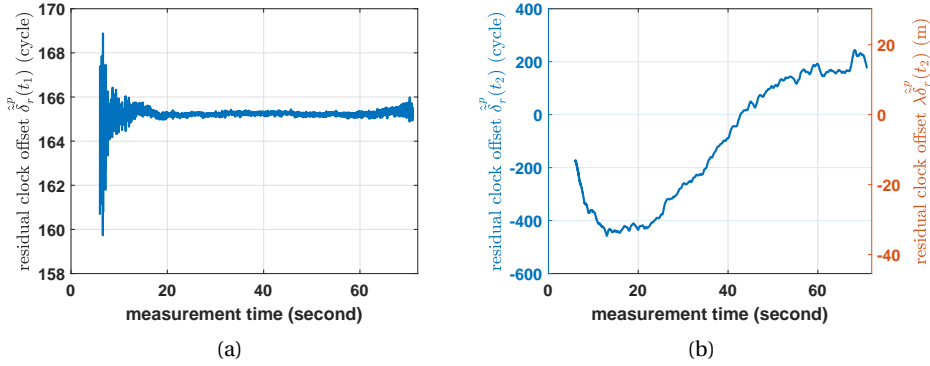
Figure 7.50: (a) Residual clock offset $\hat{\tilde{\delta}}_r^p(t_1)$ of pivot transmitter Tx-1 ($p = 1$), (b) residual clock offset $\hat{\tilde{\delta}}_r^p(t_2)$. Coarse carrier frequency offset has been estimated and compensated by using the shortened Moose's symbol (cf. (4.41)), and carrier phase cycle ambiguities are treated as float numbers in (6.38).
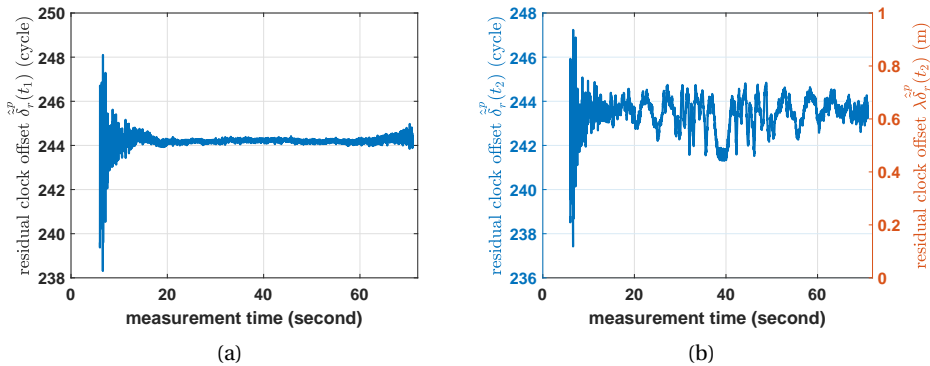


Figure 7.51: (a) Residual clock offset $\hat{\tilde{\delta}}_r^p(t_1)$ of pivot transmitter Tx-1 ($p$=1), (b) residual clock offset $\hat{\tilde{\delta}}_r^p(t_2)$. Coarse carrier frequency offset has been estimated and compensated by using a series of pseudo-range clock offset estimates $\hat{\epsilon}_r(t)$ (cf. 6.9) through ToA-based positioning model (6.38), and carrier phase cycle ambiguities are treated as float numbers in (6.38).

On the other hand, if the coarse CFO is estimated and compensated by using the pseudo-range clock offset derived from the ToA-based positioning model, Fig. 7.51 (a) and (b) shows the resulting ambiguity-float residual clock offset $\hat{\tilde{\delta}}_r^p(t_1)$ and $\hat{\tilde{\delta}}_r^p(t_2)$, respectively. As the most of the clock offset has already been compensated, the residual clock offset $\hat{\tilde{\delta}}_r^p(t_2)$ shown Fig. 7.51 (b) has far less variations than the one shown in Fig. 7.50(b).

Under the assumption that there is no cycle slips in the carrier phase measurement, and assuming the CFO to be constant within the transmission period

$T_D$ (i.e., update period of the residual clock offset estimate), the fine CFO can be determined by (6.48). Fig. 7.52 shows the resulting fine CFO estimate, based on the residual clock offset $\tilde{\hat{\delta}}_r^p(t_2)$ shown in Fig. 7.50(b) and Fig. 7.51 (b). The carrier frequency offset estimate $\Delta \hat{f}_c$ is updated at the transmission rate $T_D$ (i.e, 1 ms) during the phase unwrapping (see Fig. 4.15), when using the coarse CFO estimates obtained through the ToA-based positioning model. When using the shortened Moose's symbol, the carrier frequency offset estimate is only updated for every 1 second, and the update value is the mean value over this 1 second time span (see Fig. 7.49). Consequently, the variation of the fine CFO estimate derived through the ToA-based positioning model (see 7.52(b)) is slightly larger than the one derived through the shortened Moose's symbol (see Fig. 7.52(a)).
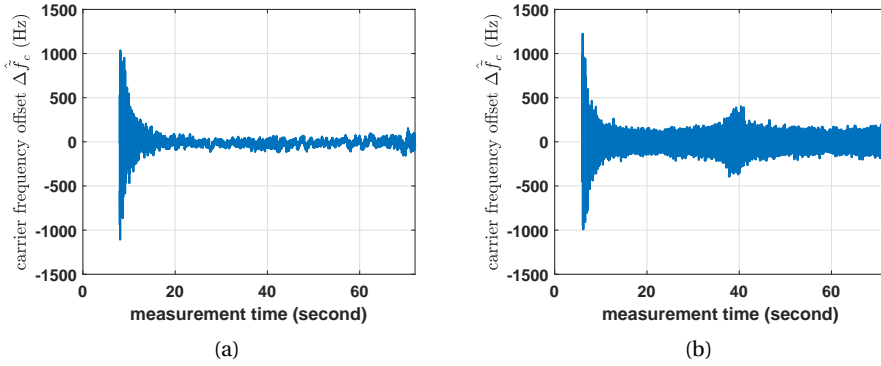


Figure 7.52: Fine carrier frequency offset estimated based on carrier phase measurements, in which carrier frequency offset has been coarsely compensated using estimated clock offset based on (a) shortened Moose's symbol, (b) ToA-based positioning model.

Finally, one can reconstruct the CFO $\Delta \hat{f}_c(t)$ by combining the coarse CFO estimate $\Delta \check{f}_c(t)$ and the fine CFO estimate $\Delta \tilde{\hat{f}}_c(t)$ (cf. (6.51)). Fig. 7.53 (a) shows the combination of the coarse and fine CFO estimates (cf. (6.51)). Although different approaches can be applied for coarse CFO estimation and compensation, the combination of the coarse and fine estimate will be approximately the same, and the ultimate precision of the CFO estimator will be determined by the precision of the fine CFO estimator. Additionally, the formal standard deviation of the fine normalized frequency offset (NFO), propagated from the formal standard deviation of the fine CFO estimator (cf. (6.50)), is shown in Fig. 7.53 (b). Compared with the formal standard deviation of the coarse NFO shown in Fig. 7.22, the fine NFO estimator, derived from the residual clock offset through the PoA-based positioning model, can achieve a higher precision (i.e., smaller formal standard deviation).
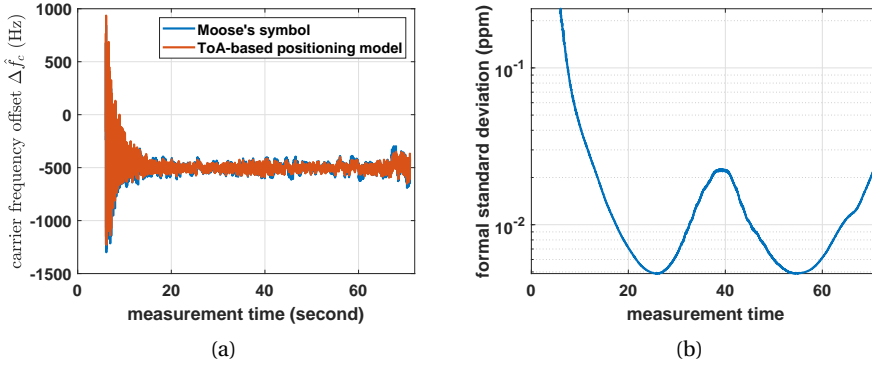
Figure 7.53: (a) Carrier frequency offset $\Delta \hat{f}_c$ (cf. (6.51)), reconstruct by adding coarse CFO estimate $\Delta \check{f}_c$ and fine CFO estimate $\Delta \hat{\hat{f}}_c$. The coarse CFO estimate is derived by using either shortened Moose's symbol (blue-line) or ToA-based positioning model (red-line). (b) Formal standard deviation of fine normalized frequency offset (NFO) estimator (derived from fine CFO estimator, cf. (2.5)), when SNRs of all Tx-Rx pairs are assumed to be 10 dB, and all signal bands ($M = M_a = 16$) are used for ranging.

## 7.5. Summary

In this chapter, several experiments were carried out to evaluate the performance of positioning and frequency synchronization, using the on-purpose built SuperGPS prototype system.

First, based on the phase-of-arrival (PoA)-based relative positioning model (cf. (6.53)), in which the carrier phase cycle ambiguities are eliminated, one can jointly estimate the 2D receiver position coordinates and the antenna phase center offset (PCO). In the experiment, both the transmitters and the receiver were equipped with the same type of antenna, and were synchronized through a commonly distributed time and frequency reference signal. The position of the antenna reference points (ARP) are determined a priori by a land-surveying total station. The experimental result shows that the PCO of the antenna [157] used in our experiments, is offset by about 8.04 cm with respect to the user-defined ARP.

Then, outdoor experiments were carried out, in which all transmitters were synchronized by an optically distributed time and frequency reference signal through the White-Rabbit Precision Time Protocol (WR-PTP). The ranging signal occupying a bandwidth of 160 MHz was up-converted to the central carrier frequency $f_c$ of 3960 MHz. By default, all $M = 16$ signal bands of 10 MHz each are used for ranging. All transmitters transmitted their ranging signals in a time division multiplexing (TDM) scheme, with a transmission period of $T_D = 1$ ms (see Fig. 2.2). The time delay and carrier phase are estimated based on a simplified model, in which only a single path is considered (cf. 3.35 and (4.22)).

Positioning based on the time delay measurement (i.e., time-of-arrival (ToA) measurement) generally delivers a decimeter level accuracy and a centimeter level precision. To reduce the computational complexity and improve spectrum effi-

ciency, one can occupy only a few signal bands for ranging (e.g., $M_a$ = 7). The resulting accuracy of the position solution only slightly deteriorates, compared with using all $M$ = 16 signal bands, and overall a decimeter level accuracy can be maintained. Based on the ToA-based positioning model, the pseudo-range clock offset $\epsilon_r(t)$ estimated along with the receiver position coordinates, can be used for coarse frequency offset estimation and compensation. Generally, the formal standard deviation of the coarse normalized frequency offset (NFO) was found to be smaller than 0.045 ppm (part-per-million) in our experiment, when the SNR is assumed to be 10 dB.

Based on the carrier phase measurement (i.e., phase-of-arrival (PoA) measurement), or the differenced carrier phase measurement (i.e., phase-difference-of-arrival (PDoA) measurement), a centimeter to decimeter level accuracy is achieved for the ambiguity-float position solution. To be able to exploit the integer nature of the carrier phase cycle ambiguities, a correction file produced by the carrier phase measurements taken from all transmitters at a known position is used to account for different initial phase offsets and hardware delays among transmitters. Then a centimeter level accuracy and millimeter level precision is achieved for the ambiguity-fixed solution. The experimental results also show that fast and correct integer ambiguity resolution is possible, which largely reduces the requirement for receiver displacement in a terrestrial positioning system. As the carrier frequency offset has been coarsely compensated prior to phase unwrapping, the residual clock offset can be estimated along with the receiver position coordinates and the carrier phase ambiguities. Based on a series of residual clock offset estimates, one can estimate the residual frequency offset. The formal standard derivation of the fine NFO is generally smaller than 0.02 ppm, when the SNR is assumed to be 10 dB.

**7**

# 8

# Conclusions and Recommendations

As a backup or a complement to existing GNSS, and to provide accurate positioning navigation and timing (PNT) services, the project 'SuperGPS: accurate timing and positioning through an optical-wireless distributed time and frequency reference' has been proposed and launched. The project is funded by the Dutch Research Council (NWO) under Grant 13970. This thesis covers wireless-related research subjects of this project, including ranging signal design, range estimation, and positioning. The details of these subjects and the experimental validations have been presented in previous chapters. In this chapter, we conclude the main findings of the research and present recommendations for further research, as well as practical implementation.

## 8.1. Conclusions

The requirements of a terrestrial positioning system have been described in section 1.1.4. Here, we conclude our work in relation to these requirements, and summarize the positioning performance of the developed SuperGPS prototype system.

### 8.1.1. Methodologies

In this subsection, we summarize our work presented in this thesis, as solutions to meet the requirements as presented in section 1.1.4.

- *the radio transmitters should be synchronized in time and frequency*

For positioning, all transmitters need to be synchronized in time and frequency. In this work, all transmitters were synchronized in time and frequency, using a 1 PPS (pulse-per-second) and 10 MHz reference signal, based on white rabbit precision

time protocol (WR-PTP) through an optical Ethernet network, with hundreds of pico-seconds accuracy.

- *to compute the position solution of a radio receiver, the position of the transmitters should be measured/estimated a priori*

In order to accurately compute the receiver position coordinates, the electromagnetic (EM) antenna phase center for both the transmitters and the receiver need to be accurately determined. In our system, all transmitters and the receiver are equipped with the same type of antenna, and it is assumed that the antenna phase center offset (PCO) between the user-defined antenna reference point (ARP) and the EM phase center is mainly present along the vertical axis. The antenna phase center offset can be determined by using the carrier-phase-based relative positioning model with a known receiver starting position. As the antenna PCO is a time-invariant parameter, it can be derived from the recursive average of a time series of estimates.

- *to support emerging applications, such as IoT, unmanned driving, at least a sub-meter positioning accuracy is required*

In our work, propagation time delay and carrier phase are used for positioning. The precision of the time delay estimator is mainly determined by the ranging signal bandwidth. In a multipath condition, the received signal contains both the LoS and reflected components. If the reflections are not considered in a *simplified* model for time delay estimation, the resulting estimator will become biased. The bias can be evaluated by the *measure of bias*, which depends on the relative gain and relative delay of the reflection with respect to the LoS path. On the other hand, one can consider the reflections in a *full* model, so that the LoS estimator can be unbiased, but the computational complexity will be larger than the one of using the simplified model. In addition, the precision of the LoS estimator derived from the full model may be poor, and this can be evaluated by the *measure of dependence*, which only depends on the relative delay between the reflection and the LoS path.

On the other hand, like in GNSS, one can use carrier phase measurement for precise positioning. Similar to time delay estimation, one can use a simplified model to obtain a biased complex gain estimator with low computational complexity and good precision, or use a full model that considers all reflections to improve the overall accuracy but with high computational complexity. From the estimated complex gain, one can determine the carrier phase. As one can only compute a fractional carrier phase in the range from $-\pi$ to $\pi$, the associated carrier phase cycle ambiguity needs to be resolved in order to compute the position solution. Additionally, to keep the carrier phase cycle ambiguity constant, carrier phase tracking is required, so that any change in carrier phase cycle will be absorbed in the carrier phase measurements for positioning.

The ranging signal from each transmitter is transmitted as burst-like packets with an update period of $T_D$. Hence, the carrier phase cannot be continuously

tracked, and it is computed with an update period of $T_D$. If the change of the carrier phase within the period of $T_D$ is larger than one cycle (for instance due to a frequency offset at the receiver, or due to receiver motion), cycle slips will occur in the resulting series of carrier phase measurements. To avoid such an issue, one can coarsely compensate the carrier frequency offset when estimating the carrier phase, based on a series of clock offset estimates obtained through a time-delay-based positioning model, or based on a shortened Moose's symbol (see Fig. 2.2).

Alternatively, to avoid cycle slips introduced by the receiver frequency offset, one can compute differences of carrier phase measurements between transmitters (i.e., phase-difference-of-arrival (PDoA) measurement), as all transmitters are frequency synchronized, and the clock offset introduced by the receiver frequency offset can be effectively eliminated. Using the PDoA measurement for positioning can also enable a large transmission period $T_D$, though the receiver moving speed should still be taken into consideration, to avoid the occurrence of cycle slips in series of carrier phase measurements.

Positioning based on the time delay measurement is straightforward. One can instantaneously compute the receiver position coordinates and the clock offset using a single epoch of measurements taken from at least $N_d$+1 transmitters, where $N_d$ is the positioning dimension. Positioning based on carrier phase measurements requires a change of geometry, and hence a time series of carrier phase measurements taken from the transmitters is needed. As the transmitters in a terrestrial positioning system are static, receiver displacement is required to create the change of the positioning geometry. Using the carrier phase measurements taken from two epochs, of at least $2N_d + 1$ transmitters are needed for carrier-phase-based positioning.

By default, due to different phase biases among different transmitters, which are time-invariant and transmitter-dependent, and cannot be separated from the carrier phase cycle ambiguities that are also time-invariant and transmitter-dependent, the carrier phase cycle ambiguities are treated as constant float values in the positioning model. Consequently, one can only obtain the so-called *float* solution. As a change of the geometry is required for carrier-phase-based positioning, depending on the geometry, the receiver may need to move for a large distance in order to let the precision of the position solution converge to centimeter level.

Once the phase biases in the transmitters are accounted for, one can exploit the integer nature of the carrier phase cycle ambiguities. As all transmitters are synchronized through the optically distributed time and frequency reference signal, the phase biases in the transmitters are time invariant, as long as the operational condition (e.g., temperature) does not change significantly, and the transmitters are not restarted. Then, a snapshot carrier phase measurement taken from a known transmitter at a known position is used to produce a *correction* for each Tx-Rx link. By taking the difference between the snapshot correction and a carrier phase measurement, the integer nature of the carrier phase cycle ambiguity is preserved. Then, using the LAMBDA method, one can fix the carrier phase cycle ambiguities into integer number, and obtain the so-called *fixed* solution. An ambiguity-fixed position solution can provide a high precision, and fixing is al-

**8**

ready possible with a little change of geometry.

> • *A relatively large (virtual) signal bandwidth is needed to improve the resolvability of different paths and overcome multipath effects, which often occur in an urban and indoor environment*

The precision of time delay estimation is inversely proportional to the signal bandwidth, based on the analysis of the Cramér-Rao lower bound (CRLB). At least a few MHz signal bandwidth is needed for a decimeter-level ranging precision, and hundreds of MHz signal bandwidth is required for a centimeter-level ranging precision. Instead of using a large total signal bandwidth entirely, one can, for example, use a multi-band signal occupying only some of the spectral resources of the total signal bandwidth. The ranging performance can still benefit from a large virtual signal bandwidth, which is the bandwidth between two signal bands at the edges of the occupied spectrum.

To sparsely select signal bands for ranging, one needs to consider multipath which is the major error source in a terrestrial positioning system. Given the signal spectrum, the CRLB derived from a single path channel indicates the best precision of time delay estimation. If the ranging signal design is only guided by the CRLB of time delay estimation derived from a single-path channel, then the designed signal will be likely very sparse, which indeed offers good ranging precision, but could lead to a large bias and ultimately poor accuracy in multipath conditions.

The measure of dependence for time delay estimation, defined in this thesis, indicates how precision changes, when a reflection in a multipath channel is additionally considered in the model. The measure of bias shows how large a bias can be, when a certain reflection is not considered in the model for time delay estimation. We proposed to design a sparse multiband signal based on the CRLB of time delay estimation derived from a single path channel, the measure of dependence and the measure of bias, as overall ranging performance metrics. Consequently, not every reflection needs to be considered in the model for time delay and carrier phase estimation, such that the ranging precision will not deteriorate by considering many reflections in the model, and the bias due to neglecting some reflections in the model will be kept small.

### **8.1.2.** Validation Results

An indoor experiment was carried out to determine the antenna phase center of the wideband antenna [157]. Using carrier phase measurements, the antenna phase center offset (PCO) between the actual phase center and the user-defined antenna reference point (ARP) is about 8.0 cm, which serves as a calibration value for later experiment.

An outdoor experiment was carried out to evaluate the positioning performance of using time delay and carrier phase, with the developed SuperGPS prototype system. All six transmitters were synchronized through the optically distributed time and frequency reference signal, generated from a central atomic clock. The transmitters were placed in an area of 20-by-50 m, at heights between

3.5 m and 5.5 m. Considering a 2D positioning scenario, the receiver antenna height is assumed to be constant and known during the experiment, and one only needs to estimate the receiver position coordinates in local East and North direction.

To estimate the time delay and carrier phase, only a simplified model is used, in which no reflection is considered. Particularly, for carrier phase tracking, the carrier frequency offset needs to be coarsely compensated to avoid cycle slips. The coarse carrier frequency offset estimates were derived from the shortened Moose's symbol or a series of pseudo-range clock offsets through a time-delay-based positioning model. One can also compute the carrier phase differences between the transmitters, to effectively remove the receiver clock offset, and avoid the occurrence of cycle-slips in carrier phase measurements due to the receiver frequency offset.

Using time delay measurements, the root-mean-square-error (RMSE) of the position solution is about 10 cm in both East and North direction. Using carrier phase measurements obtained at two different epochs, of which the first epoch is fixed at the starting epoch and the second epoch is changed till the end of the experiment, the RMSE of the ambiguity-float position solution is generally at a decimeter to centimeter level, depending on the positioning geometry. Using the corrections to account for the different phase biases among the transmitters, such that the integer nature of the carrier phase cycle ambiguities can be exploited, the ambiguity-fixed solution has a centimeter level accuracy and a millimeter level precision, with fast convergence (the receiver only needs to move over a decimeter distance). Additionally, the positioning performance using a sparse multiband signal is only slightly poorer than using all available signal bandwidth.

The clock offset computed along with the receiver position coordinates through the positioning model, can be used for frequency synchronization. A time series of the pseudo-range clock offset estimates obtained from the time-based positioning model can be used for coarse receiver frequency synchronization. The synchronization performance (i.e., variance) depends on the length of the transmission period and the variance of the time delay measurement error. Additionally, the residual clock offset obtained from a carrier-phase-based positioning model can be used for fine receiver frequency offset estimation, as the resulting synchronization performance depends on the variance of the carrier phase measurement error, which is much smaller than the one of the time delay measurement.

## **8.2.** Recommendations

In this thesis, we cover time delay and carrier phase estimation, the design of a sparse multiband ranging signal, positioning models using time delay or carrier phase measurement, and experimental validation results based on the developed SuperGPS terrestrial positioning system. In this section, we provide recommendations for future research, to improve the positioning performance, and to pave the way for implementation of the system in practice.

### 8.2.1. Ranging Signal

As proposed in this thesis, one can use a sparse multiband signal for ranging, of which the signal bands are sparsely placed in the available spectrum. In order to improve the range estimation performance by exploiting a large virtual signal bandwidth, one needs to coherently use the information from all sparsely placed signal bands. In this work, all signal bands are coherently and simultaneously transmitted/received through a single RF front-end, in order to keep all signal bands phase synchronized (i.e., $\theta_m$ in (2.21) equals to 0). In future research, this may be done more efficiently through frequency hopping. The receiver can then transmit each of the signal bands sequentially on a different central carrier frequency through a single RF front-end. Transmitting and receiving the multiband signal based on frequency hopping, can largely reduce the sampling rate of the ADC/DAC, which no longer needs to cover the entire virtual signal bandwidth. However, different central carriers generated for different signal bands should be phase synchronized, in order to coherently combine the received signal from different signal bands. To estimate and compensate the phase differences on different central carriers, the reader can refer to [57, 166]

Additionally, in this work, it is assumed that all signal bands experience the same channel. However, in practice, the gain and the phase distortion can be frequency-dependent, particularly due to the RF front-end (e.g., amplifier, filters) that covers a large virtual signal bandwidth (e.g., $\geq 500$ MHz). An additional calibration for different signal bands is required. For example, the reader can refer to [167]

Moreover, the ranging signal packet, as shown in Fig. 2.2, can be simplified in future research. In principle, only one OFDM training symbol is needed to estimate the channel frequency response, from which one can derive the range information. In addition, as much larger signal bandwidths will become available (e.g., 80 MHz ~ 160 MHz) in emerging wireless communication networks, such as WiFi [168] and 5G [44], one can use such signals for opportunistic ranging and positioning, based on channel sounding measurements [169] obtained through the training symbols.

### 8.2.2. Range Observable

In this work, we only focus on using time delay and carrier phase for positioning. As shown in Fig. 4.13, one can apply a loop filter in the PLL for carrier phase tracking, so that part of the error introduced by multipath and the clock jitter (see Fig. 7.28) can be mitigated, which, however, also changes the noise characteristic of the carrier phase observable. Similarly, a delay-locked-loop (DLL) with a loop filter can also be applied for time delay tracking.

In addition, future wireless communication networks tend to apply millimeter-wave (mmWave) in order enable ultra-low-latency and ultra-wideband services. As the wavelength of the central carrier is at the mm-level, carrier phase tracking is unlikely achievable, as any variation larger than the millimeter wavelength will cause a cycle slip. Hence, in a mmWave-based system, with more bandwidth available, it will be more practical to use time delay or angle measurement for po-

sitioning.

Recently, Angle-of-Arrival (AoA) or Direction-of-Arrival (DoA) becomes more and more attractive, because of the resulting spatial information obtained from an antenna array. For example, multiple-input multiple-output (MIMO) has been adopted in 5G/6G [170, 171] and WiFi (IEEE 802.11n/ac/ax) [168, 172]. Based on the available angle measurements, such signals can be used as Signal-of-Opportunities (SOP) for positioning.

### 8.2.3. Positioning Models

Time delay and carrier phase have been used separately for positioning in this thesis. Combining the time delay and carrier phase measurements for positioning is left for future research. The clock offset in the time delay ($\rho_\eta(t)$ in (6.4)) and carrier phase ($\tilde{\phi}_\eta(t)$ in (6.17)) measurement can be different, as a part of the clock offset in the carrier phase measurement can have been compensated. To effectively remove the clock offset, one can use the differenced time delay (i.e., time-difference-of-arrival (TDoA) measurement) and the differenced carrier phase measurement (i.e., phase-difference-of-arrival (PDoA) measurement) together for positioning.

In addition, a Kalman filter [173] can be applied on a series of range observation to improve the precision. Non-line-of-sight (NLoS) identification and mitigation techniques [27] should be applied in conditions with blockage.

### 8.2.4. System

To fully support a three dimensional (3D) positioning scenario, one needs to create sufficient transmitter height-diversity, so that also the up-direction can be adequately estimated. Additionally, though each transmitter transmits its own ranging signal in a time-division multiplexing scheme to avoid interference from other transmitters, one can also exploit the possibility of using code-division or frequency-division multiplexing scheme in future research. For example, different transmitters can use different sub-carriers/ signal-bands for ranging, but then the unambiguous ranging distance may become different for different transmitters (see Fig. 5.1).

In order to seamlessly integrate the SuperGPS system with GNSS, the position solution obtained from the SuperGPS system presented in a local ENU (East, North, Up) reference system should be transformed into, for example, the European Terrestrial Reference System ETRS89. Alternatively, one can directly survey the SuperGPS transmitter positions with high precision RTK-GNSS, which deliveries coordinates in ETRS89 in Europe. Consequently, the position solutions obtained from the SuperGPS system will be in ETRS89, and can be integrated with the ones obtained from the GNSS.

**8**

# Bibliography

[1] J. A. Klobuchar, "Ionospheric time-delay algorithm for single-frequency GPS users," *IEEE Transactions on Aerospace and Electronic Systems*, no. 3, pp. 325–331, 1987.

[2] D. Odijk, "Positioning model," in *Springer handbook of Global Navigation Satellite Systems* (P. Teunissen and O. Montenbruck, eds.), ch. 21, pp. 605–638, Springer, 2017.

[3] G. Wübbena, M. Schmitz, and A. Bagge, "PPP-RTK: precise point positioning using state-space representation in RTK networks," in *Proceedings of the 18th International Technical Meeting of the Satellite Division of The Institute of Navigation (ION GNSS 2005)*, vol. 5, pp. 13–16, 2005.

[4] S. Skone, "The impact of magnetic storms on GPS receiver performance," *Journal of Geodesy*, vol. 75, no. 9-10, pp. 457–468, 2001.

[5] X. Luo, S. Gu, Y. Lou, C. Xiong, B. Chen, and X. Jin, "Assessing the performance of GPS precise point positioning under different geomagnetic storm conditions during solar cycle 24," *Sensors*, vol. 18, no. 6, p. 1784, 2018.

[6] T. Humphreys, "Interference," in *Springer handbook of Global Navigation Satellite Systems* (P. Teunissen and O. Montenbruck, eds.), ch. 16, pp. 469–594, Springer, 2017.

[7] A. Goldsmith, *Wireless communications*. Cambridge University Press, 2005.

[8] M. S. Braasch, "Multipath," in *Springer handbook of Global Navigation Satellite Systems* (P. Teunissen and O. Montenbruck, eds.), ch. 15, pp. 443–468, Springer, 2017.

[9] J.-H. Won and T. Pany, "Signal processing," in *Springer handbook of Global Navigation Satellite Systems* (P. Teunissen and O. Montenbruck, eds.), ch. 14, pp. 401–442, Springer, 2017.

[10] V. L. Knoop, P. F. de Bakker, C. C. Tiberius, and B. van Arem, "Lane determination with GPS precise point positioning," *IEEE Transactions on Intelligent Transportation Systems*, vol. 18, no. 9, pp. 2503–2513, 2017.

[11] S. Stephenson, X. Meng, T. Moore, A. Baxendale, and T. Ford, "Accuracy requirements and benchmarking position solutions for intelligent transportation location based services," in *Proceedings of the 8th international symposium on location-based services*, 2011.

[12] K.-W. Chiang, G.-J. Tsai, H.-J. Chu, and N. El-Sheimy, "Performance enhancement of INS/GNSS/refreshed-SLAM integration for acceptable lane-level navigation accuracy," *IEEE Transactions on Vehicular Technology*, vol. 69, no. 3, pp. 2463–2476, 2020.

[13] X. Lin, J. Bergman, F. Gunnarsson, O. Liberg, S. M. Razavi, H. S. Razaghi, H. Rydn, and Y. Sui, "Positioning for the internet of things: A 3GPP perspective," *IEEE Communications Magazine*, vol. 55, no. 12, pp. 179–185, 2017.

[14] X. Feng, J. Zhang, J. Chen, G. Wang, L. Zhang, and R. Li, "Design of intelligent bus positioning based on internet of things for smart campus," *IEEE Access*, vol. 6, pp. 60005–60015, 2018.

[15] A. F. G. Ferreira, D. M. A. Fernandes, A. P. Catarino, and J. L. Monteiro, "Localization and positioning systems for emergency responders: A survey," *IEEE Communications Surveys & Tutorials*, vol. 19, no. 4, pp. 2836–2870, 2017.

[16] R. Gold, "Optimal binary sequences for spread spectrum multiplexing (corresp.)," *IEEE Transactions on Information Theory*, vol. 13, no. 4, pp. 619–621, 1967.

[17] J. W. Betz, "Binary offset carrier modulations for radionavigation," *Navigation*, vol. 48, no. 4, pp. 227–246, 2001.

[18] J. Barnes, C. Rizos, J. Wang, D. Small, G. Voigt, and N. Gambale, "Locata: A new positioning technology for high precision indoor and outdoor positioning," in *Proceedings 2003 International Symposium on GPS/GNSS*, pp. 9–18, 2003.

[19] C. Rizos and L. Yang, "Background and recent advances in the Locata terrestrial positioning and timing technology," *Sensors*, vol. 19, no. 8, p. 1821, 2019.

[20] J.-P. Montillet, G. Roberts, C. Hancock, X. Meng, O. Ogundipe, and J. Barnes, "Deploying a Locata network to enable precise positioning in urban canyons," *Journal of Geodesy*, vol. 83, no. 2, pp. 91–103, 2009.

[21] H. S. Cobb, *GPS pseudolites: Theory, design, and applications*. PhD thesis, Stanford University Stanford, CA, USA:, 1997.

[22] J. Barnes, C. Rizos, M. Kanli, A. Pahwa, D. Small, G. Voigt, N. Gambale, and J. Lamance, "High accuracy positioning using Locata's next generation technology," in *Proceedings of the 18th International Technical Meeting of the Satellite Division of The Institute of Navigation (ION GNSS 2005)*, pp. 2049–2056, 2005.

[23] X. Guo, Y. Zhou, J. Wang, K. Liu, and C. Liu, "Precise point positioning for ground-based navigation systems without accurate time synchronization," *GPS Solutions*, vol. 22, no. 34, pp. 1–12, 2018.

[24] G. Bellusci, G. J. Janssen, J. Yan, and C. C. Tiberius, "A sub-sampling receiver architecture for ultra-wideband time of arrival based ranging," in *Proceedings of the 22nd International Technical Meeting of the Satellite Division of The Institute of Navigation (ION GNSS 2009)*, pp. 471–480, 2009.

[25] G. Bellusci, G. J. Janssen, J. Yan, and C. C. Tiberius, "Modeling distance and bandwidth dependency of TOA-based UWB ranging error for positioning," *Research Letters in Communications*, vol. 2009, pp. 1–4, 2009.

[26] Y. Xie, G. J. Janssen, S. Shakeri, and C. C. Tiberius, "UWB pulse detection and TOA estimation using GLRT," *EURASIP Journal on Advances in Signal Processing*, vol. 2017, no. 1, pp. 1–12, 2017.

[27] J. Yan, C. C. Tiberius, G. Bellusci, and G. J. Janssen, "Non-line-of-sight identification for indoor positioning using ultra-wideband radio signals," *Navigation: Journal of The Institute of Navigation*, vol. 60, no. 2, pp. 97–111, 2013.

[28] B. Denis, J.-B. Pierrot, and C. Abou-Rjeily, "Joint distributed synchronization and positioning in UWB ad hoc networks using TOA," *IEEE Transactions on Microwave Theory and Techniques*, vol. 54, no. 4, pp. 1896–1911, 2006.

[29] C. Zhang, M. J. Kuhn, B. C. Merkl, A. E. Fathy, and M. R. Mahfouz, "Real-time noncoherent UWB positioning radar with millimeter range accuracy: Theory and experiment," *IEEE Transactions on Microwave Theory and Techniques*, vol. 58, no. 1, pp. 9–20, 2009.

[30] A. R. J. Ruiz and F. S. Granja, "Comparing Ubisense, Bespoon, and Decawave UWB location systems: Indoor performance analysis," *IEEE Transactions on Instrumentation and Measurement*, vol. 66, no. 8, pp. 2106–2117, 2017.

[31] A. De Angelis, M. Dionigi, A. Moschitta, R. Giglietti, and P. Carbone, "Characterization and modeling of an experimental UWB pulse-based distance measurement system," *IEEE Transactions on Instrumentation and Measurement*, vol. 58, no. 5, pp. 1479–1486, 2009.

[32] S. Marano, W. M. Gifford, H. Wymeersch, and M. Z. Win, "NLOS identification and mitigation for localization based on UWB experimental data," *IEEE Journal on Selected Areas in Communications*, vol. 28, no. 7, pp. 1026–1035, 2010.

[33] I. Güvenç, C.-C. Chong, F. Watanabe, and H. Inamura, "NLOS identification and weighted least-squares localization for UWB systems using multipath channel statistics," *EURASIP Journal on Advances in Signal Processing*, vol. 2008, pp. 1–14, 2007.

[34] J. Khalife, K. Shamaei, and Z. M. Kassas, "Navigation with cellular CDMA signals—part I: Signal modeling and software-defined receiver design," *IEEE Transactions on Signal Processing*, vol. 66, no. 8, pp. 2191–2203, 2018.

[35]  J. Khalife and Z. M. Kassas, "Navigation with cellular CDMA signals—part II: Performance analysis and experimental results," *IEEE Transactions on Signal Processing*, vol. 66, no. 8, pp. 2204–2218, 2018.

[36]  J. J. Caffery and G. L. Stuber, "Overview of radiolocation in CDMA cellular systems," *IEEE Communications Magazine*, vol. 36, no. 4, pp. 38–45, 1998.

[37]  K. Shamaei and Z. M. Kassas, "LTE receiver design and multipath analysis for navigation in urban environments," *Navigation*, vol. 65, no. 4, pp. 655–675, 2018.

[38]  P. Wang and Y. J. Morton, "Multipath estimating delay lock loop for LTE signal TOA estimation in indoor and urban environments," *IEEE Transactions on Wireless Communications*, vol. 19, no. 8, pp. 5518 – 5530, 2020.

[39]  J. A. del Peral-Rosado, J. A. López-Salcedo, G. Seco-Granados, F. Zanier, and M. Crisci, "Joint maximum likelihood time-delay estimation for LTE positioning in multipath channels," *EURASIP Journal on Advances in Signal Processing*, vol. 2014, no. 33, pp. 1–13, 2014.

[40]  K. Shamaei, J. Khalife, and Z. M. Kassas, "Exploiting LTE signals for navigation: Theory to implementation," *IEEE Transactions on Wireless Communications*, vol. 17, no. 4, pp. 2173–2189, 2018.

[41]  J. J. Khalife, S. Bhattacharya, and Z. M. Kassas, "Centimeter-accurate UAV navigation with cellular signals," in *Proceedings of the 31st International Technical Meeting of the Satellite Division of The Institute of Navigation (ION GNSS+ 2018)*, pp. 2321–2331, 2018.

[42]  H. Wymeersch, G. Seco-Granados, G. Destino, D. Dardari, and F. Tufvesson, "5G mmWave positioning for vehicular networks," *IEEE Wireless Communications*, vol. 24, no. 6, pp. 80–86, 2017.

[43]  M. Koivisto, M. Costa, J. Werner, K. Heiska, J. Talvitie, K. Leppänen, V. Koivunen, and M. Valkama, "Joint device positioning and clock synchronization in 5G ultra-dense networks," *IEEE Transactions on Wireless Communications*, vol. 16, no. 5, pp. 2866–2881, 2017.

[44]  A. A. Abdallah, K. Shamaei, and Z. M. Kassas, "Assessing real 5G signals for opportunistic navigation," in *Proceedings of the 33rd International Technical Meeting of the Satellite Division of The Institute of Navigation (ION GNSS+ 2020)*, pp. 2548–2559, 2020.

[45]  J. Khalife, M. Neinavaie, and Z. M. Kassas, "Blind doppler estimation from LEO satellite signals: A case study with real 5G signals," in *Proceedings of the 33rd International Technical Meeting of the Satellite Division of The Institute of Navigation (ION GNSS+ 2020)*, pp. 3046–3054, 2020.

[46] D. Serant, P. Thevenon, M.-L. Boucheret, O. Julien, C. Macabiau, S. Corazza, M. Dervin, and L. Ries, "Development and validation of an OFDM/DVB-T sensor for positioning," in *IEEE/ION Position, Location and Navigation Symposium*, pp. 988–1001, IEEE, 2010.

[47] L. Chen, R. Piché, H. Kuusniemi, and R. Chen, "Adaptive mobile tracking in unknown non-line-of-sight conditions with application to digital tv networks," *EURASIP Journal on Advances in Signal Processing*, vol. 2014, no. 1, pp. 1–10, 2014.

[48] L. Chen, O. Julien, P. Thevenon, D. Serant, A. G. Peña, and H. Kuusniemi, "TOA estimation for positioning with DVB-T signals in outdoor static tests," *IEEE Transactions on Broadcasting*, vol. 61, no. 4, pp. 625–638, 2015.

[49] L. Chen, P. Thevenon, G. Seco-Granados, O. Julien, and H. Kuusniemi, "Analysis on the TOA tracking with DVB-T signals for positioning," *IEEE Transactions on Broadcasting*, vol. 62, no. 4, pp. 957–961, 2016.

[50] J. Huang, L. Lo Presti, and R. Garello, "Digital video broadcast-terrestrial (DVB-T) single frequency networks positioning in dynamic scenarios," *Sensors*, vol. 13, no. 8, pp. 10191–10218, 2013.

[51] C. Yang, L. Chen, O. Julien, S. Andrey, and R. Chen, "Carrier phase tracking of OFDM-based DVB-T signals for precision ranging," in *Proceeding of the 30th International Technical Meeting of The Satellite Division of the Institute of Navigation (ION GNSS+ 2017)*, pp. 736–748, 2017.

[52] Y. Wang, X. Yang, Y. Zhao, Y. Liu, and L. Cuthbert, "Bluetooth positioning using RSSI and triangulation methods," in *2013 IEEE 10th Consumer Communications and Networking Conference (CCNC)*, pp. 837–842, IEEE, 2013.

[53] A. Bekkelien, M. Deriaz, and S. Marchand-Maillet, "Bluetooth indoor positioning," *Master's thesis, University of Geneva*, 2012.

[54] G. De Blasio, A. Quesada-Arencibia, C. R. García, J. C. Rodríguez-Rodríguez, and R. Moreno-Díaz, "A protocol-channel-based indoor positioning performance study for bluetooth low energy," *IEEE Access*, vol. 6, pp. 33440–33450, 2018.

[55] C. Yang and H.-R. Shao, "WiFi-based indoor positioning," *IEEE Communications Magazine*, vol. 53, no. 3, pp. 150–157, 2015.

[56] M. Kotaru, K. Joshi, D. Bharadia, and S. Katti, "Spotfi: Decimeter level localization using WiFi," in *Proceedings of the 2015 ACM Conference on Special Interest Group on Data Communication*, pp. 269–282, 2015.

[57] D. Vasisht, S. Kumar, and D. Katabi, "Decimeter-level localization with a single WiFi access point," in *13th USENIX Symposium on Networked Systems Design and Implementation (NSDI 16)*, pp. 165–178, 2016.

[58] W. Gong and J. Liu, "SiFi: Pushing the limit of time-based WiFi localization using a single commodity access point," *Proceedings of the ACM on Interactive, Mobile, Wearable and Ubiquitous Technologies*, vol. 2, no. 1, pp. 1–21, 2018.

[59] L. Giugno and M. Luise, "Optimum pulse shaping for delay estimation in satellite positioning," in *2005 13th European Signal Processing Conference*, pp. 1–6, IEEE, 2005.

[60] F. Zanier and M. Luise, "Fundamental issues in time-delay estimation of multicarrier signals with applications to next-generation GNSS," in *2008 10th International Workshop on Signal Processing for Space Communications*, pp. 1–8, IEEE, 2008.

[61] F. Zanier, G. Bacci, and M. Luise, "Criteria to improve time-delay estimation of spread spectrum signals in satellite positioning," *IEEE Journal of Selected Topics in Signal Processing*, vol. 3, no. 5, pp. 748–763, 2009.

[62] S. M. Kay, *Fundamentals of statistical signal processing*. Prentice Hall PTR, 1993.

[63] F. Benedetto, G. Giunta, E. S. Lohan, and M. Renfors, "A fast unambiguous acquisition algorithm for BOC-modulated signals," *IEEE Transactions on Vehicular Technology*, vol. 62, no. 3, pp. 1350–1355, 2012.

[64] A. Dammann, T. Jost, R. Raulefs, M. Walter, and S. Zhang, "Optimizing waveforms for positioning in 5G," in *2016 IEEE 17th International Workshop on Signal Processing Advances in Wireless Communications (SPAWC)*, pp. 1–5, IEEE, 2016.

[65] Y. Karisan, D. Dardari, S. Gezici, A. A. D'Amico, and U. Mengali, "Range estimation in multicarrier systems in the presence of interference: Performance limits and optimal signal design," *IEEE Transactions on Wireless Communications*, vol. 10, no. 10, pp. 3321–3331, 2011.

[66] M. D. Larsen, G. Seco-Granados, and A. L. Swindlehurst, "Pilot optimization for time-delay and channel estimation in OFDM systems," in *2011 IEEE International Conference on Acoustics, Speech and Signal Processing (ICASSP)*, pp. 3564–3567, IEEE, 2011.

[67] H. Liu, R. Zhang, J. Liu, and M. Zhang, "Time synchronization in communication networks based on the Beidou foundation enhancement system," *Science China Technological Sciences*, vol. 59, no. 1, pp. 9–15, 2016.

[68] D. Pallier, V. Le Cam, and S. Pillement, "Energy-efficient GPS synchronization for wireless nodes," *IEEE Sensors Journal*, vol. 21, no. 4, pp. 5221–5229, 2020.

[69] K. F. Hasan, Y. Feng, and Y.-C. Tian, "GNSS time synchronization in vehicular ad-hoc networks: benefits and feasibility," *IEEE Transactions on Intelligent Transportation Systems*, vol. 19, no. 12, pp. 3915–3924, 2018.

[70] H. Li, L. Han, R. Duan, and G. M. Garner, "Analysis of the synchronization requirements of 5G and corresponding solutions," *IEEE Communications Standards Magazine*, vol. 1, no. 1, pp. 52–58, 2017.

[71] P. Defraigne and M. C. Martinez, "Combination of TWSTFT and GPS data for time transfer," in *Proceedings of the 22nd European Frequency and Time Forum (EFTF)*, pp. 23–25, 2008.

[72] P. Carbone, A. Cazzorla, P. Ferrari, A. Flammini, A. Moschitta, S. Rinaldi, T. Sauter, and E. Sisinni, "Low complexity UWB radios for precise wireless sensor network synchronization," *IEEE Transactions on Instrumentation and Measurement*, vol. 62, no. 9, pp. 2538–2548, 2013.

[73] K. Czuba and D. Sikora, "Temperature stability of coaxial cables," *Acta Phys. Pol. A*, vol. 119, no. EuCARD-PUB-2011-001, pp. 333–337, 2011.

[74] W. Zhu, E. R. N. Fokoua, Y. Chen, T. D. Bradley, S. R. Sandoghchi, M. Ding, G. T. Jasion, M. N. Petrovich, F. Poletti, M. Zhao, *et al.*, "Toward high accuracy positioning in 5G via passive synchronization of base stations using thermally-insensitive optical fibers," *IEEE Access*, vol. 7, pp. 113197–113205, 2019.

[75] M. Lipinski, T. Włostowski, J. Serrano, and P. Alvarez, "White rabbit: A PTP application for robust sub-nanosecond synchronization," in *2011 IEEE International Symposium on Precision Clock Synchronization for Measurement, Control and Communication*, pp. 25–30, IEEE, 2011.

[76] J. Serrano, M. Lipinski, T. Wlostowski, E. Gousiou, E. van der Bij, M. Cattin, and G. Daniluk, "The white rabbit project," in *Proceedings of the 2nd International Beam Instrumentation Conference (IBIC)*, p. THBL2, 2013.

[77] E. F. Dierikx, A. E. Wallin, T. Fordell, J. Myyry, P. Koponen, M. Merimaa, T. J. Pinkert, J. C. Koelemeij, H. Z. Peek, and R. Smets, "White rabbit precision time protocol on long-distance fiber links," *IEEE Transactions on Ultrasonics, Ferroelectrics, and Frequency Control*, vol. 63, no. 7, pp. 945–952, 2016.

[78] T. Bigler, A. Treytl, D. Löschenbrand, and T. Zemen, "High accuracy synchronization for distributed massive MIMO using White Rabbit," in *2018 IEEE International Symposium on Precision Clock Synchronization for Measurement, Control, and Communication (ISPCS)*, pp. 1–6, IEEE, 2018.

[79] G. Bellusci, G. J. Janssen, J. Yan, and C. C. Tiberius, "Performance evaluation of a low-complexity receiver concept for TOA-based ultrawideband ranging," *IEEE Transactions on Vehicular Technology*, vol. 61, no. 9, pp. 3825–3837, 2012.

[80] A. Alarifi, A. Al-Salman, M. Alsaleh, A. Alnafessah, S. Al-Hadhrami, M. A. Al-Ammar, and H. S. Al-Khalifa, "Ultra wideband indoor positioning technologies: Analysis and recent advances," *Sensors*, vol. 16, no. 5, p. 707, 2016.

[81] K. Yu, K. Wen, Y. Li, S. Zhang, and K. Zhang, "A novel NLOS mitigation algorithm for UWB localization in harsh indoor environments," *IEEE Transactions on Vehicular Technology*, vol. 68, no. 1, pp. 686–699, 2018.

[82] H. Dun, C. Tiberius, C. Diouf, and G. Janssen, "Design of sparse multiband signal for precise positioning with joint low-complexity time delay and carrier phase estimation," *IEEE Transactions on Vehicular Technology*, vol. 70, no. 4, pp. 3552–3567, 2021.

[83] C. Knapp and G. Carter, "The generalized correlation method for estimation of time delay," *IEEE Transactions on Acoustics, Speech, and Signal Processing*, vol. 24, no. 4, pp. 320–327, 1976.

[84] A. Van Dierendonck, P. Fenton, and T. Ford, "Theory and performance of narrow correlator spacing in a GPS receiver," *Navigation*, vol. 39, no. 3, pp. 265–283, 1992.

[85] J. Benesty, J. Chen, and Y. Huang, "Time-delay estimation via linear interpolation and cross correlation," *IEEE Transactions on Speech and Audio Processing*, vol. 12, no. 5, pp. 509–519, 2004.

[86] R. D. Van Nee, "The multipath estimating delay lock loop," in *Proc. IEEE Second Symposium on Spread Spectrum Techniques and Applications*, pp. 39–42, 1992.

[87] R. D. Van Nee, J. Siereveld, P. C. Fenton, and B. R. Townsend, "The multipath estimating delay lock loop: approaching theoretical accuracy limits," in *Proceedings of 1994 IEEE Position, Location and Navigation Symposium-PLANS'94*, pp. 246–251, IEEE, 1994.

[88] I. F. Progri, M. C. Bromberg, and W. R. Michalson, "Maximum-likelihood GPS parameter estimation," *Navigation*, vol. 52, no. 4, pp. 229–238, 2005.

[89] T. G. Manickam, R. J. Vaccaro, and D. W. Tufts, "A least-squares algorithm for multipath time-delay estimation," *IEEE Transactions on Signal Processing*, vol. 42, no. 11, pp. 3229–3233, 1994.

[90] I. Ziskind and M. Wax, "Maximum likelihood localization of multiple sources by alternating projection," *IEEE Transactions on Acoustics, Speech, and Signal Processing*, vol. 36, no. 10, pp. 1553–1560, 1988.

[91] A. Paulraj, R. Roy, and T. Kailath, "Estimation of signal parameters via rotational invariance techniques-ESPRIT," in *Nineteeth Asilomar Conference on Circuits, Systems and Computers, 1985.*, pp. 83–89, IEEE, 1985.

[92] P. Stoica and A. Nehorai, "MUSIC, maximum likelihood, and Cramer-Rao bound," *IEEE Transactions on Acoustics, Speech, and Signal Processing*, vol. 37, no. 5, pp. 720–741, 1989.

[93] A.-J. van der Veen and G. Leus, *Signal processing for communications*. Delft University of Technology, 2005.

[94] J. Khalife and Z. M. Kassas, "Opportunistic UAV navigation with carrier phase measurements from asynchronous cellular signals," *IEEE Transactions on Aerospace and Electronic Systems*, vol. 56, no. 4, pp. 3285–3301, 2020.

[95] P. Wang and Y. Morton, "Carrier phase tracking architecture for positioning in LTE networks under channel fading conditions," in *Proceedings of the 33rd International Technical Meeting of the Satellite Division of The Institute of Navigation (ION GNSS+ 2020)*, pp. 2605–2617, 2020.

[96] R. Yang, K.-V. Ling, E.-K. Poh, and Y. Morton, "Generalized GNSS signal carrier tracking: Part I—modeling and analysis," *IEEE Transactions on Aerospace and Electronic Systems*, vol. 53, no. 4, pp. 1781–1797, 2017.

[97] A. Razavi, D. Gebre-Egziabher, and D. M. Akos, "Carrier loop architectures for tracking weak GPS signals," *IEEE Transactions on Aerospace and Electronic Systems*, vol. 44, no. 2, pp. 697–710, 2008.

[98] Y. Shen and M. Z. Win, "Fundamental limits of wideband localization—Part I: A general framework," *IEEE Transactions on Information Theory*, vol. 56, no. 10, pp. 4956–4980, 2010.

[99] L. Taponecco, A. A. D'Amico, and U. Mengali, "Joint TOA and AOA estimation for UWB localization applications," *IEEE Transactions on Wireless Communications*, vol. 10, no. 7, pp. 2207–2217, 2011.

[100] K. Yu and Y. J. Guo, "Statistical NLOS identification based on AOA, TOA, and signal strength," *IEEE Transactions on Vehicular Technology*, vol. 58, no. 1, pp. 274–286, 2008.

[101] E. Hernández-Orallo, C. T. Calafate, J.-C. Cano, and P. Manzoni, "Evaluating the effectiveness of COVID-19 Bluetooth-based smartphone contact tracing applications," *Applied Sciences*, vol. 10, no. 20, pp. 1–19, 2020.

[102] P. Di Marco, P. Park, M. Pratesi, and F. Santucci, "A Bluetooth-based architecture for contact tracing in healthcare facilities," *Journal of Sensor and Actuator Networks*, vol. 10, no. 1, pp. 1–15, 2021.

[103] H. Sallouha, M. M. Azari, A. Chiumento, and S. Pollin, "Aerial anchors positioning for reliable RSS-based outdoor localization in urban environments," *IEEE Wireless Communications Letters*, vol. 7, no. 3, pp. 376–379, 2017.

[104] C. Feng, W. S. A. Au, S. Valaee, and Z. Tan, "Received-signal-strength-based indoor positioning using compressive sensing," *IEEE Transactions on Mobile Computing*, vol. 11, no. 12, pp. 1983–1993, 2011.

[105] P. Moreira, J. Serrano, T. Wlostowski, P. Loschmidt, and G. Gaderer, "White rabbit: Sub-nanosecond timing distribution over ethernet," in *2009 International Symposium on Precision Clock Synchronization for Measurement, Control and Communication*, pp. 1–5, IEEE, 2009.

[106] W. P. Siriwongpairat and K. R. Liu, "UWB: multiband OFDM approach," in *Ultra-wideband communications systems: multiband OFDM approach*, ch. 4, pp. 53–74, John Wiley & Sons, 2007.

[107] H. Dun, C. Tiberius, and G. J. Janssen, "Positioning based on OFDM signals through phase measurements," in *Proceedings of the 9th ESA Workshop on Satellite Navigation Technologies and European Workshop on GNSS Signals and Signal Processing (NAVITEC)*, 2018.

[108] H. Dun, C. Tiberius, and G. Janssen, "Positioning in a multipath channel using OFDM signals with carrier phase tracking," *IEEE Access*, vol. 8, pp. 13011–13028, 2020.

[109] Y. G. Li and G. L. Stuber, "Basic concepts," in *Orthogonal frequency division multiplexing for wireless communications*, ch. 2, pp. 19–46, Springer Science & Business Media, 2006.

[110] Y. Li, "Channel estimation," in *Orthogonal frequency division multiplexing for wireless communications* (Y. Li and G. L. Stuber, eds.), ch. 5, pp. 145–198, Springer Science & Business Media, 2006.

[111] S. K. Wilson, "Synchronization," in *Orthogonal frequency division multiplexing for wireless communications* (Y. G. Li and G. L. Stuber, eds.), ch. 4, pp. 113–144, Springer, 2006.

[112] G. H. Golub and V. Pereyra, "The differentiation of pseudo-inverses and nonlinear least squares problems whose variables separate," *SIAM Journal on numerical analysis*, vol. 10, no. 2, pp. 413–432, 1973.

[113] G. Xu, R. H. Roy, and T. Kailath, "Detection of number of sources via exploitation of centro-symmetry property," *IEEE Transactions on Signal processing*, vol. 42, no. 1, pp. 102–112, 1994.

[114] T. Söderström and P. Stoica, *System identification*. Prentice-Hall, Inc., 1988.

[115] E. G. Larsson, G. Liu, J. Li, and G. B. Giannakis, "Joint symbol timing and channel estimation for OFDM based WLANs," *IEEE Communications letters*, vol. 5, no. 8, pp. 325–327, 2001.

[116] J. A. del Peral-Rosado, J. A. López-Salcedo, F. Zanier, and G. Seco-Granados, "Position accuracy of joint time-delay and channel estimators in LTE networks," *IEEE Access*, vol. 6, pp. 25185–25199, 2018.

[117] P. J. G. Teunissen, "Nonlinear least squares," *Manuscripta Geodaetica*, 1990.

[118] P. J. G. Teunissen, "Nonlinear inversion of geodetic and geophysical data: diagnosing nonlinearity," in *Developments in Four-Dimensional Geodesy*, pp. 241–264, Springer, 1990.

[119] J. Yan, G. Bellusci, C. Tiberius, and G. Janssen, "Analyzing non-linearity effect for indoor positioning using an acoustic ultra-wideband system," in *IEEE 5th Workshop on Positioning, Navigation and Communication (WPNC)*, pp. 95–101, IEEE, 2008.

[120] J. Yan, C. Tiberius, G. Janssen, P. J. G. Teunissen, and G. Bellusci, "Review of range-based positioning algorithms," *IEEE Aerospace and Electronic Systems Magazine*, vol. 28, no. 8, pp. 2–27, 2013.

[121] J. Yan, C. Tiberius, P. J. G. Teunissen, G. Bellusci, and G. J. Janssen, "A framework for low complexity least-squares localization with high accuracy," *IEEE Transactions on Signal Processing*, vol. 58, no. 9, pp. 4836–4847, 2010.

[122] A. Goldsmith, "Digital modulation and detection," in *Wireless communications*, ch. 5, Cambridge University Press, 2005.

[123] H. Dun, C. Tiberius, G. Janssen, and C. Diouf, "Time delay estimation based on multi-band multi-carrier signal in multipath environments," in *Proceedings of the 32nd International Technical Meeting of the Satellite Division of The Institute of Navigation (ION GNSS+ 2019)*, pp. 2299–2313, ION-Inst. of Navigation, 2019.

[124] P. Stoica, *Introduction to spectral analysis*. Prentice hall, 1997.

[125] B. Yang, K. B. Letaief, R. S. Cheng, and Z. Cao, "Channel estimation for OFDM transmission in multipath fading channels based on parametric channel modeling," *IEEE Transactions on Communications*, vol. 49, no. 3, pp. 467–479, 2001.

[126] O. Simeone, Y. Bar-Ness, and U. Spagnolini, "Pilot-based channel estimation for OFDM systems by tracking the delay-subspace," *IEEE Transactions on Wireless Communications*, vol. 3, no. 1, pp. 315–325, 2004.

[127] A.-J. Van Der Veen, E. F. Deprettere, and A. L. Swindlehurst, "Subspace-based signal analysis using singular value decomposition," *Proceedings of the IEEE*, vol. 81, no. 9, pp. 1277–1308, 1993.

[128] M. Morelli and U. Mengali, "A comparison of pilot-aided channel estimation methods for OFDM systems," *IEEE Transactions on Signal Processing*, vol. 49, no. 12, pp. 3065–3073, 2001.

[129] R. Negi and J. Cioffi, "Pilot tone selection for channel estimation in a mobile OFDM system," *IEEE Transactions on Consumer Electronics*, vol. 44, no. 3, pp. 1122–1128, 1998.

[130] H. Dun, C. Tiberius, C. Diouf, and G. Janssen, "Sparse signal bands selection for precise time-based ranging in terrestrial positioning," in *2020 IEEE/ION Position, Location and Navigation Symposium (PLANS)*, pp. 1372–1380, IEEE, 2020.

[131] C. Suh, C.-S. Hwang, and H. Choi, "Preamble design for channel estimation in MIMO-OFDM systems," in *GLOBECOM'03. IEEE Global Telecommunications Conference (IEEE Cat. No. 03CH37489)*, vol. 1, pp. 317–321, IEEE, 2003.

[132] P. Teunissen, "Partitioned model representations," in *Adjustment theory: an introduction*, ch. 6, pp. 89–136, VSSD Press, 2000.

[133] A. A. Saleh and R. Valenzuela, "A statistical model for indoor multipath propagation," *IEEE Journal on Selected Areas in Communications*, vol. 5, no. 2, pp. 128–137, 1987.

[134] H. Hashemi, "Impulse response modeling of indoor radio propagation channels," *IEEE Journal on Selected Areas in Communications*, vol. 11, no. 7, pp. 967–978, 1993.

[135] H. Dun, C. Tiberius, C. Diouf, and G. Janssen, "Terrestrial precise positioning system using carrier phase from burst signals and optically distributed time and frequency reference," in *Proceedings of the 2021 International Technical Meeting of The Institute of Navigation (ION ITM2021)*, pp. 510–524, 2021.

[136] J. Morton, R. Yang, and B. Breitsch, "GNSS receiver signal tracking," in *Position, Navigation, and Timing Technologies in the 21st Century : Integrated Satellite Navigation, Sensor Systems, and Civil Applications*, ch. 15, John Wiley & Sons, Incorporated, 2021.

[137] T. M. Schmidl and D. C. Cox, "Robust frequency and timing synchronization for OFDM," *IEEE Transactions on Communications*, vol. 45, no. 12, pp. 1613–1621, 1997.

[138] J. J. Khalife and Z. M. Kassas, "Evaluation of relative clock stability in cellular networks," in *Proceedings of the 30th International Technical Meeting of the Satellite Division of The Institute of Navigation (ION GNSS+ 2017)*, pp. 2554–2559, 2017.

[139] S. Joshi and S. Boyd, "Sensor selection via convex optimization," *IEEE Transactions on Signal Processing*, vol. 57, no. 2, pp. 451–462, 2008.

[140] S. P. Chepuri and G. Leus, "Sparsity-promoting sensor selection for non-linear measurement models," *IEEE Transactions on Signal Processing*, vol. 63, no. 3, pp. 684–698, 2014.

[141] E. Tohidi, M. Coutino, S. P. Chepuri, H. Behroozi, M. M. Nayebi, and G. Leus, "Sparse antenna and pulse placement for colocated MIMO radar," *IEEE Transactions on Signal Processing*, vol. 67, no. 3, pp. 579–593, 2018.

[142] M.-H. Hsieh and C.-H. Wei, "Channel estimation for OFDM systems based on comb-type pilot arrangement in frequency selective fading channels," *IEEE Transactions on Consumer Electronics*, vol. 44, no. 1, pp. 217–225, 1998.

[143] M. Meurer and F. Antreich, "Signals and modulation," in *Springer handbook of global navigation satellite systems* (P. Teunissen and O. Montenbruck, eds.), ch. 4, Springer, 2017.

[144] M. Grant and S. Boyd, "CVX: Matlab software for disciplined convex programming, version 2.1," 2014.

[145] R. H. Tütüncü, K.-C. Toh, and M. J. Todd, "Solving semidefinite-quadratic-linear programs using SDPT3," *Mathematical Programming*, vol. 95, no. 2, pp. 189–217, 2003.

[146] P. Teunissen, "The least-squares ambiguity decorrelation adjustment: a method for fast GPS integer ambiguity estimation," *Journal of Geodesy*, vol. 70, pp. 65–82, 1995.

[147] P. Teunissen, "A new GLONASS FDMA model," *GPS Solutions*, vol. 23, no. 4, p. 100, 2019.

[148] T. Wang, Z. Yao, and M. Lu, "On-the-fly ambiguity resolution involving only carrier phase measurements for stand-alone ground-based positioning systems," *GPS Solutions*, vol. 23, no. 2, p. 36, 2019.

[149] J. Yan, C. Tiberius, G. Bellusci, and G. Janssen, "Feasibility of Gauss-Newton method for indoor positioning," in *2008 IEEE/ION Position, Location and Navigation Symposium (PLANS)*, pp. 660–670, IEEE, 2008.

[150] P. Teunissen and A. Khodabandeh, "Review and principles of PPP-RTK methods," *Journal of Geodesy*, vol. 89, no. 3, pp. 217–240, 2015.

[151] P. Teunissen, "Carrier phase integer ambiguity resolution," in *Springer handbook of Global Navigation Satellite Systems* (P. Teunissen and O. Montenbruck, eds.), ch. 23, pp. 661–686, Springer, 2017.

[152] P. Teunissen, "The probability distribution of the GPS baseline for a class of integer ambiguity estimators," *Journal of Geodesy*, vol. 73, no. 5, pp. 275–284, 1999.

[153] P. Teunissen, "Theory of carrier phase ambiguity resolution," *Wuhan University Journal of Natural Sciences*, vol. 8, no. 2, p. 471, 2003.

[154] W. Baarda, "S-transformations and criterion matrices," *Netherlands Geodetic Commission*, 1973.

[155] P. Teunissen, "Zero order design: generalized inverses, adjustment, the datum problem and S-transformations," in *Optimization and design of geodetic networks*, pp. 11–55, Springer, 1985.

[156] A. Hauschild, "Basic observation equations," in *Springer handbook of global navigation satellite systems* (P. Teunissen and O. Montenbruck, eds.), ch. 19, Springer, 2017.

[157] "Ceiling-mounted 3dBi wide-band antenna 700MHz to 6GHz." https://www.taoglas.com/wp-content/uploads/2015/04/CM.02.03F21.02806.pdf, 2015.

[158] "OctoClock." https://www.ettus.com/wp-content/uploads/2019/01/Octoclock_Spec_Sheet.pdf, 2019.

[159] C. Diouf, H. Dun, T. Kazaz, G. Janssen, and C. Tiberius, "Demonstration of a decimeter-level accurate hybrid optical-wireless terrestrial positioning system," in *Proceedings of the 33nd International Technical Meeting of the Satellite Division of The Institute of Navigation (ION GNSS+ 2020)*, pp. 2220–2228, 2020.

[160] C. Diouf, G. J. Janssen, T. Kazaz, H. Dun, F. Chamanzadeh, and C. C. Tiberius, "A 400 Msps SDR platform for prototyping accurate wideband ranging techniques," in *2019 16th Workshop on Positioning, Navigation and Communications (WPNC)*, pp. 1–6, IEEE, 2019.

[161] C. Diouf, G. J. M. Janssen, H. Dun, T. Kazaz, and C. C. J. M. Tiberius, "A USRP-based testbed for wideband ranging and positioning signal acquisition," *IEEE Transactions on Instrumentation and Measurement*, vol. 70, pp. 1–15, 2021.

[162] The Green Village. https://www.thegreenvillage.org/.

[163] F. M. Dekking, C. Kraaikamp, H. P. Lopuhaä, and L. E. Meester, *A Modern Introduction to Probability and Statistics: Understanding why and how*. Springer Science & Business Media, 2005.

[164] S. Verhagen and B. Li, "LAMBDA software package: Matlab implementation, version 3.0," *Delft University of Technology and Curtin University*, 2012.

[165] P. J. Teunissen and S. Verhagen, "The GNSS ambiguity ratio-test revisited: a better way of using it," *Survey Review*, vol. 41, no. 312, pp. 138–151, 2009.

[166] E. Yuan, W. Qi, P. Liu, L. Wei, and L. Chen, "Ranging method for navigation based on high-speed frequency-hopping signal," *IEEE Access,* vol. 6, pp. 4308–4320, 2017.

[167] T. Kazaz, M. Coutino, G. J. Janssen, and A.-J. van der Veen, "Joint blind calibration and time-delay estimation for multiband ranging," in *ICASSP 2020-2020 IEEE International Conference on Acoustics, Speech and Signal Processing (ICASSP),* pp. 4846–4850, IEEE, 2020.

[168] B. Bellalta, "IEEE 802.11 ax: High-efficiency WLANs," *IEEE Wireless Communications,* vol. 23, no. 1, pp. 38–46, 2016.

[169] P.-H. Tseng, Y.-C. Chan, Y.-J. Lin, D.-B. Lin, N. Wu, and T.-M. Wang, "Ray-tracing-assisted fingerprinting based on channel impulse response measurement for indoor positioning," *IEEE Transactions on Instrumentation and Measurement,* vol. 66, no. 5, pp. 1032–1045, 2017.

[170] K. S. V. Prasad, E. Hossain, and V. K. Bhargava, "Energy efficiency in massive MIMO-based 5G networks: Opportunities and challenges," *IEEE Wireless Communications,* vol. 24, no. 3, pp. 86–94, 2017.

[171] C. Huang, S. Hu, G. C. Alexandropoulos, A. Zappone, C. Yuen, R. Zhang, M. Di Renzo, and M. Debbah, "Holographic MIMO surfaces for 6G wireless networks: Opportunities, challenges, and trends," *IEEE Wireless Communications,* vol. 27, no. 5, pp. 118–125, 2020.

[172] J. L. Gómez-Tornero, D. Cañete-Rebenaque, J. A. López-Pastor, and A. S. Martínez-Sala, "Hybrid analog-digital processing system for amplitude-monopulse RSSI-based MIMO WiFi direction-of-arrival estimation," *IEEE Journal of Selected Topics in Signal Processing,* vol. 12, no. 3, pp. 529–540, 2018.

[173] S. Verhagen and P. J. Teunissen, "Least-squares estimation and Kalman filtering," in *Springer handbook of Global Navigation Satellite Systems* (P. Teunissen and O. Montenbruck, eds.), ch. 22, pp. 639–660, Springer, 2017.

[174] H. G. Golub and C. F. Van Loan, "Special linear systems," in *Matrix Computations,* ch. 4, pp. 153–232, Johns Hopkins Universtiy Press, 3rd edtion, 1996.

# A

# Appendices

## A.1. CFO and Received OFDM Signal

The passband OFDM signal is derived by [109]

$$
\begin{aligned}
s_p(t) &= \Re\left\{s_b(t)\exp(j2\pi f_c t)\right\} \\
&= \Re\left\{s_b(t)\right\}\cos(2\pi f_c t) - \Im\left\{s_b(t)\right\}\sin(2\pi f_c t).
\end{aligned}
$$

Considering the carrier frequency offset (CFO), the received signal passing through the channel, is obtained by

$$
r_b(t) = 2\mathscr{F}_l\left\{\left(s_p(t) * h(t)\right)\cos\left(2\pi f_c'(t)t + \vartheta\right) - j\left(s_p(t) * h(t)\right)\sin\left(2\pi f_c'(t)t + \vartheta\right)\right\} \quad \text{(A.1)}
$$

where $h(t)$ denotes the channel impulse response, $f_c'$ denotes the central frequency generated by the receiver, and $\vartheta$ denotes the initial carrier phase offset between the receiver and the transmitter. As only a single path is considered, one has

$$
\begin{aligned}
s_p(t) * h(t) &= \alpha s_p(t - \tau(t))\exp\left(j2\pi f_c(t - \tau(t))\right) \\
&= \Re\left\{\alpha s_b(t - \tau(t))\exp\left(j2\pi f_c t\right)\exp\left(-j\left(2\pi f_c\tau(t_0) - 2\pi\int_{t_0}^{t}f_c\frac{v(\zeta)\cos(\theta(\zeta))}{c}d\zeta\right)\right)\right\}.
\end{aligned}
$$
$$\text{(A.2)}$$

Let

$$
r_b'(t) = \alpha s_b(t - \tau(t))\exp\left(-j\left(2\pi f_c\tau(t_0) + \phi_D(t)\right)\right) \quad \text{(A.3)}
$$

where $\phi_D$ denotes the accumulated Doppler phase

$$
\phi_D(t) = -2\pi\int_{t_0}^{t}\Delta f_D(\zeta)d\zeta, \quad \Delta f_D(t) = f_c\frac{v(t)\cos(\theta(t))}{c},
$$

and $\Delta f_D$ denotes the Doppler frequency.

Combined with (A.2), the received baseband signal (A.1) can be rewritten by

$$
\begin{aligned}
r_b(t) =& 2\mathscr{F}_l\left\{\Re\left\{r_b'(t)\right\}\cos\left(2\pi f_c t\right)\cos\left(2\pi f_c'(t) + \vartheta\right)\right\} \\
&- 2\mathscr{F}_l\left\{\Im\left\{r_b'(t)\right\}\sin(2\pi f_c t)\cos\left(2\pi f_c'(t) + \vartheta\right)\right\} \\
&- j2\mathscr{F}_l\left\{\Re\left\{r_b'(t)\right\}\cos\left(2\pi f_c t\right)\sin\left(2\pi f_c'(t) + \vartheta\right)\right\} \\
&+ 2\mathscr{F}_l\left\{\Im\left\{r_b'(t)\right\}\sin(2\pi f_c t)\sin\left(2\pi f_c'(t) + \vartheta\right)\right\}.
\end{aligned} \tag{A.4}
$$

where $\mathscr{F}_l$ denotes the low-pass filter operator.

After some simplification, one has

$$
\begin{aligned}
r_b(t) =& \Re\left\{r_b'(t)\right\}\cos\left(\phi_\eta(t) + \vartheta\right) - \Im\left\{r_b'(t)\right\}\sin\left(\phi_\eta(t) + \vartheta\right) \\
&- j\Re\left\{r_b'(t)\right\}\sin\left(\phi_\eta(t) + \vartheta\right) - j\Im\left\{r_b'(t)\right\}\cos\left(\phi_\eta(t) + \vartheta\right) \\
=& r_b'(t)\exp\left(-j\left(\phi_\vartheta(t) + \vartheta\right)\right),
\end{aligned} \tag{A.5}
$$

where $\phi_\eta(t)$ denotes the accumulated phase offset introduced by $\Delta f(t)$, due to the asynchronous receiver clock,

$$
\phi_\eta(t) = 2\pi\int_{t_0}^t \Delta f_c(\zeta)d\zeta, \quad \Delta f_c = \eta(t)f_c. \tag{A.6}
$$

Finally, the received baseband signal is written by

$$
r_b(t) = \alpha s_b(t - \tau(t))\exp\left(-j\left(2\pi f_c\tau(t_0) + \phi_D(t) + \phi_\eta(t) + \vartheta\right)\right). \tag{A.7}
$$

## A.2. CRLB of Time Delay Estimation

### A.2.1. Single Path Channel

The probability density function (PDF) of a vector $\boldsymbol{r}$, which contains $N_s$ received ranging samples, is given by

$$f_{\underline{r}}(\boldsymbol{r}|\tau) = \frac{1}{\pi^{N_s}\det(\boldsymbol{Q_r})} \exp\left(-(\boldsymbol{r} - \bar{\boldsymbol{r}}(\tau))^{\mathrm{H}}\boldsymbol{Q_r^{-1}}(\boldsymbol{r} - \bar{\boldsymbol{r}}(\tau))\right), \tag{A.8}$$

As shown in (3.5), the variance matrix $\boldsymbol{Q_r}$ is assumed to be $\sigma_n^2\boldsymbol{I}_{N_s}$

Then, by taking the logarithm for the PDF, one has

$$\ln f_{\underline{r}}(\boldsymbol{r}|\tau) = -N_s\ln\left(\pi\sigma_n^2\right) - (r - \bar{\boldsymbol{r}}(\tau))^{\mathrm{H}}\boldsymbol{Q_r^{-1}}(r - \bar{\boldsymbol{r}}(\tau)), \tag{A.9}$$

and its first derivative is written by

$$\frac{\partial\ln f_{\underline{r}}(\boldsymbol{r}|\tau)}{\partial\tau} = \frac{\partial\bar{\boldsymbol{r}}^{\mathrm{H}}(\tau)}{\partial\tau}\boldsymbol{Q_r^{-1}}(\boldsymbol{r} - \bar{\boldsymbol{r}}(\tau)) + (\boldsymbol{r} - \bar{\boldsymbol{r}}(\tau))^{\mathrm{H}}\boldsymbol{Q_r^{-1}}\frac{\partial\bar{\boldsymbol{r}}(\tau)}{\partial\tau}. \tag{A.10}$$

By the definition of the Fisher information matrix, and considering a single unknown variable, one has

$$\begin{aligned} \mathrm{FIM}(\tau) &= -\mathbb{E}\left\{\frac{\partial^2\ln f_{\underline{r}}(\boldsymbol{r}|\tau)}{\partial\tau^2}\right\} \\ &= -\frac{\partial^2\bar{\boldsymbol{r}}(\tau)}{\partial\tau^2}\boldsymbol{Q_r^{-1}}\mathbb{E}\left\{(\underline{r} - \bar{\boldsymbol{r}}(\tau))\right\} + \frac{\partial\bar{\boldsymbol{r}}^{\mathrm{H}}(\tau)}{\partial\tau}\boldsymbol{Q_r^{-1}}\frac{\partial\bar{\boldsymbol{r}}(\tau)}{\partial\tau} \\ &\quad + \frac{\bar{\boldsymbol{r}}^{\mathrm{H}}(\tau)}{\partial\tau}\boldsymbol{Q_r^{-1}}\frac{\partial\bar{\boldsymbol{r}}(\tau)}{\partial\tau} + \mathbb{E}\left\{(\underline{r} - \bar{\boldsymbol{r}}(\tau))^{\mathrm{H}}\right\}\boldsymbol{Q_r^{-1}}\frac{\partial^2\bar{\boldsymbol{r}}(\tau)}{\partial\tau^2}. \end{aligned} \tag{A.11}$$

As only white Gaussian noise is considered, with

$$\mathbb{E}\left\{(\underline{r} - \bar{\boldsymbol{r}}(\tau))\right\} = 0, \tag{A.12}$$

(A.11) can be rewritten by

$$\mathrm{FIM}(\tau) = 2\left(\frac{\partial\bar{\boldsymbol{r}}^{\mathrm{H}}(\tau)}{\partial\tau}\boldsymbol{Q_r^{-1}}\frac{\partial\bar{\boldsymbol{r}}(\tau)}{\partial\tau}\right) = 2\alpha^2\left(\frac{\partial\boldsymbol{s}_b^{\mathrm{H}}(\tau)}{\partial\tau}\boldsymbol{Q_r^{-1}}\frac{\partial\boldsymbol{s}_b(\tau)}{\partial\tau}\right), \tag{A.13}$$

where $\boldsymbol{s}_b(\tau)$ contains the samples of baseband ranging signal in (3.3).

Then, the Cramer-Rao lower bound of the time delay estimation based on the ranging signal $s_b(t)$ can be given as

$$\sigma_\tau^2 \geq \frac{1}{\mathrm{FIM}(\tau)} = \frac{\sigma^2}{2\alpha^2\sum_{n=0}^{N_s-1}\left(\frac{\partial s_b[nT_s-\tau]}{\partial\tau}\right)^2}, \tag{A.14}$$

which only depends on the waveform of the ranging signal $s_b(t)$, as well as the propagation gain $\alpha$.

Additionally, the signal-to-noise ratio (SNR) is defined by

$$\text{SNR} = \frac{\frac{1}{T_{\text{sym}}} E_s}{N_0 B} = \frac{\frac{1}{N_s} 2\alpha^2 \sum_0^{N_s-1} |s_b[n]|^2}{\sigma^2}, \tag{A.15}$$

where $N_0$ denotes the noise spectral density, $B$ denotes the signal bandwidth, and $E_s$ denotes the signal energy written by

$$E_s = \int_0^{T_{\text{sym}}} |s_b(t)|^2 dt$$

Note that if the symbol rate is equal to the sample rate, then the SNR is $E_s/(N_0/2)$ [62].

In order to link the CRLB with the SNR, (A.14) can be rewritten by

$$\sigma_\tau^2 \geq \frac{1}{\frac{\frac{1}{N_s} \sum_0^{N_s-1} |s_b[n]|^2}{\sigma^2} \frac{\sum_0^{N_s-1} \left(\frac{\partial s_b[nT_s-\tau]}{\partial \tau}\right)^2}{\frac{1}{N_s} \sum_0^{N_s-1} |s_b[n]|^2}}. \tag{A.16}$$

According to Parseval's theorem, one has

$$\frac{\sum_0^{(N_s-1)} |s_b'[t]|^2 dt}{\sum_0^{(N_s-1)} |s_b[n]|^2 dt} = \frac{4\pi^2 \sum_{i=-N_s/2}^{N_s/2} \left(i\Delta f\right)^2 |S_b[i]|^2}{\sum_{i=-N_s/2}^{N_s/2} |S_b(i)|^2} = 4\pi^2 \beta^2 \tag{A.17}$$

where $S_b[i]$ denotes the spectrum of the ranging signal $s_b[n]$, $\Delta f$ denotes the frequency resolution (e.g., subcarrier spacing when using OFDM signal) and $\beta^2$ is a measure of the signal bandwidth [62].

Finally, the CRLB of time delay estimation is given as

$$\sigma_\tau^2 \geq \frac{1}{4\pi^2 \text{SNR} N_s \beta^2}. \tag{A.18}$$

## A.2.2. Two-Path Channel

In this appendix, we derive the elements of the FIM considering a multiband signal in a two-path channel. For the ease of derivation, the modulation on each subcarrier is assumed to be BPSK (i.e., $|c_i|^2 = 1$).

The first derivatives of mean $\bar{r}_m(u)$ with respect to the unknown parameters are

given by

$$\frac{\partial \bar{r}_m[n, \boldsymbol{u}]}{\partial \tau_1} = -j2\pi\alpha_1 \sum_{i=-N_s/2}^{N_s/2-1} c_i \exp\left(j2\pi\frac{in}{N_s}\right)(f_m + f_i)\exp\left(-j2\pi(f_m + f_i)\tau_1\right)$$

$$\frac{\partial \bar{r}_m[n, \boldsymbol{u}]}{\partial \tau_2} = -j2\pi\alpha_2 \sum_{i=-N/2}^{N/2-1} c_i \exp\left(j2\pi\frac{in}{N_s}\right)(f_m + f_i)\exp\left(-j2\pi(f_m + f_i)\tau_2\right)$$

$$\frac{\partial \bar{r}_m[n, \boldsymbol{u}]}{\partial \alpha_1} = \sum_{i=-N_s/2}^{N_s/2-1} c_i \exp\left(j2\pi\frac{in}{N_s}\right)\exp\left(-j2\pi(f_m + f_i)\tau_1\right)$$

$$\frac{\partial \bar{r}_m[n, \boldsymbol{u}]}{\partial \alpha_2} = \sum_{i=-N_s/2}^{N_s/2-1} c_i \exp\left(j2\pi\frac{in}{N_s}\right)\exp\left(-j2\pi(f_m + f_i)\tau_2\right)$$

where $f_m$ is the central frequency of the $m$-th signal band.

Considering a single band OFDM signal in a two-path channel, the elements of the FIM can be derived as follows.

$$\frac{\partial \bar{\boldsymbol{r}}_m^{\mathrm{H}}(\boldsymbol{u})}{\partial \tau_1}\frac{\partial \bar{\boldsymbol{r}}_m(\boldsymbol{u})}{\partial \tau_1} = \alpha_1^2 4\pi^2 \sum_{i=-N_s/2}^{N_s/2-1}(f_i + f_m)^2$$

$$\frac{\partial \bar{\boldsymbol{r}}_m^{\mathrm{H}}(\boldsymbol{u})}{\partial \tau_1}\frac{\partial \bar{\boldsymbol{r}}_m(\boldsymbol{u})}{\partial \tau_2} = \alpha_1\alpha_2 4\pi^2 \sum_{i=-N_s/2}^{N_s/2-1}(f_i + f_m)^2 \exp\left(-j2\pi(f_i + f_m)(\tau_1 - \tau_2)\right)$$

$$\frac{\partial \bar{\boldsymbol{r}}_m^{\mathrm{H}}(\boldsymbol{u})}{\partial \tau_1}\frac{\partial \bar{\boldsymbol{r}}_m(\boldsymbol{u})}{\partial \alpha_1} = -j\alpha_1 2\pi \sum_{i=-N_s/2}^{N_s/2-1}(f_i + f_m)$$

$$\frac{\partial \bar{\boldsymbol{r}}_m^{\mathrm{H}}(\boldsymbol{u})}{\partial \tau_1}\frac{\partial \bar{\boldsymbol{r}}_m(\boldsymbol{u})}{\partial \alpha_2} = -j\alpha_1 2\pi \sum_{i=-N_s/2}^{N_s/2-1}(f_i + f_m)\exp(-j2\pi(f_i + f_m)(\tau_1 - \tau_2))$$

$$\frac{\partial \bar{\boldsymbol{r}}_m^{\mathrm{H}}(\boldsymbol{u})}{\partial \tau_2}\frac{\partial \bar{\boldsymbol{r}}_m(\boldsymbol{u})}{\partial \tau_2} = \alpha_2^2 4\pi^2 \sum_{i=-N_s/2}^{N_s/2-1}(f_i + f_m)^2$$

$$\frac{\partial \bar{\boldsymbol{r}}_m^{\mathrm{H}}(\boldsymbol{u})}{\partial \tau_2}\frac{\partial \bar{\boldsymbol{r}}_m(\boldsymbol{u})}{\partial \alpha_1} = j\alpha_2 2\pi \sum_{i=-N_s/2}^{N_s/2-1}(f_i + f_m)\exp(-j2\pi(f_i + f_m)(\tau_1 - \tau_2))$$

$$\frac{\partial \bar{\boldsymbol{r}}_m^{\mathrm{H}}(\boldsymbol{u})}{\partial \tau_2}\frac{\partial \bar{\boldsymbol{r}}_m(\boldsymbol{u})}{\partial \alpha_2} = -j\alpha_2 2\pi \sum_{i=-N_s/2}^{N_s/2-1}(f_i + f_m)$$

**A**

$$\frac{\partial \bar{\boldsymbol{r}}_m^{\mathrm{H}}(\boldsymbol{u})}{\partial \alpha_1} \frac{\partial \bar{\boldsymbol{r}}_m(\boldsymbol{u})}{\partial \alpha_1} = \frac{\partial \bar{\boldsymbol{r}}_m^{\mathrm{H}}(\boldsymbol{u})}{\partial \alpha_2} \frac{\partial \bar{\boldsymbol{r}}_m(\boldsymbol{u})}{\partial \alpha_2} = N_s$$

$$\frac{\partial \bar{\boldsymbol{r}}_m^{\mathrm{H}}(\boldsymbol{u})}{\partial \alpha_1} \frac{\partial \bar{\boldsymbol{r}}_m(\boldsymbol{u})}{\partial \alpha_2} = \sum_{i=-N_s/2}^{N_s/2-1} \exp(-j2\pi(f_i + f_m)(\tau_1 - \tau_2))$$

The FIM based on a single band OFDM signal is written by

$$\boldsymbol{F}_m(\boldsymbol{u}) = \frac{2}{\sigma^2} \begin{bmatrix} \boldsymbol{A}_m & \boldsymbol{B}_m \\ \boldsymbol{C}_m & \boldsymbol{D}_m \end{bmatrix}$$

$$[\boldsymbol{F}_m(\boldsymbol{u})]_{ij} = \frac{2}{\sigma^2} \Re \left[ \frac{\partial \boldsymbol{\mu}^{\mathrm{H}}(\boldsymbol{u})}{\partial u_i} \frac{\partial \boldsymbol{\mu}(\boldsymbol{u})}{\partial u_j} \right].$$

(A.19)

In addition, to simplify the notations, we define

$$\tilde{\boldsymbol{f}}_m = \begin{bmatrix} f_{i=-N_s/2} \\ f_{i=-N_s/2+1} \\ \vdots \\ f_{i=N/2-1} \end{bmatrix} + f_m, \quad \tilde{\boldsymbol{f}}_m^2 = \tilde{\boldsymbol{f}}_m \odot \tilde{\boldsymbol{f}}_{m'}$$

$$\boldsymbol{q}_m(\tau) = \begin{bmatrix} \cos(2\pi(f_m + f_{i=-N_s/2})\tau) \\ \cos(2\pi(f_m + f_{i=-N_s/2+1})\tau) \\ \vdots \\ \cos(2\pi(f_m + f_{i=N_s/2-1})\tau) \end{bmatrix},$$

$$\boldsymbol{p}_m(\tau) = \begin{bmatrix} \sin(2\pi(f_m + f_{i=-N_s/2})\tau) \\ \sin(2\pi(f_m + f_{i=-N_s/2+1})\tau) \\ \vdots \\ \sin(2\pi(f_m + f_{i=N/2-1})\tau) \end{bmatrix},$$

where $\odot$ denotes the dot product.

In addition, letting the relative delay as $\tau_{2,1} = \tau_2 - \tau_1$, the FIM in (A.19) can be given by

$$\boldsymbol{A}_m = \alpha_1^2 4\pi^2 \begin{bmatrix} \tilde{\boldsymbol{f}}_m^T \tilde{\boldsymbol{f}}_m & \frac{\alpha_2}{\alpha_1} \boldsymbol{q}_m^{\mathrm{T}}(\tau_{2,1}) \tilde{\boldsymbol{f}}_m^2 \\ \frac{\alpha_2}{\alpha_1} \boldsymbol{q}_m^{\mathrm{T}}(\tau_{2,1}) \tilde{\boldsymbol{f}}_m^2 & \frac{\alpha_2^2}{\alpha_1^2} \tilde{\boldsymbol{f}}_m^T \tilde{\boldsymbol{f}}_m \end{bmatrix}$$

$$\boldsymbol{B}_m = \alpha_1 2\pi \begin{bmatrix} 0 & \boldsymbol{p}_m^{\mathrm{T}}(\tau_{2,1}) \tilde{\boldsymbol{f}}_m \\ -\frac{\alpha_2}{\alpha_1} \boldsymbol{p}_m^{\mathrm{T}}(\tau_{2,1}) \tilde{\boldsymbol{f}}_m & 0 \end{bmatrix} = \boldsymbol{C}_m^{\mathrm{T}}$$

$$\boldsymbol{D}_m = \begin{bmatrix} N_s & \boldsymbol{1}_N^{\mathrm{T}} \boldsymbol{q}_m(\tau_{2,1}) \\ \boldsymbol{1}_N^{\mathrm{T}} \boldsymbol{q}_m(\tau_{2,1}) & N_s \end{bmatrix}.$$

## A.3. Flop Count

The computational complexity is evaluated by the number of required flops. First, we compute the required flops for time delay estimation, which is based on (3.27). Given $M_a$ signal bands with $N_s$ subcarriers in each of the bands, and considering an $L$-path propagation channel in the estimation model, the design matrix $\boldsymbol{A}(\boldsymbol{\tau})$ becomes an $M_aN_s$-by-$L$ matrix.

It should be noted that instead of computing the number of the flops separately for the imaginary part and the real part, the complex value component is treated as a single term when we compute the number of flops. In addition, for notation simplicity, the variable $\boldsymbol{\tau}$ is removed in the following derivations.

One can first analyse the computational complexity of the following term

$$\boldsymbol{B} = \left(\boldsymbol{A}^{\mathrm{H}}\boldsymbol{Q}_{\boldsymbol{H}}^{-1}\boldsymbol{A}\right)^{-1}\boldsymbol{A}^{\mathrm{H}}\boldsymbol{Q}_{\boldsymbol{H}}^{-1}\boldsymbol{H}, \tag{A.20}$$

which is part of the cost function (3.27), and can be rewritten by

$$\begin{aligned}\left(\boldsymbol{A}^{\mathrm{H}}\boldsymbol{Q}_{\boldsymbol{H}}^{-1}\boldsymbol{A}\right)\boldsymbol{B} &=\boldsymbol{A}^{\mathrm{H}}\boldsymbol{Q}_{\boldsymbol{H}}^{-1}\boldsymbol{H}\\ \boldsymbol{C}\boldsymbol{C}^{\mathrm{H}}\boldsymbol{B} &=\boldsymbol{r}.\end{aligned} \tag{A.21}$$

Given an $M_aN_s$-by-$M_aN_s$ variance matrix $\boldsymbol{Q}_{\boldsymbol{H}}$, the inverse of such a matrix requires $2(M_aN_s)^3/3$ flops [174]. However, it is only computed once, and will be applied for both time delay and carrier phase estimation. Therefore, the number of required flops for $\boldsymbol{Q}_{\boldsymbol{H}}^{-1}$ is not taken into consideration in the following derivations.

By applying the triangular decomposition (e.g., Cholesky decomposition), $\boldsymbol{A}^{\mathrm{H}}\boldsymbol{Q}_{\boldsymbol{H}}^{-1}\boldsymbol{A}$ $=\boldsymbol{C}\boldsymbol{C}^{\mathrm{H}}$ requires $L^3/3$ flops [174], when $L$ is larger than 1.

Let $\boldsymbol{z} = \boldsymbol{C}^{\mathrm{H}}\boldsymbol{B}$, one can have

$$\boldsymbol{C}\boldsymbol{z} = \boldsymbol{r}, \quad \boldsymbol{C}^{\mathrm{H}}\boldsymbol{B} = \boldsymbol{z}.$$

As shown in [121], to obtain an $L$-by-1 vector $\boldsymbol{z}$ requires $L^2$ flops. Afterwards, another $L^2$ flops are needed to obtain $\boldsymbol{B}$ from $\boldsymbol{z}$.

In addition, $L(M_aN_s)(2M_aN_s-1)$ flops are required to obtain $\boldsymbol{A}^{\mathrm{H}}\boldsymbol{Q}_{\boldsymbol{H}}^{-1}$, and $L^2(2M_aN_s-1)$ flops for $\boldsymbol{A}^{\mathrm{H}}\boldsymbol{Q}_{\boldsymbol{H}}^{-1}\cdot\boldsymbol{A}$, $(2M_aN_s-1)L$ flops for $\boldsymbol{A}^{\mathrm{H}}\boldsymbol{Q}_{\boldsymbol{H}}^{-1}\cdot\boldsymbol{H}$. Then, $M_aN_s(2L-1)$ flops are needed to compute $\boldsymbol{A}\boldsymbol{B}$, and $(M_aN_s)^2$ flops for $\boldsymbol{A}\boldsymbol{B}\cdot\boldsymbol{H}^{\mathrm{H}}$ to compute the cost function in (3.27). Finally, the *trace* requires $(M_aN_s - 1)$ flops.

Therefore, to compute the cost function (3.27) for each grid point, the number of required flops is derived by

$$\mathrm{flops}_{\mathrm{tde}} =(1 + 4L)(M_aN_s)^2 + 2(L^2 + L)(M_aN_s) + L^3/3 + L^2 - L - 1, \quad L > 1. \tag{A.22}$$

If there is only a single path considered in the simplified model for time delay estimation, the number of flops is given by

$$\mathrm{flops}_{\mathrm{tde}} = 5(M_aN_s)^2 + 4M_aN_s - 1, \quad L = 1. \tag{A.23}$$

Then the number of flops required for the complex gain estimation (3.24), from which the carrier phase of the LoS path is derived, is identical to the one in **B** as shown in (A.20), which is given by

$$\text{flops}_{\text{cge}} = 4L(M_a N_s)^2 + 2L^2(M_a N_s) + L^2 - L + L^3/3, \quad L > 1. \tag{A.24}$$

Similarly, if there is only path considered for carrier phase estimation, the number of flops is derived as

$$\text{flops}_{\text{cge}} = 4(M_a N_s)^2 + 2(M_a N_s), \quad L = 1. \tag{A.25}$$

## A.4. Correlation Function of OFDM Signal
### A.4.1. Single Band Signal

Based on the received signal and the locally generated reference signal (5.1) with BPSK modulation, the correlation function is written by

$$c_{sb}(\tilde{\tau}) = \frac{1}{N_s} \sum_{n=0}^{N_s-1} \frac{\exp\left(-j2\pi f_c \tau\right)}{\sqrt{N_p}} \sum_{i=0}^{N_p-1} \exp\left(j2\pi i P \Delta f (nT_s - \tau)\right) \exp\left(-j2\pi \frac{N_p P \Delta f}{2}(nT_s - \tau)\right)$$

$$\cdot \frac{1}{\sqrt{N_p}} \sum_{k=0}^{N_p-1} \exp\left(-j2\pi k P \Delta f (nT_s - \tilde{\tau})\right) \exp\left(j2\pi \frac{N_p P \Delta f}{2}(nT_s - \tilde{\tau})\right)$$

$$= \frac{\exp(-j2\pi f_c \tau)}{N_s N_p} \exp\left(j2\pi \frac{N_p P \Delta f}{2}(\tau - \tilde{\tau})\right) \sum_{i=0}^{N_p-1} \sum_{k=0}^{N_p-1} \exp\left(-j2\pi (i\tau - k\tilde{\tau}) P \Delta f\right)$$

$$\cdot \sum_{n=0}^{N_s-1} \exp\left(j2\pi \frac{i-k}{N_s} Pn\right),$$

(A.26)

where $P$ stands for the pilot spacing (if all subcarriers are used as pilots, then $P = 1$), $N_p$ denotes the number of pilots out of $N_s$ subcarriers in the OFDM signal, and $T_s$ denotes the sample interval, $\Delta f$ denotes the subcarrier spacing, $\tau$ stands for the propagation time delay, and $\tilde{\tau}$ denotes the variable of the correction function. Since

$$\sum_{n=0}^{N_s-1} \exp\left(j2\pi \frac{i-k}{N_s} n\right) = \frac{\sin\left(2\pi \frac{i-k}{2}\right)}{\sin\left(2\pi \frac{i-k}{2N_s}\right)} \exp\left(j2\pi \frac{i-k}{N_s} \frac{N_s-1}{2}\right),$$

and

$$\frac{\sin\left(2\pi \frac{i-k}{2}\right)}{\sin\left(2\pi \frac{i-k}{2N_s}\right)} = \begin{cases} N_s, & i = k \\ 0, & i \neq k \end{cases},$$

(A.26) can be rewritten by

$$c_{sb}(\tilde{\tau}) = \frac{\exp(-j2\pi f_c \tau)}{N_p} \exp\left(j\pi N_p P \Delta f (\tau - \tilde{\tau})\right) \sum_{i=0}^{N_p-1} \exp\left(-j2\pi i P \Delta f (\tau - \tilde{\tau})\right)$$

$$= \frac{\exp(-j2\pi f_c \tau)}{N_p} \exp\left(j\pi N_p P \Delta f (\tau - \tilde{\tau})\right) \exp\left(-j2\pi P \Delta f \frac{N_p-1}{2}(\tau - \tilde{\tau})\right) \quad \text{(A.27)}$$

$$\frac{\sin\left(2\pi \frac{N_p}{2} P \Delta f (\tau - \tilde{\tau})\right)}{\sin\left(2\pi \frac{1}{2} P \Delta f (\tau - \tilde{\tau})\right)}.$$

### A.4.2. Multiband Signal

Assuming each band has the same modulation given by (5.1), and the spacing be-tween two adjacent activated signal bands is $S\Delta f_G$, so the received signal from the $m$-th activated band is written by

$$
\begin{aligned}
r_m[n;\tau] =& \frac{\alpha_m}{N_p} \sum_{i=-N_p/2}^{N_p/2-1} \exp\left(j2\pi\frac{iP}{N_s}n\right) \exp\left(-j2\pi(iP\Delta f + (mS-M/2)\Delta f_G + f_c)\tau\right) \\
=& \frac{\alpha_m}{N_p} \sum_{i=0}^{N_p-1} \exp\left(j2\pi iP\Delta f(nT_s - \tau)\right) \exp\left(-j2\pi\frac{N_pP\Delta f}{2}(nT_s - \tau)\right) \\
& \exp\left(-j2\pi((mS-M/2)\Delta f_G + f_c)\tau\right), m = 1, \dots M_a,
\end{aligned}
\tag{A.28}
$$

where $M_a$ denotes the total number of activated signal bands for ranging,

$$
M_a = \lfloor \frac{M-1}{S} \rfloor + 1.
\tag{A.29}
$$

If all signal bands shown in Fig. 2.4 are used for ranging, then $M_a = M$ and $S = 1$.

In addition, if the multiband signal only appears in a certain range of the spec-trum (e.g., about hundreds of MHz), the attenuation $\alpha_m$ is approximately assumed to be the same. Hence, for simplicity, $\alpha_m$ is set to 1 for all $M_a$ activated signal bands. Combining the correlation function based on a single band OFDM signal (A.27), the correlation function of the multiband signal can be rewritten by

$$
\begin{aligned}
c_{mb}(\tilde{\tau}) =& \frac{1}{M_a} \sum_{m=1}^{M_a} \left( \sum_{n=0}^{N_s-1} r_m[n;\tau]s_m^*[n;\tilde{\tau}] \right) \\
=& c_{sb}(\tilde{\tau}) \frac{1}{M_a} \sum_{m=0}^{M_a-1} \exp\left(-j2\pi mS\Delta f_G(\tau-\tilde{\tau})\right) \exp\left(-j2\pi(M/2-S)\Delta f_G(\tau-\tilde{\tau})\right) \\
=& c_{sb}(\tilde{\tau}) \exp\left(-j2\pi(M/2-S)\Delta f_G(\tau-\tilde{\tau})\right) \exp\left(-j2\pi S\Delta f_G(\tau-\tilde{\tau})\frac{M_a-1}{2}\right) \\
& \frac{1}{M_a} \frac{\sin\left(2\pi S\Delta f_G(\tau-\tilde{\tau})T_s\frac{M_a}{2}\right)}{\sin\left(2\pi S\Delta f_G(\tau-\tilde{\tau})T_s\frac{1}{2}\right)}.
\end{aligned}
\tag{A.30}
$$

## **A.5.** Minimum Eigenvalue

Considering the following random $n$ dimensional vector $\underline{x}$

$$\underline{x} \sim \mathcal{N}\left(\bar{x} \in \mathbb{R}^{N_u}, Q_{xx} \in \mathbb{R}^{N_u \times N_u}\right) \tag{A.31}$$

we can have the following inequality (i.e., Chebyshev's inequality)

$$P\left(\|\underline{x} - \bar{x}\|_2^2 \geq r_e^2\right) \leq \frac{\text{trace}(Q_{xx})}{r_e^2}, \tag{A.32}$$

and

$$P\left(\|\underline{x} - \bar{x}\|_2^2 \leq r_e^2\right) \geq 1 - \frac{\text{trace}(Q_{xx})}{r_e^2}. \tag{A.33}$$

Now, the estimator is assumed to be constrained in an origin-centered circle of radius $r_e$, with a probability larger than $P_e$ (i.e., $P\left(\|\underline{x} - \bar{x}\|_2^2 \leq r_e^2\right) \geq P_e$). One can have the following sufficient condition

$$P_e \leq 1 - \frac{\text{trace}(Q_{xx})}{r_e^2}, \tag{A.34}$$

and

$$\text{trace}(Q_{xx}) \leq (1 - P_e)r_e^2. \tag{A.35}$$

Here, as the variance matrix $Q_{xx}$ is presented by the CRLB, one can have the following inequality

$$\text{trace}(Q_{xx}) \leq \frac{N_u}{\lambda_{\min}\{\text{FIM}\}} \leq (1 - P_e)r_e^2, \tag{A.36}$$

where $\lambda_{\min}\{\text{FIM}\}$ denotes the minimum eigenvalue of the FIM. Now, we can derive the lower bound for the minimum eigenvalue of the FIM, which is given by

$$\lambda_{\min}\{\text{FIM}\} \geq \frac{N_u}{(1 - P_e)r_e^2}. \tag{A.37}$$

# Notation

$\mathbb{E}\{\cdot\}$        expectation
$\mathbb{D}\{\cdot\}$        variance
$\mathbb{R}^n$        $n$-dimensional space of real variables
$\mathbb{C}^n$        $n$-dimensional space of complex variables
$\mathbb{Z}^n$        $n$-dimensional space of integer variables
$\boldsymbol{I}_N$        identity matrix of size $N$
$\boldsymbol{1}_N$        $N$-by-1 vector of 1
$(\cdot)^{\mathrm{T}}$        transposition
$(\cdot)^*$        conjugate
$(\cdot)^{\mathrm{H}}$        Hermitian operation
$\sum$        summation
$\int$        integral
$\overset{\scriptstyle{(\cdot)}}{}$        random variable
$\widehat{(\cdot)}$        estimate
$j$        imaginary unit
$\Re\{\cdot\}$        real part of a complex value
$\Im\{\cdot\}$        imaginary part of a complex value
$\mathscr{F}$        Fourier transform
$\mathscr{F}_l$        low-pass filter
$\mathrm{tr}\{\cdot\}$        trace of a matrix
$\mathrm{diag}(\cdot)$        diagonal matrix formed by its vector argument
$\det(\cdot)$        determinant of a matrix
$\mathrm{avg}\{\cdot\}$        average of a vector
$\arg\{\cdot\}$        argument of a complex value
$[\cdot]_{i,j}$        element in the $i$-th row and the $j$-th column of a matrix
$[\cdot]_i$        the $i$-th element in a column vector
$\mathscr{N}(\boldsymbol{\mu}, \boldsymbol{Q})$        Gaussian distribution with mean $\boldsymbol{\mu}$ and variance matrix $\boldsymbol{Q}$
$\mathscr{C}\mathscr{N}(\boldsymbol{\mu}, \boldsymbol{Q})$        complex Gaussian distribution with mean $\boldsymbol{\mu}$ and variance matrix $\boldsymbol{Q}$
$\chi^2(n, \lambda)$        noncentral Chi-square distribution with $n$ degrees of freedom and noncentrality parameter $\lambda$
$\|\boldsymbol{x}\|^2$        Euclidean norm ($\|\boldsymbol{x}\|^2 = \boldsymbol{x}^{\mathrm{T}}\boldsymbol{x}$)
$\|\boldsymbol{x}\|_1$        $l_1$ norm ($\|\boldsymbol{x}\|_1 = |x_1| + ... + |x_N|$, $\boldsymbol{x} \in \mathbb{R}^N$)
$H$        vector of channel frequency response
$A$        generic symbol for a design matrix
$\boldsymbol{u}$        generic symbol for a vector of unknowns

uppercase boldface letters (e.g., $\boldsymbol{F}$, except $H$) are generally used for matrices, and lowercase boldface letters (e.g., $\boldsymbol{r}$) are used for column vectors.

# List of Acronyms

| | |
|---|---|
| ACF | autocorrelation function |
| AoA | angle-of-arrival |
| ARP | antenna reference point |
| BOC | binary offset carrier |
| BPSK | binary phase shift keying |
| CDF | cumulative distribution function |
| CDMA | code division multiple access |
| CFO | carrier frequency offset |
| CIR | channel impulse response |
| CP | cyclic prefix |
| CPE | carrier phase estimation |
| CRLB | Cramér-Rao lower bound |
| ESPRIT | Estimation of Signal Parameters via Rotational Invariance Technique |
| FIM | Fisher information matrix |
| FSPL | free-space path loss |
| GB | Gabor bandwidth |
| GNSS | global navigation satellite systems |
| ICI | inter-channel interference |
| (I)FFT | (inverse) fast Fourier transform |
| ISI | inter-symbol interference |
| LAMBDA | Least-squares AMBiguity Decorrelation Adjustment |
| LoS | line-of-sight |
| LS(E) | least-squares (estimation) |
| MF | matched filter |
| MIMO | multiple-input and multiple-output |
| ML(E) | maximum likelihood (estimation) |
| MUSIC | MUltiple SIgnal Classification |
| NCO | numerically controlled oscillator |
| NFO | normalized frequency offset |
| NLoS | non-line-of-sight |
| OFDM | orthogonal frequency division multiplexing |
| PCO | phase center offset |
| PCV | phase center variation |
| PDF | probability density function |
| PDoA | phase-difference-of-arrival |
| PLL | phase locked loop |
| PoA | phase-of-arrival |

| | |
|---|---|
| PPM | part-per-million |
| PPS | pulse-per-second |
| PPP | precise point positioning |
| PRN | pseudo-random noise |
| PSD | power spectral density |
| (R)MSE | (root) mean-square-error |
| RSS | received signal strength |
| RTK | real-time kinematic |
| Rx | receiver |
| SC | subcarrier |
| SFO | sampling frequency offset |
| SNR | signal-to-noise ratio |
| SOP | signal-of-opportunity |
| TDoA | time-difference-of-arrival |
| TDM | time division multiplexing |
| TDE | time delay estimation |
| ToA | time-of-arrival |
| Tx | transmitter |
| USRP | Universal Software Radio Peripheral |
| UWB | ultra wideband |
| WR-PTP | White-Rabbit precision time protocol |

# List of Publications

## Journal Publications

[J1] **H. Dun**, C. Tiberius, G. Janssen (2020), *Positioning in a Multipath Channel Using OFDM Signals with Carrier Phase Tracking*, IEEE Access, Vol. 8, pp. 13011-13028. ([108])

[J2] **H. Dun**, C. Tiberius, C. Diouf, and G. Janssen (2021), *Design of Sparse Multiuband Signal for Precise Positioning with Joint Low Complexity Time Delay and Carrier Phase Estimation*, IEEE Transactions on Vehicular Technology, vol. 70, no. 4, pp. 3552-3567. ([82])

[J3] **H. Dun**, C. Tiberius, C. Diouf, and G. Janssen (2021), *Terrestrial Precise Positioning with Asynchronous Receiver Based on Carrier Phase through Burst Wideband Signals* (under review)

[J4] C. Diouf, G. Janssen, **H. Dun**, T. Kazaz, and C. Tiberius, (2021), *A USRP based testbed for wideband ranging and positioning signal acquisition*, IEEE Transactions on Instrumentation and Measurement, vol. 70, pp. 1-15 ([161])

## Conference Publications

[C1] **H. Dun**, C. Tiberius, and G. Janssen (2018), *Positioning based on OFDM Signals through Phase Measurements*, in proceedings of ESA Workshop on Satellite Navigation Technologies and European Workshop on GNSS Signals and Signal Processing (NAVITEC), pp. 1-9.([107])

[C2] **H. Dun**, C. Tiberius, G. Janssen, and C. Diouf (2019), *Time Delay Estimation Based on Multi-band Multi-carrier Signal in Multipath Environments*, in Proceedings of the 32nd International Technical Meeting of the Satellite Division of The Institute of Navigation (ION GNSS+ 2019), September 16 - 20, Miami, Florida, pp. 2299-2313. ([123])

[C3] **H. Dun**, C. Tiberius, C. Diouf, and G. Janssen (2020), *Sparse Signal Bands Selection for Precise Time-based Ranging in Terrestrial Positioning*, in Proceedings of IEEE/ION Position, Location and Navigation Symposium (PLANS), April, pp. 1372-1380. ([130])

[C4] **H. Dun**, C. Tiberius, C. Diouf, and G. Janssen (2021), *Terrestrial Precise Positioning System Using Carrier Phase from Burst Signals and Optically Distributed Time and Frequency Reference*, in Proceedings of The Institute of Navigation International Technical Meeting (ION ITM), January, 25-28, pp. 510-524.([135])

[C5] C. Diouf, **H. Dun**, T. Kazaz, G. Janssen and C. Tiberius (2020), *Demonstration of a decimeter-level accurate hybrid optical-wireless terrestrial positioning system*,

in Proceedings of the 33rd International Technical Meeting of the Satellite Division of the Institute of Navigation, ION GNSS+ 2020), pp. 2220-2228.([159])

[C6] C. Diouf, G. Janssen, T. Kazaz, **H. Dun**, and C. Tiberius (2019), *A 400 Msps SDR platform for prototyping accurate wideband ranging techniques*, in Proceedings of 2019 16th Workshop on Positioning, Navigation and Communications (WPNC), October, 23, pp. 1-6. ([160])

# Curriculum Vitæ

Han Dun (顿涵), was born in Hubei, China, in 1991, and raised in Guangdong, China. In 2013, he received his B.E. degree in Communication Engineering from Shanghai University with a thesis on communication network performance analysis. In 2016, he received his M.E. degree in Communication and Information System from Shanghai University with a thesis on OFDM-PON (Orthogonal Frequency Division Multiplex Passive Optical Network). In the same year, he joined the department of Geoscience and Remote Sensing, Delft University of Technology, as a Ph.D. student. His doctoral research is funded by the Dutch Research Council (NWO) with the project "SuperGPS: Accurate timing and positioning through an optical-wireless distributed time and frequency reference".

# Acknowledgements

My PhD journey finally comes to the end, and it would not have been possible without the help from many people. I would like to take this opportunity to express my gratitude.

Foremost, I would like to thank my supervisor and promotor Dr. Christian Tiberius who offered me an opportunity to pursue my PhD degree in TU Delft, and also introduced me to the field of positioning. He is always patient, optimistic, supportive, and gave me much freedom on my research. It has been a great pleasure working with him. Particularly, I would also like to thank him for making a lot of creative non-electrical components and devices for both indoor and outdoor experiments, and the hard-work during the field trials at The Green Village. In addition, I would like to thank my promotor Prof. Ramon Hanssen, who gave me many useful advice for my research.

I am also deeply grateful to my co-supervisor Dr. Gerard Janssen, for the insightful discussions and constructive comments, and acting as our hardware consultant. I would also like to thank Dr. Jeroen Koelemeij from Vrije Universiteit Amsterdam, who is the initiator of the SuperGPS-project, for his supports and encouragement.

The experiments presented in this thesis would not be possible without Dr. Cherif Diouf, who developed the SuperGPS prototype system. I am also grateful for his friendship, great companion and support over the past two and half years. I would also like to thank Tarik Kazaz, my colleague PhD candidate in the SuperGPS-project, for the discussions in the project meetings.

Besides, I would like to thank Hans van der Marel and René Reudink for providing GNSS receivers, total stations and auxiliary surveying equipment, Lolke Boonstra and Terence Theijn from TU-Delft ICT-FM for their expertise and support on the optical infrastructure, Erik Dierikx of VSL and Rob Smets of SURF for providing the time-frequency reference, and Loek Colussi and Frank van Osselen of Agentschap Telecom, and René Tamboer and Tim Jonathan of The Green Village for their support in realizing the SuperGPS prototype and the experiment at The Green Village.

I would like to thank Sandra Verhagen, Dimitrios Psychas, Hongyang Ma and Lotfi Massarweh, for the insightful discussions on carrier-phase-based positioning. I am also thankful to Lidwien de Jong, Debbie Rietdijk and Suzanne de Hoog-Dollée from Geoscience and Remote Sensing (GRS) and Irma Zomerdijk from Circuits and Systems (CAS) for their administrative assistance.

It has been a great time working in GRS, and I would like to thank Christos Gatidis, Reenu Toodesh, Marcel Kleinherenbrink, Ricardo Reinoso Rondinel, Kaixuan Zhou, Jiapeng Yin, Ling Chang, Yuanhao Li, Bowen Li and Andreas Theodosious, Gert Mulder, Antoon van Hooft, Kevin Helfer, Yi Dai, Yuan Yan, Deqing

Mao, Tina Nikaein, and many former and current fantastic GRS colleagues, for their support and coffee/beer talks. I would also like to thank Elyta Widyanngrum, Lorenzo Iannini, Weiran Li, Vishal Dixit, Michelle Petrini for their lunch talks before the COVID-19 pandemic. Special thanks go to Christian Tiberius, Gerard Janssen and Mariska Koning for helping me translate the summary into Dutch.

I would like to also express my deepest appreciation to all committee members, for their time and comments.

Finally, I would like to thank my girlfriend Qiuhui Tang, for her joyful companion and understanding, and my parents Yaojun Dun and Jingzhi Shen, for their unconditional supports.

<div align="right">

Han Dun
May 2021
Rijswijk, The Netherlands

</div>